

Industrial PECVD AlO_x films with very low surface recombination for Silicon Solar Cells

Kyung Hun Kim

A thesis in fulfilment of the requirements for the degree of
Doctor of Philosophy



School of Photovoltaics and Renewable Energy Engineering
Faculty of Engineering

March 2019

THE UNIVERSITY OF NEW SOUTH WALES**Thesis/Dissertation Sheet**

Surname/Family Name : **Kim**
Given Name/s : **Kyung Hun**
Abbreviation for degree as give in the University calendar : **Doctor of Philosophy**
Faculty : **Faculty of Engineering**
School : **School of Photovoltaics and Renewable Energy Engineering**
Thesis Title : **Industrial PECVD AlO_x films with very low surface recombination for silicon solar cells**

Abstract

Aluminium oxide (AlO_x) plays a critical role in increasing silicon solar cell efficiency and is used as a rear side surface passivation layer for the passivated emitter and rear cell (PERC). Although the majority of commercial silicon solar cells are based on the PERC structure, there is still insufficient knowledge available in literature regarding the properties of the AlO_x layer. In this thesis, the impact of deposition parameters on surface passivation quality is studied. It is found that plasma power must be sufficient in order to ionise the precursor gases to acquire thermally stable AlO_x layer. The ratio between the precursor gases is also found to have a significant impact on the surface passivation quality in both as-deposited and fired states. Interestingly, despite the large difference in precursor gas ratios, which leads to AlO_x layers having different properties, all these layers are found to be almost stoichiometric. Further investigation indicates that the different surface passivation results may be explained by the different hydrogen depth profile across the AlO_x . Apart from chemical composition, change in the interfacial layer between silicon (Si) and AlO_x layer also has a strong impact on passivation quality. Nano-scale investigation of the Si/ AlO_x interface reveals that a thermal process after the AlO_x deposition can change its properties drastically. Thicker silicon oxide layer at the Si/ AlO_x interface effectively reduces the interface defect densities. The subsequent thermal process also changes the chemical configuration of the AlO_x layer and it is shown to be the origin of negative charge (Q_{tot}) within the layer. It is found that the ratio of the two chemical configurations (tetrahedral- to octahedral- aluminium ratio) and the resulting Q_{tot} has a linear relationship. The root cause of surface passivation degradation at elevated temperature in the dark is also investigated. It is hypothesised that hydrogen may have a dominant role in the degradation. Using different sample structures, the modulated effective lifetime is correlated with hydrogen migration between the Si surface and the bulk.

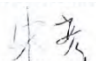
Declaration relating to disposition of project thesis/dissertation

I hereby grant to the University of New South Wales or its agents the right to archive and to make available my thesis or dissertation in whole or in part in the University libraries in all forms of media, now or here after known, subject to the provisions of the Copyright Act 1968. I retain all property rights, such as patent rights. I also retain the right to use in future works (such as articles or books) all or part of this thesis or dissertation.

I also authorise University Microfilms to use the 350 word abstract of my thesis in Dissertation Abstracts International (this is applicable to doctoral theses only).



Signature



Witness Signature

.....29/03/2019.....

Date

The University recognises that there may be exceptional circumstances requiring restrictions on copying or conditions on use. Requests for restriction for a period of up to 2 years must be made in writing. Requests for a longer period of restriction may be considered in exceptional circumstances and require the approval of the Dean of Graduate Research.

FOR OFFICE USE ONLY

Date of completion of requirements for Award:

Originality Statement

‘I hereby declare that this submission is my own work and to the best of my knowledge it contains no materials previously published or written by another person, or substantial proportions of material which have been accepted for the award of any other degree or diploma at UNSW or any other educational institution, except where due acknowledgement is made in the thesis. Any contribution made to the research by others, with whom I have worked at UNSW or elsewhere, is explicitly acknowledged in the thesis. I also declare that the intellectual content of this thesis is the product of my own work, except to the extent that assistance from others in the project's design and conception or in style, presentation and linguistic expression is acknowledged.’



Signed.....

Date.....29/03/2019.....

..

COPYRIGHT STATEMENT

'I hereby grant the University of New South Wales or its agents a non-exclusive licence to archive and to make available (including to members of the public) my thesis or dissertation in whole or part in the University libraries in all forms of media, now or here after known. I acknowledge that I retain all intellectual property rights which subsist in my thesis or dissertation, such as copyright and patent rights, subject to applicable law. I also retain the right to use all or part of my thesis or dissertation in future works (such as articles or books).'

'For any substantial portions of copyright material used in this thesis, written permission for use has been obtained, or the copyright material is removed from the final public version of the thesis.'



Signed

Date29/03/2019.....

AUTHENTICITY STATEMENT

'I certify that the Library deposit digital copy is a direct equivalent of the final officially approved version of my thesis.'



Signed

Date29/03/2019.....

INCLUSION OF PUBLICATIONS STATEMENT

UNSW is supportive of candidates publishing their research results during their candidature as detailed in the UNSW Thesis Examination Procedure.

Publications can be used in their thesis in lieu of a Chapter if:

- The student contributed greater than 50% of the content in the publication and is the “primary author”, ie. the student was responsible primarily for the planning, execution and preparation of the work for publication
- The student has approval to include the publication in their thesis in lieu of a Chapter from their supervisor and Postgraduate Coordinator.
- The publication is not subject to any obligations or contractual agreements with a third party that would constrain its inclusion in the thesis

Please indicate whether this thesis contains published material or not.

☐

This thesis contains no publications, either published or submitted for publication (if this box is checked, you may delete all the material on page 2)

☒

Some of the work described in this thesis has been published and it has been documented in the relevant Chapters with acknowledgement (if this box is checked, you may delete all the material on page 2)

☐

This thesis has publications (either published or submitted for publication) incorporated into it in lieu of a chapter and the details are presented below

CANDIDATE'S DECLARATION

I declare that:

- I have complied with the Thesis Examination Procedure
- where I have used a publication in lieu of a Chapter, the listed publication(s) below meet(s) the requirements to be included in the thesis.

Name: Kyung Hun Kim

Signature:



Date (dd/mm/yy): 29/03/19

Postgraduate Coordinator's Declaration (to be filled in where publications are used in lieu of Chapters)

I declare that:

- the information below is accurate
- where listed publication(s) have been used in lieu of Chapter(s), their use complies with the Thesis Examination Procedure
- the minimum requirements for the format of the thesis have been met.

PGC's Name

PGC's Signature

Date (dd/mm/yy)

Acknowledgement

Firstly, I would like to express my deepest gratitude to my supervisor Dr. Ziv Hameiri. I have learnt a lot from you, not only about the academic research process but also about the resolution of various types of problems with logic. You consistently demonstrated your motivation, passion, pride and much more to me, always with positive and supportive language. I have really enjoyed working with you. Thank you for your continuous support and guidance, for sharing your intelligence and knowledge. The lessons I have learnt from you will be a great asset for my carrier and life ahead.

I was also very fortunate to have Dr. Saul Winderbaum as my joint-supervisor. I enjoyed our discussions and your knowledge of PECVD was always enlightening. I also really appreciate your consultation on the journey of a life dedicated to research. I would also like to thank Prof. Chee Mun Chong as my co-supervisor. I appreciate your encouragement throughout my degree. Our many industry-related conversations have kept me from being too biased and have allowed me to balance academic and industrial topics in my research.

I cannot forget to thank my former co-supervisor Prof. Stuart Wenham. I was really lucky to have you in my supervision team. I would like to thank to all your kindness, warm-hearted supervision and sharing your stories. I hope you rest in peace and please do not worry. We will take it from now.

I want to express my huge appreciation for the SIRF team: Angus, Ly, Nino, Alex K., Huy and Fred. If you hadn't done such a wonderful job keeping SIRF running in great condition, this thesis would not have been possible. I have really enjoyed working with you and I appreciate your kindness in treating me as a team member. I would call SIRF my nest (not only because of the coffee machines and hammocks). I will miss you all.

Of course, I would like to thank the whole LDOT team. I appreciate your keeping the labs and equipment running. In particular, I would like to acknowledge Mark and Tom. The hands-on work and discussions on the PECVD system installation and modification were a really valuable experience during my PhD.

I cannot forget to thank all of our CCD group members (Ziv's kids). It is a great team and I respect your work ethic, your individual expertise and genuine passion to **Save the World!** Let's keep in touch and go forward to **Save the World Together!**

My appreciation is also for the 1st Gen. Group. I have learnt a lot from you in particular Mal, Brett, Cath, Ali, Dave, Michael, Phill, Ned, Ran, Dan and Moonyong. Thank you all for such a great team work and immediate discussions.

I also really thank my SERIS friends. Shubham, Naomi and Xin. Your willingness to share your knowledge and your active collaboration have made this thesis much improved. I also appreciate your effort and time for fruitful discussion for a couple of great journal papers.

To all my friends, I like you all and thank you all for everything. Oliver, Rob D, Yan, Carlos, Justin, Alex T and Mattias, casual talks and playing sports on campus have been wonderful for refreshing my spirits and keeping me running for the goal. I would like to express appreciation to my friends in Korean society (Korean gangs). Jongsung, Jae, Jincheol and Daseul, you are great guys. Speaking and having jokes in Korean were such relaxing moments for me. I am sure we will keep working on saving Korea! My old friends here and there, in particular, I would like to thank OAK members. I appreciate our trust and respect each other, which made our relationship so strong and I really appreciate your encouraging me all the time. My old friend Young and Jay, you have made my life since I was young, and I have to say I have relied on you guys when I feel difficulties.

Johannes, I particularly appreciate your comments till the end. I am lucky that I could have you as a friend and a reviewer. I also appreciate your advice on the life in Germany.

Captain Craig is my life saver. Your huge support and advice to polish this thesis until the last minute is highly appreciated. Yes, I agree that you are worth being promoted to Major Craig!

My special thanks to my wife Su Jin and my daughter Dain. Making my mind up to build a family in the 3rd year of PhD was not an easy decision. However, it was possible only because it was you! I am really grateful for your support, patience and understanding. Dain, my lovely five-month-old daughter, thank you for coming to us and I am really happy that I can write your name here as our new family member. I am proud of you and I love you!

Finally, to my parents and my sister, thank you for your constant support and encouraging me with love. I can never repay all that you have done for me. Thank you and I love you.

Table of Contents

1	Introduction	1
1.1	Climate change	1
1.2	Thesis objectives	3
1.3	Thesis outline.....	4
2	Review: Surface passivation.....	6
2.1	Recombination theory	6
2.1.1	Radiative recombination.....	7
2.1.2	Auger recombination	7
2.1.3	Recombination via defect levels	8
2.2	Surface recombination theory and passivation	9
2.3	Evaluation of surface recombination.....	10
2.4	Aluminium oxide for surface passivation.....	14
2.4.1	Aluminium oxide for PV applications.....	15
2.4.2	ALD-deposited Al_2O_3 and PECVD-deposited AlO_x layers.....	15
2.4.3	Thermal annealing and stability of the surface passivation.....	17
2.4.4	Properties of PECVD AlO_x layers.....	18
2.5	Other dielectric layers for surface passivation.....	20
2.5.1	Silicon nitride (SiN_x)	20
2.5.2	Silicon oxide (SiO_x).....	21
2.6	Chapter summary.....	22
3	Experimental methods	23
3.1	Design of experiments and statistical analysis	23
3.2	Sample preparation	24
3.2.1	Sample structure	24
3.2.2	Sample preparation.....	24
3.3	Deposition systems	25
3.3.1	Overview of the deposition system	26
3.3.2	Design of shower head	27
3.3.3	Deposition mechanism	27
3.3.4	Uniformity	28
3.3.5	Temperature profile	30
3.4	Characterisation methods	31
3.4.1	Photoconductance measurements	31
3.4.2	Contactless capacitance-voltage (CV) measurements	35
3.4.3	Fourier transform infrared (FTIR) spectroscopy	37
3.5	Chapter summary.....	38
4	Investigation of PECVD AlO_x layer on c-Si surface passivation.....	40

4.1	Introduction.....	40
4.2	Experiments	42
4.2.1	Design of experiment	42
4.2.2	Sample Preparation	43
4.2.3	Characterisation	44
4.3	Result and discussion.....	45
4.3.1	Thermal stability	45
4.3.2	Electrical properties	46
4.3.3	Chemical Properties	59
4.3.4	Hydrogen in the layer.....	62
4.3.5	Chemical composition.....	63
4.4	Summary	65
5	Interface study of c-Si/AlO _x	67
5.1	Introduction.....	67
5.2	Experiments	68
5.3	Results and discussion	70
5.4	Chapter summary	82
6	Degradation of surface passivation and bulk in <i>p</i> -type c-Si wafers at elevated temperature 83	
6.1	Motivation: Degradation in silicon solar cells	83
6.2	Experiments	84
6.3	Different effects of various surface passivation layers	87
6.3.1	c-Si/SiN _x structure.....	87
6.3.2	c-Si/AlO _x /SiN _x structure	89
6.3.3	<i>n</i> ⁺ /SiN _x structure.....	93
6.3.4	<i>n</i> ⁺ /SiO ₂ structure.....	95
6.3.5	Lifetime fitting using Quokka 2.....	96
6.4	Proposed hydrogen-based models.....	97
6.5	Chapter summary	100
7	Conclusions.....	101
7.1	Main conclusions and original contributions	101
7.2	Future works	103
	Appendix 1: Publications list	105
	Appendix 2: List of acronyms.....	107
	Appendix 3: Plasma diagnostics for remote PECVD process	108
	Bibliography	119

1 Introduction

1.1 Climate change

Numerous reports have demonstrated evidence of *climate change* particularly in the last half century [1]–[3]. The reason is the greenhouse effect caused not only by carbon dioxide (CO₂) mainly emitted by fossil fuel usage [1], [4] but also by other gases such as methane, nitrous oxide and ozone. Fig. 1-1 shows the annual global temperature anomaly. Although there are slight variations year to year, all the five institutes show temperature rise in a good agreement with each other. It is clear that rapid temperature rise has been occurring for the last few decades.

Fig. 1-2 shows northern-hemisphere temperature of every month since 1880 as reported by NASA, which could be a representative indicator of climate change since nearly 90% of the human population is in the northern-hemisphere. It shows the monthly temperature difference above or below the annual mean temperature between 1980 and 2015. The figure also shows that the temperature has been rising for the last few decades by almost 2 °C. Climate change has been shown to cause abnormal weather such as drought and floods, which also threatens the extinction of species [5].

In addition to global warming blamed on fossil fuel usage, we have to cope with increasing global energy consumption at the same time. We have to manage both reducing conventional fossil fuel usage and increasing energy demands. Therefore, we need alternative types of energy generation which are clean, efficient and applicable for a large amount of energy generation. There are several alternative energies to fossil fuels. Nuclear energy is one of the most commonly-mentioned energy types. However, nuclear plants have been an issue due to their safety concerns.

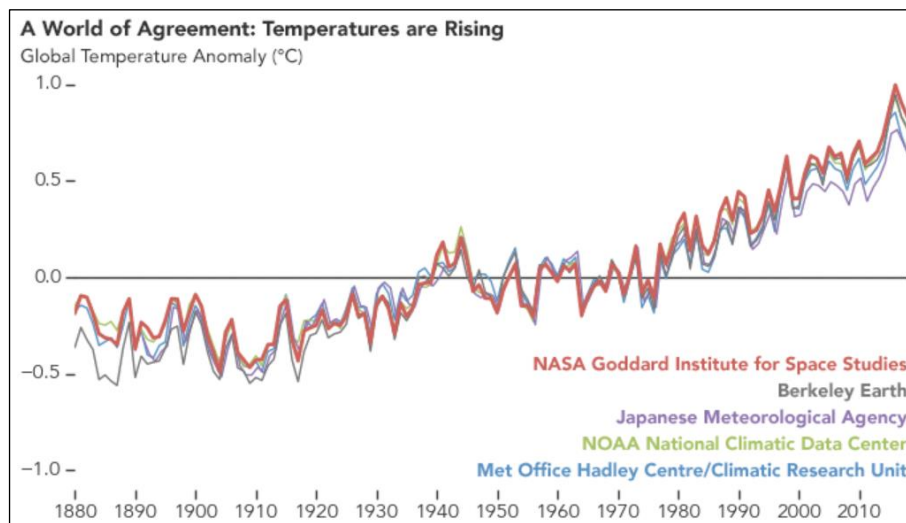


Fig. 1-1. Temperature anomalies from 1880 to 2018 with respect to the mean temperature between 1951 and 1980 (Source: <https://svs.gsfc.nasa.gov/13142>).

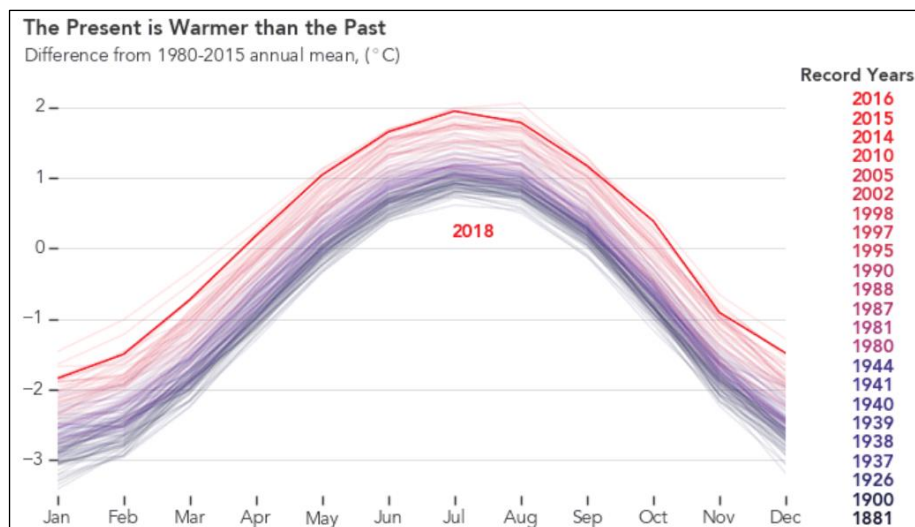


Fig. 1-2. Seasonal cycle in northern-hemisphere temperature anomalies of every month since 1880 (Source: <https://svs.gsfc.nasa.gov/13142>)

The concerns have increased especially after tragic accidents such as the Fukushima nuclear accident in Japan in 2011. Even when plants are managed to run safely, the waste disposal, human health concerns, the limited supply of uranium, and their cost are inherent problem of the nuclear energy. It cannot be a long-term solution to increasing energy consumption.

Therefore, renewable energies such as solar energy, wind energy and biomass energy have been receiving attention. Fortunately, the necessity of renewable energy has been acknowledged by almost all of the countries in the world according to the *Paris Agreement* in 2015 (although the USA withdrew from the Paris Agreement in 2017). These countries have been putting their efforts to reduce greenhouse gas emission and

transforming the energy generating paradigm forward to renewable energies. The cost of renewable energy was once a barrier to large-scale uptake, but the costs have been decreasing significantly for the last decade. As of January 2018 global average photovoltaic (PV) schemes cost USD 0.10 per kWh which is a comparable cost to fossil fuels (which range from USD 0.05 to 0.14 per kWh [6]). Amongst the various types of renewable energies, solar energy is commonly considered as the most powerful technology mainly due to almost infinite amount of energy from the sun. The energy earth receives from the sun each hour is more than the entire global energy consumption for a whole year [7]. Increasing the use of solar energy will slow down climate change and deal with increasing energy demands.

To make clean solar energy a more commonly used energy source, there have been three major ongoing efforts on the following aspects: (1) increasing the solar cell energy conversion efficiency, (2) enhancing the long-term stability (minimising degradation) and (3) reducing the manufacturing cost. Amongst these three topics this thesis focuses on the first two approaches. The detail of the two motivations are presented in the following section.

1.2 Thesis objectives

The objectives of this thesis are (1) to increase crystalline silicon (c-Si) solar cells energy conversion efficiency and (2) to minimise the degradation of c-Si solar cells amongst the mentioned three major aspects of efforts in solar energy.

With regard to the increasing the c-Si solar cell efficiency, improving the *surface passivation* quality of the c-Si solar cell is the first major objective. In detail, as wafer thickness decreases, the influence of the recombination losses (a detailed discussion regarding recombination is presented in *Section 2.2*) at the Si surface on the solar cell efficiency significantly increases [8]. More importantly, we have reached the efficiency limit of what can be done with the *p*-type Si solar cell with aluminium back surface field (Al-BSF: applied on the rear side surface the solar cell) given the same Si wafer thickness.

Therefore, improving the surface passivation quality becomes more important. The passivated emitter and rear cell (PERC) structure is an example for a solar cell design with improved rear surface passivation by aluminium oxide (commonly written as Al_2O_3 or AlO_x) [9]. The improved efficiency has made PERC a dominant industrial Si solar cell in the last few years [9]. It has been regularly predicted that PERC will continue to

be the dominant Si solar cell technology for at least the next decade [10]–[13]. As most of the major PV manufacturers produce PERC, AlO_x ¹ has become a key dielectric layer [9]. Despite its wide use in PV manufacturing, there are still significant knowledge gaps regarding this material. In particular, the investigation of AlO_x layers deposited by *industrial-type* plasma-enhanced chemical vapor deposition (PECVD) systems has become more necessary, as the majority of the studies so far have been based on Al_2O_3 layers deposited by atomic layer deposition (ALD) systems [14]–[17]. Therefore, the first objective of this thesis is to investigate the properties of the AlO_x layer deposited by an industrial PECVD system and to investigate the interface between the c-Si and the AlO_x layer, where the surface recombination occurs.

Reducing the degradation of the solar cell efficiency is also important. Moreover, a recent report by the US Department of Energy indicates that reducing the degradation of PV systems is a very promising method of lowering the price of PV energy [18], especially considering that increasing the efficiency is becoming more difficult as the fundamental limit [19] is approached. Therefore, improving the reliability of PV systems is a key requirement for making PV energy cheaper. Although degradation of AlO_x surface passivation under illumination and at elevated temperatures has been previously reported [20], [21], the mechanism and root cause are not yet known. Therefore, the second objective of this thesis is to investigate the possible root cause of this degradation which in turn can serve as the foundation for resolving this degradation issue.

1.3 Thesis outline

This thesis consists of two main parts; the first (Chapters 4 and 5) studies properties of various compositions of industrial type PECVD AlO_x layers and the c-Si/ AlO_x interface whereas the second part (Chapter 6) investigates the degradation mechanisms of the c-Si using different types of surface passivation layers.

Chapter 2 reviews the different types of recombination mechanisms in Si solar cells. The recombination mechanisms and the concept of the effective lifetime are discussed. A detailed study of the surface passivation quality evaluation methods is also presented. A summary of the previous studies regarding AlO_x and Al_2O_3 as surface passivation layers is presented. Knowledge gaps regarding the AlO_x properties are identified. Other

¹ Hereafter I use the term ' AlO_x ' because almost all PV manufacturers use plasma enhanced chemical vapor deposition (PECVD) due to its high throughput whereas ' Al_2O_3 ' is the term for stoichiometric deposition techniques such as atomic layer deposition (ALD).

dielectric layers such as silicon nitride (SiN_x) and silicon oxide (SiO_x) which are used in this thesis are also briefly introduced.

Chapter 3 describes the experimental methods used in this thesis. It reviews the sample preparation and the characterisation techniques, as well as the PECVD system used for this project. The chapter also discusses the procedures from design of the experiments to the evaluation and the analysis of the experiments.

Chapter 4 studies the impact of the main deposition conditions on the electrical and chemical properties of the AlO_x layers. Comparison of the AlO_x surface passivation efficacy on the *p*-type and *n*-type c-Si surfaces is also investigated. The conclusions of this chapter may be particularly useful for PV manufacturers since it clearly correlates the deposition conditions with the surface passivation performance.

Chapter 5 focuses on the sub-nano scale of the c-Si/ AlO_x interface. It studies the key mechanisms of the surface passivation (chemical passivation and field-effect passivation) in depth. The spatially-resolved chemical configuration of the c-Si/ AlO_x interface and AlO_x layer is presented to determine the origin of the surface passivation efficacy.

Chapter 6 investigates the degradation of the c-Si bulk and the c-Si/ AlO_x interface. It focuses on the degradation at elevated temperature in the dark to eliminate any possible influences of illumination on the process. Possible degradation mechanisms of both the bulk and the c-Si/ AlO_x interface are suggested.

Chapter 7 summarises and emphasises the key findings and important results of this thesis.

2 Review: Surface passivation

Electrons and holes, the charge carriers in semiconductors, are generated when energy is provided to the semiconductor in excess of the forbidden band gap. The energy can be provided either by absorption of light or by thermal processes. However, generated electrons (situated at the energy level of the conduction band) will eventually lose energy and stabilise back to the energy level of the valence band by recombining with holes. When the electrons and holes recombine, photons or phonons may be emitted [22]. This *recombination* process limits solar cell performance. Although it is not possible to eliminate it completely, it is desirable to minimise recombination.

Recombination processes are generally classified as *intrinsic* or *extrinsic* processes [23]. Intrinsic recombination processes include radiative recombination [24], [25] and Auger recombination [26], [27]. They are therefore not avoidable since they are inherent processes [28]. On the other hand, extrinsic recombination is caused by the defect levels within the bandgap which behave as recombination paths for minority carriers. Extrinsic recombination processes involve processing-related defects and can be reduced by proper treatment such as hydrogenation and annealing [29], [30]. Since crystalline silicon (c-Si) is an *indirect* semiconductor, the losses from the recombination process occur mainly via defect levels [23]. These defects are present both within the volume ('bulk') and at the surface of the Si material (bulk defects and surface defects, respectively). The main focus of this thesis is to investigate methods to minimise surface defects although correlated influence on the bulk is also studied. Methods to reduce surface recombination are discussed hereafter throughout this thesis.

2.1 Recombination theory

It is important to study radiative recombination and Auger recombination to understand surface recombination theory. For all of the recombination types, it is possible to define the *recombination lifetime* accordingly. The recombination lifetime is also called the *minority carrier lifetime* as it is limited and hence determined by the average time elapsed between the generation and subsequent recombination of minority carriers [31]. The minority carrier lifetime for *p*-type wafers can be expressed as:

$$\tau \equiv \frac{\Delta n}{U} \quad \text{Equation 2-1}$$

where τ is the carrier lifetime, Δn is the excess minority carrier concentration (in a p -type wafer) and U is the net recombination rate. Under real operation conditions of the solar cell, the different types of mentioned recombination occur in parallel and the *effective* minority carrier lifetime can be expressed as [32]:

$$\frac{1}{\tau_{eff}} = \sum_i \frac{1}{\tau_i} \quad \text{Equation 2-2}$$

2.1.1 Radiative recombination

Radiative recombination is the reverse process of light absorption [33], [34]. When an electron in the conduction band falls to the valence band, there is a probability that its excess energy will be lost by the emission of a photon [22]. For direct-bandgap semiconductors, radiative recombination is the dominant recombination process, which is the base mechanism of lasers and light emitting diodes (LEDs) [31]. However, in indirect-bandgap materials such as Si, radiative recombination is suppressed due to involvement of an additional particle (a phonon). The net recombination rate for radiative recombination can be defined as [33], [34]:

$$U_{rad} = B(np - n_i^2) \quad \text{Equation 2-3}$$

where B is the radiative recombination coefficient [35], [36] for the semiconductor material, n and p are the electron and hole concentrations, respectively, and n_i is the intrinsic carrier concentration of Si [35], [36]. The carrier lifetime for radiative recombination is also given by [31]:

$$\tau_{rad} = \frac{1}{B(n_0 + p_0 + \Delta n)} \quad \text{Equation 2-4}$$

where n_0 and p_0 are the electron and hole thermal equilibrium concentrations, respectively.

2.1.2 Auger recombination

Auger recombination occurs when an electron combines with a hole and a third carrier is given the excess energy. When the excited third carrier returns to the initial state, it emits phonons [26], [27], [32]. Auger recombination is more common in heavily doped material or under higher injection conditions [31]. It can be considered as two different processes depending on the third carrier. The net recombination rates for the two processes can be expressed as:

$$U_{eeh} = C_n(n^2p - n_0^2p_0) \text{ and}$$

$$U_{ehh} = C_p(np^2 - n_0p_0^2) \quad \text{Equation 2-5}$$

where C_n and C_p are the Auger coefficients [26], [27], [32]. The carrier lifetime of Auger recombination for p -type Si can be expressed by combining Eq. 2-1 and Eq. 2-5:

$$\tau_{Auger} = \frac{1}{(C_n n^2 + C_p n \Delta n)} \quad \text{Equation 2-6}$$

2.1.3 Recombination via defect levels

As mentioned above, some defects manifest as discrete energy levels within the bandgap. These defects include crystallographic defects such as dislocations, grain boundaries and non-saturated (dangling) bonds [23]; metallic impurities [37] can also cause defects. The presence of these discrete energy levels leads to a two-step recombination process via the defect level within the bandgap. In this case, an electron from the conduction band relaxes to the defect level before it recombines with a hole in the valence band [23], [37]. The physical mechanism of this process was developed by Shockley and Read [38] using statistical modelling and by Hall [39] empirically. Therefore, it is commonly called Shockley-Read-Hall recombination (SRH recombination) and can be expressed as:

$$U_{SRH} = \frac{np - n_i^2}{\tau_{p0}(n + n_1) + \tau_{n0}(p + p_1)} \quad \text{Equation 2-7}$$

where τ_{p0} and τ_{n0} are the capture time constants and n_1 and p_1 are SRH densities. The capture time constants are related to the capture cross sections σ_p and σ_n , thermal velocity (V_{th}) of the carriers and the defect concentration N_t . The capture time constants are given by:

$$\tau_{p0} \equiv \frac{1}{\sigma_p V_{th} N_t} \quad \text{and} \quad \tau_{n0} \equiv \frac{1}{\sigma_n V_{th} N_t} \quad \text{Equation 2-8}$$

and n_1 and p_1 are defined as:

$$n_1 \equiv N_c \exp\left(-\frac{E_c - E_t}{kT}\right) \quad \text{and} \quad p_1 \equiv N_v \exp\left(-\frac{E_t - E_v}{kT}\right) \quad \text{Equation 2-9}$$

where N_c and N_v are the effective densities of states in the conduction and valance bands, E_t is the energy level of the defect centre, and E_c and E_v are the energies of the conduction and the valance bands, k is the Boltzmann constant, T is the temperature in Kelvin. The corresponding carrier lifetime is given by [38]:

$$\tau_{SRH} = \tau_{n0} \frac{p_0 + p_1 + \Delta n}{n_0 + p_0 + \Delta n} + \tau_{p0} \frac{n_0 + n_1 + \Delta n}{n_0 + p_0 + \Delta n} \quad \text{Equation 2-10}$$

Therefore the effective recombination centres depend on the capture cross section and they lie near the middle of the forbidden bandgap (also called mid-gap) [31].

2.2 Surface recombination theory and passivation

In this section, the aspects of the *surface* of a material (c-Si in this thesis) are discussed. The surface is the exposed plane due to the *discontinuity* of the crystallinity of a material [23], [40]. The surface inherently includes an increased density of defects due to the discontinuity of the crystal. Partially bonded Si atoms, so called *dangling bonds* and Si atoms bonded to other atoms are the most common defect types at the c-Si surface [41], [42]. The recombination at the surface via these defects can be described by the SRH theory mentioned in *Section 2.1.3*.

However, a modification needs to be made since the recombination at the surface is the process per *unit area*, whereas the recombination in the bulk is the one per *unit volume*. Using Eq. 2-7, the surface recombination rate (via a single defect) can be expressed as:

$$U_s = \frac{n_s p_s - n_i^2}{\frac{(n_s + n_1) + (p_s + p_1)}{S_{p0}} + \frac{1}{S_{n0}}} \quad \text{Equation 2-11}$$

where n_s and p_s are the electron and hole concentrations at the surface and S_{n0} and S_{p0} are the *surface recombination velocity* parameters (SRV parameters, unit: cm/s). The S_{n0} and S_{p0} are given as:

$$S_{p0} \equiv \sigma_p v_{th} N_{st} \quad S_{n0} \equiv \sigma_n v_{th} N_{st} \quad \text{Equation 2-12}$$

where N_{st} is a surface defect concentration, more commonly called surface state density. In reality, however, other aspects need to be considered. The different defects are distributed across the Si bandgap, which means the interface defect parameters such as

σ_p , σ_n , p_1 , n_1 and N_{st} are not constant. Therefore, they need to be integrated over the continuum of the energy levels (from valence band to conduction band). In this case, Eq. 2-11 can be expressed as [43]:

$$U_s = v_{th} \int_{E_v}^{E_c} \frac{n_s p_s - n_i^2}{\frac{(n_s + n_1)}{\sigma_p(E)} + \frac{(p_s + p_1)}{\sigma_n(E)}} D_{it}(E) dE \quad \text{Equation 2-13}$$

where $D_{it} \equiv N_{st}/dE$ which is the interface trap density at a certain energy level.

In a real wafer, however, there is a bending of the energy band towards the surface due to electrical charges at the silicon surface (that is, flat band conditions no longer obtain) [44], [45]. Therefore, it needs to be noted that the U_s depends not only on the surface states (i.e. energy level via n_1 and p_1 , σ_n , σ_p), but also on the injection level at the surface (Δn_s) as already shown in Eq. 2-11. Furthermore, it seems this dependence becomes larger in the case of a non-diffused silicon surface since a small surface charge increment could make this dependency larger [46]. Therefore, to evaluate the surface passivation quality, the surface recombination rate must be calculated using Eq. 2-13 with the surface carrier concentrations n_s and p_s . Then the concept of effective SRV (S_{eff}) is can be defined as [47], [48]:

$$S_{eff} = \frac{U_s}{\Delta n(x=d)} \quad \text{Equation 2-14}$$

at a virtual surface within the wafer (d is the distance from the edge of the space charge region) at the edge.

2.3 Evaluation of surface recombination

To evaluate surface recombination, it is not possible to measure S_{eff} directly. However it is possible to measure τ_{eff} — using, for example, the well-known photoconductance (PC) method [49], [50] — as a function of Δn . The measured PC takes recombination both in the c-Si bulk (τ_{bulk}) and at the c-Si surface ($\tau_{surface}$) of both sides into account for the calculation [51], [52]. If one side of the surface can be perfectly passivated, the surface recombination can be assumed to be due to the other side. However, the most commonly used method is to passivate both surfaces symmetrically and to include both sides for the calculation. The important assumption for this calculation is that both surfaces have the same surface recombination velocity. This assumption is widely accepted, as far as the same surface treatment is applied during the sample

preparation/fabrication, although a concern can be raised for the second surface in case where the two surfaces are not passivated simultaneously.

In this thesis, I adopt this assumption, as does most of the reported work for Si surface passivation. Therefore, τ_{eff} for the symmetrically-structured sample can be expressed as:

$$\frac{1}{\tau_{eff}} = \frac{1}{\tau_{bulk}} + \frac{2}{\tau_{surface}} \quad \text{Equation 2-15}$$

where τ_{bulk} is given by:

$$\frac{1}{\tau_{bulk}} = \frac{1}{\tau_{rad}} + \frac{1}{\tau_{Auger}} + \frac{1}{\tau_{SRH}} \quad \text{Equation 2-16}$$

In addition, $\tau_{surface}$ can be acquired from the equation in a transient PC measurement:

$$\frac{1}{\tau_{surface}} = \alpha_1^2 D \quad \text{Equation 2-17}$$

where D (in the unit of cm^2/s) is the minority carrier diffusion constant under low injection and the ambipolar diffusion constant under high injection level [53] and α_1 is the solution of the transcendental equation:

$$\tan\left(\frac{\alpha_1 W}{2}\right) = \frac{S_{eff}}{\alpha_1 D} \quad \text{Equation 2-18}$$

where W (in the unit of cm) is the wafer thickness. Inserting α_1 from Eq. 2-17 into the Eq. 2-18, S_{eff} can be expressed as:

$$S_{eff} = \sqrt{D \left(\frac{1}{\tau_{eff}} - \frac{1}{\tau_{bulk}} \right)} \tan \left(\frac{W}{2} \sqrt{\frac{1}{D} \left(\frac{1}{\tau_{eff}} - \frac{1}{\tau_{bulk}} \right)} \right) \quad \text{Equation 2-19}$$

In the case of a well-passivated sample, where $S_{eff} < D/(4W)$ [32], [54], which is the case for the samples used in this thesis, τ_{eff} is independent of D and is determined only by the recombination in the bulk and at the surfaces (both sides). Assuming both surfaces are passivated symmetrically, S_{eff} can be expressed as:

$$S_{eff} = \frac{W}{2} \left(\frac{1}{\tau_{eff}} - \frac{1}{\tau_{bulk}} \right) \quad \text{Equation 2-20}$$

The accuracy of Eq. 2-20 is discussed by Sproul [32], [54]. For sufficiently low values of S ($S_{front} = S_{rear} = S_{eff} < D/4W$), the accuracy of the equation is high (the relative deviation is below 4%). However, when the surface passivation quality is poor, the surface lifetime is limited by the diffusion of minority carriers. In this case, Eq. 2-19 needs to be used.

For cases in which D is large or τ_{eff} is high (that is, $1/\tau_{eff}$ is very small), high-quality-bulk material such as float-zone (FZ) Si has been commonly chosen to study surface passivation although recent study reports its material-related defects [55]–[57]. In this case, the total recombination losses are assumed to be dominated by surface recombination, which means τ_{bulk} can be assumed to be infinite. Then, the surface recombination velocity is assumed to take the maximum value it can have, $S_{eff,max}$:

$$S_{eff,max} = \frac{W}{2\tau_{eff}} \quad \text{Equation 2-21}$$

On the one hand the surface recombination can also be evaluated by the surface saturation current density (J_{0s} ; where ‘s’ stands for ‘surface’). The key importance of J_{0s} is its capability to separate the surface lifetime from the overall lifetime, which accounts for both the recombination mechanisms at the surface and in the bulk. This term has been more widely used as J_{0e} (where ‘e’ stands for ‘emitter’) for a surface with a heavily diffused region. It is important to reduce the saturation current density, as otherwise it limits the device open-circuit voltage and hence its efficiency. A slope-based method for extracting J_{0e} was introduced by Kane and Swanson [58]. Their method (the ‘slope method’) is based on the dependence of the surface lifetime on Δn [59]:

$$\begin{aligned} \frac{1}{\tau_{eff}} &= \frac{1}{\tau_{radiative}} + \frac{1}{\tau_{Auger}} + \frac{1}{\tau_{SRH}} + \frac{2}{\tau_{emitter}} \\ &\cong \frac{1}{\tau_{Auger}} + \frac{1}{\tau_{SRH}} + J_{0e} \frac{2(N_d + \Delta n)}{qWn_i^2} \end{aligned} \quad \text{Equation 2-22}$$

$$\frac{1}{\tau_{eff}} - \frac{1}{\tau_{Auger}} = \frac{1}{\tau_{SRH}} + J_{0e} \frac{2(N_d + \Delta n)}{qWn_i^2} \quad \text{Equation 2-23}$$

where N_d is the base doping concentration of the Si wafer bulk. In these equations, radiative recombination has negligible influence on the τ_{eff} in Si. Also, in the case of $\Delta n \gg N_d$ (by at least one order of magnitude: so-called high-injection conditions), the term $(N_d + \Delta n)$ can be simplified to be Δn . Therefore, when $1/\tau_{eff} - 1/\tau_{Auger}$ is presented

as a function of Δn and the slope is linear, J_{oe} can be acquired from the linear slope. This method also allows the extraction of τ_{SRH} from the intercept of the acquired graph. Note that the PC signal within the heavily doped regions can be neglected because they are very thin ($< 0.5 \mu\text{m}$) compared to the wafer thickness (between $170 \mu\text{m}$ and $190 \mu\text{m}$ for the wafers used in the experiment for this thesis). Moreover, the Si surface studied in this thesis is non-diffused (without an emitter) and the measurement was done at high injection with a symmetrically-structured sample [51], [60]. Therefore, the surface saturation current density is expressed as J_{0s} hereafter instead of J_{oe} . However, its use requires several assumptions to be made:

- (1) Auger recombination does not impact the measurement
- (2) n_i is constant across the injection range of investigation
- (3) The SRH recombination is constant for the lifetime data analysed
- (4) Δn is uniform for the whole depth of the wafer

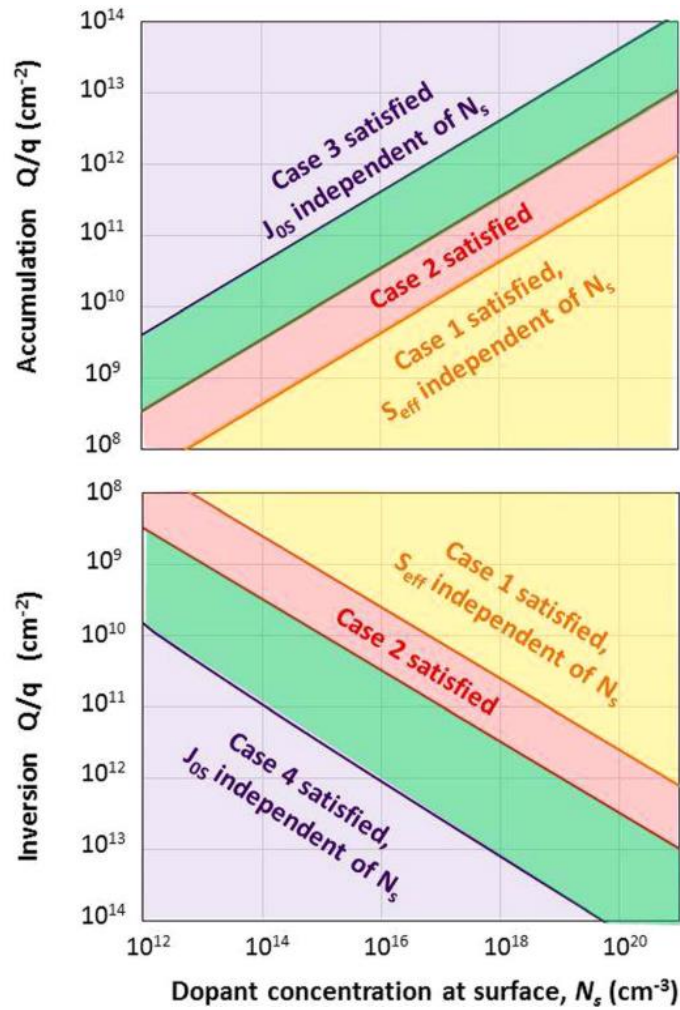


Fig. 2–1. Contours show where the given assumption represents a 10% error in the calculation of surface dopant concentration in low injection for c-Si at 300 K; valid for either p -type or n -type c-Si [46].

It is worth noting that I use J_{0s} instead of S_{eff} according to the intensive study by McIntosh [46], [61]. The reason is that J_{0s} is the suitable parameter to evaluate the surface passivation for non-diffused wafers passivated with high-charge dielectric, mainly due to the independence of this parameter on the surface doping of the wafers, which is the exact case of the samples I use in this thesis as shown in Fig 2–1 (Case 3 for accumulation and Case 4 in inversion condition). To minimise the uncertainty generated by the 4 assumptions mentioned above of the measurement and the slope method, I also use Quokka 2 modelling [62], [63] and assess the accuracy of the acquired J_{0s} . A detailed discussion of the measurement and the accuracy of the fit of the slope method will be discussed in *Section 3.4.1*.

2.4 Aluminium oxide for surface passivation

As interest grows in reducing the thickness of the c-Si wafer in order to reduce the cost of solar cell manufacturing, the surface-to-volume ratio of the wafer increases, further highlighting the importance of surface passivation. A large number of studies have focused on the minimisation of surface recombination; Two fundamental approaches for reducing the recombination losses at the surfaces have been reported [23], [64]–[66]. The first is based on the reduction of the interface defect density (D_{it}), which is directly proportional to the recombination rate (as discussed in Eq. 2-13). D_{it} can be reduced significantly by passivating the crystallographically unstable defects such as dangling bonds (undercoordinated atoms), which is commonly called *chemical passivation*. Atomic hydrogen, thin dielectric layers or amorphous semiconductor film can be used for this purpose. The second method is to reduce either the electron or hole concentration at the semiconductor interface by integrating a fixed electric field, an approach called *field effect passivation*. The electric field can be built either by forming a doped layer below the interface or by applying a dielectric layer containing a fixed electric charge or often even the combination of both.

Among the various methods used to achieve these goals, aluminium oxide (AlO_x) was intensively studied for *p*-type silicon surfaces by Agostinelli in the mid-2000's [15], [67]. AlO_x films naturally contain hydrogen, and, more importantly, they have a large amount of negative charge near the interface [15]. This induces an accumulation layer close to the interface of non-diffused *p*-type wafers, which results in an efficient field-effect passivation [15], [67]. The surface passivation obtained by AlO_x , the main topic of this thesis, is reviewed in the following sections.

2.4.1 Aluminium oxide for PV applications

Most of the study on AlO_x layers was done in the microelectronics industry [68]–[70]. AlO_x layers were found to have superior capability to reduce leakage current and drew attention as an alternative high- k gate dielectric layer to silicon dioxide (SiO_2) [68]–[70]. AlO_x as a surface passivation layer for PV was first introduced by Jaeger [71] and Hezel [72] using atmospheric pressure chemical vapour deposition (APCVD) in the 1980s. Attention to the layer for PV applications was increased in the mid-2000's as the need for passivation of p -type surfaces grew, particularly for the rear side passivation of p -type passivated emitter and rear cell (PERC) [11]–[13], [73]. The early PV-related studies on Al_2O_3 used ALD systems. Agostinelli initiated the study for applications for Si solar cells [15], [67]. In the work sufficient negative charge in the range between -10^{12} cm^{-3} and -10^{13} cm^{-3} was achieved using an ALD system. The τ_{eff} was shown to reach about 1 ms using a p -type Cz wafer without a diffused layer, proving that Al_2O_3 is a promising candidate for p -type Si surface passivation. An intensive study was subsequently carried out by Hoex, also using ALD. His study emphasised the benefit of a subsequent annealing process, which was shown to significantly increase the total negative charge (Q_{tot}) by one order of magnitude up to $-9 \times 10^{12} \text{ cm}^{-3}$. It also identified the presence of an interfacial oxide layer (SiO_x) by high resolution transmission electron microscopy (HR-TEM) and discussed the possible origin of the negative charge. It is suggested that the presence of the interfacial layer causes the tetrahedral coordination of the aluminium (Al) and oxygen (O) bond and results in an Al vacancy which generates negative charge. After this work the interest in Al_2O_3 layers increased and various types of deposition systems for PV application were explored [14], [74]. In the following sections the advantages and disadvantages of different deposition systems are reviewed.

2.4.2 ALD-deposited Al_2O_3 and PECVD-deposited AlO_x layers

Various types of deposition systems have been used to form AlO_x layers: the list includes the above-mentioned APCVD [71], [72], [75], [76] and ALD [15], [67], [77]–[86]; it also includes remote plasma chemical vapour deposition (RPCVD) [70], chemical vapour deposition (CVD) [87] and PECVD [14], [68]–[72], [88], [89]. Most of the early studies on AlO_x in PV were done on ALD Al_2O_3 layers [15], [67], [77]–[86], [90]. After the promising results for ALD Al_2O_3 layers were reported, studies using PECVD-deposited AlO_x layers became increasingly common due to its higher throughput.

Given that ALD materials are deposited one atomic monolayer at a time, the chemical composition of the layers is inherently stoichiometric ($\text{Al}:\text{O} = 2:3$). Hence, the compound is written as Al_2O_3 instead of AlO_x . The ALD process is preferred for research due to the ability to finely control the chemical composition of the resulting layer, especially for the initial growth at the Si surface. The precursors for Al_2O_3 are usually trimethyl aluminium (TMA) as an aluminium source and vaporised water (H_2O) or gaseous oxygen (O_2) as an oxygen (O) source. The method also demonstrates superior thickness control and film uniformity.

However, the throughput of ALD is very low, particularly when compared to a method such as *in-line* PECVD. The advantage of the latter system is that its throughput can be increased by simply adding a plasma source in conjunction with precursor gases, which enables the transport speed to be increased [91]. A detailed description of such a system is presented in *Section 3.3*. Although the throughput of ALD is inferior to *in-line* PECVD due to their inherently different deposition mechanisms, spatial ALD has improved the throughput such that ALD can now be considered for industrial applications [17]. However, a majority of the AlO_x deposition systems in PV manufacturing are still *in-line* PECVD, a trend that is predicted to continue [91], [92].

As the PERC solar cell becomes the commercially-dominant Si solar cell structure [10]–[12], the need for a high-throughput deposition process increases. This inspires the study of PECVD-deposited AlO_x , which is written as such due to its non-stoichiometric chemical composition. In particular, it is important to note that almost all solar cell manufacturers use PECVD systems for AlO_x layer deposition in PERC production lines since: (1) they already use such tools for front-side anti-reflection coating layer disposition [91] and (2) the throughput of PECVD is one to two orders of magnitude greater than ALD [89]. The PERC solar cell is anticipated to dominate the Si solar cell market for the next decade [11]–[13] and, therefore, PECVD for AlO_x deposition has been a topic of intensive study since about 2010 [88], [89], [93]–[102]. AlO_x deposited by *in-line* PECVD is now widespread, having been estimated at 2.5 GW of capacity in August 2014 [9]. This thesis therefore focuses on AlO_x layers deposited by *in-line* PECVD, given the results can be considered for direct application to industry for commercial PV products.

2.4.3 Thermal annealing and stability of the surface passivation

Regardless which of the deposition systems mentioned in *Section 2.4.2* is used, the excellence of the surface passivation quality of the AlO_x layer is particularly observed after subsequent thermal processes. Common processes include thermal annealing in nitrogen ambient (N_2), forming gas annealing (FGA) with diluted (5 – 10%) hydrogen (H_2) in N_2 and industrial type metallisation firing under either N_2 or clean dry air (CDA) ambient [88], [89], [91], [98]–[101], [103], [104]. Most of the ALD-deposited Al_2O_3 layers are found to have a thermal optimum between 400 °C and 450 °C. The thermal annealing process has been shown to be critical for decreasing interface defect density (D_{it}) from $1 - 3 \times 10^{12} \text{ cm}^{-2} \text{ eV}^{-1}$ to about $1 \times 10^{11} \text{ cm}^{-2} \text{ eV}^{-1}$. Thermal annealing also increases negative Q_{tot} , from $3 - 20 \times 10^{11} \text{ cm}^{-2}$ to about $5 - 8 \times 10^{12} \text{ cm}^{-2}$ [88], [89], [97]–[101].

Compatible thermal annealing for ALD Al_2O_3 is processed at rather low temperature (between 400 °C and 450 °C as mentioned above) whereas the PECVD AlO_x generally considered for manufacturing must undergo a much higher-temperature firing (between 700 °C and 850 °C) [95]. The industrial fast-firing process is the most common thermal treatment process for PECVD [89], [97], [98], [100], [101], [104], [105] since it is necessary for the metallisation of screen-printed solar cells (the typical industrial method for Si solar cell metallisation).

In some cases, degradation of surface passivation quality has been reported due to the PECVD firing process [106]. It is observed that the hydroxides, which are essential for Si surface passivation, out-diffuse from the c-Si/ AlO_x interface. It has been suggested that the loss of hydroxides from the c-Si/ AlO_x interface may be avoided by reducing the duration of the firing process. Given the importance of the thermal annealing process, this thesis also investigates how to increase the surface passivation stability. The main focus for thermally stable AlO_x in this thesis is to find deposition process conditions that ensure an AlO_x without surface passivation degradation due to thermal processing.

In addition, the firing process has been reported to cause blistering when the AlO_x layer contains excessive hydrogen. Although the concentration of the hydrogen may be adjusted by optimising deposition process conditions, a simple method to avoid the blistering is to keep the AlO_x layer thin (<30 nm) [96], [98]. However, it is also noted that the minimum required thickness to guarantee reasonable surface passivation quality

is 10 nm for ALD [17] or 15 nm for PECVD [96]. Therefore, the AlO_x layer thickness used for all experiments in this thesis is targeted between 20 and 25 nm.

2.4.4 Properties of PECVD AlO_x layers

Various properties such as optical, electrical and chemical properties of PECVD AlO_x layers have been reported. The refractive index (RI) of AlO_x is almost constant (ranging from 1.60 to about 1.66 in the spectral region between 250 nm and 1000 nm), regardless of the deposition system and deposition conditions [89], [91], [97], [107]. Given its use as the rear side passivation of Si solar cells, only light with an incident angle lower than 26° can transmit through it [97]. Therefore, it is confirmed that AlO_x is well suited for the application on the rear side of Si solar cells, although its optical properties have not been as thoroughly studied as those of SiN_x or SiO_xN_y .

In contrast, the electrical properties of AlO_x have been thoroughly investigated. In particular, Q_{tot} and D_{it} at the c-Si/ AlO_x interface have been reported since these two factors are critical indicators to evaluate the surface passivation quality [88], [89], [91], [96], [97], [99], [102], [106], [108]. The Q_{tot} (negative charge) contained in the layer when deposited on p -type c-Si has been reported to be around $1\text{-}5 \times 10^{11} \text{ cm}^{-2}$ before the firing process and increases by about one order of magnitude to be in the range of $1\text{-}5 \times 10^{12} \text{ cm}^{-2}$ through fast firing (800 – 850 °C) [88], [89], [91], [96], [97], [99], [102], [106], [108]. In the same way, it is observed that D_{it} decreases by one order of magnitude through the same thermal processes to around $1\text{-}2 \times 10^{11} \text{ eV}^{-1}\text{cm}^{-2}$. The correlation between Q_{tot} , D_{it} and S_{eff} has been intensively studied by Saint-Cast *et al* [96], who presented a set of equations linking the three parameters. The study demonstrates a linear relationship between S_{eff} and D_{it} (chemical passivation) whereas S_{eff} has an inversely quadratic relationship with Q_{tot} (field effect passivation) [96].

Most of the studies use boron-doped high-quality FZ Si wafers ($1\text{-}2 \text{ } \Omega \text{ cm}$) with the assumption of infinite wafer τ_{bulk} such that $S_{eff,max}$ is commonly reported. While these studies focus on p -type surfaces, Duttagupta *et al.* compared the surface passivation quality on p -type to n -type (both with diffused surfaces) [109]. The quality of the surface passivation by PECVD AlO_x results in $S_{eff,max}$ values of around 10 cm/s and J_{0e} values of 10 fA/cm^2 . It is interesting to note that the J_{0e} for the n^+ emitter and p^+ emitter show similarly excellent surface passivation with values of 12 fA/cm^2 and 8 fA/cm^2 , respectively. This is different from surface passivation by ALD-deposited Al_2O_3 layers [110] but the underlying mechanism of this difference is not yet understood.

Although not yet reported in the literature, it would be valuable to compare the surface passivation quality of non-diffused *p*-type and *n*-type Si passivated by PECVD AlO_x. In particular, investigating which of Q_{tot} and D_{it} has a stronger impact on J_{0s} will be of interest since it would help explain the mechanism of surface passivation dependence on doping polarity. This is one of the main topics of this thesis.

The chemical properties of PECVD AlO_x have also been reported, with a similar focus on the mechanism of low D_{it} [89], [96], [104], [106]. Of interest are the chemical composition of the AlO_x layer itself and the interfacial layer at the c-Si/AlO_x interface. The most common characterisation method used to investigate chemical bonding in AlO_x is Fourier transform infrared spectroscopy (FTIR) [111]–[113], which is capable of revealing changes in the Al-O bond [Al-O] and whether the interfacial layer consists primarily of Si-O bonds [Si-O] or Al-O-Si bonds [Al-O-Si] through thermal processes [96], [97], [99], [100], [106], [107]. It has been observed that thermal processes enhance the growth of a silica (SiO₂) layer at the c-Si/AlO_x interface, which results in a decrease of D_{it} . The presence of the interfacial layer can be observed by high resolution transmission electron microscopy (HR-TEM) [100]. The mechanism to form the interfacial layer is believed to be related to the change of the chemical configuration in [Al-O] bonds [98]–[100], [106]. Although nano-scale study on the interfacial layer and the chemical configuration of the Al₂O₃ layer has been undertaken for ALD-deposited Al₂O₃ layers [77], a similar level of understanding has not yet been achieved for PECVD AlO_x. Therefore, this thesis aims to investigate the PECVD AlO_x interfacial layer at the nano-scale. It will be more valuable since the PECVD AlO_x layers result in more variation in terms of the chemical compositions than ALD Al₂O₃ layers.

It is also important to determine the hydrogen concentration in the AlO_x layer as it is believed to reduce D_{it} by passivating dangling bonds at the Si surface. However, no study has identified the hydrogen atomic concentration in AlO_x. Elastic recoil detection analysis (ERDA) or nuclear resonance reaction analysis (NRA) can calculate the hydrogen concentration in atomic percentage [114]. The correlation of the chemical configuration with the resulting Q_{tot} and D_{it} , which can reveal the origin of the negative fixed charge and a critical factor for reducing D_{it} on different stoichiometries of AlO_x layers, has also not yet been reported for PECVD AlO_x. Therefore, it is investigated in this thesis for various AlO_x layers with different film properties.

Mechanical properties such as the stress contained in PECVD AlO_x layers have also been also reported [91], [107]. PECVD AlO_x is revealed to have a tensile stress for both as-deposited and thermally-treated (fast-firing) layers. Given that an AlO_x layer requires a capping layer for thermal stability, SiN_x and SiO_xN_y layers have also been studied to check the compatibility with AlO_x . The PECVD SiN_x layer also shows tensile stress whereas the SiO_xN_y layer shows compressive stress which cannot be compatible with AlO_x due to the possibility of cracking or poor adhesion [91].

Recently a number of studies have reported on the degradation of the PERC solar cell under illumination and at elevated temperature [115]–[121]. The mechanism of this degradation is still not fully understood, but for further progress in this field it will be necessary to know: (1) whether this degradation is dominated by the surface of the silicon bulk and (2) whether the degradation can occur without light (that is, whether it is actually thermally- or optically-activated degradation). This thesis investigates the origin of the degradation and it is hypothesised that the degradation is caused by transport of hydrogen. Different structures of samples with different surface states such as inversion or accumulation layers are prepared and investigated regarding degradation of the τ_{eff} .

2.5 Other dielectric layers for surface passivation

It is worth understanding the behaviour of other dielectric layers, especially SiN_x since it is used as the capping layer of AlO_x and typically serves as the solar cell front-side anti-reflection coating (ARC) layer. It is also important to understand the characteristics of SiO_x since it is believed to be present at the c-Si/ AlO_x interface and is key to lowering D_{it} there.

2.5.1 Silicon nitride (SiN_x)

In this thesis, SiN_x is mainly used as a capping layer on top of the AlO_x . Although there are more applications of SiN_x in standard solar cell design, I present here only a brief literature review on SiN_x for its use as (1) a hydrogen source and (2) a capping layer for AlO_x .

Silicon nitride was developed in the 1970s and it began to be used in the microelectronics industry in the 1980s. Hezel *et al.* [122] introduced the use of SiN_x for PV devices in the 1980s. In the long history of the study of SiN_x , the hydrogen concentration of SiN_x (also commonly written as $\text{SiN}_x\text{:H}$) has been highlighted due to

its beneficial passivation effect for both Si bulk and surfaces [122]–[133]. The hydrogen contained in the SiN_x layer is known to passivate dangling bonds at the Si surface and at crystallographic defects such as grain boundaries [124], [129], [132], [134]–[138]. The resulting SiN_x layer includes three types of bonds: [Si-N], [Si-H] and [N-H] [133], [139]. In general the hydrogen concentration (H-conc.) in the SiN_x layer is reported to be between 10 and 20% [123], [140], [141]. It has also been reported that the hydrogen concentration at the interface, as measured by NRA, and the Q_{tot} and D_{it} are correlated with τ_{eff} and sample preparation [142]. Although SiN_x is used as a capping layer in this thesis, the hydrogen in the SiN_x layer can migrate to the c-Si/AlO_x interface during thermal processes. It has also been reported that the amount of hydrogen released and the penetrability are highly dependent on the thermal treatment temperature and the film synthesis method [136], [143]. A number of reports attest to the benefits of SiN_x as a capping layer [21], [90], [98], [103], [144]. SiN_x is also used as an ARC layer on the front side of the solar cell. The RI of SiN_x is tuneable by varying PECVD deposition parameters such as the gas ratio between SiH₄ and NH₃ [82], [125], [138], [145]. Therefore, SiN_x offers the ability to optimise the RI of the ARC layer of the silicon solar cell.

The benefit of SiN_x use as a capping layer of AlO_x has also been studied by Saint-Cast *et al.* [98] and Niewelt [144]. It has been reported that the as-deposited AlO_x/SiN_x stack performs just as well as AlO_x-only surface passivation annealed at 450°C and fired at 870°C [98]. This may be due to an increased hydrogen concentration added by the SiN_x layer. A more stable surface passivation has been also observed when the AlO_x is capped by a SiN_x layer [144]. The SiN_x behaves as a protecting layer which prevents AlO_x layer from absorbing moisture and also as an additional hydrogen source which results in more hydrogen concentration in AlO_x layer [83], [98]. Therefore, I use an AlO_x/SiN_x stack for superior surface passivation quality and stability.

2.5.2 Silicon oxide (SiO_x)

Silicon oxide has been used as a surface passivation layer for decades [22], [44], [146], [147]. Early SiO_x fabricated for research was mostly thermally grown [65]. The widespread application of SiO_x in the microelectronics industry can be attributed to the high electrical quality of the Si/SiO_x interface [146], [147]. Optimised surface passivation by SiO_x results in D_{it} values on the order of 10⁹ eV⁻¹cm⁻² [43], [148], [149]. Although the high fabrication temperatures (800 °C – 1100 °C) required may result in

detrimental influence on commercial Cz Si wafers, the resulting high-quality surface passivation has been utilised for decades. This adverse impact of thermal SiO_x has inspired other types of SiO_x such as PECVD-deposited SiO_x [65].

However, thermally-grown SiO_x is used in this thesis as a surface passivation layer since a hydrogen-poor material is necessary to prove the hypothesis: the observed degradation in surface passivation quality originates from the migration of hydrogen as discussed in *Section 2.4.4*. The motivation of the study on non-hydrogenated SiO_x layers is that all reported LeTID of surface passivation occurs with dielectric layers that contain hydrogen. Therefore PECVD-deposited SiO_x cannot be used since hydrogen is included in the precursor gas SiH_4 . In addition, wet oxidation cannot be used due to possible hydrogen involvement from the H_2O ambient during the process. Therefore, dry oxidation which only uses O_2 gas is a good candidate for this thesis due to the absence of hydrogen in the layer.

2.6 Chapter summary

With the increasing attention on the importance of surface passivation for silicon solar cells, different dielectric layers such as AlO_x , SiN_x and SiO_2 have been studied as surface passivation layers. The literature covers the properties of the layers and various deposition techniques.

However, none of these studies adequately explores the process window of the deposition parameters, which have an impact on the resulting layer. In order for PERC solar cell manufacturers to continue to decrease production costs, it is important to understand the impact of the deposition process parameters on the properties of the resulting layers. A detailed understanding of the impacts of the deposition process parameters on the surface passivation quality and the layer properties can allow one to decide how much the process parameters can be adjusted (for example, reducing the use of the expensive process gases without sacrificing the surface passivation quality). Therefore, in this thesis, I focus on the impact of the deposition conditions on the surface passivation quality using an industrial in-line PECVD system much like that utilised by many solar cell manufacturers. The substrate for the investigation is non-diffused p -type crystalline Si wafers which is the rear side of the PERC solar cell.

3 Experimental methods

In this chapter the entire procedure from the designing of the experiments to the analysis methods used in this thesis is presented. A statistical software package is employed to design experiments and analyse results systematically. Detailed sample preparation procedures for different assessments are also described. In the last part of this chapter characterisation methods to evaluate electrical and chemical properties of AlO_x layers are discussed.

3.1 Design of experiments and statistical analysis

The design of experiments (DoE) in this thesis was systematically planned using the statistical software package STATISTICA [150], [151]. Microwave power (MWP), total gas flow rate (TGFR), temperature, pressure and gas flow rate ratio (GFRR) of nitrous oxide (N_2O) to TMA [$\text{Al}(\text{CH}_3)_3$] were selected as the variables of interest. After the samples were processed as dictated by the DoE, their electrical and material properties were characterised. When the measurements were completed, the values were fed back to STATISTICA (as observed values) to create statistical models for the electrical and material properties. Correlation between STATISTICA-modelled (predicted) values and measured (observed) values was assessed to confirm the reliability of the statistical model.

Using STATISTICA, an experiment (such as Chapter 4 and Appendix 3). can be designed in several different ways. Two models are used in this thesis:

1. The central composite design [152], [153], which analyses two factors using nine conditions and ten runs (two centre points).
2. The Box-Behnken design [153], [154], which analyses three factors in conjunction with three levels with 13 conditions and 15 runs (three centre points).

The advantage of the central composite design lies in its speed and efficiency in terms of time and the resource required. The main advantage of the Box-Behnken design is that it is able to assess the process window almost like the full factorial design. If the R^2 value is sufficiently high (>0.98 for the purposes of this thesis), it is possible to determine whether the effect is linear or quadratic; this is possible only for the 3-level design since the 2-level assessment is not able to reveal a possible vertex. The impact

of process parameters on the measured values (electrical and chemical properties) was assessed by the ‘*p*-value test’ [155]. A *p*-value below 0.05 indicates a *significant impact* of the parameter on the property.

3.2 Sample preparation

3.2.1 Sample structure

In this thesis two different sample structures are used:

- (1) Symmetrical samples passivated on both sides by an $\text{AlO}_x/\text{SiN}_x$ stack were prepared for studying electrical properties. The SiN_x capping is used to prevent the AlO_x layer from absorbing moisture. The SiN_x is also used as an additional hydrogen source. To avoid any possible influence by the SiN_x on the different AlO_x layers, I used the same SiN_x for all the different AlO_x layers. For the same reason I chose the SiN_x deposition temperature to be the same as the lowest temperature used in the AlO_x deposition (350 °C). As discussed in *Section 2.3*, the symmetrical-structured samples are for determining τ_{eff} and J_{0s} . With this structure, the saturation current density of one surface can be easily acquired by halving the acquired J_{0s} value. In addition, the symmetric structure can be used for the capacitance-voltage (C-V) measurement which will be discussed in detail in *Section 3.4.2*. Planarised (saw damage etched; 30% NaOH etches of 10 μm on each side) wafers were used such that the surface is similar to the rear side of a PERC structure.
- (2) Single-side AlO_x on a mirror-like double-side-polished (DSP) silicon wafer is used for investigating chemical and physical properties. The polished surfaces are useful when the measurement requires a transmission or a reflectance mode to avoid scattering of the light source during the measurement. For example, for Fourier transform infrared (FTIR) measurements to identify chemical bonds in the AlO_x and ellipsometry measurements to determine the layer’s thickness. Details of these characterisation methods are presented in *Section 0*.

3.2.2 Sample preparation

Commercially available (156 mm \times 156 mm) planarised Czochralski (Cz) wafers were used (final thickness was 175 ± 10 μm). Both polarities are used to study the comparative efficacy of surface passivation. The *p*-type (boron-doped) and *n*-type (phosphorus-doped) wafers have a resistivity of 1.6 ± 1.0 $\Omega\cdot\text{cm}$ and 6.0 ± 1.0 $\Omega\cdot\text{cm}$, respectively. All

the *p*-type and *n*-type wafers underwent Radio Corporation of America (RCA) cleaning [156] and were dipped in hydrofluoric acid (HF) solution (mass fraction 5%) in the same batch before the AlO_x deposition. The double side polished (DSP) samples (2-inch diameter) were also processed in the same batch in the RCA cleaning and HF finish to achieve the same hydrophobic surface before deposition. All samples were then stored in an N_2 -flushed desiccator to keep the surface hydrophobic until the AlO_x deposition.

An industrial in-line PECVD system (MAiA XS, Meyer Burger) was used for the deposition of AlO_x with a thickness of 25 ± 5 nm. The AlO_x was then capped with SiN_x (75 nm thick with a refractive index of 2.08 at 633 nm) deposited at 350 °C. High-temperature processing was performed to activate the analysed samples [101] using an industrial metallisation furnace (7K9-70C69-5LIR, Schmid) in a clean dry air (CDA) ambient. The *set* firing temperature was adjusted to maintain a fixed *wafer* temperature of 740 ± 5 °C (the standard firing temperature in our facilities) for all the wafers and the duration at the peak temperature was about 0.6 seconds. The wafer temperature during the firing process was measured using thermocouple and data logger (Q18, DATAPAQ). Three points were measured on the 156 mm \times 156 mm size wafer as shown in Fig. 3-1.

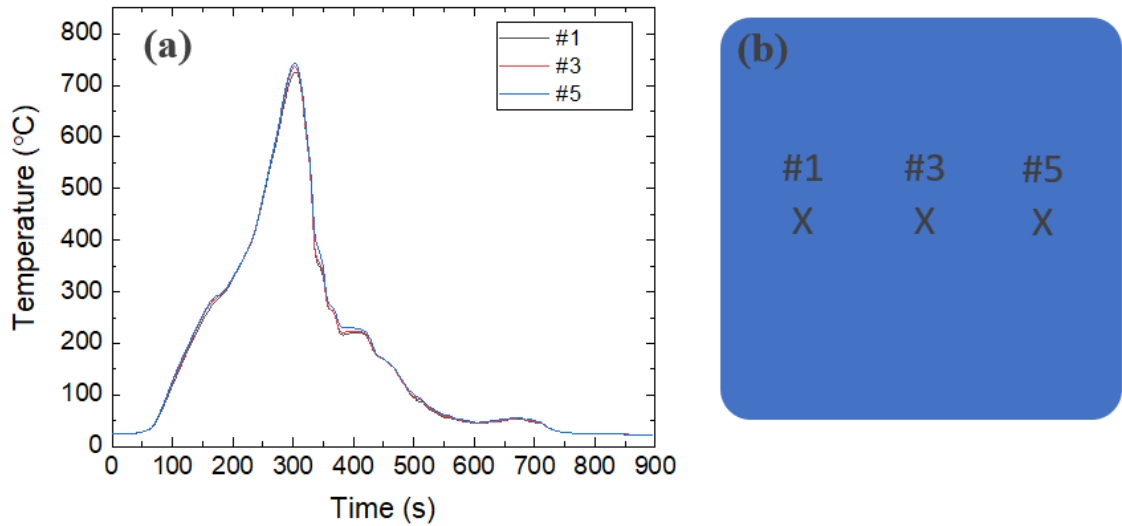


Fig. 3-1. (a) Wafer temperature profile during the firing process and (b) positions of the three measurement points on the 156 mm \times 156 mm wafer.

3.3 Deposition systems

As discussed in *Section 2.4.2*, there are various deposition systems for AlO_x . The deposition system I use in this thesis is an industrial-type in-line microwave (MW) PECVD system from Meyer Burger (MAiA) [91]. All the dielectric layers (both AlO_x and capping SiN_x) are deposited using the system.

3.3.1 Overview of the deposition system

The MAiA system used in this thesis has been widely used in PV manufacturing facilities. All the chambers are made of stainless and acid-proof steel. A schematic side-view image of the MAiA system is presented in Fig. 3-2. The main body consists of a loading chamber (LC), process chamber 1 (PC1), transfer chamber (TC), process chamber 2 (PC2) and unloading chamber (ULC). Samples are loaded on a sample carrier to the LC and are moved through the system by means of transportation rollers. The samples receive depositions as they pass through the process chambers: SiN_x layer deposition in PC1 and AlO_x in PC2.

In the LC and TC, the samples are heated by infrared (IR) heating lamps, while the PCs are equipped with resistive heaters to maintain the temperature of the samples during the deposition process. In the PCs, the two MW generators (frequency of 2.45 GHz) comprise one linear plasma source (PS). A MW antenna is located in the centre of a quartz tube and transfers the MW power (MWP) from one side to the other side. It is important to set the MWP to adjust since the excessive power from one side can be reflected from the other side of the MW generator. The reflected power creates either constructively or destructively-interfering wave to the forward power from both sides of the MW generator. If these forward and reflected powers are tuned imperfectly, standing waves can be created and cause non-uniformity across the wafer carrier width. Therefore, the adjustment of the MW power should be fine-tuned and well-chosen.

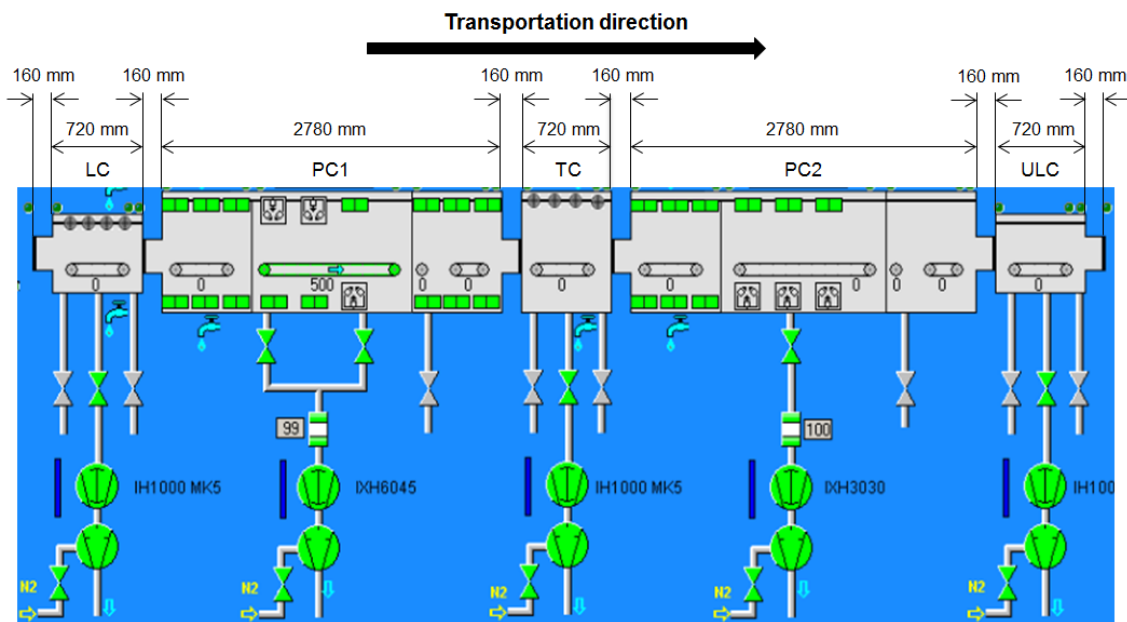
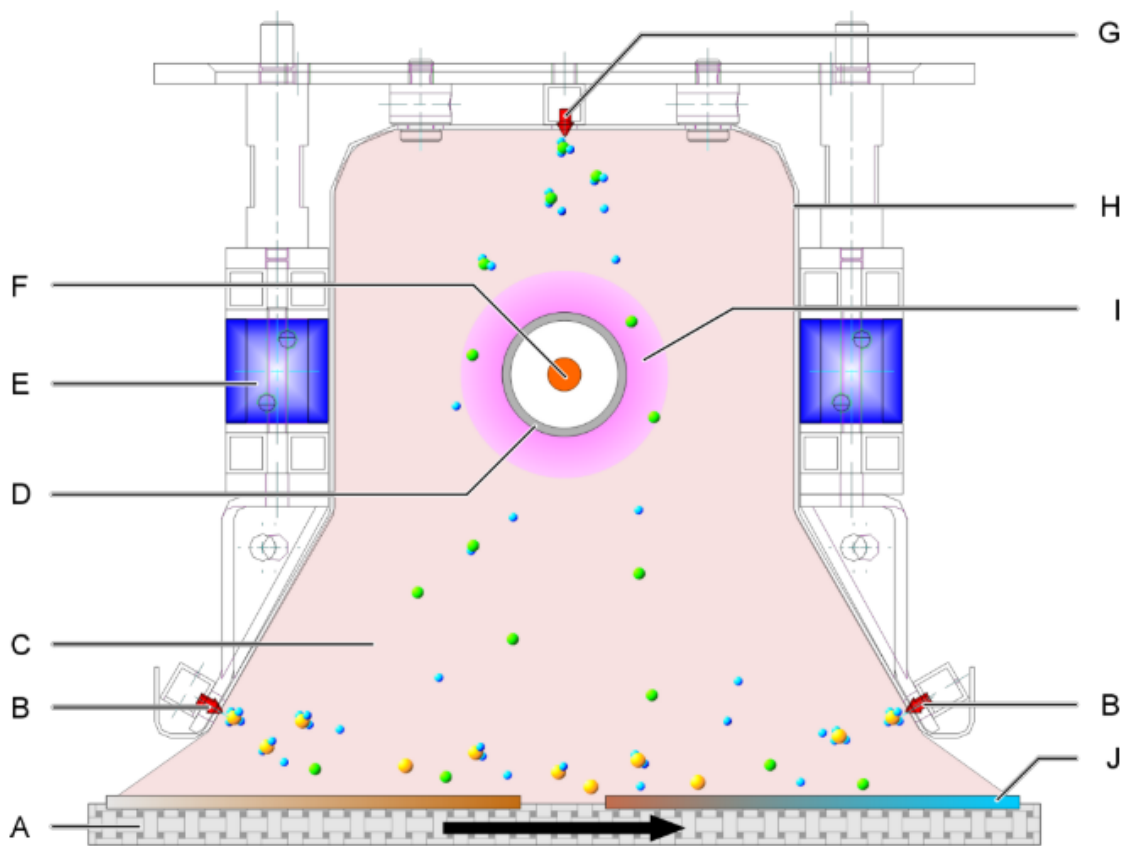


Fig. 3-2. Schematic side view of the MAiA system and the dimension of each chamber.

3.3.2 Design of shower head

A schematic of the plasma source is presented in Fig. 3-3 in detail, showing the SiN_x process. The AlO_x process uses the same plasma source and the same shower head design but the only difference is the different use of precursor gases: instead of silane and ammonia ('B' and 'G' in Fig. 3-3, respectively), the AlO_x process uses TMA instead of silane and N_2O instead of ammonia. Alongside the quartz tube, two rows of magnets are employed. The magnets help to spatially stabilise the plasma by forcing electrons to follow particular contours, making as dense a plasma as possible.

3.3.3 Deposition mechanism



Cross-section view and principal mode of function of the plasma source for standard silicon-nitride process

- A Carrier
- B Silane gas shower
- C Plasma
- D Quartz tube
- E Magnet system
- F Inner conductor
- G Ammonia gas shower
- H Radiation guard = plasma enclosure
- I Highly-tight plasma zone = outer coaxial conductor
- J Substrate (wafer)

Fig. 3-3. Cross-sectional view and principal mode of function of the plasma source for example silicon nitride process [157].

During the deposition the sample carrier is positioned underneath the quartz tube, about 12 cm below the PS. All the chambers stay under vacuum throughout the whole experiment, which minimises any possible contamination or unexpected influences from the ambient, such as moisture. It is also necessary to check the uniformity of the experimental deposition conditions. Therefore, I tested uniformity across the carrier and the results follow in the next section (*Section 3.3.4*).

3.3.4 Uniformity

The uniformity of the deposition system was tested before the DoE since the non-uniformity may influence the resulting layer property. Fig. 3-4 shows the schematic dimension of the deposition chamber, carrier and the process gas shower with the position of shower holes. The mechanical design of the system seems to provide uniform deposition across the carrier (left to right) since the shower head gas holes cover the whole width of the carrier. The uniformity test is done using SiN_x since it is easier to notice thickness differences due to its refractive index (RI).

Fig. 3-5, presents thickness and RI of the SiN_x over across the carrier left to right (perpendicular to the transport direction). As can be seen, the thickness and RI toward the edges of the carrier are not uniform. The gas shower holes are designed to cover an area wider than the carrier width and the possible reason is the difference in the actual wafer temperature during the deposition. The uniformity across the middle wafer is in the range of 4.5% for thickness and 0.4% for RI, which is within the acceptable range by the industry. To allow comparison between wafers and to avoid non-uniformity problems, all the wafers deposited for this thesis have been deposited using only the middle position of the carrier.

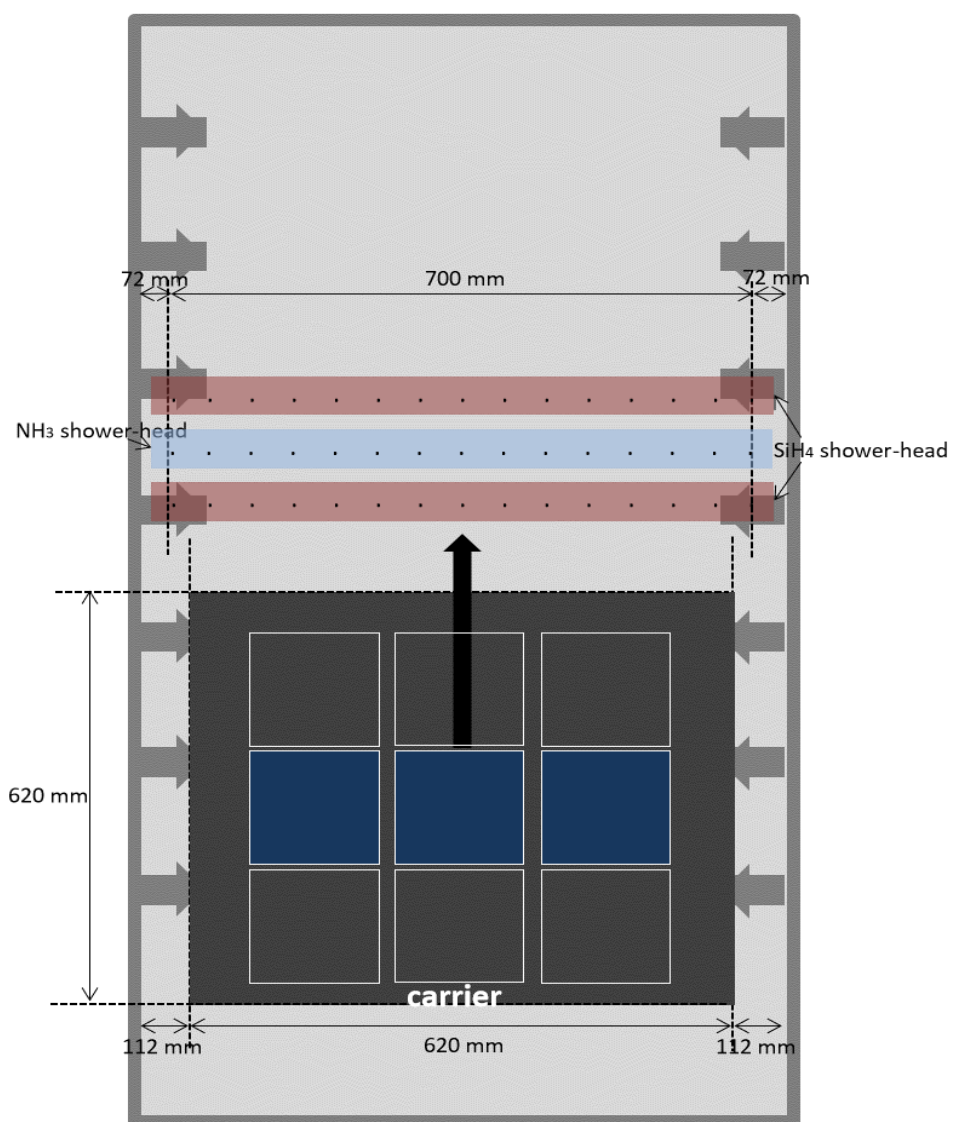


Fig. 3-4. Schematic drawing of the top-view of the PC1 which shows carrier and gas shower heads. The quartz tube is just below the NH₃ gas shower head.

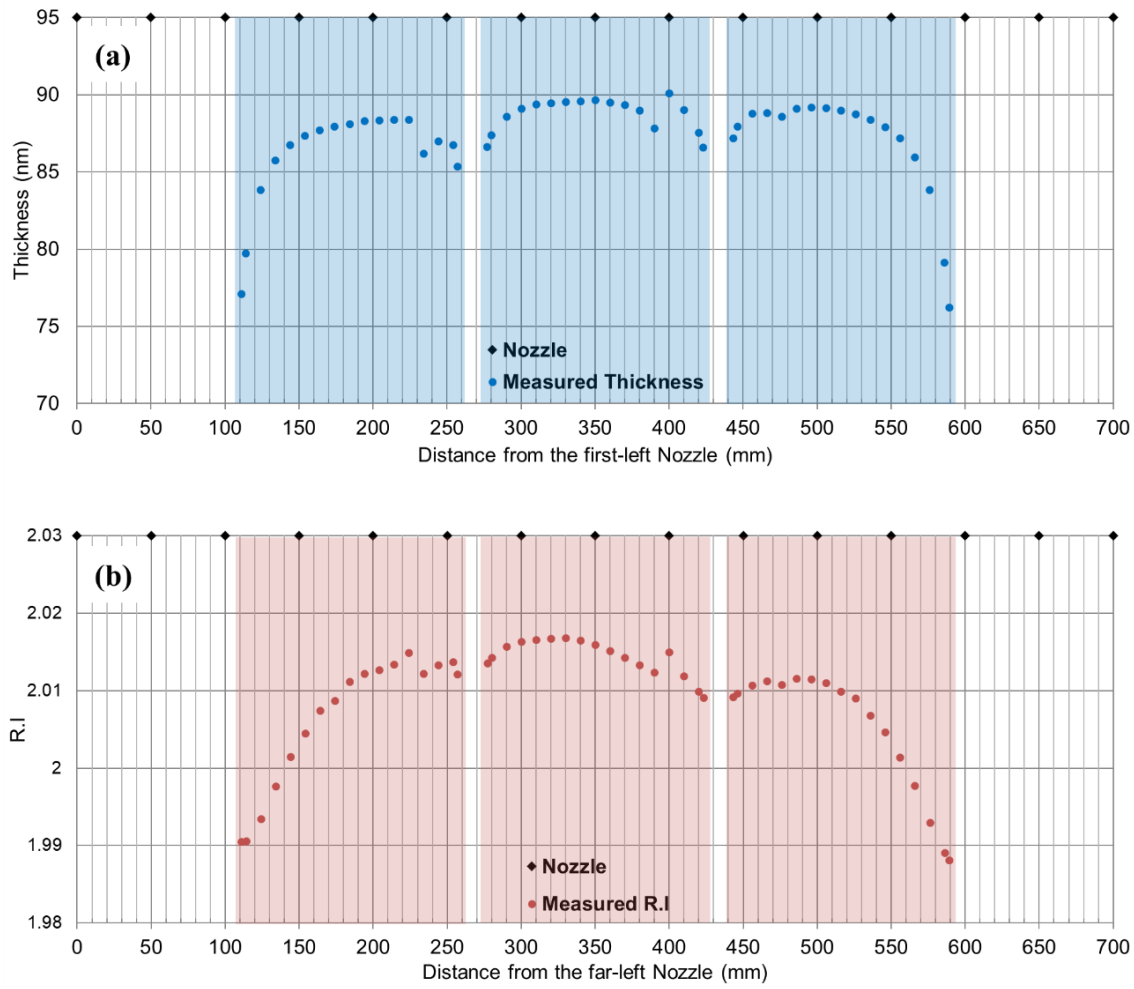


Fig. 3-5. Uniformity test on (a) thickness and (b) RI across the three wafers from the left to right of the carrier. The blue and red rectangles represent the ranges of actual wafer widths.

3.3.5 Temperature profile

Due to the non-uniformity observed in *Section 3.3.4*, actual wafer temperature measurement during the deposition process is conducted. It is known that the deposition temperature influences properties of resulting layers such as deposition rate, density, hydrogen concentration, initial growth at the interface of substrate and layer. It is therefore important to determine the *actual* temperature of the wafers during the deposition process. It is necessary to measure the wafer's temperature profile across the carrier such that the experimental results can be corrected, if needed, to the position of the wafer.

Fig. 3-6 shows the image of the setup used to measure the wafer's temperature using thermocouples (labelled as #1 to #6 in Fig. 3-6) and a six-channel Datapaq Q18 (Fluke Process Instruments). Based on the length of each chamber and the different transport speed through each chamber, the time duration in each chamber was calculated, and is

shown in Fig. 3-7. It is observed that the *actual* wafer temperatures of wafers loaded at the middle column are similar (in the range of 2-3%) and lower than the set temperature by ~ 50 °C when the wafer pass under the plasma source. Temperatures of the left and right column are slightly lower than the middle column wafers and the far edge point of the left column wafer results in a significantly lower temperature than the middle column wafers (by 75 °C). It may be because the transport roller which is mechanically connected to the stainless-steel chamber wall and the chamber wall stays cooled by cooling water below 40 °C. Therefore, the side parts (left and right) of the carrier which sit on the transport roller for moving are cooler than the middle part. This result influences my decision to use only the middle column for all the experiments in this thesis.

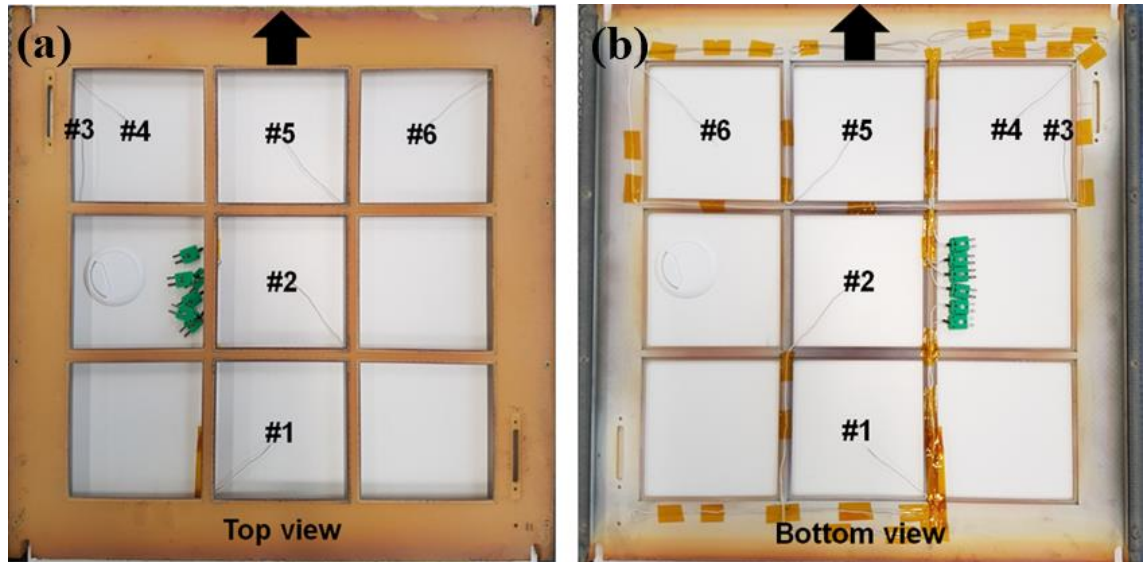


Fig. 3-6. Images of wafer carrier with attached thermocouples: (a) top view and (b) bottom view.

3.4 Characterisation methods

The characterisation methods for electrical properties and chemical properties are presented in this section since they are used in all the following main chapters. However, a method which was used only one chapter is included in the specific chapter accordingly.

3.4.1 Photoconductance measurements

In *Section 2.3* the theoretical background of τ_{eff} and J_{0s} was studied. As discussed, knowledge regarding these values, in particular J_{0s} , is critical for the evaluation of the surface passivation quality. This section reviews one of the most widely used methods to measure τ_{eff} and J_{0s} .

3.4.1.1 Transient decay method

In the transient decay method, excess carriers are generated by a laser or a flash lamp. The decay of the carrier density after the excitation is then measured. The decay of the carrier density is due to recombination. Using Eq. 2-1, the τ_{eff} can be expressed as:

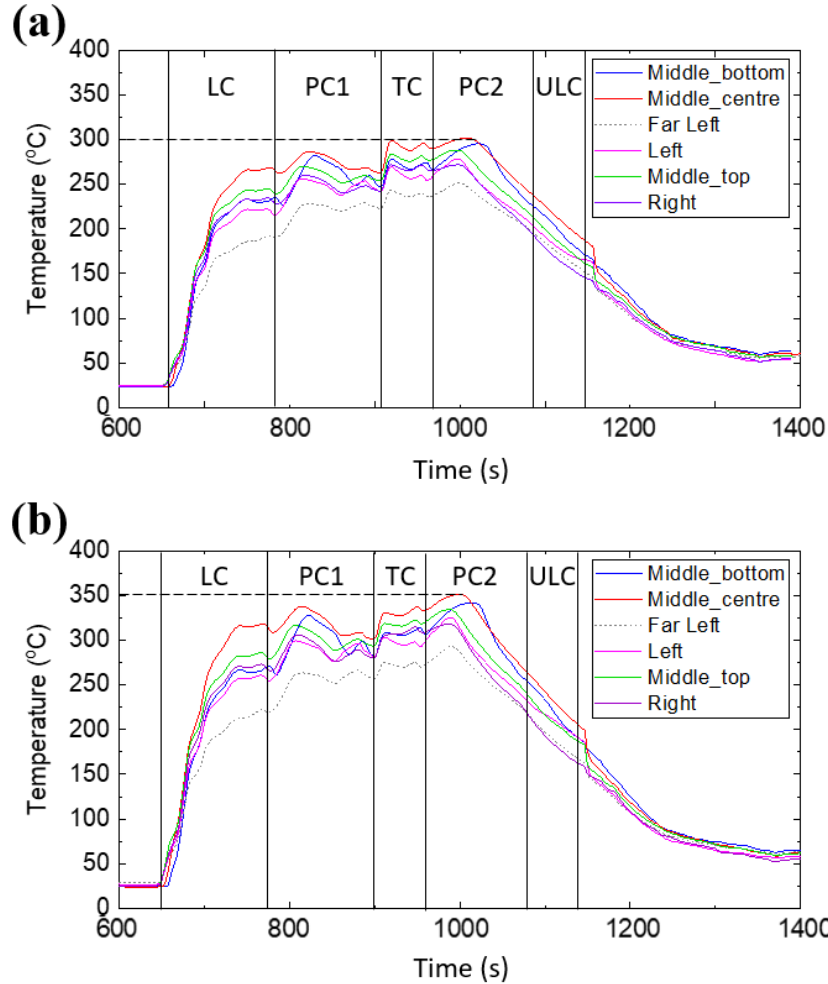


Fig. 3-7. Measured wafer temperature trend for the AlO_x process in each chamber for (a) 350 °C and (b) 400 °C deposition. The dashed line is a guide to the eyes.

$$-\frac{d(\Delta n)}{dt} = U = \frac{\Delta n}{\tau_{eff}} \quad \text{and then} \quad \tau_{eff} = -\frac{\Delta n}{\frac{d(\Delta n)}{dt}} \quad \text{Equation 3-1}$$

The first application of this method was the PC decay (PCD) measurement in 1955 [158]. The conductivity of the sample is sensed by an electrical circuit and converted to Δn using:

$$\sigma = q(\mu_n n + \mu_p p) \quad \text{and then} \quad \Delta\sigma = q\Delta n(\mu_n + \mu_p) \quad \text{Equation 3-2}$$

where μ_n and μ_p are the electron and hole mobility, respectively. Δn is extracted by Eq. 3-2 and then τ_{eff} can be acquired by Eq. 3-1. The main benefit of this method is that it requires determination of the generation rate and therefore is not impacted by uncertainty associated with this parameter. Only the relative change of Δn is required in the measurement. However, this method requires a sharp decay of the optical excitation and fast enough electronics to detect the decay of the Δn . Therefore, it is most suitable for samples with lifetime higher than 100 μs [159].

3.4.1.2 Steady state method

In this method the *generation* rate G is steady and known. Given that the rates of recombination and generation of the excess carriers are balanced under equilibrium conditions, the effective lifetime can be expressed as:

$$U = G = \frac{\Delta n}{\tau_{eff}} \quad \text{and then} \quad \tau_{eff} = \frac{\Delta n}{G} \quad \text{Equation 3-3}$$

This equation assumes that G and Δn are both uniform across the sample, which is an accurate assumption when the carrier diffusion length is larger than the wafer thickness. In the steady-state method, both G and Δn must be measured. Although the advantage of this method is that effective lifetime is measured under the condition where solar cell operates, it is not simple to measure τ_{eff} as a function of Δn . Instability in the light source and variable temperature during the measurement due to heating from the light source make an accurate measurement challenging [160].

3.4.1.3 Quasi steady-state method

The light source used for the quasi steady-state (QSS) method has a slower decay time (a few milliseconds) than the transient method (tens to a hundred microseconds). As long as the decay time is longer than the effective lifetime of a sample, the QSS condition is maintained. However, it is recommended to measure under QSS conditions when the effective lifetime of a sample is one order of magnitude shorter than the decay time [159]. The QSS-PC measurement was first proposed by Sinton *et al.* using a flash lamp with an adjustable decay time [49], [51]. The τ_{eff} can be measured over a wide range of Δn . The benefit of this method is the quick measurement time which is able to avoid unintended heating of the sample. Like the steady-state method, QSS-PC also requires the measurement of generation rate. Results from the QSS-PC and transient methods have been shown to agree [161].

The generalised analysis method to calculate τ_{eff} was proposed by Nagel *et al.* [50]. It can be expressed as:

$$\tau_{eff} = \frac{\Delta n}{G - \frac{d(\Delta n)}{dt}} \quad \text{Equation 3-4}$$

Note that the transient condition is when $G=0$ which is Eq. 3-1 and the steady-state condition is when $[d(\Delta n)/dt = 0]$ which is Eq. 3-3. With this generalised method samples with a wide range of effective lifetime values can be measured [50].

3.4.1.4 QSS-PC and PCD measurement

In this thesis two lifetime tester, the WCT-120 and the WCT-120TS (both from Sinton Instruments), are used for τ_{eff} and J_{0s} measurement under QSS and transient conditions. The systems are based on a radio-frequency (RF) circuit with a coil [162] inductively coupled to the sample which is placed above it. When the coil emits electromagnetic radiation from the RF generator, it induces an electromagnetic field across the sample. The electromagnetic field is almost constant across the sample since the sample thickness is relatively thin (170–180 μm in this thesis). The system needs to measure the background conductance of the sample before each measurement (before flash ignition). When the flash lamp illuminates the sample, the *conductivity* of the sample increases due to the generated carriers (Δn). The G is determined using a calibrated detector (such as a silicon solar cell, also called a reference cell). For the calculation of the G of the measured sample, a factor called the *optical constant* needs to be input. An optical constant value lower than one means the absorption of the sample is lower than that of the calibrated detector; a value higher than one is used in the case of a well-textured sample with greater absorption than the detector.

All the measurements of τ_{eff} and J_{0s} in this thesis are done using both generalised [50] and transient modes [158]. In all cases, good agreements between the two methods have been shown. As discussed in Chapter 2, based on the study of McIntosh and Black [46], J_{0s} is used as a figure of merit to evaluate surface passivation quality. In their study, it was concluded that J_{0s} is a more suitable parameter to evaluate the surface passivation for non-diffused wafers, particularly for wafers passivated by dielectrics that contain a large amount of charge, such as in this study.

It is important to note that the value of J_{0s} is extracted using two methods: the Kane-Swanson method (also known as the slope-based method) and Quokka simulation. In

the Kane-Swanson method, bandgap narrowing is taken into account for the calculation of the intrinsic carrier concentration n_i using Schenk's model [163], while the model of Richter *et al.* is used to determine the intrinsic lifetime [110]. The value of J_{0s} is extracted at Δn of 10^{16} cm^{-3} using a linear fit in the range between $7 \times 10^{15} \text{ cm}^{-3}$ and $1.3 \times 10^{16} \text{ cm}^{-3}$. The J_{0s} is acquired at high injection level (Δn of 10^{16} cm^{-3}) and all the slopes of “inverse lifetime as a function of minority carrier density” is then checked if they are linear at this injection range. The linearity of the graph shows that τ_{eff} is not dominated by τ_{SRH} of the bulk. The slope method assumes a uniform Δn profile across the wafer thickness. This assumption can be invalid in the case of industrial Cz wafers or in the case of moderate surface passivation [164]. Therefore the obtained values are confirmed using a detailed analysis using Quokka version 2.5 [63]. Quokka simulates the depth profile of Δn , hence, the extraction of J_{0s} via curve fitting does not require any assumption [164]. All the J_{0s} values used in this thesis are acquired by Quokka simulation which has a good agreement with the extracted J_{0s} (with $0.91 < R^2 < 0.98$).

3.4.2 Contactless capacitance-voltage (CV) measurements

It is known that the surface passivation quality is significantly influenced by the fixed charge density within the dielectric (Q_f) and the density of interface traps (D_{it}), also called the interface defect density [22], [38], [39], [44], [165]. The Q_f is present in an overlaying dielectric layer or at the interface of c-Si and the dielectric layer induces a compensating net charge in the c-Si and more accurately near the surface [166]. This induced “space-charge-region” forms an accumulation layer, inversion layer or depletion layer depending on the polarity and the density of the net charge [167]. The detail of the different components of charge in different regions was studied by Pawlik *et al.* [167]–[169]. It was also defined where Q_s (charge in the space-charge region), Q_{it} (charge trapped in interface) and Q_f actually exist [167].

Due to the fact that the semiconductor is in a quasi-neutral state, the net charge in the space-charge region (Q_s) must balance the total net charge (Q_{tot}) such that $Q_s + Q_{tot} = 0$ [166]. In the general case of a semiconductor, Q_{tot} is the sum of Q_f , Q_{it} and Q_g (charge in a gate contact). Q_g is absent in lifetime test structures used in this thesis, leading to the equation: $Q_{tot} = Q_f + Q_{it}$. When the surface is well-passivated, Q_{it} is negligible and Q_{tot} is dominated by Q_f [166]. Therefore, Q_{tot} is used as an indicator of total net charge in this thesis.

The Q_{tot} and D_{it} are measured using a contactless capacitance-voltage (C-V) measurement system, the photovoltaic (PV) metrology system from Semilab (PV-2000) [170], [171]. The measurement setup is presented in Fig. 3-8. The contact potential difference (V_{cpd}) between the wafer and the reference electrode is measured by vibrating non-contact Kelvin probe [172], [173]. Corona charge is then deposited on the dielectric layer in the air and the change of the electrostatic potential in the dielectric and the semiconductor is measured by the non-contact Kelvin probe [172], [173] based on the V_{cpd} . The reference electrode vibrates above the wafer, which modulates the wafer-electrode capacitance C . The bias V_B is applied in series with V_{cpd} , which induces an electric charge on the capacitor $Q(t) = (V_{CPD} + V_B) C(t)$. Then, a bias feedback loop automatically searches for $J = 0$ and $V_{CPD} = -V_B$. Q_{tot} is directly measured by the system from the difference between the initial charge state and the flat band condition [170], [171]. In addition, light pulse is generated to measure $V_{cpd,light}$ and $V_{cpd,dark}$ to measure the capacitance difference between the two condition. Then, the surface barrier voltage (V_{sb}) is calculated by $V_{cpd,dark} - V_{cpd,light}$. The D_{it} is measured at the minimum of the ‘U-shape’ D_{it} spectrum as a function of surface barrier voltage (V_{sb}), which is typically located near the Si mid-gap [170], [171]. It is generally relatively flat near the mid-gap and increases very rapidly toward the band edges [174].

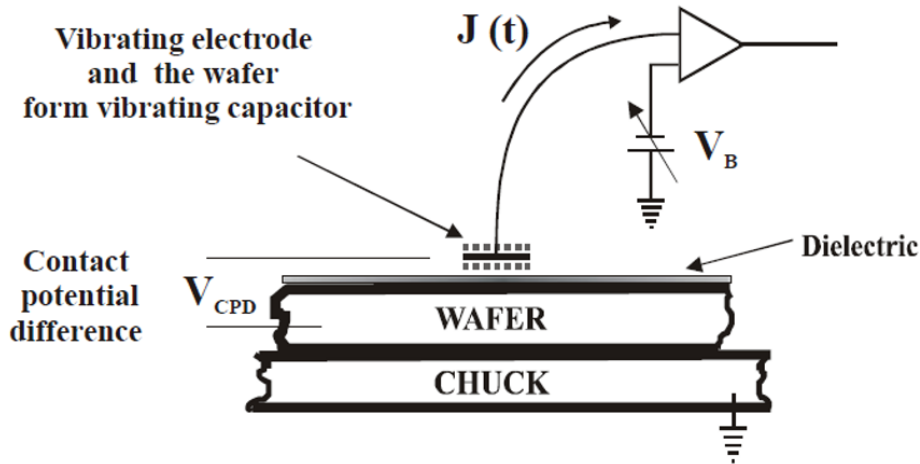


Fig. 3-8. Conceptual drawing of the contactless C-V measurement system [175]. $J(t) = (V_{CPD} + V_B)\Delta C/\Delta t$ and the bias feedback loop automatically searches for $J = 0$; then $V_{CPD} = -V_B$.

All the measured C-V raw data used in this thesis were monitored to check whether there was any charge leakage in the AlO_x layer. A typical charge leakage is shown in Fig. 3-9. V_{cpd} does not increase linearly above certain level with increase of corona

charge since the layer cannot hold the applied charge due to the leakage. Any measured data which show this behaviour are abandoned in this thesis.

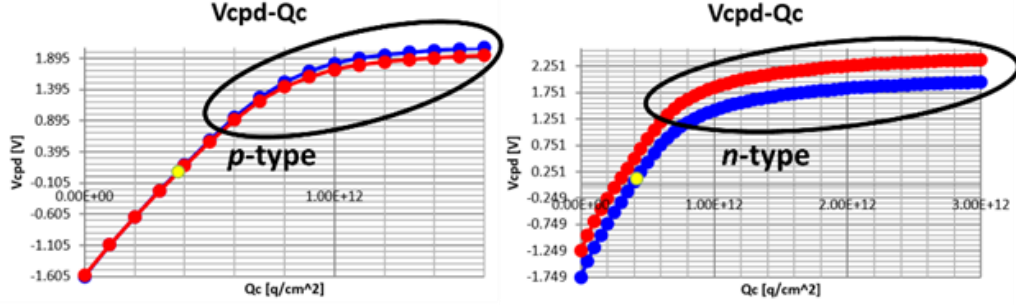


Fig. 3-9. Typical behaviour of V_{cpd} as a function of Q_c (corona charge) when there exist charge leakage for (a) p -type sample and (b) n -type sample.

3.4.3 Fourier transform infrared (FTIR) spectroscopy

In addition to the electrical properties, the surface passivation quality is closely related to the chemical composition and bonding structures at the c-Si/ AlO_x interface and in the AlO_x layer. It has been shown that the c-Si/ AlO_x interface is correlated to the chemical compositions of the AlO_x layer [166]. To identify the chemical properties, Fourier transform infrared (FTIR) spectroscopy is widely used [70], [81], [104], [107], [111], [166], [176]. In this thesis, the transmission spectra are measured using a Nicolet 5700 (Thermo Scientific). The IR light transmits through the sample (I) and a detector on the other side of the sample analyses the reduced light signal due to the absorption by the AlO_x layer. The absorption by the AlO_x layer itself is acquired by subtracting the light transmitted through the Si substrate (I_0) in accordance with the Lambert-Beer law [177]:

$$\text{Absorption spectrum } A(\nu) = -\log \frac{I}{I_0} \quad \text{Equation 3-5}$$

Various molecular bonds such as [Al-O], [O-H] and [C-H] are observed after the signal is processed by the provided software (OMNIC; Thermo Scientific [111]). For the measurement, it is also important to know the difference between FTIR spectra with and without a p -polariser in place. We used the polariser, which has capability to observe transverse optical (TO) and longitudinal optical (LO) modes for the AlO_x [113]. In addition, the Brewster's angle holder is used to eliminate IR interference within the Si wafer by using an incidence angle which minimises the internal reflection (74° in case of silicon), reducing the reflection of the p -polariser light to zero [113].

The data acquired from the measurement requires a few steps to calculate absorption. For the background subtraction the same bare Si wafer in the same air ambient as the

sample substrate is measured. Then the background signal is inserted as I_0 for calculation of absorption in Equation 3-5. In addition, the Savitzky-Golay method is used to smooth the acquired measurement signal [178]. It is necessary to process with care since the signal to noise ratio is sometimes not sufficient in this high frequency signal. The smoothing level must not sacrifice real peak and comparison two signals before and after the smoothing is essential to check none of the real signal peak is disappeared.

The wavenumber range is from 4000 cm^{-1} to 400 cm^{-1} and it is broad enough to detect the chemical bonds mentioned above ([Al-O], [O-H] and [C-H]). However, [O-H] and [C-H] bonds overlap from 2200 cm^{-1} to 3400 cm^{-1} with multiple peaks, which makes the hydrogen concentration calculation difficult. That is the reason why there has been no report to present hydrogen concentration in the AlO_x layer using FTIR measurement. As an alternative way to identify hydrogen concentration in the AlO_x layer, ERDA can be an option as discussed in Section 2.4.4 and it is also a focus of this thesis.

3.5 Chapter summary

The procedures of the experiment carried out in this thesis is presented. The systematic experimental design and the analysis of the result are carried out using a statistical package STATISTICA. Two different test structures are prepared: a symmetrical structure with $\text{AlO}_x/\text{SiN}_x$ stack and single-side AlO_x only for electrical and chemical properties respectively.

The inline PECVD deposition system used in this thesis is reviewed in detail. The uniformity of the resulting film is assessed and the uniform region is identified to minimise unwanted variation of the resulting samples. The actual wafer temperature is also investigated during the deposition such that the influence of the deposition temperature is under control. All the samples in this thesis are processed in the uniform region and the sample to sample variation is negligible.

The main characterisation methods are also assessed in this chapter. The methods to measure and acquire τ_{eff} and J_{0s} are reviewed to evaluate surface passivation quality. In addition, the C-V measurement to identify Q_{tot} and D_{it} are studied, which are the major parameters to assess the c-Si/ AlO_x interface properties. To identify chemical bonds, the AlO_x layer is analysed by FTIR which can be correlated to the electrical properties such as J_{0s} , Q_{tot} and D_{it} . A few additional analysis methods will be briefly presented in the following main chapters.

The study and the analysis presented in the following Chapter 4, 5 and 6 are based on the experimental detail reviewed in this chapter.

4 Investigation of PECVD AlO_x layer on c-Si surface passivation²

In this chapter various characteristics of the AlO_x layer deposited using an industrial in-line PECVD system are studied. The electrical, chemical and physical properties of the AlO_x layer are discussed. The properties of the AlO_x layer are investigated on both non-diffused *p*-type c-Si surface and non-diffused *n*-type c-Si surface passivation. The comparison of the characteristics of the two c-Si doping types reveals the importance of the field effect passivation and the chemical passivation.

4.1 Introduction

Improving solar cell efficiency is essential to reducing the cost of electricity generated by PV. The PERC has been proven to yield higher efficiency in industrial production lines and its production capacity is expanding rapidly [11]–[13]. The PERC structure is based on high quality rear-side surface passivation [9], [14], [15], [17], [67], [73], [179]. Amongst the various options, AlO_x seems to be the preferred option, particularly for *p*-type Si solar cells [14], [15], [17], [67], [180]. In general, AlO_x films have a large amount of negative charge [15] and therefore induce an accumulation layer near the interface of non-diffused *p*-type wafers. This results in an efficient field-effect passivation [15], [67].

As reviewed in Chapter 2, ALD systems are known as a common method to deposit AlO_x layers (Al₂O₃ in this case), particularly for research purpose. As a result, most of the AlO_x studies have been done using this type of system [74], [83], [90], [180]–[185]. A major drawback of ALD systems for industrial applications is the low deposition rates, especially when compared to in-line PECVD systems [91]. This has raised a number of studies on PECVD-based AlO_x [88], [89], [95]–[100], [102]. These studies focused on the impact of the firing stability [95], the AlO_x thickness [96], the presence of interfacial layers [99] and the subsequent thermal processes [100]. However, these studies performed using PECVD systems did not adequately explore the process window of the deposition parameters, which have an impact on the resulting layer. In this chapter, the focus is on the impact of the deposition conditions on the surface passivation quality for

² This chapter is summarised and *published* in the *Journal of Solar Energy* (DOI: doi.org/10.1016/j.solener.2019.04.091).

both non-diffused p -type and n -type crystalline Si wafers using an industrial in-line PECVD system.

I investigate the impact of the five most critical PECVD process parameters on the obtained surface passivation quality provided by both as-deposited and fired AlO_x . These parameters include MWP, TGFR, temperature, pressure and GFRR of the N_2O to TMA. Experiments are designed to study the impact of the five deposition process parameters on the electrical and chemical properties using statistical software. It is worth noting that ALD Al_2O_3 layers are inherently stoichiometric, which means that the resulting layers have the same atomic concentrations of Al and O regardless of the precursor gas mixtures. Therefore, variation in the ALD Al_2O_3 layer properties is limited. This is a fundamental difference between ALD Al_2O_3 and PECVD AlO_x layers since PECVD relies on an inherently different deposition mechanism. Although the temperature and pressure have an impact on the properties of the ALD Al_2O_3 layers, a PECVD-based process has a larger number of critical process parameters which influence the growing film. This enables process parameters to have wide range of process windows such that the properties of the resulting AlO_x layer can be flexible depending on various purposes. To date, however, not many studies have been done to correlate deposition conditions and the obtained passivation quality of PECVD AlO_x .

The study is carried out for the non-diffused p -type wafer first and the comparison to the result for the non-diffused n -type wafer. It is interesting to study whether the similar excellent surface passivation can be demonstrated for n -type Si. If the PECVD AlO_x has the capability to provide high-quality surface passivation for both p -type and n -type Si, it can be used for advanced solar cell structures that require simultaneous surface passivation for both dopant types (p - and n -doped), such as interdigitated back contact (IBC) solar cells [186] and n -type inversion layer solar cell [187], which has the benefit of avoiding a boron diffusion process in the fabrication.

For ALD Al_2O_3 films, the dependency of the surface passivation efficacy on different types of dopant polarities is reported [188]. The passivation of a heavily-doped n^+ Si surface by Al_2O_3 shows lower performance compared to a p^+ Si surface [188], [189]. This is due to a less efficient field effect in the case of n -type surface since the minority carriers are not effectively repelled effectively from the surface. Interestingly, it has been reported that PECVD AlO_x provides excellent passivation for both p^+ - and n^+ -type

surfaces [109]. However, the efficacy of surface passivation by PECVD on non-diffused *n*-type surfaces has not yet been studied.

4.2 Experiments

4.2.1 Design of experiment

The experiment is designed using the statistical software package STATISTICA [150], [151]. As discussed in *Section 3.1* the critical process parameters such as MWP, TGFR, temperature, pressure and GFRR of N₂O/TMA were selected as variables. The impact of MWP and TGFR on the surface passivation is studied in the first experiment (Exp. #1). The rest of the parameters (temperature, pressure and GFRR) are investigated in the second experiment (Exp. #2) using the optimum MWP and TGFR as determined by Exp. #1.

Exp. #1 is designed using a central composite design [152], [153], which analyses two factors using nine conditions and ten runs (the centre point is tested twice). In Exp. #2, three factors (deposition temperature, deposition pressure and GFRR) are analysed at three levels using the Box-Behnken design [153], [154] with 13 conditions and 15 runs (the centre point is tested three times). The process conditions of both experiments are listed in the Table 4-1 and Table 4-2. The correlation is evaluated using the *R*-squared (R^2) value; only STATISTICA models that have R^2 values higher than 0.98 are considered in this chapter.

Table 4-1. Deposition conditions for Experiment #1 (temperature is 400 °C, pressure is 0.095 mbar and GFRR is 10)

Recipe ID	TMA [sccm]	Ar [sccm]	N ₂ O [sccm]	Total gas Flow [sccm]	Microwave power [W]
1	523	225	52	800	1000
2	654	281	65	1000	1000
3	523	225	52	800	2000
4	654	281	65	1000	2000
5 (C)	588	253	59	900	1500
6	588	253	59	900	800
7	588	253	59	900	2200
8	497	214	50	760	1500
9	680	292	68	1040	1500
10 (C)	588	253	59	900	1500

Table 4-2. Deposition conditions for Experiment #2 (total gas flow rate is 1000 sccm and microwave power is 2000 W)

Recipe ID	TMA [sccm]	N ₂ O [sccm]	GFRR	Temperature [°C]	Pressure [mbar]
1	485	97	5	350	0.095
2	586	78	7.5	350	0.080
3	586	78	7.5	350	0.110
4	654	65	10	350	0.095
5	485	97	5	375	0.080
6	485	97	5	375	0.110
7 (C)	586	78	7.5	375	0.095
8 (C)	586	78	7.5	375	0.095
9 (C)	586	78	7.5	375	0.095
10	654	65	10	375	0.080
11	654	65	10	375	0.110
12	485	97	5	400	0.095
13	586	78	7.5	400	0.080
14	586	78	7.5	400	0.110
15	654	65	10	400	0.095

4.2.2 Sample Preparation

As discussed in *Section 3.2*, commercially available 156 mm × 156 mm planarised Czochralski (Cz) wafers were used (final thickness was 175±10 µm). The Cz wafers used in the thesis were supplied by one of the major PERC manufacturers [190]. Both polarities are used to study the comparative efficacy of surface passivation. The *p*-type (boron-doped) and *n*-type (phosphorus-doped) wafers have a resistivity of 1.6±1.0 Ω·cm and 6.0±1.0 Ω·cm, respectively. To study the chemical properties, DSP 50 mm-diameter *p*-type wafers (1-10 Ω·cm, 175±10 µm thick) are used for FTIR. All the wafers were RCA cleaned [156] and dipped in HF solution (mass fraction 5%) before the AlO_x deposition. An industrial in-line PECVD system (MAiA XS, Meyer Burger) was used for the deposition of AlO_x with a thickness of 25±5 nm. The AlO_x was then capped with silicon nitride (75 nm thick with a refractive index of 2.08 at 633 nm) deposited at 350 °C. High temperature processing was performed to activate the passivation [101] using an industrial metallization furnace (7K9-70C69-5LIR, Schmid) in a clean dry air

(CDA) ambient. The *set* firing temperature was adjusted to maintain a fixed *wafer* temperature of 740 ± 5 °C (the standard firing temperature in our facilities) for all the wafers. The duration at the peak temperature was about 0.6 seconds.

4.2.3 Characterisation

Contactless C-V measurements were performed using a PV metrology system from Semilab (PV-2000), see *Section 3.4.2*. Q_{tot} is directly measured by the system from the difference between the initial charge state and the flat band condition, while D_{it} is measured at the minimum of the ‘U-shape’ D_{it} spectrum which is typically located near mid-gap for c-Si [170], [171].

An FTIR spectrometer (Nicolet 5700 from Thermo Fisher) is used in order to investigate the chemical bond configuration. I mainly focus on the aluminium-oxygen bonds ([Al-O]) and the hydrogen-related bonds ([O-H] and [C-H]) in the layers (see *Section 3.4.3*).

For more accurate analysis regarding the hydrogen concentration in the AlO_x layer and its depth profile, elastic recoil detection analysis (ERDA) was applied for selected samples. The technique is especially for depth profiling of light elements. The sensitivity for light elements is enhanced by detecting the recoiled particles, which helps in background free detection of the light elements. Therefore ERDA is able to identify the content of hydrogen in thin films [114]. The analysis was performed with an acceleration of 2.8 MeV He^+ ions ($0.5 \text{ mm} \times 0.5 \text{ mm}$ size), using a scattering angle of 25 and with the detector placed at an exit angle of 10° from the surface of the sample. A $12 \text{ }\mu\text{m}$ mylar stopping foil was placed in front of the detector to block forward scattered He^+ ions and allow recoiled hydrogen to be detected. The accelerator used for the measurements was a National Electrostatics Corporation (NEC) 5SDH-1 1.7 MV tandem accelerator with a radio frequency (RF) charge exchange ion-source.

Furthermore, the concentrations of atoms, such as Al and O, throughout the depth of the layer were investigated by X-ray photoelectron spectroscopy (XPS; ESCALAB250Xi, Thermo Scientific). A monochromated 144.72-W Al K- α (energy 1486.68 eV) beam with a spot size of $500 \text{ }\mu\text{m} \times 500 \text{ }\mu\text{m}$ was used as a source. An argon ion beam was used to etch the layer (etched area of $2.5 \text{ mm} \times 2.5 \text{ mm}$). The measurements were analysed using the Advantage software package [191].

A JEOL ARM200F scanning transmission electron microscope (STEM) fitted with a cold field emission gun electron source was used to carry out the sub-nanoscale

investigation of the c-Si/ AlO_x interface. For the analysis, the wafers were sputter-coated with 29 nm gold layer and milled using a FEI XT Nova Nanolab 200 Dual-beam workstation. The specimens were then placed on a standard copper gridded carbon film using an ex-situ lift-out method.

4.3 Result and discussion

4.3.1 Thermal stability

The firing of metal contacts is a critical process in the fabrication of Si solar cells. Improvement of the passivation provided by the AlO_x layer caused by the firing process are often reported and attributed to the reduction of D_{it} and to the increase in the absolute value of Q_{tot} [98], [102], [180]. Previous studies on the thermal and long-term stability of PECVD layers indicate that the deposition temperature and stoichiometry of the layer are critical parameters to prevent degradation of the passivation [17], [88], [95], [98], [100]. To my knowledge, no study has investigated the impact of the MWP and TGFR on the thermal stability of AlO_x surface passivation quality, although these parameters were found to be important in the investigation of the stability of other films such as SiN_x and SiO_x [192].

In this experiment (Exp. #1) the temperature, pressure, and GFRR were fixed at 400 °C, 0.095 mbar and 10, respectively, whereas MWP and TGFR were varied. The changes in both τ_{eff} and J_{0s} were monitored after the standard firing process. Fig. 4-1 presents the relative change in both parameters as a function of MWP and TGFR. Note that τ_{eff} and J_{0s} show similar trend, probably as the surface degradation dominates the τ_{eff} . It shows that the ratio of MWP to TGFR is a critical factor for the thermal stability of the PECVD AlO_x layer. The firing process degrades the passivation quality for MWP/TGFR values lower than 1.67. Similar results were obtained for other firing temperatures above 600 °C and for a different combination of temperature, pressure and GFRR. I believe that the reason for the degradation is the non-ionized state of the elements when the MWP is not sufficient. It may cause imperfect ionization of the TMA which leads to possible involvement of CH_3 radicals in Al-O bonds ([Al-O]). Then, the resulting layer may have an imperfect molecular structure in terms of the layer density and stability. This discovery can provide an acceptable process window for process optimization based on MWP or TGFR.

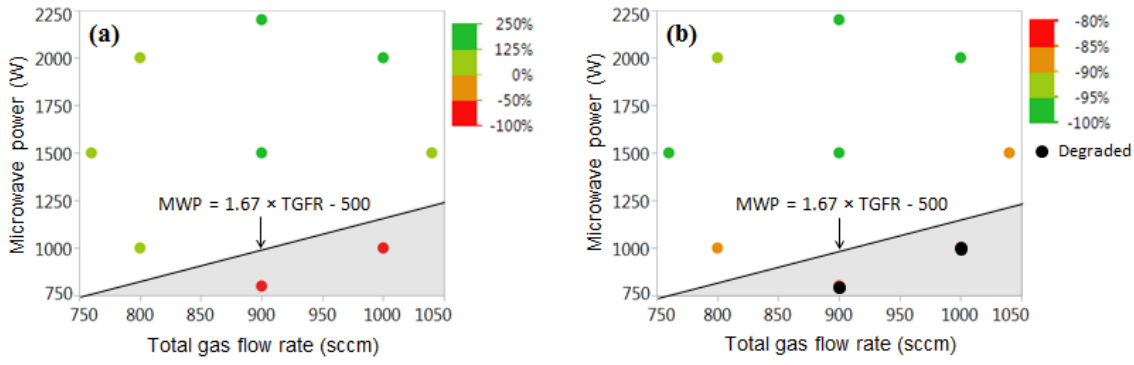


Fig. 4-1. Relative change of (a) τ_{eff} and (b) J_{0s} after firing as a function of MWP and TGFR.

4.3.2 Electrical properties

Considering the results of Exp. #1, the next experiment (Exp. #2) was designed while keeping the MWP/TGFR ratio at two in order to investigate the impact of the deposition conditions on the electrical and chemical properties of as-deposited and fired PECVD AlO_x . Firstly, the impact on J_{0s} using STATISTICA-based models is studied. J_{0s} was obtained using two methods (slope-based and Quokka). The extracted values show good agreement for the 15 runs (R^2 is 0.98 for as-deposited and 0.91 for fired wafers). As mentioned previously, all the J_{0s} values presented in this study are extracted from the Quokka simulation to avoid underestimation of J_{0s} .

The quality of the obtained STATISTICA-based model is assessed by the correlation between the predicted and the observed values. Fig. 4-2 (a) and (c) present this correlation for the as-deposited and fired cases. The good agreement ($R^2 > 0.98$) indicates the reliability of the obtained models. The models are presented using a contour plot [see Fig. 4-2 (b) and (d)]. The open dots indicate nine of the 13 experimental points as required by the Box-Behnken design of experiment. As discussed previously (see Section 3.1), the p -value is used to evaluate the significance of the experimental parameters on the output (J_{0s} in this case).

The lower GFRRs result in better passivation for as deposited layers. J_{0s} below 10 fA/cm^2 was achieved for GFRR of five. These are very low values for as-deposited AlO_x . Examining the p -values indicates that all three deposition parameters have a strong impact on the as-deposited J_{0s} ($p < 0.034$ for all of them) with GFRR being the most significant parameter ($p < 0.006$). As for the effect of firing, it results in a reduction of J_{0s} for most cases; the reduction is more significant for higher GFRR. Extremely low J_{0s} ($\sim 4 \text{ fA/cm}^2$) is achieved for GFRR of ten. For the fired films, both GFRR ($p < 0.008$) and temperature ($p < 0.039$) have significant impacts on J_{0s} , however, no strong impact

was found from the deposition pressure. The strong impact of the GFRR on J_{0s} is supposed to be due to the different chemical bonding configurations of the resulting AlO_x layer and interface. This impacts both Q_{tot} and D_{it} [76], [77], [193]. Investigations on the interface between crystalline Si and AlO_x (c-Si/ AlO_x) are reported on a nanometer-scale in references [76], [77], [193] and will be discussed in Chapter 5. The dependence of J_{0s} on the GFRR in conjunction with the analysis on Q_{tot} and D_{it} is presented below in *Section 4.3.2*.

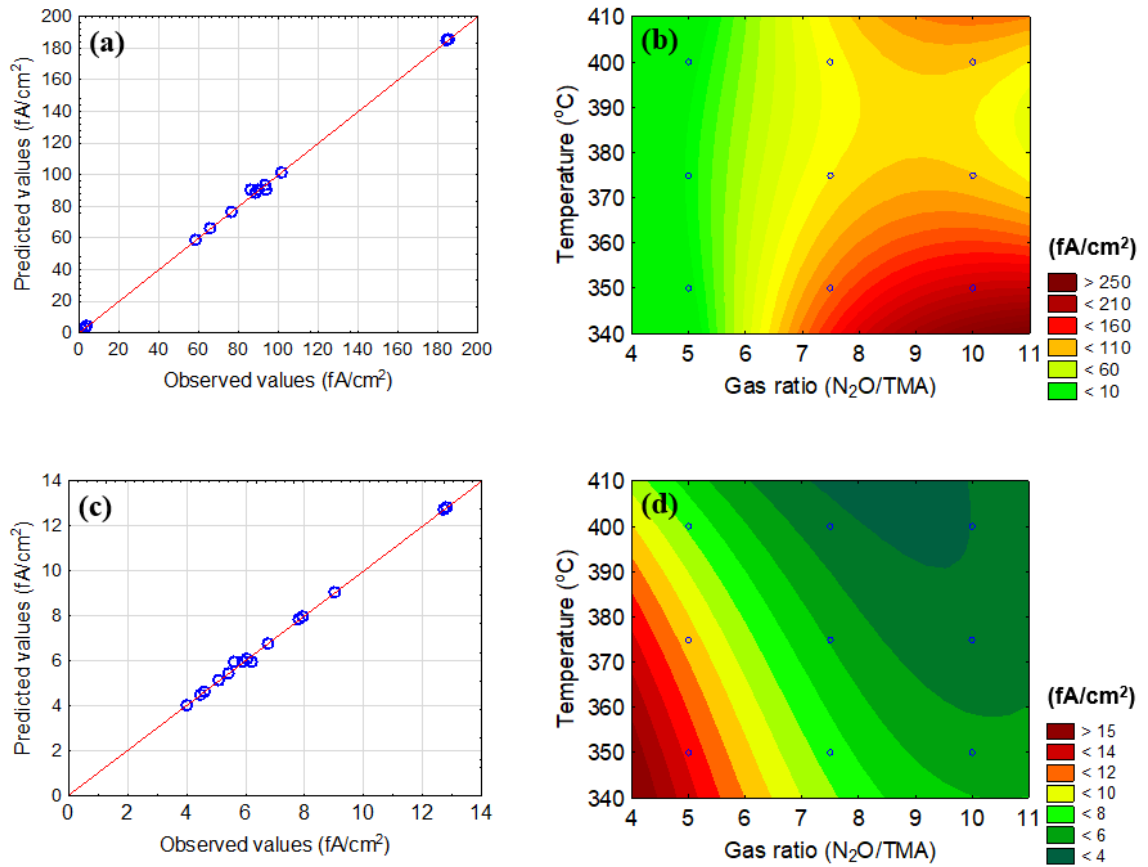


Fig. 4-2. (a) Correlation between predicted and observed J_{0s} values, (b) STATISTICA models for as-deposited J_{0s} , (c) correlation between predicted and observed J_{0s} values and (d) STATISTICA model for fired J_{0s} .

The Auger-corrected inverse lifetime curves of the central point condition film (Run #8 in Table 4-2) in Exp. #2 and the values extracted from Quokka-based modelling are presented in Fig. 4-3. The Quokka fitting covers the entire range from 10 μs to 6000 μs . This wide range should be sufficient for both p -type and n -type samples. Despite the slight difference between the obtained values, both methods (slope-based and Quokka) indicate that high quality passivation has been achieved after firing.

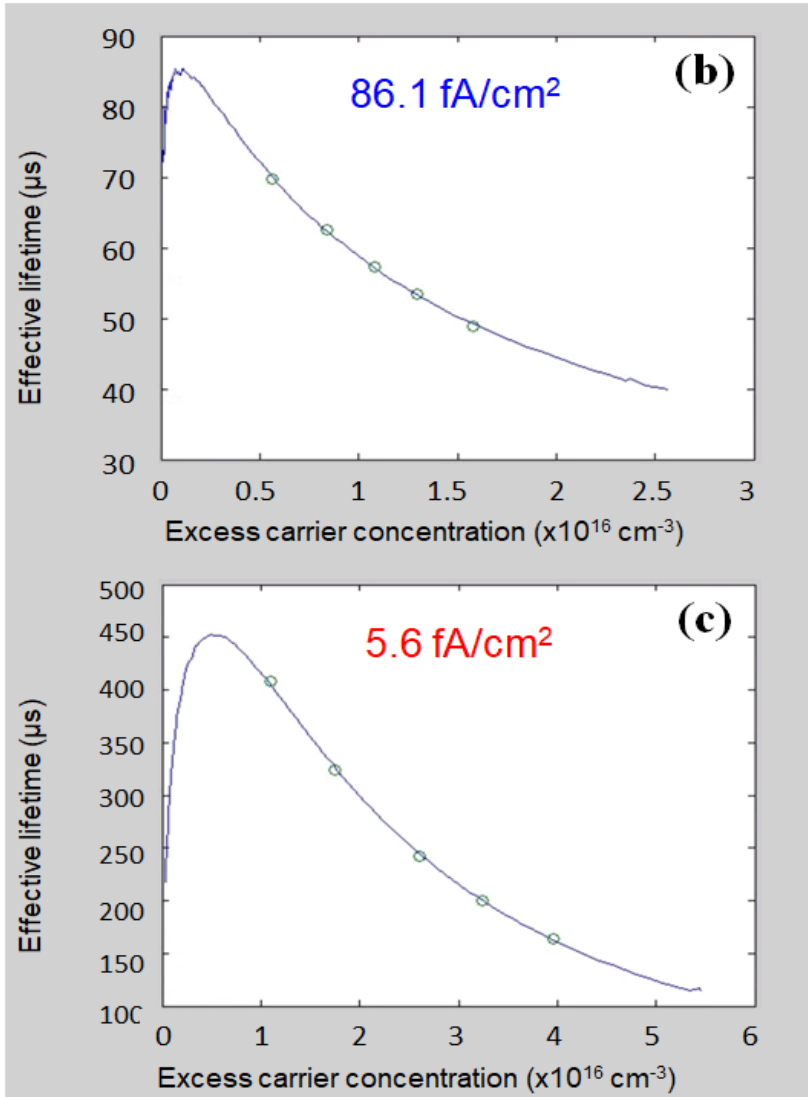
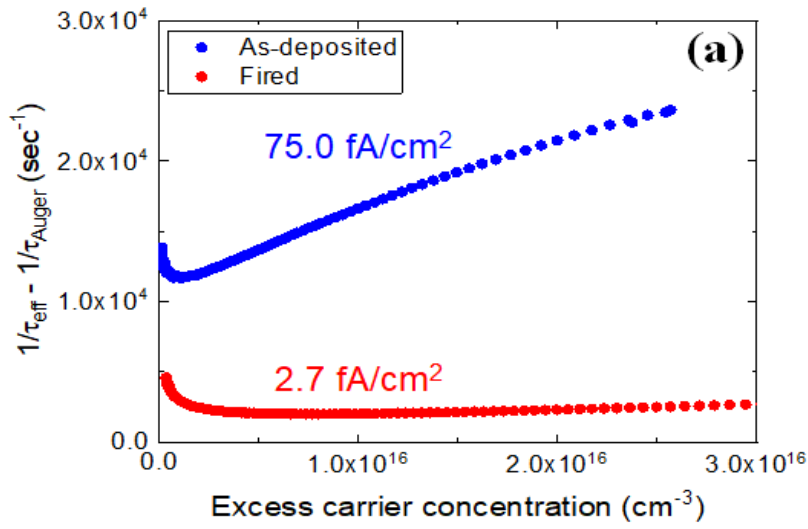


Fig. 4-3. Representative example of a central point sample: (a) Auger-corrected inverse lifetime curves of as-deposited and fired wafers and Quokka simulation result of (b) as-deposited wafer and (c) fired wafer. Green open dots in (b) and (c) are the actual points used for curve fitting.

Fig. 4-4 presents contour plots of τ_{eff} for (a) as-deposited and (b) fired wafers for p -type wafers. It is interesting to note that the model for the as-deposited τ_{eff} [Fig. 4-4 (a)] is different from the model obtained for as-deposited J_{0s} [Fig. 4-2 (b)]. Assuming the used wafers have a similar initial bulk quality, it can be expected that τ_{eff} would follow the changes in the surface passivation. However, the difference between J_{0s} and τ_{eff} in the resulting model indicates a modification of the bulk quality which occurs during the low temperature (350 °C) deposition process, as also reported in [194].

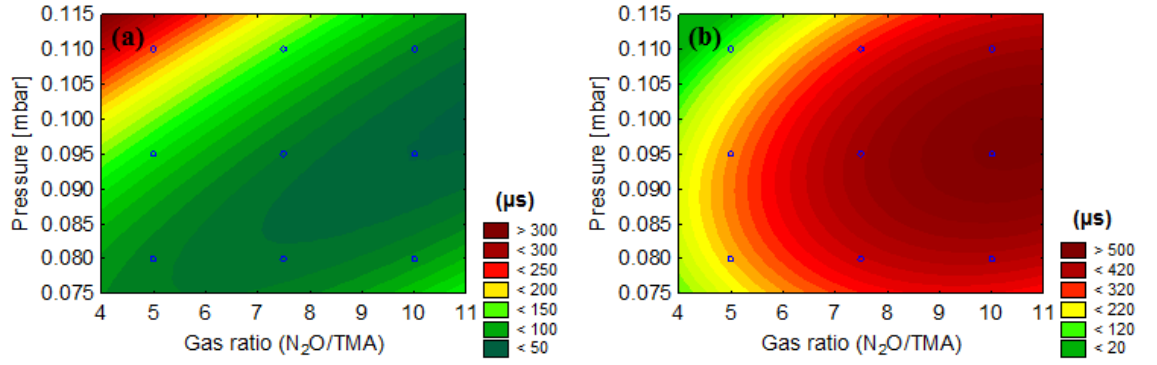


Fig. 4-4. Effective lifetime contour plots of (a) as-deposited and (b) fired wafers for p -type wafers.

The impact of the deposition parameters on J_{0s} for n -type wafers is presented using a contour plot in Fig. 4-5. The p -value is used to evaluate the significance of the experimental parameters on J_{0s} and τ_{eff} . As discussed, the J_{0s} values presented in this chapter are the ones extracted from the Quokka simulation to avoid underestimation of J_{0s} , as discussed above. It is observed that GFRR has the most significant impact ($p < 0.005$) on J_{0s} for both as-deposited and fired wafers; similar to p -type surfaces [Fig. 4-2 (b) and (d)]. The deposition temperature ($p < 0.010$) and the deposition pressure ($p < 0.041$) also influence the as-deposited and fired J_{0s} values. Lower GFRRs result in better surface passivation, where GFRR of 5 achieves J_{0s} below 10 fA/cm²; these are very low values for as-deposited AlO_x. Firing is found to lead to a reduction in J_{0s} for most cases, except for samples deposited with GFRR of 5 (similar to the results for p -type samples; see Fig. 4-2). Larger improvement of the surface passivation (reduction of J_{0s}) is observed for higher GFRR. Extremely low J_{0s} (~4 fA/cm²) is achieved for GFRR of 10, similar to the p -type samples [Fig. 4-2 (c) and (d)]. The possible reason for the strong impact of the GFRR on J_{0s} is discussed in the chemical properties (see *Section 4.3.3*).

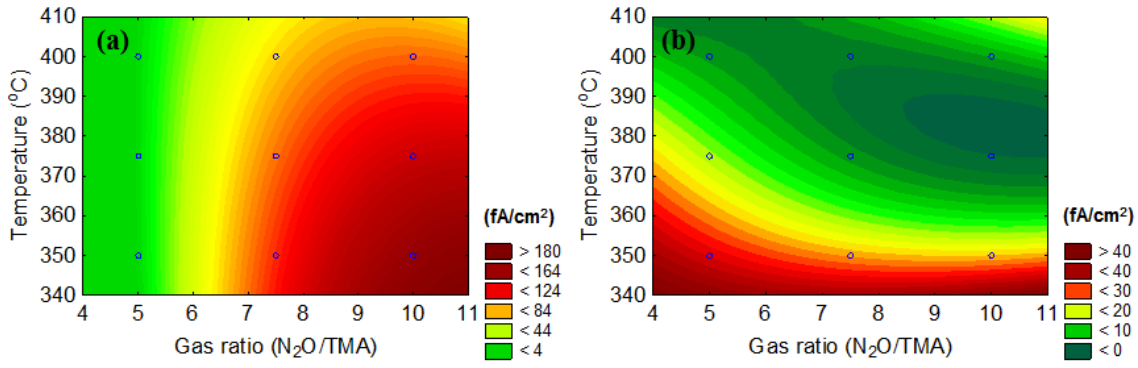


Fig. 4-5. STATISTICA model contour plot of *n*-type wafers for (a) as-deposited J_{0s} and (b) fired J_{0s} .

For a better understanding of the c-Si/ AlO_x interface, corona-charge contactless C-V measurements [170], [171] were used to extract Q_{tot} and D_{it} . As it is discussed in *section 3.4.2*, Q_{tot} is dominated by Q_f when the surface is well-passivated (surface-limited) since Q_{it} is negligible [166]. Therefore, the comparison using Q_{tot} is reasonable especially for comparing between samples. Example (Run ID #8) C-V measurements of *p*-type and *n*-type wafers are shown in Fig. 4-6. The contact potential difference (V_{cpd}) as a function of the deposited charge is presented in Fig. 4-6 (a) and (d). The initial state of the sample is marked as larger circles. It is clear that the initial state (indicated as a large circle) of the *p*-type and *n*-type samples creates an accumulation and inversion layer, respectively. Firstly, the V_{cpd} between the wafer and the vibrating reference electrode is determined. The surface barrier, sometimes called the surface barrier voltage (V_{sb}) that is created by the negative charge of the AlO_x layer is shown in Fig. 4-6 (b) and (e) for both as-deposited and fired samples. It is defined as the difference between V_{cpd} measurements done in the dark and under illumination. Under accumulation for *n*-type wafers (sufficient positive ions $[(\text{H}_2\text{O})_n\text{H}^+]$ are applied on the sample), the V_{cpd} measurements under in the dark and the light are similar, resulting in $V_{sb} \approx 0$. The D_{it} is measured at the minimum of the ‘U-shape’ D_{it} spectrum as a function of surface barrier voltage (V_{sb}), which is typically located near the Si mid-gap [170], [171]. It is generally relatively flat near the mid-gap and increases very rapidly toward the band edges [174].

The STATISTICA-based models for both parameters before and after firing are presented in Fig. 4-7. The validity of the models was confirmed with very high R^2 values (> 0.98) for all the predicted versus measured graphs.

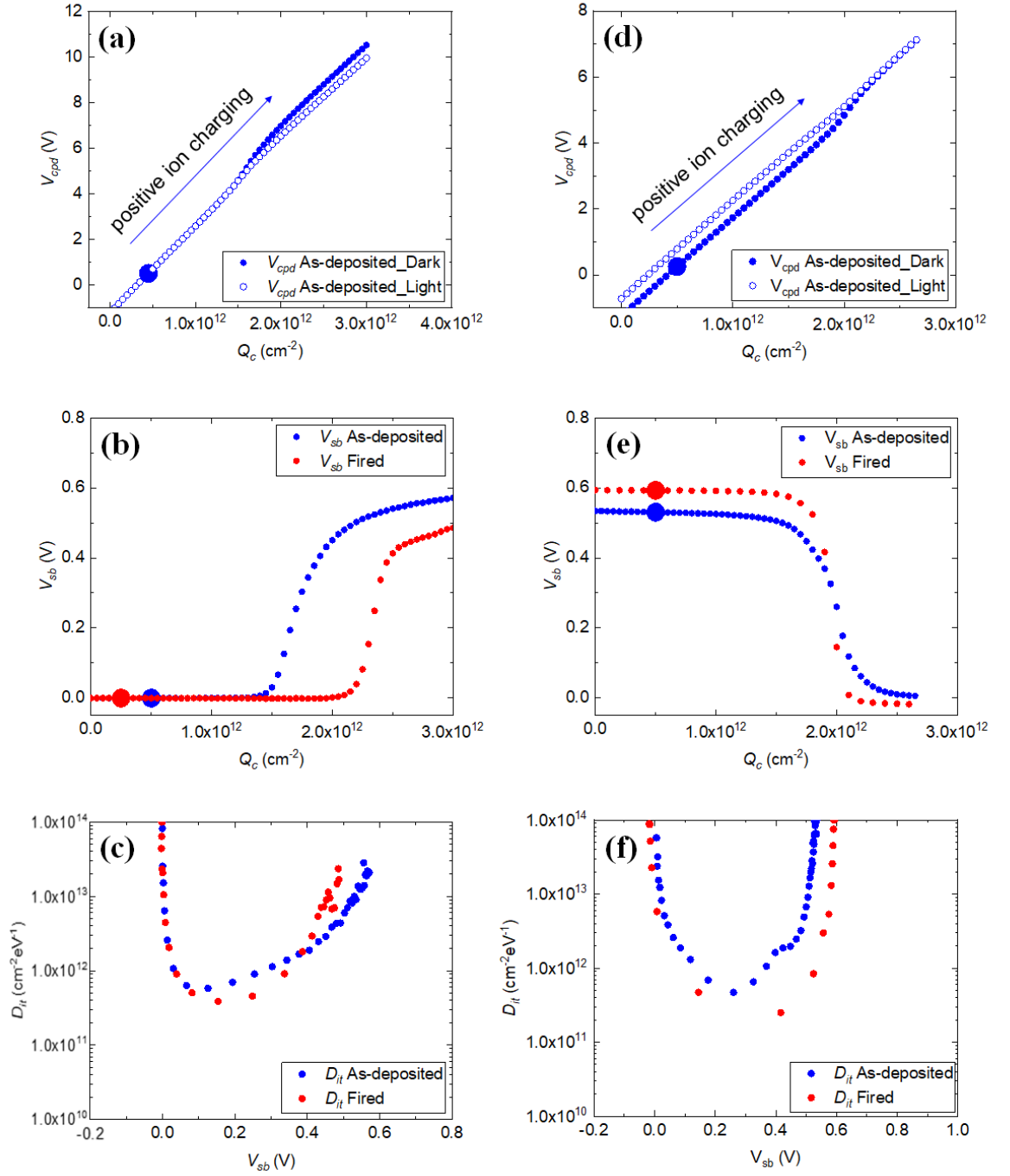


Fig. 4-6. Example of the C-V measurement for p -type and n -type samples for both as-deposited and fired samples. (a) The difference in V_{cpd} , (b) the change of V_{sb} and (c) D_{it} along the positive corona charge for p -type samples. (d) The difference in V_{cpd} , (e) the change of V_{sb} and (f) D_{it} along the positive corona charge for n -type samples. The large circle indicates the initial state of the samples before charging any ions on the sample surface.

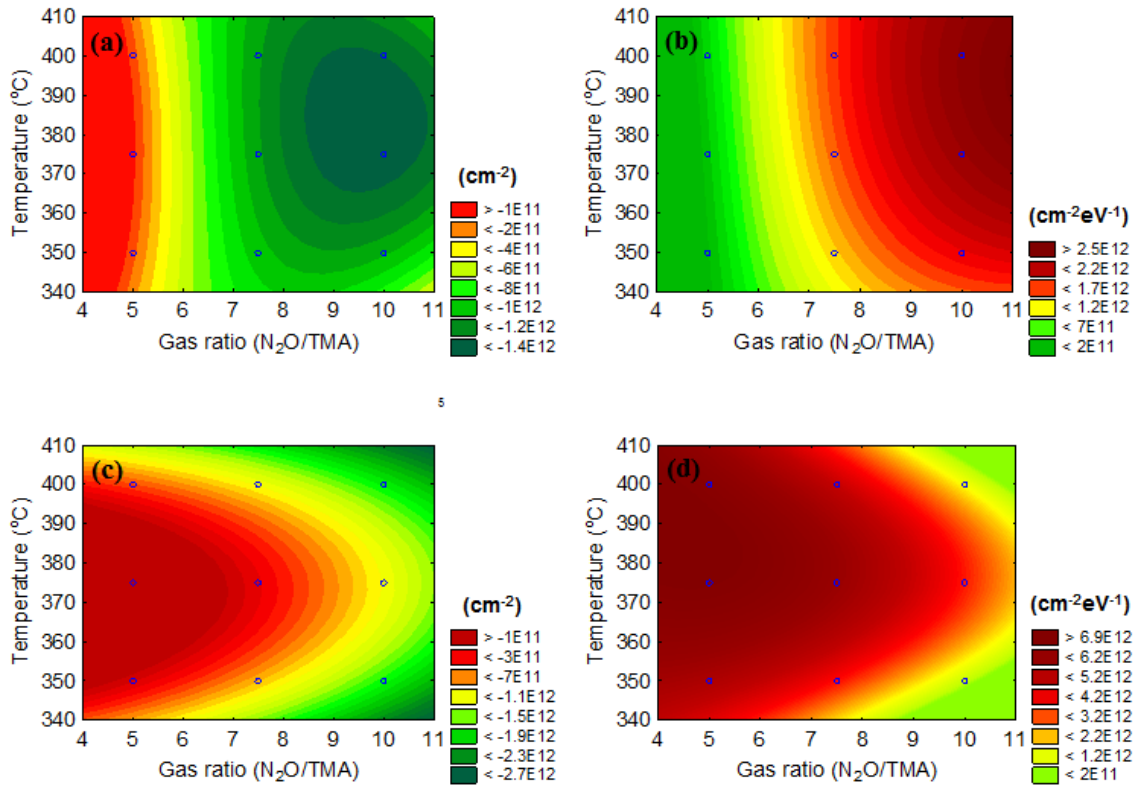


Fig. 4-7. Contour plot of p -type (a) Q_{tot} , (b) D_{it} of as-deposited wafers and (c) Q_{tot} , (d) D_{it} of fired wafers.

For as-deposited layers, GFRR has been found to have the most significant impact on both Q_{tot} and D_{it} . Lower GFRR results in both lower Q_{tot} and lower D_{it} . Hence, the reduction of J_{0s} for as-deposited layers achieved with lower GFRR [Fig. 4-2 (b)] is attributed mainly to the reduction of D_{it} . It seems that D_{it} has such a strong impact on J_{0s} that it overcomes the simultaneous reduction in Q_{tot} . For fired layers, again GFRR is the most significant factor for both Q_{tot} and D_{it} . Pressure also has an impact on both parameters, whereas temperature has an impact only on Q_{tot} . For fired layers, higher GFRR reduces D_{it} and increases Q_{tot} , which coincides with the effect of GFRR on J_{0s} , as observed in Fig. 4-2 (d). As mentioned previously, the difference in GFRR plays a dominant role, which causes different chemical bonding configurations in the resulting layer (i.e. the ratio of tetrahedral aluminium to octahedral aluminium) and it leads to a difference in the Q_{tot} [76], [77], [193]. With regard to the change of D_{it} through firing, Zhang *et al.* reported that the thermal process (firing in this case) has a significant impact on the layer's chemical composition near the interface [76], [77], [193]. Chapter 5 will present a detailed sub-nanoscale investigation regarding the impact of GFRR on both Q_{tot} and D_{it} .

STATISTICA-based models of Q_{tot} and D_{it} for both as-deposited and fired n -type samples are also presented in Fig. 4-8. The validity of the models was confirmed with very high R^2 values (> 0.98) for all the predicted-versus-measured graphs. For as-deposited layers, all the three parameters (temperature, pressure and GFRR) have significant impact on both Q_{tot} and D_{it} , while GFRR has the most significant impact ($p < 0.001$). Lower GFRR results both in a lower D_{it} and in a lower Q_{tot} , which does not contribute to lowering J_{0s} . Hence, the lower J_{0s} for as-deposited layers with lower GFRR [Fig. 4-5 (a)] can be attributed mainly to the reduction of D_{it} . It is the same result as that observed for p -type surfaces (Fig. 4-7). It seems that again D_{it} has a strong enough impact on J_{0s} to overcome the simultaneous reduction in Q_{tot} .

For fired samples, GFRR also shows the most significant impact ($p < 0.001$) on both Q_{tot} and D_{it} . Pressure also has an impact on both parameters, whereas temperature has an impact only on Q_{tot} . Note that the largest amount of negative charge is acquired with GFRR of 7.5 [Fig. 4-8 (c)], whereas the lowest D_{it} is achieved with GFRR of 10. Given that the lowest J_{0s} is achieved with GFRR of 10, it seems that D_{it} contributes more dominantly to the J_{0s} for the fired samples as well. The lower D_{it} in the higher GFRR samples may owe to the slightly higher oxygen concentration in the layer as discussed. This oxygen may be attributed to form an interfacial SiO_2 layer which is known to reduce the D_{it} [76], [77].

Fig. 4-9 presents Q_{tot} and D_{it} for both as-deposited and fired p -type wafers. Similar to previous studies [74], [85], [98], [102], [104], [106], in most cases, the absolute Q_{tot} increases after firing. Interestingly, D_{it} increases for most of the conditions as well (except for the wafers with GFRR of ten). This is different from previous investigations where reduction of D_{it} is commonly observed [74], [85], [98], [102], [104], [106]. The reduction of D_{it} is, in general, attributed to the increase of the silicate (SiO_2) layer thickness and the involvement of hydrogen at the $c\text{-Si}/\text{AlO}_x$ interface through a thermal process. However, Kühnhold *et al.* reported degradation of surface passivation with an increase of D_{it} through a similar firing process to what was done here [106]. It was found that the D_{it} increase is attributed to the loss of hydrogen-related bonds, particularly for [O-H]. A detailed discussion related to these chemical bonds is presented in Section 4.3.3.

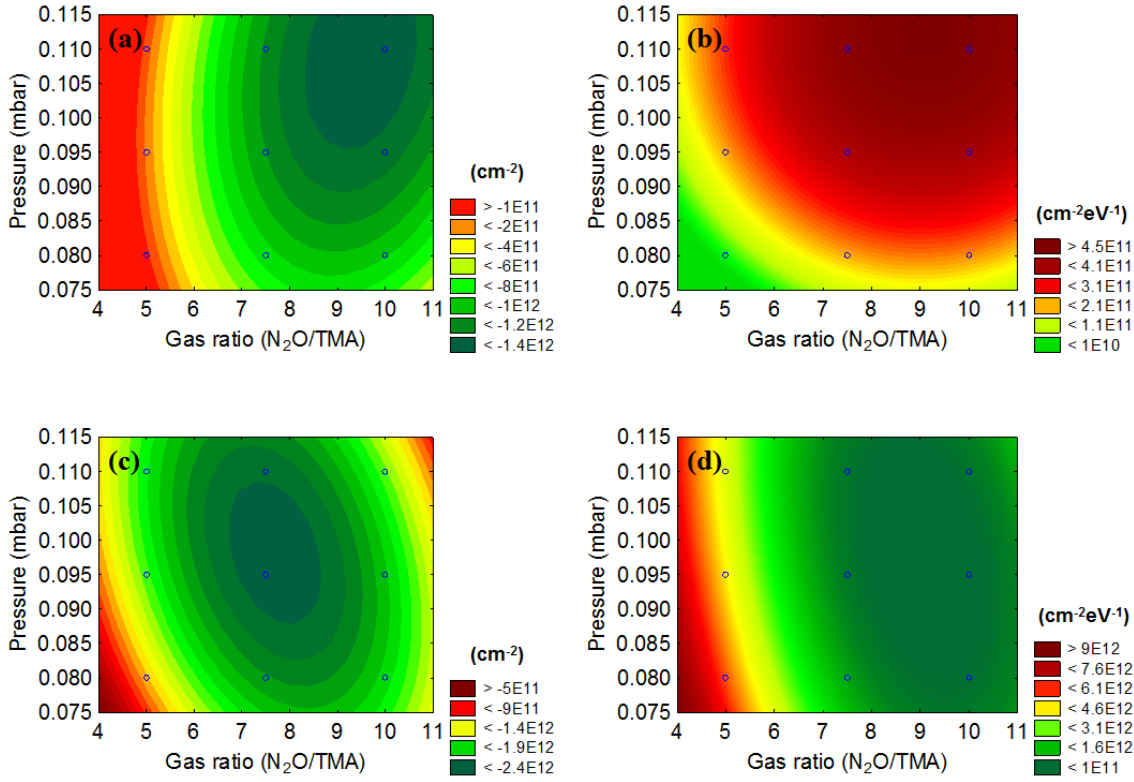


Fig. 4-8. Contour plot based on a STATISTICA model of (a) Q_{tot} , (b) D_{it} of as-deposited n -type samples and (c) Q_{tot} , (d) D_{it} of fired n -type samples.

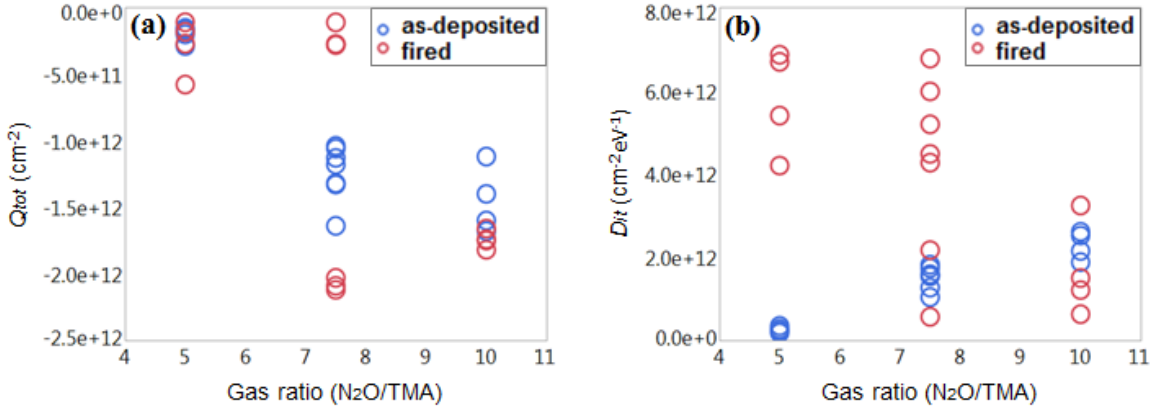


Fig. 4-9. (a) Q_{tot} of both as-deposited and fired wafers and (b) D_{it} of both as-deposited and fired wafers for p -type wafers.

To investigate the impact of the firing process, Q_{tot} and D_{it} are presented in Fig. 4-10, before and after firing for n -type wafers. Similar to previous studies [74], [85], [98], [102], [104], [106], the negative Q_{tot} increases after firing in most cases. However, D_{it} increases for most of the conditions as well (except for the wafers with GFRR of 10). These observations regarding Q_{tot} and D_{it} are exactly the same as what is observed in p -type samples [Fig. 4-9 (a)]. Although the firing process increases the amount of negative charge, lower GFRR causes a large increase in D_{it} . This leads to an increase in J_{0s} as

observed in Fig. 4-5 (a) and (b) and confirms that D_{it} plays a dominant role in J_{0s} at lower GFRR.

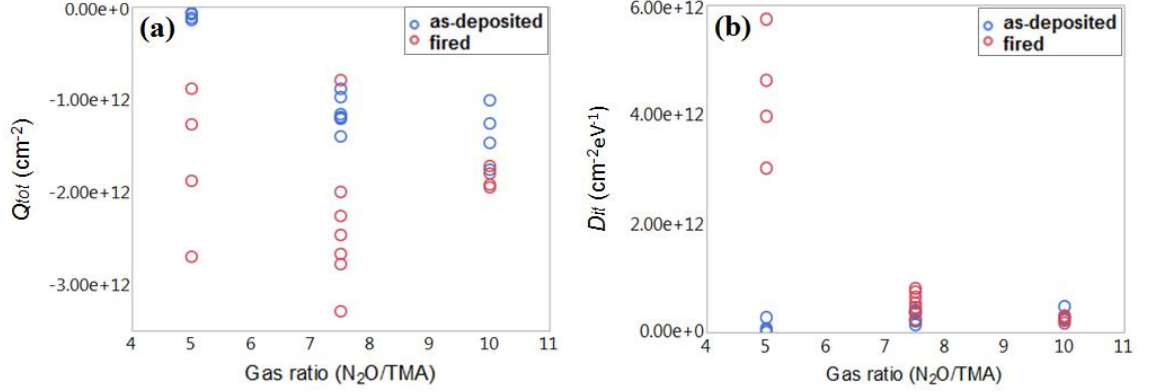


Fig. 4-10. (a) Q_{tot} of both as-deposited and fired wafers and (b) D_{it} of both as-deposited and fired wafers for n -type wafers.

I also investigate the correlation of J_{0s} with D_{it} and Q_{tot} . The relation of J_{0s} to D_{it} and Q_{tot} can be explained by Eq. 4-1 in terms of the SRH recombination as discussed by McIntosh *et al.* [46]. For the range of base doping and the amount of negative Q_{tot} of this study, a strong accumulation (in the case of p -type wafers) or strong inversion (in case of n -type wafers) layer is formed. Then J_{0s} can be expressed as below:

$$J_{0s} = qS_{n0} \frac{2kT\epsilon_{Si}}{Q_{tot}^2} n_i^2 = qV_{th} D_{it} \sigma_n \frac{2kT\epsilon_{Si}}{Q_{tot}^2} n_i^2$$

Equation 4-1

where S_{n0} is the surface recombination velocity of electrons ($S_{n0} = V_{th} D_{it} \sigma_n$) and ϵ_{Si} is the permittivity of the semiconductor (Si). Hence, Eqs. 4-1 indicates that J_{0s} is linearly proportional to D_{it} and inversely proportional to Q_{tot}^2 .

It is previously noted that D_{it} seems to dominate J_{0s} for as-deposited films [compare Fig. 4-2 (b) and Fig. 4-7 (b)] and both D_{it} and Q_{tot} impact J_{0s} in case of fired wafers [compare Fig. 4-2 (d) and Fig. 4-7 (c) and (d)]. Further investigation on the correlation using Eq. 4-1 and Eq. 4-2, is presented in Fig. 4-11. For as-deposited films, it is observed that J_{0s} has a linear trend to D_{it} , with no significant impact by Q_{tot} . More interestingly, it seems that proportionality between J_{0s} and D_{it} exhibits a dependence on the deposition temperature. The films deposited at 350 °C have higher proportionality than the films deposited at 375 °C and 400 °C, as shown in Fig. 4-11 (a). It may be related to Q_{tot} which is slightly lower for films deposited at 350 °C than for films deposited at 375 °C and 400 °C, as shown in Fig. 4-7 (a). Regarding the fired wafers, J_{0s} shows the expected gradual increase as D_{it}/Q_{tot}^2 value increases. The slight spreading of the measurements

is probably due to other parameters contributing to J_{0s} , (except for D_{it} or Q_{tot}), such as a space charge barrier as reported in [195] and uncertainties related to both lifetime and C-V measurements.

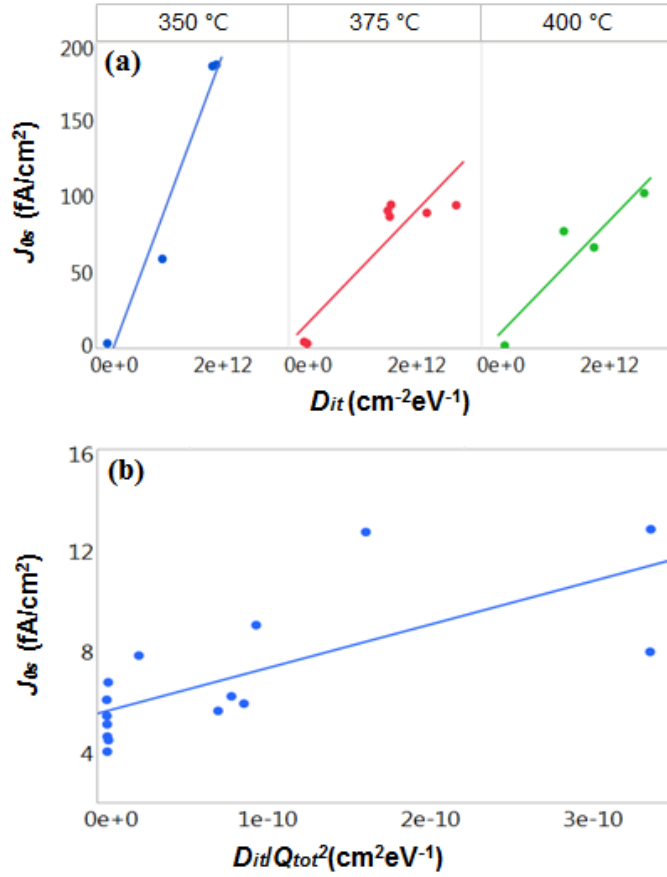


Fig. 4-11. Correlation between (a) J_{0s} and D_{it} for as-deposited wafers with dependence on deposition temperature and (b) J_{0s} and D_{it}/Q_{tot}^2 for fired wafers. The solid lines only serve as guides to the eyes.

The differences in surface passivation quality between the p -type and n -type samples will now be discussed in depth. The comparison between J_{0s} obtained for p -type and n -type are presented in Fig. 4-12. The p -type and n -type are cleaned (RCA clean) and deposited (PECVD) at the same time to avoid any possible variation. For the as-deposited samples, the surface passivation efficacy between p -type and n -type the same regardless of the polarity of the Si wafer [Fig. 4-12 (a)]. As discussed, it seems that in this study, the J_{0s} value of the as-deposited samples is dominated by D_{it} rather than Q_{tot} . This indicates that the impact of the chemical passivation is more critical than the field effect passivation on J_{0s} for the as-deposited wafers.

However, for fired samples a difference in the surface passivation quality between the p -type and n -type samples can be observed [Fig. 4-12 (b)]. It seems that J_{0s} values of n -

type samples are higher than those of p -type for certain samples. This different effect of surface passivation depending on the different types of base-doping can be explained by the field effect passivation. For fired samples, increased negative charges form stronger accumulation layer which repels minority carriers (electrons) in p -type samples. However, on the other hand, stronger inversion layer is created by the increased negative charges in n -type samples. Therefore, field effect is less efficient, and the surface passivation may rely more on the chemical passivation.

It is also interesting that the J_{0s} ratio of n -type to p -type becomes lower as deposition temperature goes higher for fired wafers, whereas the J_{0s} ratio becomes lower with increasing temperature for as-deposited wafers, as shown in Fig. 4-13. This indicates the efficacy of the improvement in J_{0s} through firing has dependence on the deposition temperature. It seems that the increased D_{it} may dominantly contribute to the increase of J_{0s} , since D_{it} shows the same dependency as J_{0s} (on the deposition temperature).

As discussed in Eq. 4-1 [46], J_{0s} depends on S_{n0}/Q_{tot}^2 (n -type) or S_{p0}/Q_{tot}^2 (p -type). The S_{n0} and S_{p0} are $\sigma_n V_{th} N_{st}$ and $\sigma_p V_{th} N_{st}$, respectively, as discussed in Eq. 2-12. Note that V_{th} is constant and N_{st} of n -type wafers are smaller than p -type wafers but by less than one order of magnitude for the wafers used in this thesis (see and compare Fig. 4-7 and Fig. 4-8). However, σ_n is higher than σ_p by about two to three orders of magnitude for PECVD AlO_x according to literature [196] and empirical measurement by Saint-Cast [96]. Hence, J_{0s} values tend to be higher for n -type than for p -type surfaces; the ratio between the electron and the hole capture cross sections is more dominant than the other parameters such as Q_{tot} and D_{it} .

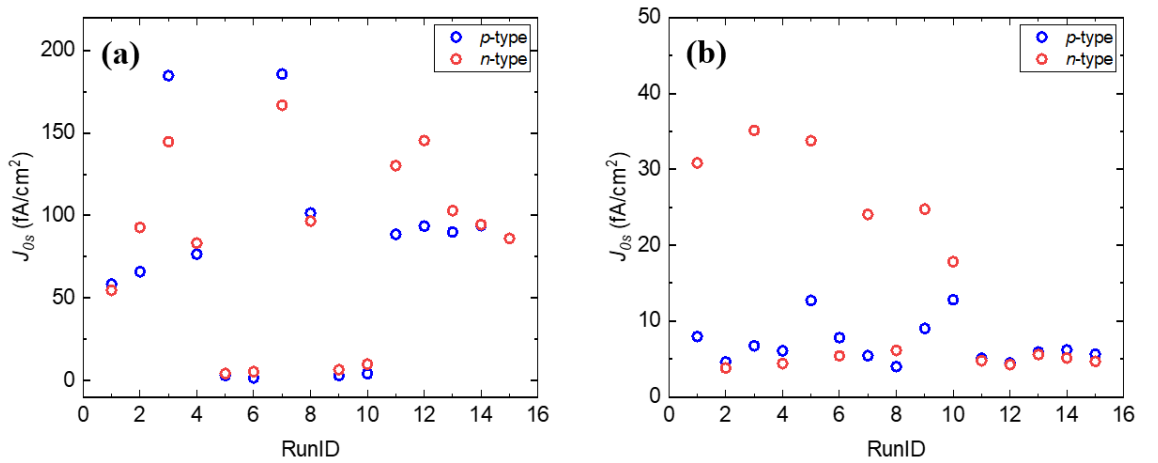


Fig. 4-12. Comparison of J_{0s} between p -type and n -type for (a) as-deposited and (b) fired samples. Both the p -type and n -type samples are processed at the same time using the same Run ID.

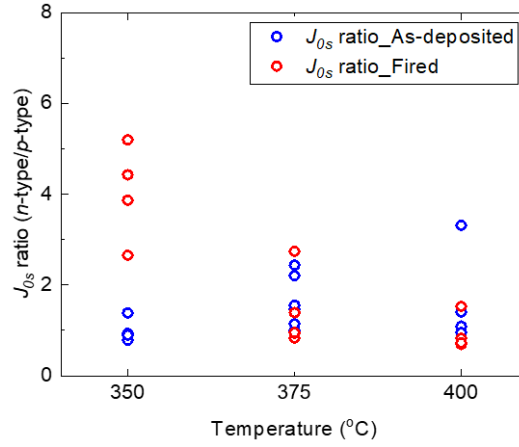


Fig. 4-13. J_{0s} ratio of n -type to p -type for as-deposited and fired samples.

For further consideration of the data presented in Fig. 4-12 (b) and Fig. 4-13, direct comparisons between J_{0s} for p -type and n -type wafers are presented in Fig. 4-14 as a function of deposition parameters, GFRR and deposition temperature. It seems that the samples, which are deposited at low temperature (350 °C) show the biggest difference between p -type and n -type samples. This temperature dependence seems to be larger than the impact of GFRR. Note that the GFRR impact is larger for the low temperature samples and becomes smaller for 375 °C samples and disappears at 400 °C samples. Further investigation is needed to determine the mechanism of this deposition temperature effect. It may be related to the chemical composition or effective thickness of the interfacial layer between Si and AlO_x layer. A sub-nanoscale study of the interfacial layer is presented in *Chapter 5*.

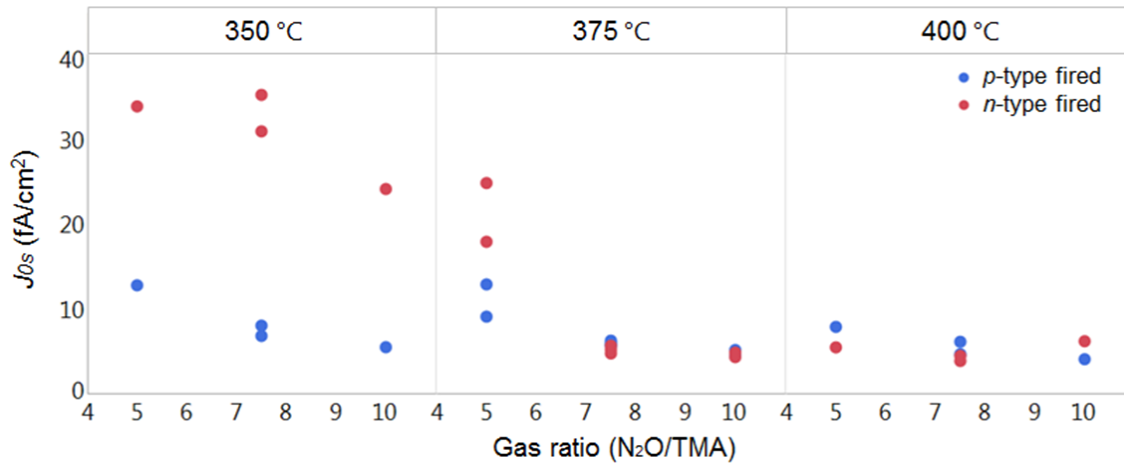


Fig. 4-14. J_{0s} of fired samples for both p -type and n -type as a function of deposition temperature and GFRR.

4.3.3 Chemical Properties

Chemical bonding configurations of the AlO_x layers were investigated using FTIR spectroscopy. The strongest absorption is observed in the $850\text{--}1000\text{ cm}^{-1}$ range, which correlates to the Al-O bond ([Al-O]) [70], [81], [104], [107], [166], [176]. The hydrogen-related bonds ([C-H] and [O-H]) are observed in the range $2300\text{--}3500\text{ cm}^{-1}$ [70], [81], [104], [107], [166], [176]. Representative FTIR spectra, including identified absorption peaks, are shown in Fig. 4-15.

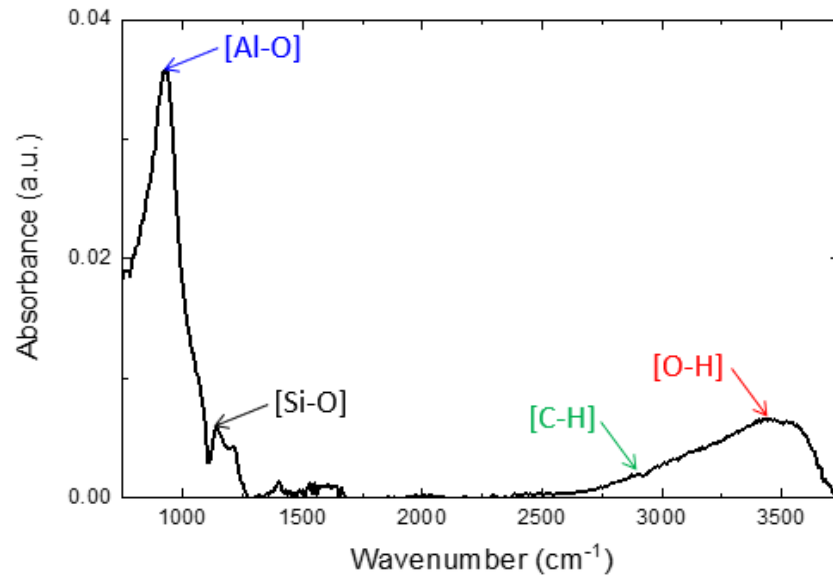


Fig. 4-15. FTIR absorbance of a representative sample (Run 12)

Similar to other AlO_x related studies [70], [81], [104], [107], [166], [176], I have used the amplitude of the absorbance and not the bond concentration (as used for SiN_x [125]) to evaluate the bond concentration since it is difficult to determine hydrogen concentrations in AlO_x layers with FTIR. This is because both [O-H] and [C-H] have a broad spectrum of absorption over a similar range of wavenumbers and they overlap as shown in Fig. 4-15. Fig. 4-16 presents contour plots of the FTIR absorption amplitude of [Al-O] and the sum of amplitudes of the hydrogen-related bonds ([C-H] + [O-H]), for as-deposited and fired layers. To compare the bond density, the absorbance has been normalized by the thickness of each layer. All the chemical bonds were found to be strongly impacted by GFRR (with $p < 0.03$ for both as-deposited and fired). Furthermore, pressure also has an impact on forming [Al-O] for as-deposited layers, whereas temperature influences the hydrogen-related bonds of fired layers. It seems that more [Al-O] is detected at lower deposition pressure [see Fig. 4-16 (a)], similar to reports by several studies that indicate that lower deposition pressure causes a lower deposition rate

and results in higher concentration of [Al-O] which means a denser film [192], [197], [198]. Although there is no significant impact of the deposition temperature on the hydrogen concentration ($p = 0.09$), the concentration of hydrogen-related bonds is reduced by firing. This reduction is less pronounced for layers deposited at higher temperatures and higher GFRR [Fig. 4-16 (d)].

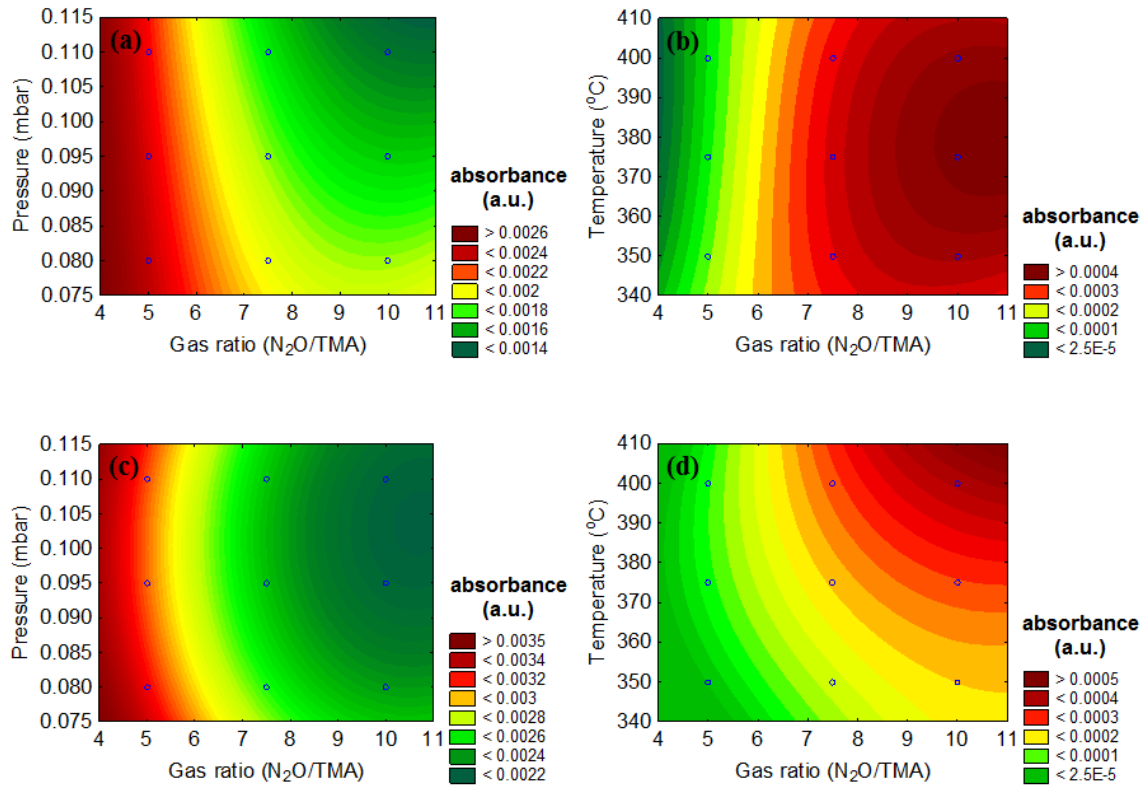


Fig. 4-16. Absorbance corresponding to (a) Al-O bonds, (b) H-related bonds of as-deposited wafers, (c) Al-O bonds and (d) H-related bonds of fired wafers.

As presented in the Fig. 4-17, it is observed that the increase of [Al-O] through the firing process is more obvious for the layers deposited at higher GFRR [Fig. 4-17 (a)]. It is also observed that the decrease of hydrogen-related bonds is more severe in films that were deposited at lower temperatures [Fig. 4-17 (b)]. These changes in the amount of bonds through the firing process is mainly due to the diffusion of oxygen and hydrogen as reported by Kühnhold *et al.* [106] and Levin *et al.* [199]. The involvement of the additional oxygen results in an increased number of [Al-O] and decreased [O-H] for the same reason. The decreased [O-H] is also attributed to the hydrogen release from the film to the Si bulk, which caused a decrease of [C-H] in the same way [200]. The decrease of hydrogen in the layer also densifies the film.

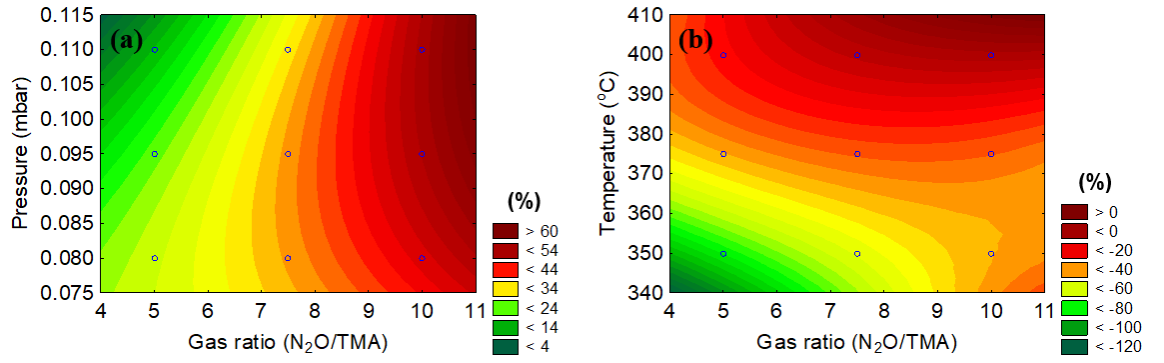


Fig. 4-17. Relative changes of (a) [Al-O] bonds and (b) H-related bonds through firing.

Hydrogen has a critical impact on the passivation of the interface and reduction of D_{it} [64], [72], [122], [201], [202]. Kühnhold *et al.* reported a correlation between changes in the density of [O-H] and D_{it} , although [C-H] was excluded from their analysis [106]. Here I investigate the correlation between all the H-related bonds (sum of [O-H] and [C-H]) and D_{it} . Fig. 4-18 presents the correlation between the relative changes of D_{it} and hydrogen-related bonds linked to the firing process. It is observed that the linear relation between the reduction of H-related bonds and the increase of D_{it} is stronger for lower GFRR films, as also reported in [106]. It seems that H-related bonds are not a dominant contributing factor to D_{it} for higher GFRR, in particularly for GFRR of 10. This may be due to a higher concentration of oxygen which possibly forms a SiO_x layer at the interface. This could also explain the low D_{it} for samples of GFRR of 10, as shown in Fig. 4-9 (b). Furthermore, three interesting observations can be noticed:

- (1) Lower GFRR films result in higher D_{it} that increases through firing.
- (2) Lower GFRR films generally lose more hydrogen through firing.
- (3) The linearity (slope) between D_{it} increase and hydrogen release is stronger for lower GFRR.

It is believed that the hydrogen release occurs either from the AlO_x layer or from the c-Si/ AlO_x interface [106]. Part of the released hydrogen from the AlO_x layer can migrate towards the Si/ AlO_x interface to form [O-H] bonds and [Si-H] bonds [106]. Therefore, the relative decrease of hydrogen can be taken as the sum of hydrogen release (from the AlO_x layer and the interface) and the newly bonded hydrogen at the c-Si/ AlO_x interface. Conclusively, the higher D_{it} and the steeper slope of low GFRR (= 5) indicates that hydrogen effusing out is more effective than forming [O-H] bonds at the interface.

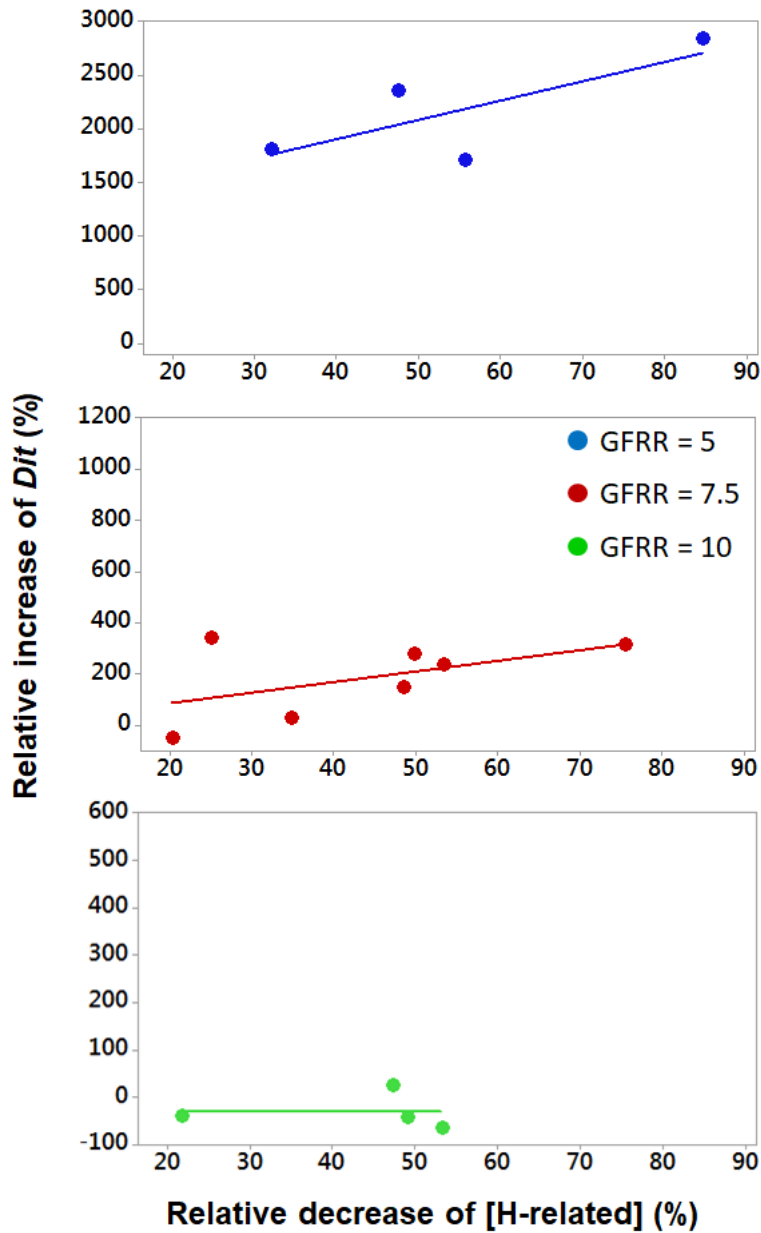


Fig. 4-18. Relative increase of D_{it} as a function of the relative decrease of H-related bonds ($[O-H] + [C-H]$). The solid lines only serve as guides to the eyes.

4.3.4 Hydrogen in the layer

To further investigate the change of hydrogen concentration and migration of the released hydrogen, ERDA measurements are carried out. I chose two representative samples for these measurements [low GFRR (= 5) Fig. 4-19 (a) and high GFRR (= 10) Fig. 4-19 (b)]. The deposition conditions for the two layers are listed in Table 4-2 as Recipe #12 and #15, respectively. Fig. 4-19 presents hydrogen atomic concentration along the depth of the AlO_x layer.

Firstly, the ERDA measurements confirm the FTIR results regarding the reduction in hydrogen concentration due to firing. For both GFRRs, the hydrogen concentration in

the AlO_x layer decreases. As concluded previously, a sample that was deposited using lower GFRR loses a larger amount of hydrogen. More interestingly, the low GFRR as-deposited sample has a higher hydrogen concentration towards the atmosphere, as shown by the depth profile in Fig. 4-19 (a). This may indicate that the AlO_x layer near the atmosphere contains hydrogen originating from ambient moisture. The hydrogen absorbed from the ambient is believed to be released more easily by the firing process and cause increased effusion from the AlO_x layer. This agrees with the stronger reduction of hydrogen-related bonds and higher D_{it} increase for the low GFRR wafers as discussed in Fig. 4-18.

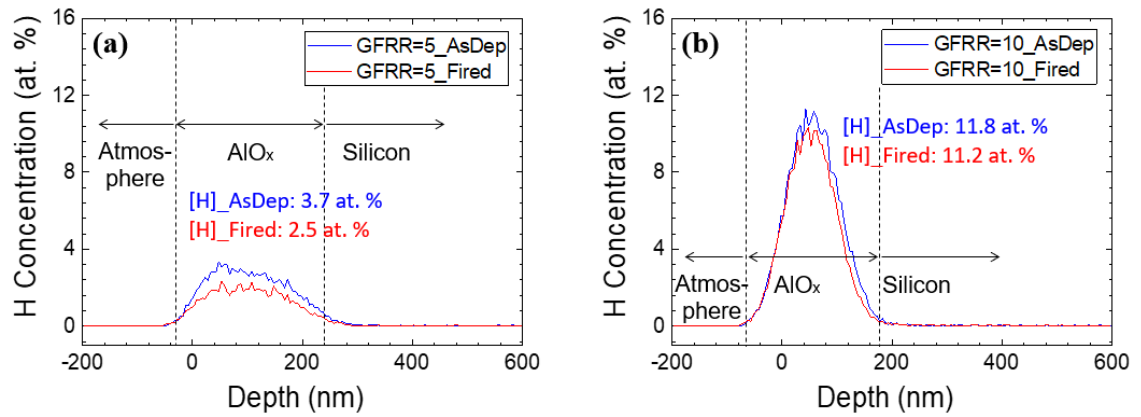


Fig. 4-19. ERDA measurements of as-deposited and fired films deposited with (a) GFRR of 5 and (b) GFRR of 10.

4.3.5 Chemical composition

With the dominant impact of GFRR on most of the investigated electrical and chemical properties, it is interesting to determine the stoichiometry level of AlO_x films deposited with different GFRRs. The two films used previously for the ERDA measurements were also analyzed using XPS. Fig. 4-20 presents the atomic percentage of aluminium and oxygen throughout the as-deposited AlO_x layer. Surprisingly, both samples show near-stoichiometric composition, regardless of the large gas ratio difference (GFRR 5 and 10). In detail, the ratio of O to Al seems to be slightly higher for the high GFRR sample. Given that aluminium vacancies (V_{Al}) and interstitial oxygen (O_i) can be negatively charged [176], [203], the samples with low GFRR may have a lower probability to create a negative fixed charge than those with higher GFRR [77], [180], [193]. This result can partly explain why lower Q_{tot} was observed for the low GFRR ($-1.55 \times 10^{11} \text{ cm}^{-3}$) wafers than high GFRR wafers ($-1.40 \times 10^{12} \text{ cm}^{-3}$) as seen in Fig. 4-7 (a).

Note that drop of the Al profile and the corresponding rise of Si profile for high GFRR [Fig. 4-20 (b)] at the $\text{AlO}_x/\text{c-Si}$ interface is more gradual than for the low GFRR (= 5)

sample. It may indicate that an interfacial layer composed of Al, Si and O (i.e. aluminosilicate glass) is thicker in high GFRR samples. It may also suggest that the high GFRR film is slightly denser. A detailed analysis of the interfacial layer is necessary to properly understand this. The follow-up study involving transmission electron microscopy (TEM) in conjunction with electron energy loss spectroscopy (EELS) will reveal more details about the nano-structural features of the interfacial layer. It is presented in *Chapter 5*.

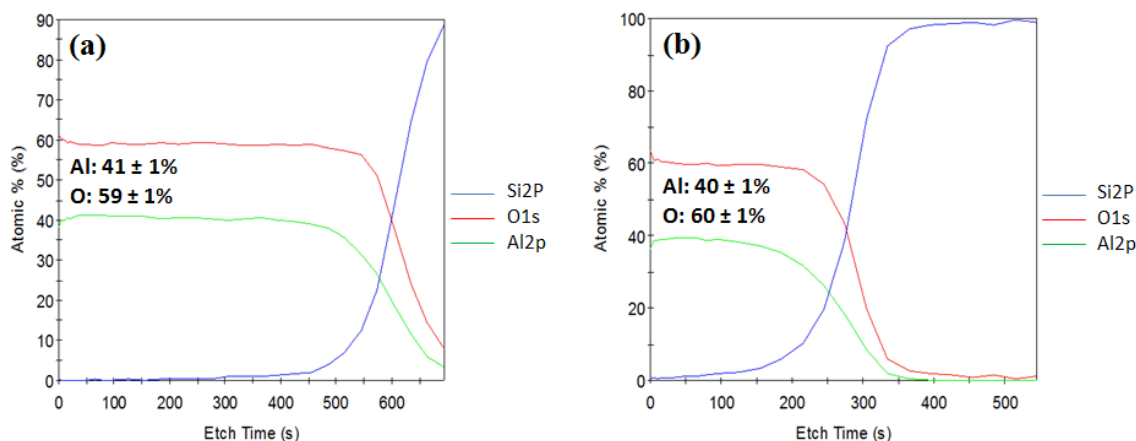


Fig. 4-20. XPS measurements of films deposited with (a) GFRR of 5 and (b) GFRR of 10.

It is still questionable whether there are other properties which cause the different electrical properties of the AlO_x layer. According to previous studies, the aluminosilicate glass layer has a significant impact on the interface properties [23], [76], [98], [188]. More precisely, the presence of SiO_x within the interfacial layer provides excellent surface passivation [23], [76], [98], [188]. Therefore, the interface of the c-Si/ AlO_x is investigated using STEM. Two fired specimens [low GFRR (=5) Fig. 4-21 (a) and high GFRR (=10) Fig. 4-21 (b)] were chosen for this analysis. Both samples show interfacial layers, however, their brightness is not the same. According to previous studies, SiO_x is shown as bright layer in bright field image of STEM [23], [76], [98], [188]. Using EELS it was confirmed that this interfacial layer mainly consists of SiO_x with various stoichiometry [76], [77]. A slightly higher portion of the oxygen for the high GFRR sample may contribute to the formation of the SiO_2 layer at the interface. It will be interesting if the more obvious presence of the SiO_x layer in the high GFRR sample can explain the lower J_{0s} obtained under this condition. Further investigation on the chemical configuration of the interfacial layers and in AlO_x films are presented in the following chapter (Chapter 5).

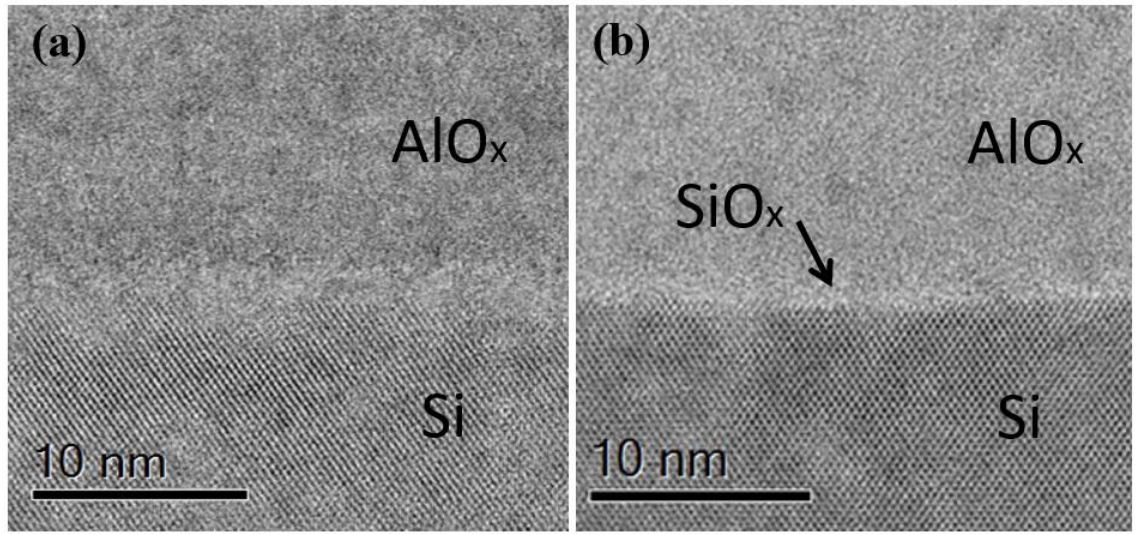


Fig. 4-21. STEM bright field image near the c-Si/AlO_x interface of a fired sample for (a) GFR=5 and (b) GFR=10.

4.4 Summary

The electrical and chemical properties of the AlO_x layer on non-diffused *p*-type and non-diffused *n*-type c-Si surface deposited by an industrial type in-line PECVD system are investigated. MWP to TGFR ratio is found to be a critical factor for the thermal stability of the deposited AlO_x layer. Furthermore, it is found that GFR has the most significant impact on both the electrical and chemical properties of as-deposited and fired layers. Higher GFR is preferred for fired samples, whereas lower GFR is ideal for non-fired samples for promising surface passivation. Further analysis reveals that a decrease in D_{it} has a critical impact on lowering the surface recombination of as-deposited samples. However, after firing, with a sufficient amount of Q_{tot} , both D_{it} and Q_{tot} have an impact on surface recombination.

Regarding the comparison between the *p*-type and *n*-type, the difference between the two different base-doping wafers is not significant for as-deposited samples. However, the difference increases for fired samples with higher J_{0s} value in *n*-type. This is believed to be attributed to the capture cross section ratio of an electron and hole (σ_n and σ_p). It is also observed that there exists an impact by the interaction between the GFR and the temperature on the fired *n*-type surface passivation. It is also found that GFR has the most significant impact on J_{0s} , Q_{tot} and D_{it} for *n*-type samples as well, which is the same result as for *p*-type samples. Higher GFR is preferred for fired samples, whereas lower GFR is better for non-fired samples to achieve lower surface recombination. In addition, as already demonstrated for *p*-type, a decrease in D_{it} has a critical impact on

lowering the surface recombination of as-deposited samples. However, after firing, with adequate Q_{tot} , both D_{it} and Q_{tot} contribute to suppressed surface recombination, which results in low J_{0s} of 4 fA/cm² as well for both p -type and n -type wafers.

The firing process increases [Al-O] bonds more effectively for higher GFRR samples whereas more hydrogen is released for lower temperature samples. These two observations are found to be related to the increase of Q_{tot} and D_{it} , respectively. The slightly reduced Al and increased O concentrations show good agreement with the resulting higher negative fixed charge in the layer, which results in low J_{0s} of 4 fA/cm².

ERDA reveals the difference in hydrogen depth profile within the AlO_x layer of low GFRR and high GFRR samples. It is also observed that release of hydrogen is more significant near the airside of the layer than silicon side.

In addition to the electrical and chemical properties of AlO_x layer. The STEM of the c-Si/AlO_x interface reveals the presence of different interfacial layer (much more clear for the fired high-GFRR (=10) sample). This raises the necessity of further study on the interface since the different properties of different AlO_x layers may be originated not only from the layer itself but also from the interface. It is believed to include a thin SiO₂ layer and further investigation on the nano-scale is presented in the following chapter.

5 Interface study of c-Si/AlO_x³

5.1 Introduction

In *Chapter 4* various properties of PECVD AlO_x film as a surface passivation layer for c-Si were studied. The excellent surface passivation of the AlO_x layer on *p*-type c-Si surfaces is mainly attributed to field effect passivation, due to its relatively large negative Q_{tot} as well as the relatively low D_{it} [14], [83], [89], [101], [108], [204]. In particular for *p*-type wafers, the field effect passivation is a result of an accumulation layer formed by the negative charge at the interface between the c-Si and the AlO_x layer that minimises minority carrier recombination [76], [205]–[208].

Although various characterisation and analysis methods reveal the electrical and chemical properties of the AlO_x layer, the sub-nanometer scale understanding of the film remains unclear. As mentioned at the end of *Chapter 4*, further investigation on the c-Si/AlO_x interface seems to be necessary for a deeper understanding of the interface. In this chapter, the origin of the negative Q_{tot} and D_{it} is examined at the sub-nanometer scale level.

The origin of the negative charge has been investigated by several studies [15], [17], [74], [193], [209], however, it seems that there are still significant gaps in understanding the AlO_x deposited by PECVD. Hoex *et al.* investigated the origin of negative charge within ALD-deposited Al₂O₃ layers on *n*-type c-Si wafers on the nanometer scale by scanning transmission electron microscopy (STEM) and electron energy loss spectroscopy (EELS) [77]. Although Q_{tot} was not measured, the impact of the thermal process on the bonding configuration of Al and O was discussed. It was suggested that the change of the bonding configuration may be correlated with the expected change in Q_{tot} after a thermal treatment. A more recent investigation was carried out by Zhang *et al.* [76]. They studied the correlation between Q_{tot} , D_{it} and the surface passivation quality provided by AlO_x deposited by atmospheric pressure chemical vapor deposition (APCVD). The two subsequent thermal processes were found to differently influence both Q_{tot} and D_{it} .

In this chapter, the c-Si/AlO_x interface with different AlO_x layers is investigated. The AlO_x layers are chosen based on the result from Chapter 4. As discussed in *Section 4.2*

³ This chapter is summarised and ***under revision*** in *ACS Applied Nano Materials* as of August 2019.

the deposition conditions which shows large difference in Q_{tot} and D_{it} are studied to enable different chemical configurations, using an industrial-type PECVD system. I focus on both Q_{tot} and D_{it} and correlate these properties with the sub-nanometer scale bond configuration. I also correlate the interfacial silicon oxide SiO_x layer thickness (formed between the c-Si and the AlO_x) with the measured surface passivation quality.

5.2 Experiments

The same commercially available (156 mm × 156 mm) *p*-type boron-doped Cz planarised wafers with a resistivity of $1.8 \pm 0.1 \, \Omega \cdot \text{cm}$ and a final thickness of $175 \pm 10 \, \mu\text{m}$, are used in this study. As in previous chapters, all the wafers are RCA cleaned [156] and dipped in HF(mass fraction 5%) solution before the AlO_x depositions. Two different deposition systems were used for comparison; an industrial in-line PECVD system (MAiA XS, Meyer Burger) and a thermal ALD system (SoLayTec, InPassionLAB). The MAiA was used to deposit $20 \pm 5 \, \text{nm}$ AlO_x , with N_2O and TMA precursor gases. The AlO_x was then capped with silicon nitride (75 nm thick with a refractive index of 2.08 at 633 nm) deposited at $350 \, ^\circ\text{C}$ [19]. A high-temperature process (“firing”) was performed to activate the surface passivation [101] for the PECVD AlO_x wafers using an industrial metallisation furnace (7K9-70C69-5LIR, Schmid) in a clean dry air CDA ambient. The *set* firing temperature was adjusted to maintain a fixed *wafer* temperature of $740 \pm 5 \, ^\circ\text{C}$, the standard firing temperature in our facilities. The duration at the peak temperature was about 0.6 seconds for all the wafers.

Based on my previous work [210], I selected three sets of deposition parameters (see Table 5-1) for the PECVD AlO_x samples. The first set leads to a maximum change of the absolute Q_{tot} after firing; the wafers deposited using this set of parameters are labelled with ‘Q’ (see table below). The second set of parameters leads to a maximum change of D_{it} after firing; while this behaviour is not commonly observed, it has been reported by others [98], [106]. The wafers included in this set are labelled with ‘D’. The last set of parameters provides the highest quality of surface passivation with the lowest surface saturation current (J_{0s}) [210]; these wafers are labelled with ‘J’. Two wafers were deposited at each condition. At the end of the fabrication process, the wafers were analysed by PL imaging (BT Imaging LIS-R1) [211] to identify representative uniform regions for contactless C-V and EELS measurements. Fig. 5-1 presents a characteristic PL image of one of the wafers, together with the selected regions for the measurements.

Contactless C-V measurements are performed using a PV metrology system from Semilab (PV-2000). As presented in *Section 3.4.2*, corona charge is deposited on the dielectric layer and the change of the electrostatic potential in the dielectric and the semiconductor is measured by a non-contact Kelvin probe [172]. Q_{tot} is directly measured by the system from the difference between the initial charge state and the flat band condition, while D_{it} is measured at the minimum of the ‘U-shape’ D_{it} spectrum, which is typically located near the Si mid-gap [171].

For STEM/EELS, the wafers were sputtered with 29 nm gold and milled using a FEI XT Nova Nanolab 200 Dual-beam workstation. The specimens were then placed on a standard copper gridded carbon film using an ex-situ lift-out method. A JEOL ARM200F microscope fitted with a cold field emission gun electron source, which provides a very narrow energy spread to the beam, was used for EELS measurements with an energy resolution down to 0.4 eV [with appropriate de-excitation of the gun extraction voltage (A1)].

Table 5-1. Electrical properties of the selected samples for STEM/EELS

Sample ID	Q_{tot} (cm ⁻²)	D_{it} (cm ⁻² eV ⁻¹)	GFRR	Note
Q-A	-1.18×10^{12}	1.33×10^{12}	7.5	Q_{tot} change study specimen (Recipe ID 3 in Table 4.2) As-deposited
Q-F	-2.09×10^{12}	4.48×10^{12}	7.5	Q_{tot} change study specimen (Recipe ID 3 in Table 4.2) Fired
D-A	-1.71×10^{11}	1.84×10^{11}	5	D_{it} change study specimen: (Recipe ID 5 in Table 4.2) As-deposited
D-F	-1.84×10^{11}	5.40×10^{12}	5	D_{it} change study specimen: (Recipe ID 5 in Table 4.2) Fired
J-A	-1.40×10^{12}	2.52×10^{12}	10	The lowest J_{0s} study specimen: (Recipe ID 8 in Table 4.2) As-deposited; 7 fA/cm ²
J-F	-1.82×10^{12}	1.50×10^{12}	10	The lowest J_{0s} study specimen: (Recipe ID 8 in Table 4.2) Fired; 4 fA/cm ²

Probe currents in the range of 10-30 pA were used. EELS spectra were recorded using a Gatan imaging filter (GIF, model 963), fitted with a $2k \times 2k$ Ultrascan charge-coupled device (CCD) camera. Spectra were acquired at various dispersions, with 0.05 eV and 0.1 eV per channel being the most commonly used. The microscope was operated in a STEM mode, using a 40 μm condenser aperture, a GIF entrance aperture of 2.5 mm and a camera length of 4 cm. This yielded beam convergence and collection angles of 24.9 and 20.4 mrad, respectively.

Spectrum imaging was used to acquire an EELS spectrum at each pixel over the region of interest, with a neighbouring region of the specimen used for periodic drift corrections. Sub-pixel scanning (within each pixel) was used to ensure the probe moves continuously during spectrum acquisition and that the effects of beam damage are minimised. Specimen damage and the effects of any superficial hydrocarbon contamination were further reduced by cooling the specimen to liquid nitrogen temperature. Spectra were acquired and processed using the DigitalMicrograph© software (Gatan Inc.) by the SITools [212].

Two specimens per condition were prepared, one of the specimens is used as a control sample to monitor possible modification on the interface characteristic due to radiation or bombardment. Fast STEM images were taken before and after each EELS acquisition. When a darkening was observed in the STEM image after the EELS measurement (due to thinning of the film), the EELS data were discarded.

5.3 Results and discussion

A representative PL image of one of the wafers is shown in Fig. 5-1, together with a STEM image of the selected region (Wafer J-F). As discussed, the STEM/EELS analysis area [marked with '□' in Fig. 5-1 (a)] was selected based on the PL image such that it precisely represents the CV measurement point [marked with '○' in Fig. 5-1 (a)]. The inset graph in Fig. 5-1 (a) shows that the deviation of the PL intensities across both regions is less than 1%. The presence of an interfacial layer can be easily observed in the STEM dark field (DF) image and the pixel intensity across the specimen distinguishes the c-Si/ AlO_x interface from the c-Si and AlO_x layer [Fig. 5-1 (b)]. I focus on this interfacial layer and on the AlO_x layer in the vicinity of this layer in the following discussion.

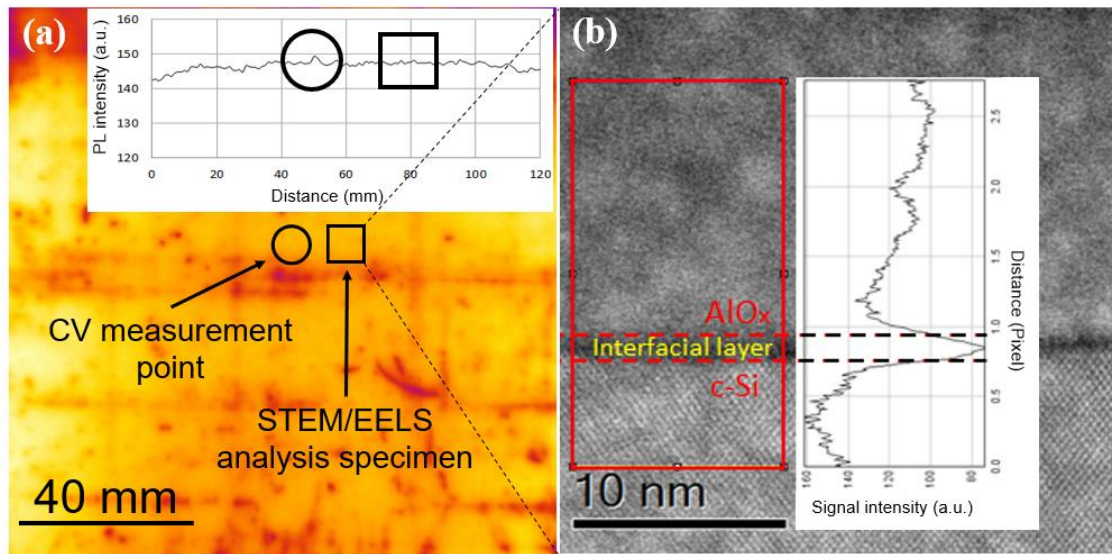


Fig. 5-1. (a) PL image of the wafer J-F showing the CV measurement point (marked as 'o') and STEM/EELS analysis area (marked as '□') with inset graph showing the image pixel intensities of the two regions and (b) TEM dark field image near the c-Si/AlO_x interface with the image pixel intensity across the TEM image (inset).

The analysis method of the EELS spectra using STEM is shown in Fig. 5-2. The first step is to select the vertical length across the layer of interest and then the horizontal width of the layer such that the selected area becomes two-dimensional (2D), as shown using the green-highlighted box (height \times width is 19.15 nm \times 9.74 nm) in Fig. 5-2 (a). The advantage of a 2D scan is a higher signal-to-noise ratio because the sampling is over a relatively large area. Fig. 5-2 (b) shows the spectrum image of the selected 2D scanning area. The size of each pixel in the image is determined by the resolution of the EELS analysis. The size of the pixels in Fig. 5-2 (b) is 0.32 nm \times 0.32 nm and the scanned area has 30 pixels horizontally, meaning the EELS analysis considers the average of 30 EELS spectra for a certain depth. It is also important to make sure the specimen is not damaged during the measurement by the e-beam. The red oval in Fig. 5-2 (b) shows e-beam damage during the measurement. When the beam-induced damage is observed, the average of the spectra is taken only with non-damaged region in the spectrum image and the data from the damaged region is rejected.

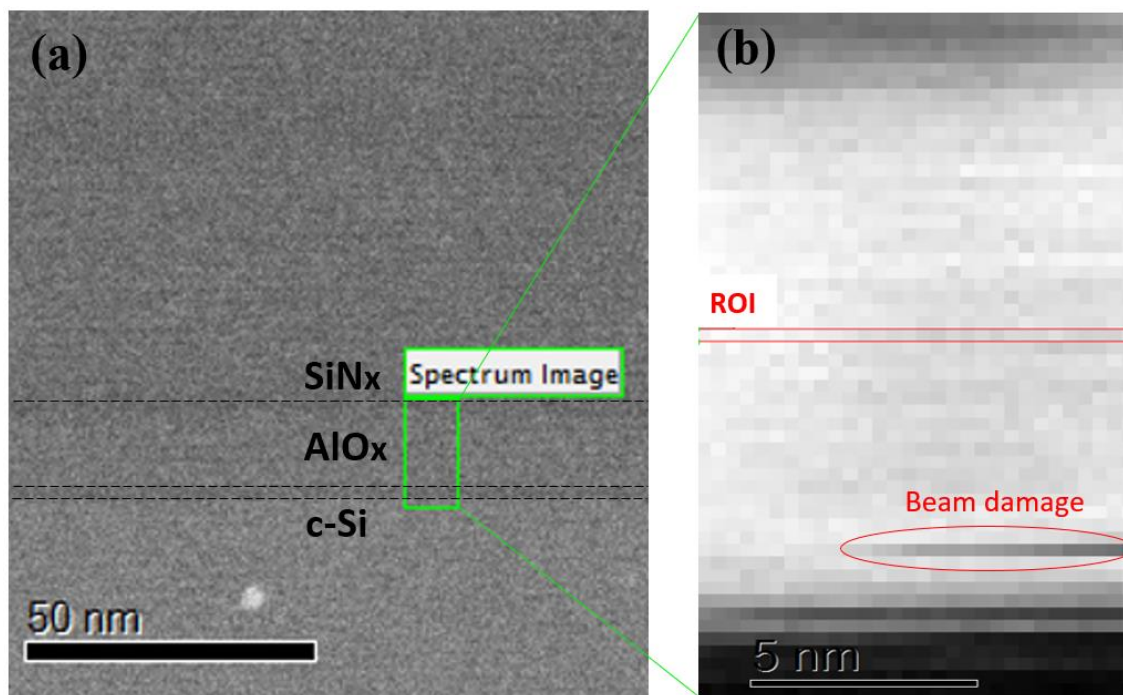


Fig. 5-2. Example of (a) STEM image for EELS spectrum with the specific area (outlined as green box) and (b) the EELS spectrum image zoomed-in with region of interest for analysis. Each pixel size is $0.32 \text{ nm} \times 0.32 \text{ nm}$.

Fig. 5-3 shows the example of EELS spectra for the region of interest (ROI) chosen in Fig. 5-2 (b). The actual signal (energy loss) of the specimen can be acquired by subtracting the background signal (red line) from the measured signal (emerald-filled graph). For better accuracy, the background signal subtraction should be carefully taken from a region adjacent to the energy level of interest. The background signal which decays exponentially as increase of energy is subtracted by the DigitalMicrograph© software. For example, the background signal range is assigned from 70 eV to 75 eV, since the peaks of interest start to be observed from around 78 eV. Considering the width of the peak, I do not assign the background signal too close to the peak of interest. The EELS peak information which correspond to chemical configurations are referred by previous studies [76], [77], [193], [209], [213], [214].

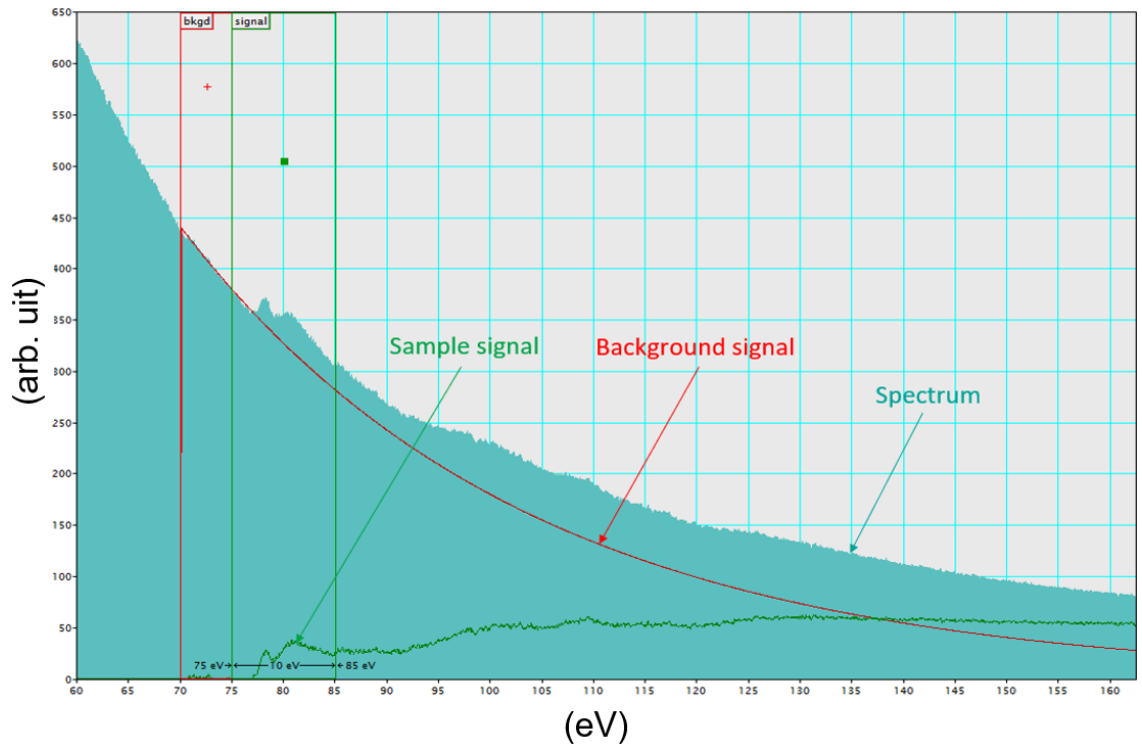


Fig. 5-3. Example of EELS spectra (filled emerald-color region), the background signal (red exponentially decreasing line) and the actual energy loss signal of the specimen (green line).

Firstly, the acquired EELS spectra of Al-L_{2,3} and Si-L_{2,3} for the samples that showed the largest increase in Q_{tot} [Q-A and Q-F; Fig. 5-4 (a) and (b)] and the ones with the largest increase in D_{it} [D-A and D-F; Fig. 5-4 (c) and (d)] through the firing process are analysed. Note that the L-edge corresponds to the principal quantum number of 2, where core electrons are excited for Al and Si. This excitation is detected as an absorption of energy which can be used as a fingerprint of each element. Fig. 5-4 presents both the as-deposited [Fig. 5-4 (a) and (c)] and fired specimens [Fig. 5-4 (b) and (d)]. I focus on the interfacial layer (red-colored spectra) which consists of Si, aluminium and silicates. According to previous studies, the change in Q_{tot} is caused by the change of the chemical configurations [76], [77]. In the case of AlO_x, the peak intensity ratio of the tetrahedrally coordinated aluminium (T-Al: peak at ~ 78.0 eV; labeled ‘T’) to octahedrally coordinated aluminium (O-Al: peak at ~80.5 eV; labeled ‘O’) is a key indicator to identify a change in the chemical configurations, which leads to a change in the amount of negative charge [76], [77]. Previous studies suggested that the ratio of T-Al intensity to O-Al intensity (T/O ratio) is a useful indicator to identify the chemical configuration of AlO_x [76], [208].

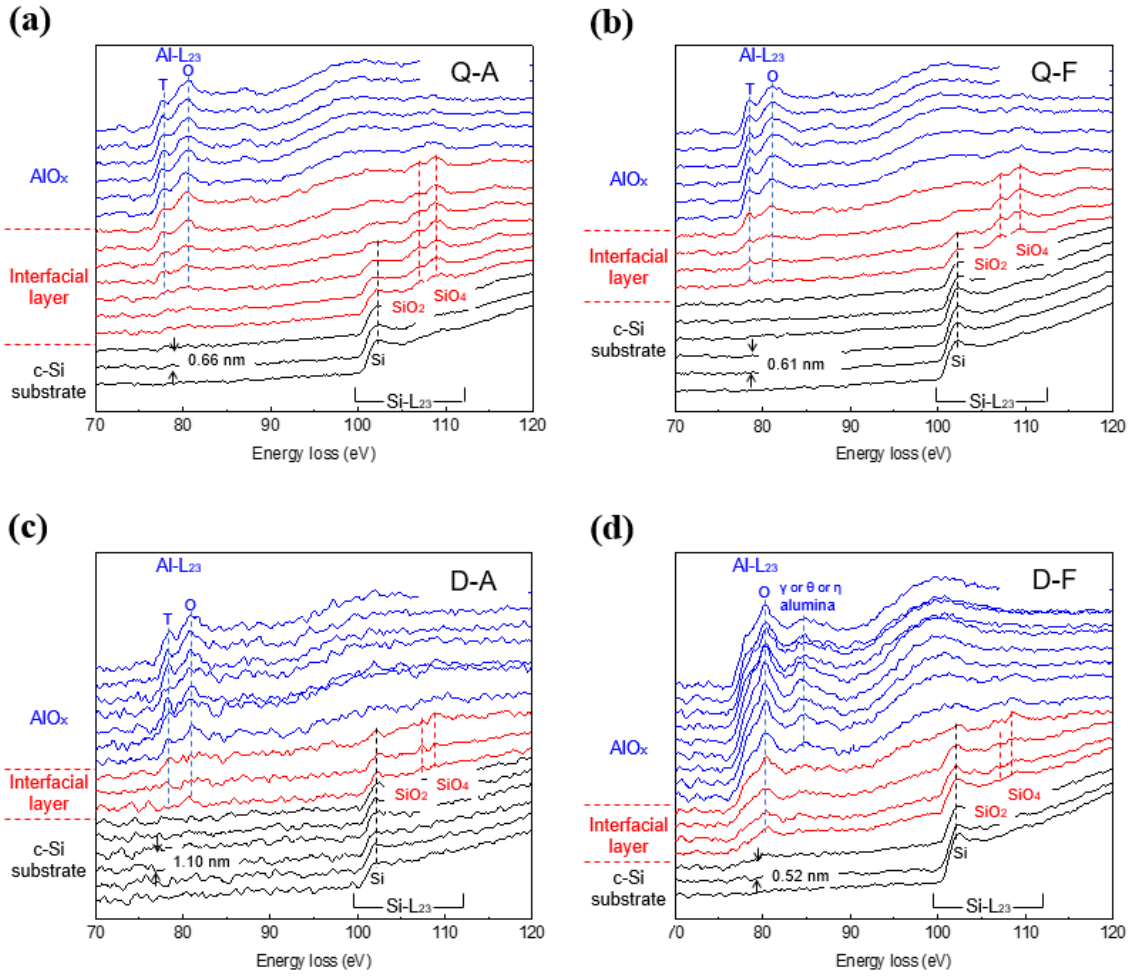


Fig. 5-4. EELS spectra of the Al-L_{2,3} and Si-L_{2,3} edges for the samples that show the largest increase in negative fixed charge for the (a) as-deposited sample, (b) fired sample and the largest increase in D_{it} for the (c) as-deposited sample and (d) fired sample.

For the specimens that show the biggest increase in Q_{tot} through firing [Q-A and Q-F], it is observed that the T-Al peak intensity is stronger (higher T/O ratio) for the fired specimen than the as-deposited specimen, particularly towards the interfacial layer. The formation of T-Al is often attributed to the effusion of oxygen from the AlO_x layer through firing which leads to rearrangement of atoms and bonds in the interfacial layer and within the AlO_x layer [17], [98], [106], [203], [215]. During the thermal process (firing in this study), both migration of cations (Al in this case) and the effusion of oxygen occur, resulting in aluminium vacancies (V_{Al}) and oxygen interstitials (O_i), respectively [199]. A correlation between the T-Al to O-Al ratio (T/O ratio) and Q_{tot} was suggested by previous studies [76], [208], where a higher ratio indicates larger Q_{tot} . A decrease of the interfacial layer thickness can be observed after firing (from about 4 nm to 2-3 nm) as shown as red spectra in Fig. 5-4 (a) and (b). However, it seems that the

chemical composition of the interfacial layer has not been changed. I will discuss this point as part of the discussion regarding Fig. 5-8.

Fig. 5-4 (c) and (d) show the spectra of the samples that demonstrate a significant increase in D_{it} after firing. Comparing the measurements before and after firing leads to five main observations:

- (1) The interfacial layer thickness decreases from 3-4 nm to 2 nm after firing.
- (2) The silicate peak (SiO_2 at ~ 107 eV) almost disappears after firing.
- (3) The T-Al peak intensity is significantly reduced.
- (4) The peak position of both T-Al and O-Al shifts towards higher and lower energies, respectively.
- (5) An additional peak can be identified at about 84.5 eV which could be either γ -, θ - or η -alumina [216].

Observations (1) and (2) are closely related to the increase of D_{it} according to previous studies [76], [208] due to lack of SiO_2 passivation effect. Especially Observation (1) is in good agreement with the study which showed that about 2.7 nm is a threshold thickness for higher τ_{eff} (for samples passivated by SiO_2) [217]. Observations (3)–(5) indicate modification of the chemical configuration of the alumina to different reported types of alumina transitions [216], [218]–[221]. It was reported that the transition type depends on the initial chemical composition of the amorphous alumina, as well as the subsequent thermal process [216], [218]–[221]. The critical impact of the GFRR between N_2O and TMA on both the electrical and chemical properties of the resulting AlO_x layer has been previously identified in *Chapter 4*. The different alumina transitions between Q-A and Q-F and between D-A and D-F are therefore due to the diverse chemical composition of the as-deposited layers originating from the variation of GFRR [218]. This explains why the D-A and D-F show significantly lower T/O ratio at the c-Si/ AlO_x interface (will be discussed in Fig. 5-6), compared to that of Q-A and Q-F. Further discussion regarding Q_{tot} and D_{it} of D-A and D-F will follow in the next sections.

I now analyse the ratio of the T-Al to O-Al peak intensity as a function of depth based on the method shown in Fig. 5-5. I calculate the area of each peak to evaluate the peak intensity. In general, the analysis of peak area after deconvolution is more accurate [222]. However, it was found that integration over the peak width of 1.2 eV (± 0.6 eV)

did not coincide with any shoulder of neighbouring peaks. Therefore, the analysis was considered sufficiently accurate without using deconvolution. Hoex *et al.* [77], [208] did the integration of the peaks using a fixed width of 2.0 eV (± 1.0 eV). In the latter case—in which only one process condition was considered for Al_2O_3 samples—integration with that width seems to present no issue. However, in my case, there are six different properties of AlO_x with different chemical configurations. I noticed that integrating across 2.0 eV could include the shoulder of the neighboring peak for some samples, as shown in Fig. 5-5 (a). It is more obvious for the sample D-F which shows that the T-Al and O-Al peaks shift towards each other. I confirm that the integration of the peak across 1.2 eV does not include any overlap of the neighboring peak [Fig. 5-5 (b)] and it is also close to the full width at half maximum (FWHM) of the two peaks.

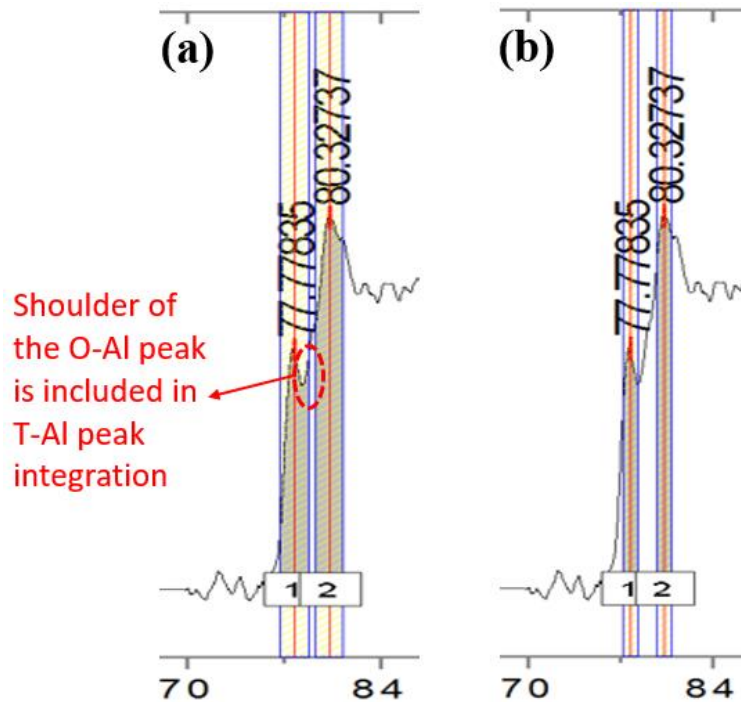


Fig. 5-5. Integration method comparison with different fixed widths: (a) width of 2.0 eV and (b) width of 1.2 eV. The dotted circle in (a) highlights the interference of the shoulder of the O-Al peak on the T-Al peak.

The ratio of T-Al to O-Al peak intensity as a function of depth is shown in Fig. 5-6. For the Q-A and Q-F specimens [Fig. 5-6 (a)], it is interesting to note that the T/O ratio is almost constant throughout the AlO_x layer (average from 5 nm to 20 nm is 0.59 and 0.60 for Q-A and Q-F, respectively). The difference between the samples is only observed near the interface (within about 2 nm from the interface). At the interface, the

T/O ratio for Q-F (fired) is about 0.82, whereas the ratio for Q-A (as-deposited) is only about 0.57 [highlighted as filled circles in Fig. 5-6 (a)]. This observation (higher T/O ratio corresponds to higher Q_{tot}) is in good agreement with previous studies on both ALD Al_2O_3 [77] and APCVD AlO_x [76]. The low T/O ratio at the interface for both the D-A specimen (0.34) and D-F specimen (0.45) may be due to the impact of the deposition parameters on the chemical bonding of the as-deposited layer and the resulting transition of alumina [216], [218]–[221]. It is also interesting to note that across most of the six PECVD AlO_x layers the T/O ratio stays within a range between 0.58 and 0.60, whilst the ratio for plasma-assisted ALD (PA-ALD) layers is about 0.45 and 0.50 for as-deposited and annealed, respectively [77]. The difference between the PECVD and ALD film is probably a result of the different surface growth mechanisms which gives rise to a difference in stoichiometry [17]. For PECVD AlO_x , it seems that the near-interface T/O ratio is a clearer indicator for the resulting Q_{tot} than the T/O ratio across the layer.

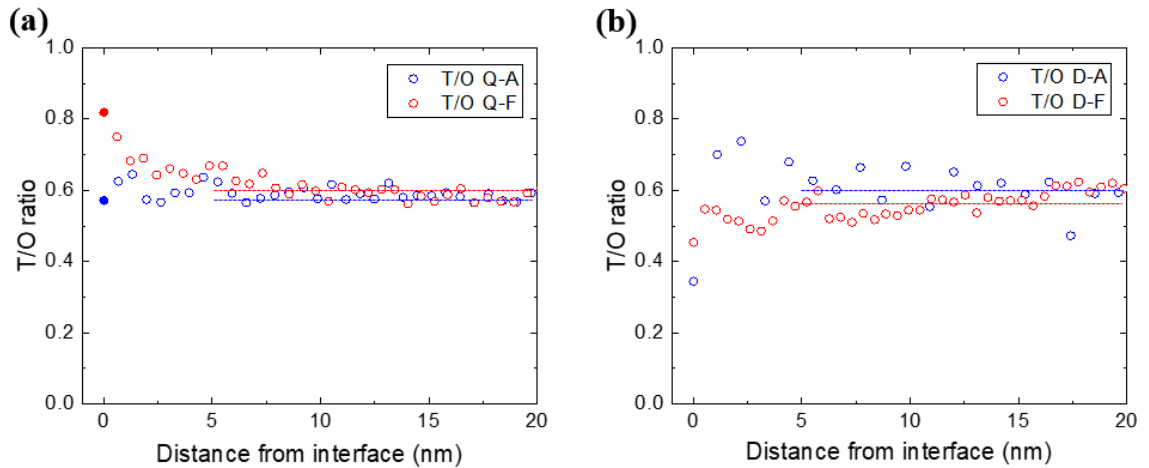


Fig. 5-6. Ratio of T-Al to O-Al peak area for the samples that show (a) the largest increase of Q_{tot} and (b) the largest increase of D_{it} through firing.

The correlation between Q_{tot} and the T/O ratio at the interface for all the six studied specimens is shown in Fig. 5-7; it includes the two additional specimens (J-A and J-F in Table 5-1). It is interesting to note that a linear relationship between Q_{tot} and the T/O ratio is found. Although previous studies [76], [208] identify higher Q_{tot} is correlated to higher T/O ratio between two samples (before/after annealing), the linear relation amongst six different properties of samples is firstly observed in this thesis. It seems that this correlation can be applied regardless of the deposition conditions and, hence, regardless of the chemical properties of the layer. This indicates that T-Al is the key

chemical coordination of aluminium, having the strongest impact on the negative fixed charge in the layer.

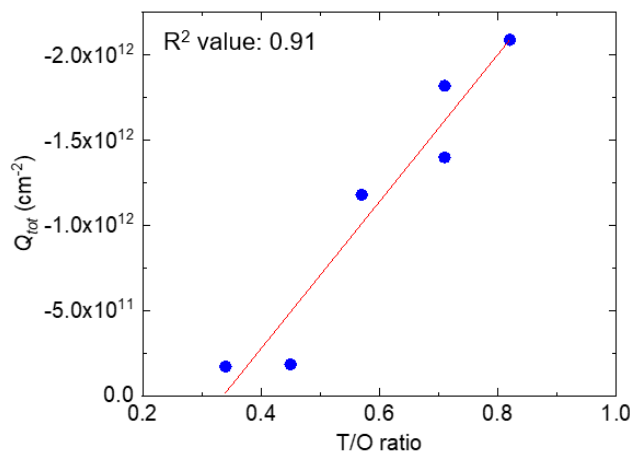


Fig. 5-7. Q_{tot} as a function of the T-Al to O-Al ratio at the interface.

With regard to D_{it} , previous studies have highlighted the critical impact of the presence of an interfacial SiO_2 layer (at the c-Si/ AlO_x interface) and its thickness on the obtained D_{it} [76], [193], [223]. Thicker SiO_2 at the c-Si/ AlO_x interface is typically correlated with lower D_{it} . The presence of SiO_2 at the interfacial layer—although T-Al exists simultaneously—is a sign of a decrease in D_{it} [76], [208]. Based on these findings, I investigate the ratio of SiO_2 to T-Al peak intensity as a function of the distance from the interface as presented in Fig. 5-8. The SiO_2 /T-Al ratio may be a useful parameter to study the interfacial layer since T-Al, Si and SiO_2 are present at the same time (often called aluminosilicate glass) [76]. It seems that for all the samples the ratio is quite constant for distances greater than 5 nm (2.47 and 2.41 for the Q-A and Q-F samples and 2.54 and 2.22 for the D-A and D-F samples, respectively). Instead, a distinct change in the ratio occurs in the interfacial layer (less than 5 nm from the c-Si/ AlO_x interface) where differences between the samples can be clearly observed.

As mentioned above, the material containing aluminium oxide and silicon oxide is often called aluminium silicate. It is observed especially when some of the Si^{4+} ions in silicates are replaced by Al^{3+} ions and for each Si^{4+} ion replaced by an Al^{3+} , the charge must be balanced by having other positive ions [224]. The change of chemical configuration in the samples may be caused by this mechanism: The Al^{3+} ions seem to replace Si^{4+} ions in the chains of corner shared tetrahedra of SiO_4 groups. Therefore, the bonding between Al and Si can be restructured. For example, in the case that the majority

is Si and not the SiO₂ of the interfacial layer, Al³⁺ has a greater chance of bonding oxygen; this results in a higher concentration of octahedrally-coordinated Al. On the other hand when SiO₂ is the majority, the tetrahedrally-coordinated Al is more likely to be observed than octahedrally-coordinated Al [224].

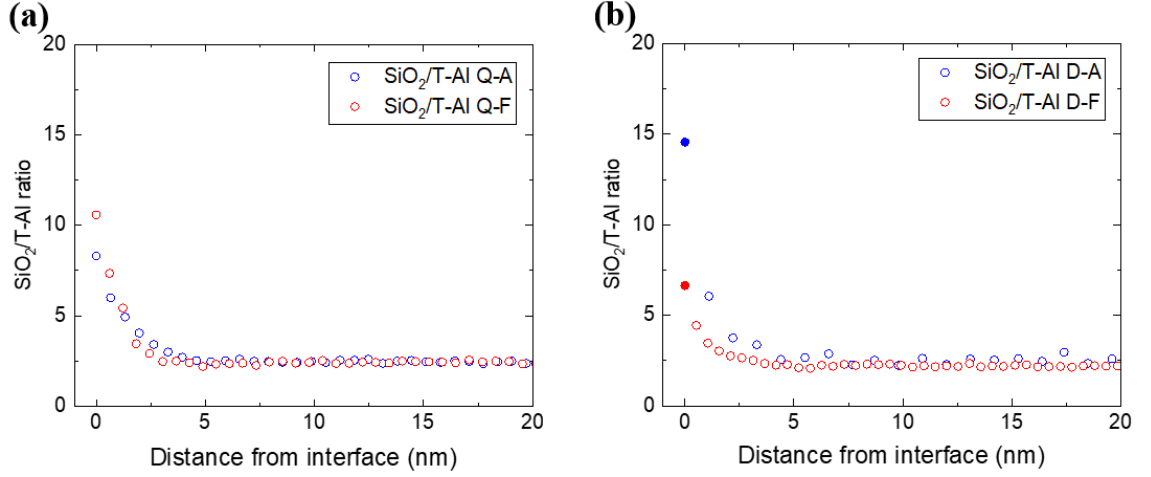


Fig. 5-8. Ratio of SiO₂ to tetrahedral-Al peak area for the samples which show (a) the largest increase of Q_{tot} and (b) the largest increase of D_{it} through firing.

Interestingly, the firing process significantly decreases the SiO₂/T-Al ratio (from 14.6 to 6.7) for the specimens that show a substantial increase in D_{it} [D-A and D-F; Fig. 5-8 (b)], whereas no notable difference is observed in Q-A and Q-F [Fig. 5-8 (a)]. The decrease of the ratio indicates a lower percentage of SiO₂ in the interfacial layer. In addition, a reduction of the interfacial layer thickness is also observed (from 3-4 nm to 2 nm), which also explains the increase of D_{it} [76], [208], [217], [225]. The relationship between the interfacial layer thickness and D_{it} can be explained by study done by Naumann *et al.* [182]. It is reported that a thicker interfacial layer is formed by the OH group which is served as a source of excessive oxygen. An increase in the Si-O coordination is assigned to the oxidation of Si when H is released during a thermal process (firing process in this case) [182]. Therefore, the more release of H can be eventually related to the increase Si-O coordination and also the decrease of D_{it} by chemical passivation.

Regarding the increase of D_{it} after firing Saint-Cast *et al.* [98] and Kühnhold *et al.* [106] also observed such behaviour after a firing process although it is not a general phenomenon. It was suggested that loss of both oxygen and hydrogen through the effusion that occurs during the thermal process is the reason for this change [98], [106]. The disappearance of T-Al near the interface in conjunction with the increase of O-Al in D-F means more oxygen becomes bonded to aluminium after firing. This may indicate

a lesser chance of oxygen forming the silicate, which explains the decrease of the interfacial layer thickness and the $\text{SiO}_2/\text{T-Al}$ ratio at the interface. Therefore, these results may suggest that the $\text{SiO}_2/\text{T-Al}$ ratio has an impact on D_{it} , although the change of D_{it} might also be partially attributed to dehydrogenation. For samples Q-A and Q-F, the $\text{SiO}_2/\text{T-Al}$ ratio at the interface slightly increases after firing. However, the interfacial layer thickness decreases through the firing process from about 5 nm to 2-3 nm. In this case, it seems that the impact of the decrease in thickness (< 2 nm) dominates the change in D_{it} , rather than the $\text{SiO}_2/\text{T-Al}$ ratio, since the impact of dehydrogenation on the D_{it} for the samples (higher GFRR) is negligible based the result of Section 4.3.4.

The correlation between D_{it} and the $\text{SiO}_2/\text{T-Al}$ ratio for all the studied specimens is investigated in Fig. 5-9. Although the correlation is not as strong as the one between Q_{tot} and the T/O ratio, it seems that there is an inverse relationship between D_{it} and the $\text{SiO}_2/\text{T-Al}$ ratio. It also seems that there is an impact of the layer thickness on the obtained correlation as mentioned above. The two samples (Q-F and D-F) with the very thin interfacial layer (< 2 nm) seem to have a shifted trend as compared to the other four samples with interfacial layer > 2 nm. Nevertheless, it seems that the $\text{SiO}_2/\text{T-Al}$ ratio at the interface can be used as an indicator of D_{it} when the interfacial layer thickness is comparable.

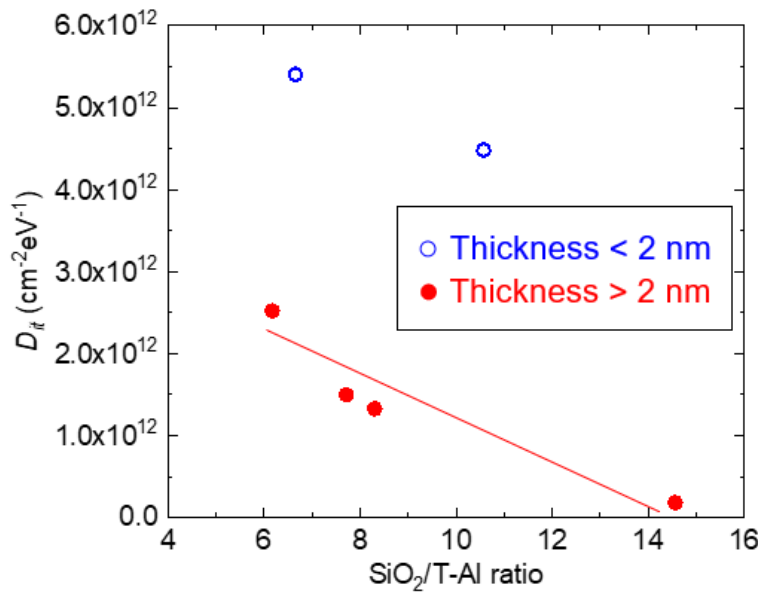


Fig. 5-9. Correlation between D_{it} and the $\text{SiO}_2/\text{T-Al}$ ratio at the interface for the studied samples.

The EELS spectra of samples J-A and J-F are also presented in Fig. 5-10. The changes in Q_{tot} and D_{it} of these samples are not outstanding. However, as shown in Table 5-1, these samples show both increase in Q_{tot} and reduction in D_{it} through firing. These are one of the few samples (samples with GFRR of 10) which show reduction in D_{it} through firing as mentioned in Section 4.3.2. It was discussed that the unwanted D_{it} increase is loss of [O-H] bonds in Section 4.3.2. Therefore, not only the T-Al/O-Al ratio but more importantly the SiO₂/T-Al ratio are investigated for these samples. Both the T-Al/O-Al ratio and the SiO₂/T-Al ratio are presented in Fig. 5-11. As expected from the small change in Q_{tot} in Table 5-1, the T-Al/O-Al ratio of these samples (0.71) does not show difference through firing. However, the SiO₂/T-Al ratio increases from 6.17 to 7.71. The increase of the SiO₂/T-Al ratio indicates more oxygen-involvement to form the interfacial layer. This may also generate a source of [O-H] bonds which in turn behave as hydrogen passivation at the c-Si/AlO_x interface. The increased involvement of oxygen is explained by higher GFRR, which originated from more N₂O.

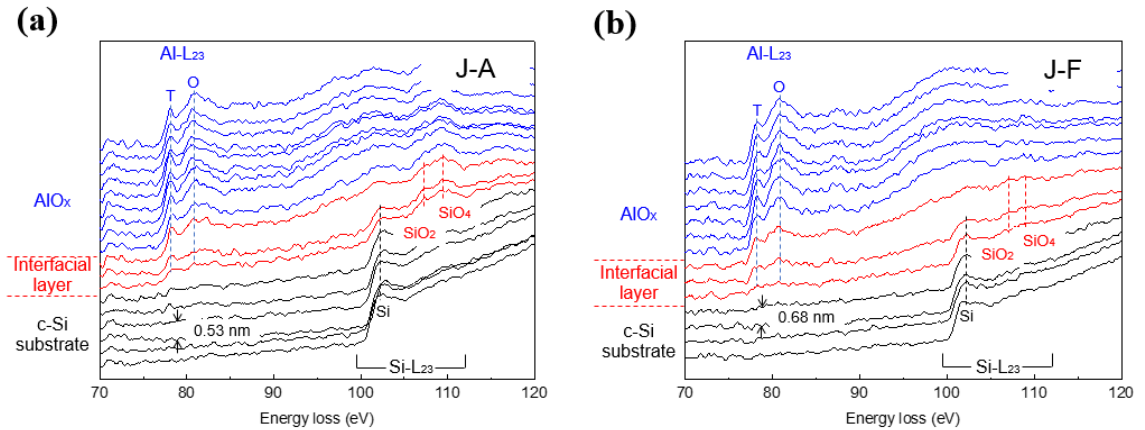


Fig. 5-10. EELS spectra of the Al-L_{2,3} and Si-L_{2,3} edges for the PECVD AlO_x samples that show the lowest J_{0s} after firing for (a) as-deposited sample, (b) fired sample.

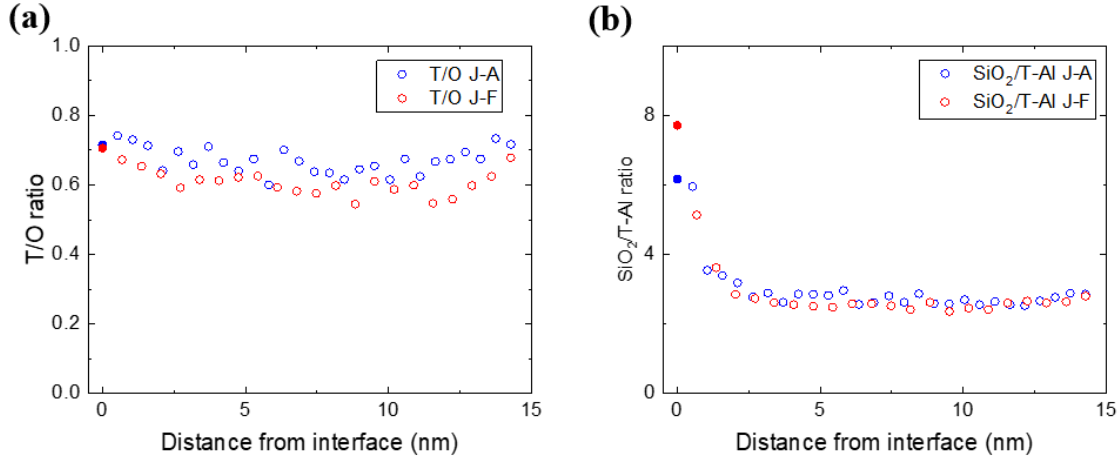


Fig. 5-11. Ratio of T-Al to O-Al peak area (a) and ratio of SiO₂ to tetrahedral-Al peak area (b) for the samples for both as-deposited and fired samples that show the lowest J_{0s} after firing.

5.4 Chapter summary

The origin of the change in the negative Q_{tot} in the AlO_x layer and the D_{it} at the c-Si/AlO_x interface is studied by STEM/EELS. It is observed that the increase of T-Al configuration leads to increase of negative Q_{tot} . It is because that higher T/O ratio indicates more aluminium vacancies and oxygen interstitials which cause PECVD AlO_x layers to be negatively charged by the effusion of oxygen. This can be identified by the increased proportion of tetrahedrally-coordinated aluminium as observed by EELS measurements. Moreover, it was found that the ratio of T-Al/O-Al at the c-Si/AlO_x interface plays a more dominant role than that within the AlO_x layer. In addition, it is found that the T-Al/O-Al ratio has a linear correlation to the amount of negative Q_{tot} in the PECVD AlO_x layer. This linear trend is confirmed by six different AlO_x layer regardless of AlO_x properties.

The condition for lower D_{it} at the c-Si/AlO_x interface is also studied. The lower D_{it} is achieved by thicker (> 2 nm) interfacial layer or by higher SiO₂/T-Al ratio or even both of the two at the c-Si/AlO_x interface. The SiO₂/T-Al ratio is suggested to be an indicator of D_{it} at the interface for comparable thickness of the interfacial layer.

It is also found that the SiO₂/T-Al ratio of the interfacial layer shows an inversely linear relationship to D_{it} ; this is much clearer for thicker interfacial layers (> 2 nm). On the other hand, a change in the interfacial layer thickness can significantly influence D_{it} for example, in the case of an interfacial layer < 2 nm thick.

6 Degradation of surface passivation and bulk in *p*-type c-Si wafers at elevated temperature⁴

6.1 Motivation: Degradation in silicon solar cells

In *Chapter 4* the electrical and chemical properties of PECVD AlO_x as a surface passivation layer were studied. In *Chapter 5*, a nano-scale investigation revealed structural features and chemical configurations of the c-Si/AlO_x interface. These studies were done for both as-deposited and fired samples. It was shown that the firing process improves the surface passivation quality, demonstrating the stability of the PECVD AlO_x layer under the high temperature firing process.

Recently, the degradation of AlO_x surface passivation under illumination and at elevated temperatures has been reported [20], [21]. At this stage the mechanism and root cause have not been identified. With the PERC structure gaining significant attention and market share within the PV industry [11]–[13], there is increasing interest in understanding the degradation of the c-Si/AlO_x/SiN_x structure [116], [119], [226]. Moreover, a recent report by the US Department of Energy indicates that reducing the degradation of PV systems is a very promising method of lowering the cost of PV energy [18], especially considering that increasing the efficiency is becoming more difficult as the fundamental limit is approached. Therefore, improving the reliability of PV systems is a key requirement for making PV energy cheaper.

In the past decades, a number of studies have been done to identify and investigate various degradation mechanisms in Si solar cells [227]–[241]. One example is the formation of metastable boron-oxygen (BO) related defects in boron-doped *p*-type Cz wafers after exposure to light [227], [228], [231], [232]. Recently, a similar degradation behaviour was identified in multicrystalline silicon (mc-Si) wafers [233]–[235], [241]. This degradation, which is known as either light and elevated temperature-induced degradation (LeTID; [229], [230], [236], [238]) or carrier-induced degradation (CID; [233], [239], [242]), is found to significantly decrease the efficiency of PERC cells fabricated using mc-Si wafers [241]. More recently, it has been reported that LeTID also

⁴ This chapter is summarised and *published* in *IEEE Journal of Photovoltaics* (DOI: [10.1109/JPHOTOV.2018.2878791](https://doi.org/10.1109/JPHOTOV.2018.2878791)).

occurs in Cz wafers [73], [243]. It has been demonstrated that the same defect can be formed by purely *thermal* process in both Cz and mc-Si wafers; hence, light is not required for LeTID [243]. A few studies have suggested involvement of hydrogen in the degradation and regeneration processes [118], [229], [243]–[249]. However, it seems that more work needs to be done in order to fully understand the role of hydrogen in LeTID.

In order to differentiate the impact of the LeTID on the surface passivation and the bulk quality, Sperber *et al.* [116], [119], [226] investigated the stability of the surface passivation under light and elevated temperature. They use the slope-based method [58] with improved parameterisation to extract J_{0s} from the injection-dependent τ_{eff} measurements [250]. Degradation of the surface passivation (with various dielectrics) has been observed in FZ, Cz and mc-Si wafers [119].

In this chapter, I aim to assess the impact of hydrogen on both the τ_{SRH} and the J_{0s} . Both hydrogen-rich dielectrics and dielectrics that are believed to be hydrogen-free are used for this assessment. Both as-deposited and fired wafers are investigated. Unlike the work of Sperber *et al.* [116], [119], [226], purely thermal-based degradation and regeneration processes are investigated by monitoring samples during dark annealing (DA) at wafer temperatures of 175 ± 2 °C.

6.2 Experiments

Commercially-available (156-mm \times 156-mm) boron-doped *p*-type Cz wafers, with resistivity of 1.7 ± 0.2 Ω cm (bulk doping concentration of $8.5 \pm 1.2 \times 10^{15}$ cm⁻³) and final thickness of 190 ± 10 μ m are used in this chapter. Four different lifetime test structures were fabricated, as shown in Fig. 6-1. Note that the reliability of initial surface passivation quality was better with n^+ layer for the SiO₂ than without it. Therefore, the n^+ layer was applied for the structure in Fig. 6-1 (d).

All the wafers were processed together until the surface passivation stage. They were textured (random upright pyramid) and RCA cleaned [156] before a POCl₃ diffusion to form an electron collector layer (commonly called the diffused layer [251]) with a sheet resistivity of 100 Ω/\square on both sides (process temperatures between 795 °C and 885 °C [252]). Then, the phosphosilicate glass (PSG) was removed before thermal oxidation at 930 °C for 15 min to grow a 50-nm-thick SiO₂ layer [253]. The final sheet resistivity after the oxidation process is 110 Ω/\square . For Structures A, B and C [Fig. 6-1 (a)-(c)], the oxide was removed using an HF solution. A sodium hydroxide solution (mass fraction

30%) was then used to etch the diffused layer ($\sim 1 \mu\text{m}$) from both sides of Structures A and B at temperature of 85°C .

An industrial in-line PECVD system (MAiA, Meyer Burger) was used for the deposition of both SiN_x and AlO_x at 400°C . A standard SiN_x anti-reflection coating (75 nm thick with a refractive index of 2.08 at 633 nm) was used for Structures A and C [125], while a 16 – 17 nm-thick AlO_x layer with a refractive index of 1.59 was used for Structure B (the recipe ID 15 in the Table 4-2 in *Section 4.2.1*). The AlO_x was then capped with SiN_x deposited at 350°C to minimise possible modification of both the bulk and the existing AlO_x as mentioned in *Section 3.2.1*.

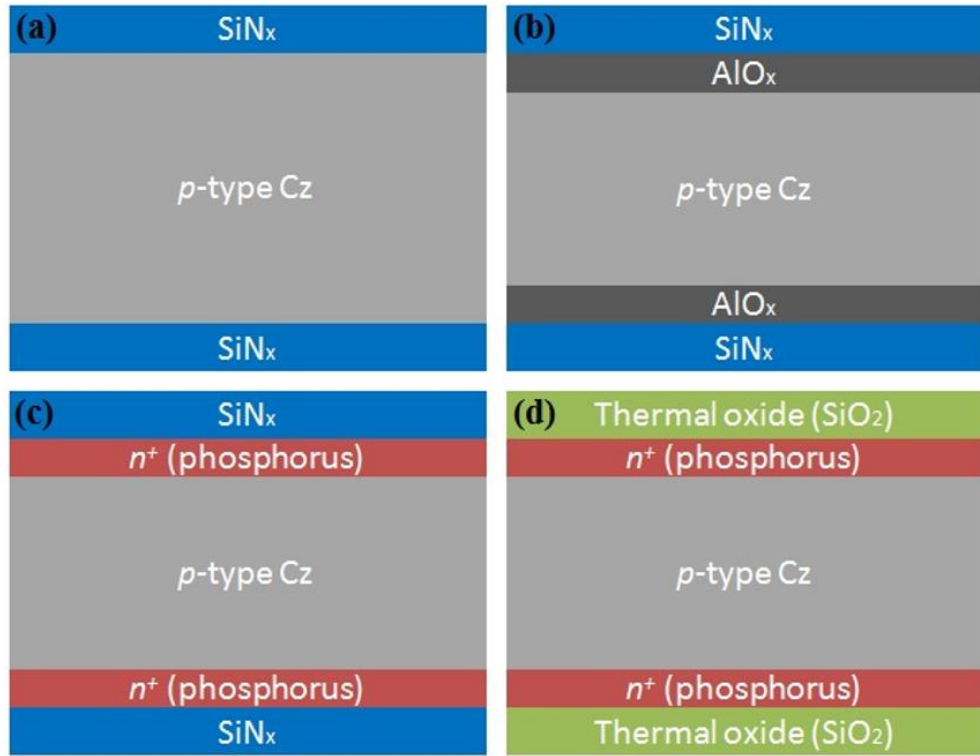


Fig. 6-1. Four different lifetime test structures (a) SiN_x , (b) $\text{AlO}_x/\text{SiN}_x$, (c) n^+/SiN_x , (d) n^+/SiO_2 .

Each wafer was then laser cleaved into 16 tokens ($39 \text{ mm} \times 39 \text{ mm}$). After cleaving, half of the tokens remained as-deposited (hereafter non-fired), while the other half underwent a fast firing process in an industrial metallisation furnace (7K9-70C69-5LIR, Schmid) within a clean dry air (CDA) ambient. The *set* firing temperature was adjusted to maintain a fixed *wafer* temperature of $740 \pm 5^\circ\text{C}$ for duration of about 0.5 seconds for all the wafers.

Samples were dark annealed at $175 \pm 2^\circ\text{C}$. *In-situ* PC lifetime measurements were made using a lifetime tester (WCT-120TS from Sinton Instruments). The samples were kept in the dark for the entire time (during measurements and between measurements). It can

therefore be assumed that there is no external influence of BO defects on the obtained results, especially considering the DA temperature [228].

To determine τ_{eff} at elevated temperature, the Dorkel-Leturcq mobility model [254] is used. The surface passivation quality is assessed by extraction of J_{0s} from the Auger-corrected τ_{eff} measurements using the Kane-Swanson method [58] and the intrinsic carrier concentration model that is implemented in the system [255]. Since the Auger lifetime remains almost constant from room temperature up to 200 °C [256] and following Sinton Instruments' recommendation [257], the Auger model of Richter *et al.* is used in this study [258]. The value of J_{0s} is extracted at an excess minority carrier concentration (Δn) of 10^{16} cm^{-3} using a linear fit in the range between $7 \times 10^{15} \text{ cm}^{-3}$ and $1.3 \times 10^{16} \text{ cm}^{-3}$. The intercept of the linear fit with the y-axis provides an estimation of τ_{SRH} at high injection.

To validate the extracted J_{0s} and τ_{SRH} , Quokka 2 [63] is also used to fit representative τ_{eff} measurements (at the end of each stage) as discussed in *Section 4.1.4*. From the highly accurate Quokka-based fits ($R^2 > 0.99$), J_{0s} and τ_{SRH} are extracted without any assumption regarding the uniformity of the Δn profile [164] and the injection dependence of τ_{SRH} . Despite the expected slight differences in the absolute values (due to the limitations of the slope-based methods [259]), the two methods are in good agreement regarding the trend of the values, which is the key information for this study. More information regarding the Quokka models is provided in *Section 6.3.5*.

While recombination at the edges can influence lifetime measurements of small samples [260], [261], Chan *et al.* confirm that the edge recombination does not have an impact on lifetime measurements at high injection ($\Delta n > 10^{15} \text{ cm}^{-3}$) [262]. It also shows both non-diffused and diffused samples and concluded that the edge does not impact the measurement at $\Delta n > 10^{13} \text{ cm}^{-3}$. Since the analysis in this study is carried out at $\Delta n > 7 \times 10^{15} \text{ cm}^{-3}$, it can be assumed that the measurements are unaffected by edge recombination. This was also supported by PL images at various intensities, which indicate that the edge-impacted regions extend less than 1 mm from the edges. The PL images also confirm that all samples used are free from scratches that could otherwise impact measurements. Additionally, the sensed area in the WCT-120TS is smaller than the sensed area of the standard WCT-120, which ensures even smaller impact of the edges. Note that in the following sections τ_{eff} and τ_{SRH} at 175 °C are presented; the values at this temperature are, of course, different from those at room temperature.

6.3 Different effects of various surface passivation layers

6.3.1 c-Si/SiN_x structure

Fig. 6-2 presents τ_{eff} [(a) and (d); at $\Delta n = 10^{15} \text{ cm}^{-3}$ and $\Delta n = 10^{16} \text{ cm}^{-3}$], the extracted J_{0s} [(b) and (e); at $\Delta n = 10^{16} \text{ cm}^{-3}$] and τ_{SRH} [(c) and (f); at $\Delta n = 10^{16} \text{ cm}^{-3}$] as a function of DA duration. Results for both non-fired and fired SiN_x samples are presented. For the non-fired case [(a)-(c)], there is very little change in the parameters (J_{0s} is degraded by about 5%, τ_{SRH} by about 8%, and τ_{eff} by about 7%) during the entire 110 hours of measurement.

The behaviour of the fired sample [Fig. 6-2 (d)-(f)], however, is very different. Firstly, as expected, the firing process improves both the surface passivation quality (J_{0s} decreases from 63 fA/cm² to 22 fA/cm²) and the bulk (τ_{SRH} increases from 280 μ s to 770 μ s). This improvement can be attributed to hydrogen release from the SiN_x layer [200] which passivates both dangling bonds at the surface [23], [201] and bulk defects [72], [122]. Interestingly, τ_{SRH} starts to degrade after 0.3 hours of the DA process. At this stage (Stage I in Fig. 6-2), no change in J_{0s} is observed. The decrease in τ_{eff} (at $\Delta n = 10^{15} \text{ cm}^{-3}$) can be therefore correlated solely with the degradation of the bulk quality. Stage I lasts for five hours. After five hours (Stage II), τ_{SRH} plateaus, while the surface passivation starts to degrade (J_{0s} increases).

In Stage III (between 20 and 110 hours), both the surface and the bulk degrade, again resulting in a degradation of τ_{eff} . Note that during Stages I and III, changes in τ_{eff} cannot be used to attribute the degradation to the bulk or the surface alone. At the most degraded state (after 110 hours of DA), the surface quality is lower than the level of the non-fired sample, whereas the bulk quality is about the same. As discussed below, this may be due to the different impact of hydrogen on the surface and the bulk.

Interestingly, significant improvement of both J_{0s} and τ_{SRH} is observed after 110 hours (Stage IV). The improvement (or regeneration) is much slower than the degradation and τ_{eff} does not fully recover to its initial value, even after 500 hours. It is also interesting that, although the degradation of the surface and the bulk start at different times, their recovery seems to start at the same time. Despite the higher temperature in this study (175 °C in the dark) and the lack of illumination, these observations are similar to the results reported by Sperber *et al.* (150 °C at about 1-sun illumination) [119]. The main difference is that here a plateau in τ_{eff} during Stage II was observed instead of an increase.

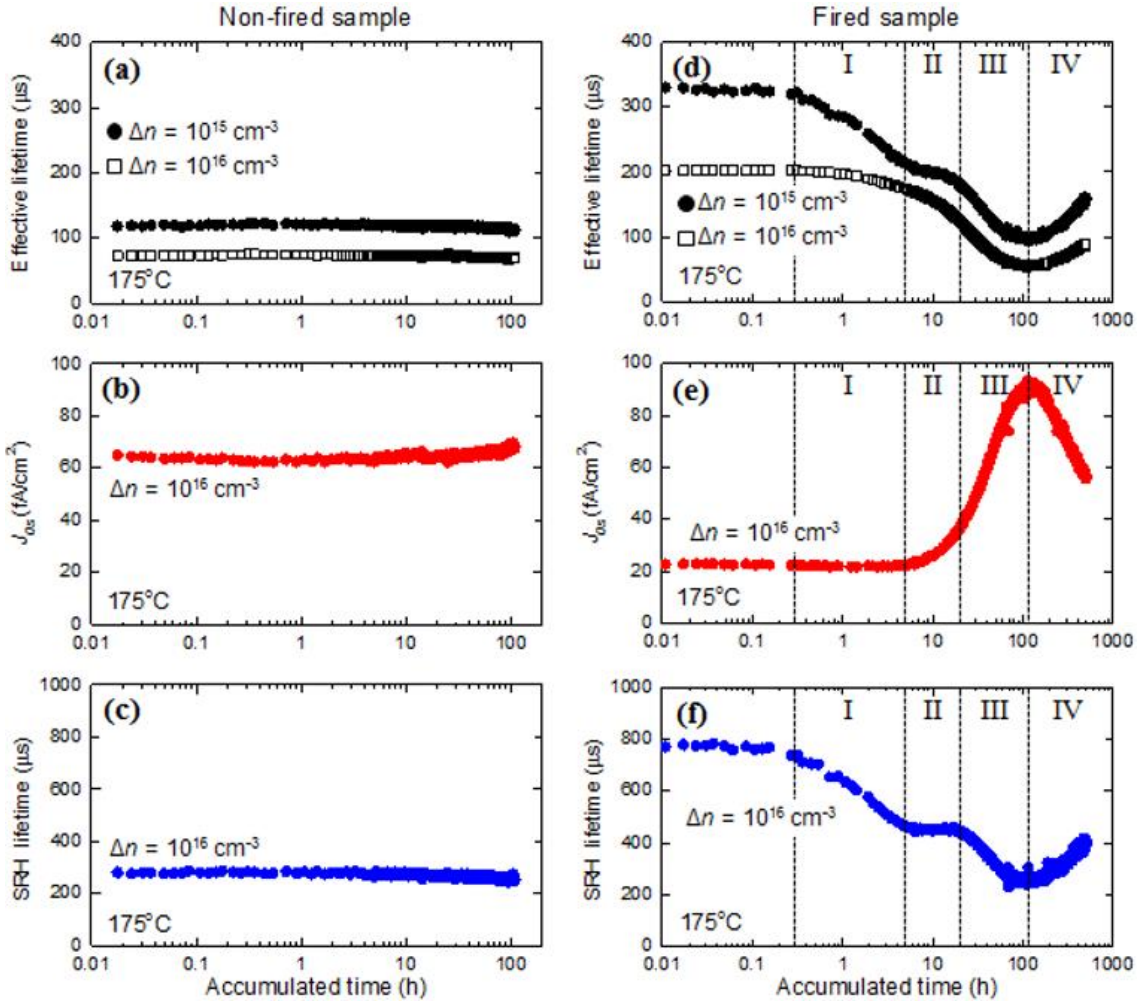


Fig. 6-2. Evolution of (a) τ_{eff} , (b) J_{0s} , (c) τ_{SRH} for non-fired SiN_x sample and (d) τ_{eff} , (e) J_{0s} , (f) τ_{SRH} for fired SiN_x sample during DA.

Fig. 6-3 depicts the injection-dependent lifetime of the fired SiN_x wafers. The presented measurements were chosen from the end of each stage. Because it is preferable to extract J_{0s} at high injection [263], measurements were done using high intensity illumination. Hence, the low-injection region of τ_{eff} was not collected. This limits the ability to fit the curves in order to extract the defect parameters, particularly for the bulk. It does appear, however, that the τ_{eff} of the degraded sample has only weak injection dependence.

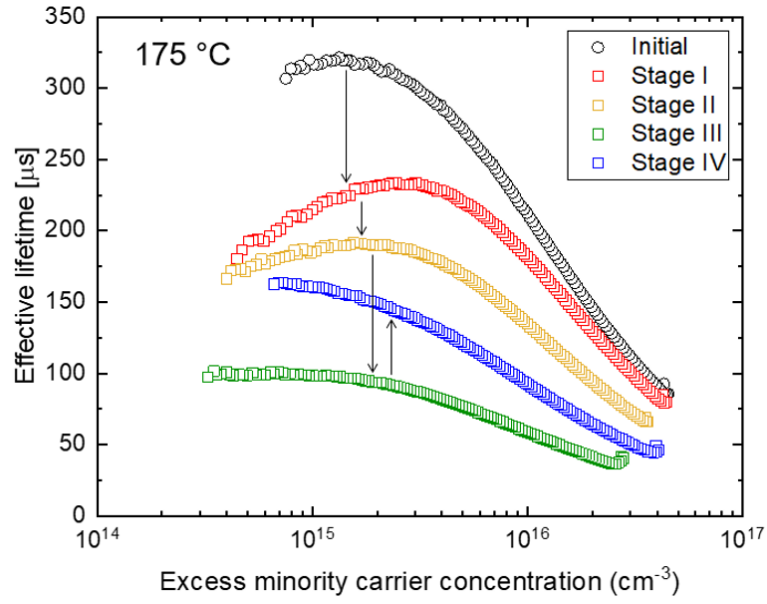


Fig. 6-3. Injection-dependent effective lifetime curves of a fired SiN_x sample at the end of each stage.

6.3.2 c-Si/AlO_x/SiN_x structure

In this section, the stability of samples with an AlO_x/SiN_x stack passivation layer is studied. Fig. 6-4 presents the evolution of τ_{eff} [(a) and (d); at $\Delta n = 10^{15} \text{ cm}^{-3}$ and $\Delta n = 10^{16} \text{ cm}^{-3}$], the extracted J_{0s} [(b) and (e); at $\Delta n = 10^{16} \text{ cm}^{-3}$] and τ_{SRH} [(c) and (f); at $\Delta n = 10^{16} \text{ cm}^{-3}$] as a function of DA duration annealing before and after firing.

I first examine the behaviour of the non-fired sample. All the parameters are constant during the first five hours of DA. After this time, both the surface and the bulk start to degrade at a relatively slow rate. No recovery of these parameters is observed during the 320 hours of measurement. A possible reason for the different behaviour of this structure, when compared to the non-fired SiN_x sample, could be the release of hydrogen from the AlO_x during the deposition of the SiN_x capping layer. It is possible that some hydrogen may have been released into the bulk during deposition, even without a deliberate firing process. The significantly higher initial τ_{SRH} of the non-fired AlO_x/SiN_x sample compared to the non-fired SiN_x sample (580 μs versus 280 μs) supports this explanation. To confirm the improvement of τ_{SRH} , the non-fired AlO_x/SiN_x layer was etched from one of the wafers. The wafer was then cleaned and re-passivated with SiN_x (identical to the one used in *Section 6.3.1*). The obtained τ_{eff} was found to be higher than that of the wafers directly passivated with the same SiN_x.

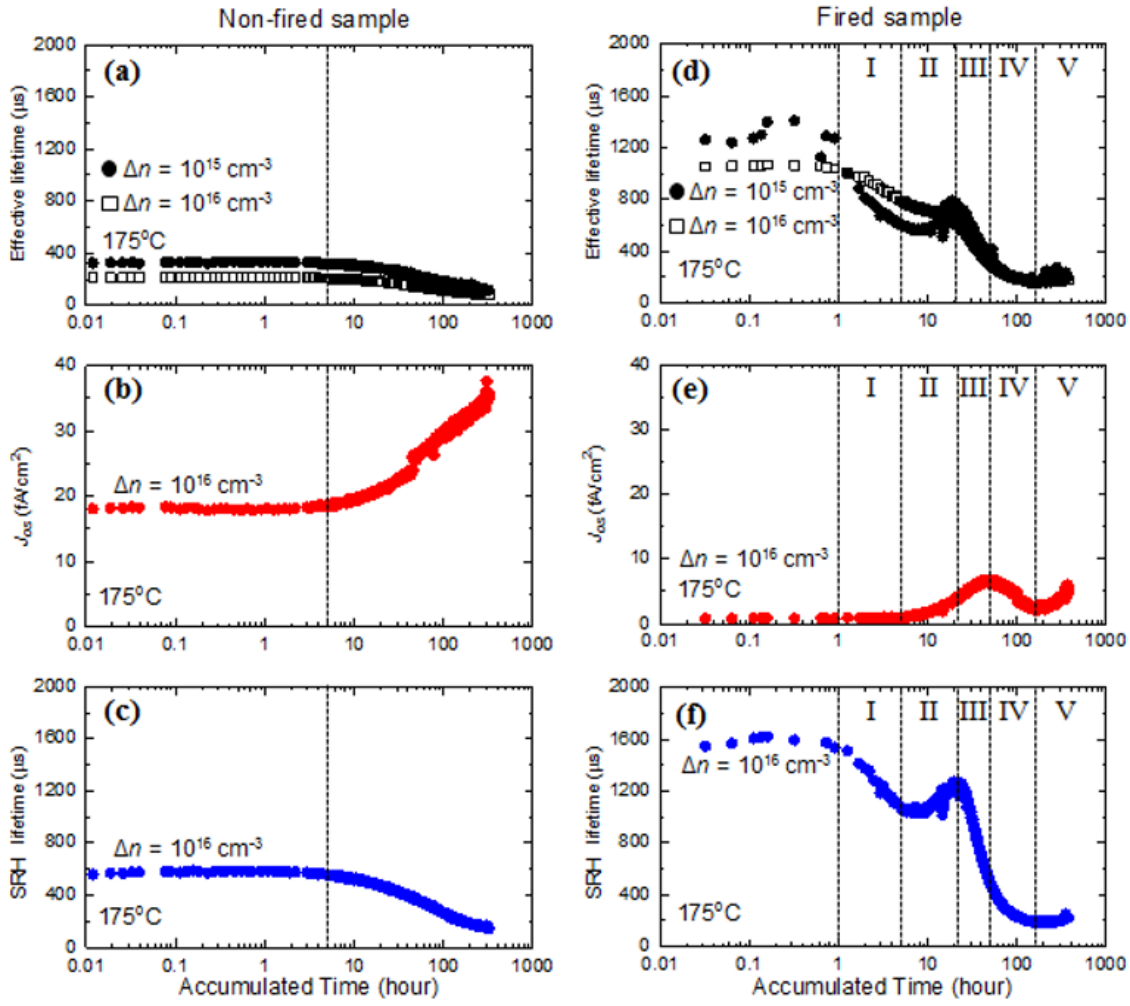


Fig. 6-4. Evolution of (a) τ_{eff} , (b) J_{0s} , (c) τ_{SRH} for non-fired AlO_x/SiN_x sample and (d) τ_{eff} , (e) J_{0s} , (f) τ_{SRH} for fired AlO_x/SiN_x sample during DA.

To test whether this assumed release of hydrogen during the capping process has any impact on subsequent degradation, I investigated the thermal impact of the SiN_x capping process on a SiN_x sample. A non-fired SiN_x sample was used to mimic the SiN_x capping layer deposition by passing the sample through the PECVD system but without precursor gases or activation of plasma. Fig. 6-5 presents the evolution of τ_{eff} , J_{0s} and τ_{SRH} of the untreated and the thermally treated SiN_x wafers during DA. The τ_{SRH} of the untreated sample degraded by about 8% whereas the treated sample degraded by about 12% and a second thermal treatment (not shown) enhanced the degradation even further. With regards to J_{0s} , the untreated sample degraded by about 5% while the treated sample degraded by about 14%. Hence, it seems that the thermal treatment enhances the degradation of both J_{0s} and τ_{SRH} (and as result, of τ_{eff}). It may indicate that hydrogen is released during the thermal treatment. This increased degradation following the thermal treatment can explain the different degradation between the non-fired SiN_x and

$\text{AlO}_x/\text{SiN}_x$ samples, although the significance of the degradation is much stronger in the case of $\text{AlO}_x/\text{SiN}_x$. It is believed that AlO_x releases more hydrogen at lower temperature ($< 500\text{ }^\circ\text{C}$) than SiN_x which requires a higher temperature ($> 600\text{ }^\circ\text{C}$) to release a significant amount of hydrogen [136], [143], [180], [264].

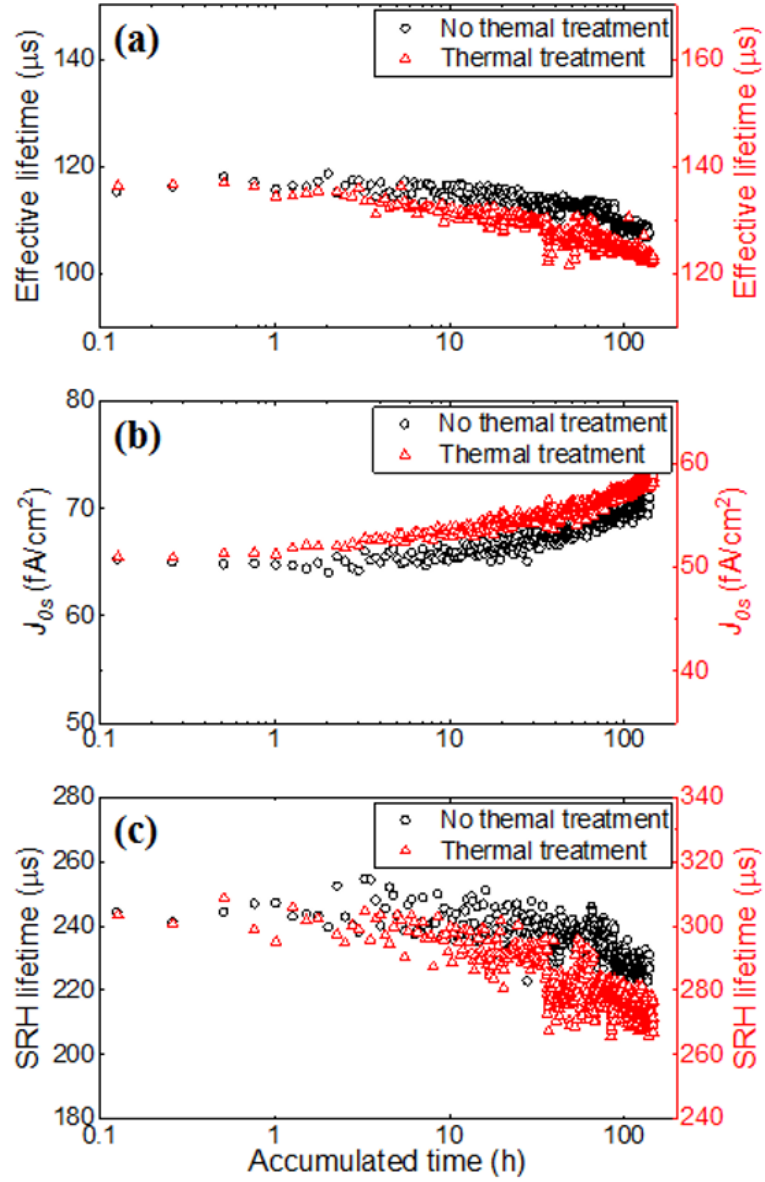


Fig. 6-5. (a) τ_{eff} , (b) J_{0s} , (c) τ_{SRH} of non-thermally treated and thermally-treated SiN_x samples during DA.

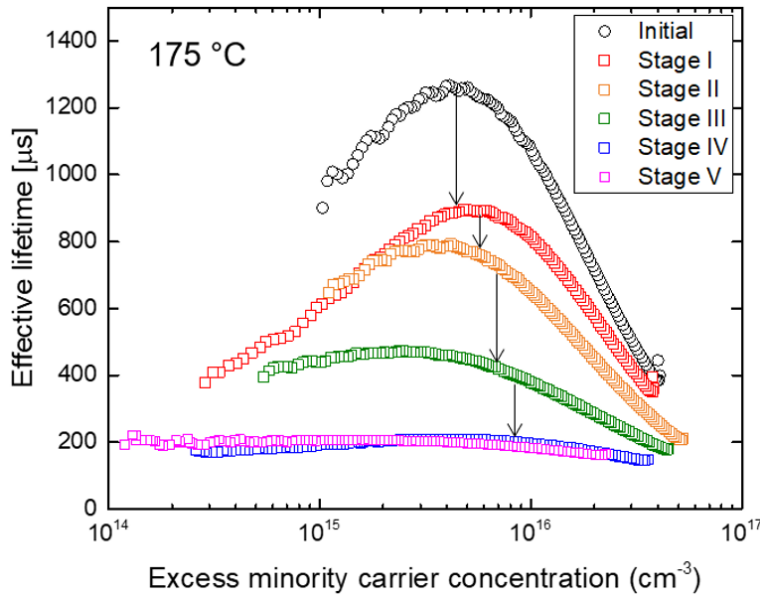


Fig. 6-6. Injection-dependent effective lifetime curves of a fired $\text{AlO}_x/\text{SiN}_x$ sample at the end of each stage.

Now I examine the fired $\text{AlO}_x/\text{SiN}_x$ sample [Fig. 6-4 (d)-(f)]. Significant improvement is observed both in the surface passivation quality (J_{0s} is reduced) and the bulk (τ_{SRH} of 1,500 μs). Due to the very low J_{0s} , τ_{eff} is primarily impacted by τ_{SRH} .

In general, the response of this wafer to the DA is comparable to that of the fired SiN_x sample, however, with a few differences. In Stage I (1-5 hours), only the bulk degrades, while J_{0s} seems to be fixed. Note that this stage starts later than for the SiN_x case. The surface passivation starts to degrade in Stage II (5-20 hours); interestingly in this case a bulk improvement is observed (compared to a constant τ_{SRH} in the SiN_x case). However, τ_{SRH} starts to degrade again with continued degradation of the surface in Stage III (20-50 hours). After 50 hours (Stage IV), J_{0s} starts to decrease (earlier than in the SiN_x case) and recovers almost to its initial value. In contrast with the SiN_x case, no recovery of the bulk is observed during this stage; τ_{SRH} continues to degrade for the rest of the measurement (until 150 hours). Stage V is an additional stage which has not been observed for the SiN_x sample. In this stage the surface passivation degrades again, while τ_{SRH} maintains almost a constant value. These results are similar to those reported for FZ wafers passivated with $\text{AlO}_x/\text{SiN}_x$ [119]. However, in my study, it seems that the processes are faster. This may indicate a strong impact of the temperature (175 °C here, compared to 80 °C in [119]) on the process and a difference between light (about 1-sun) and temperature. It may also indicate a greater hydrogen concentration in the samples of this study.

Injection-dependent lifetime curves for the fired $\text{AlO}_x/\text{SiN}_x$ sample at the end of each stage are shown in Fig. 6-6. It is observed that the injection level dependence varies for the different stages. It appears that the degraded τ_{eff} has only weak injection dependence, similar to what is observed for the fired SiN_x sample.

6.3.3 n^+/SiN_x structure

To investigate the impact of DA on the front side of a typical solar cell, the n^+/SiN_x structure [see Fig. 6-1 (c)] is now studied. With regards to the non-fired diffused sample [Fig. 6-7 (a)-(c)], the behaviour is very similar to the non-diffused sample [Fig. 6-2 (a)-(c)], where no significant change is observed in any of the parameters.

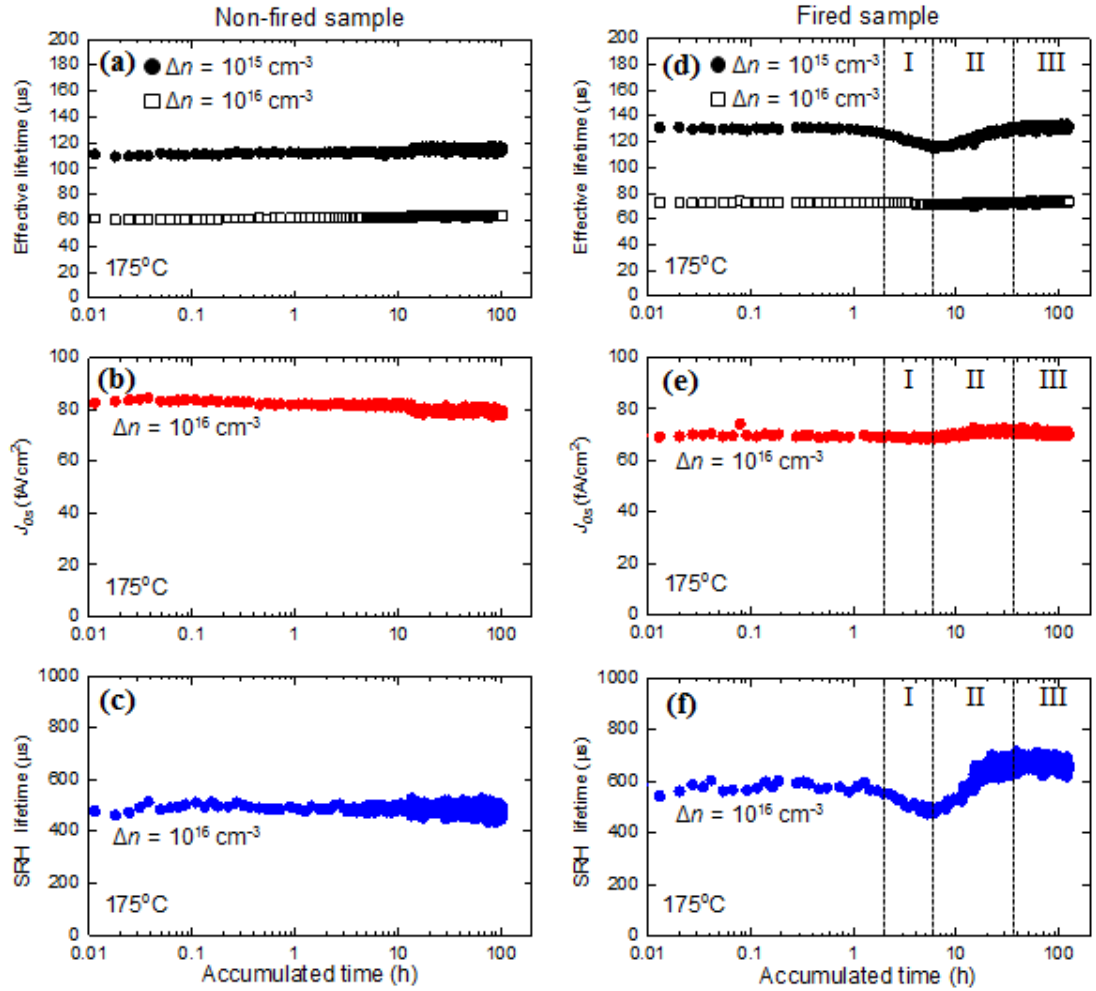


Fig. 6-7. Evolution of (a) τ_{eff} , (b) J_{0s} , (c) τ_{SRH} for non-fired n^+/SiN_x sample and (d) τ_{eff} , (e) J_{0s} , (f) τ_{SRH} for fired n^+/SiN_x sample during DA.

No significant improvement was observed in J_{0s} and τ_{SRH} due to firing. Although τ_{eff} is quite low, possible causes such as B-O defects are not activated under this dark annealing. The response to DA is quite different to that observed for the SiN_x wafer

without the diffused layer [Fig. 6-2 (d)-(f)]. During Stage I (2-6 hours) τ_{SRH} starts to degrade after two hours of DA and reaches a minimum after six hours, whereas J_{0s} remains almost constant during this period.

In comparison to the SiN_x sample (Section 6.3.1), the degradation starts later and the maximum degradation is much less in this case. Between 6 and 36 hours (Stage II), τ_{SRH} shows recovery. It is notable that the recovery of τ_{SRH} slightly exceeds its initial value by about 12% on average during Stage III (from 36 hours to 124 hours). However, this is not reflected in τ_{eff} as it is dominated by the surface. Note that the behaviour of τ_{eff} at 10^{15} cm^{-3} is very similar to that reported for CID of mc-Si [265], however, on a different time scale. This suggests that the degradation and recovery shown here using Cz may have the same root cause as that reported by Chen *et al.* [243].

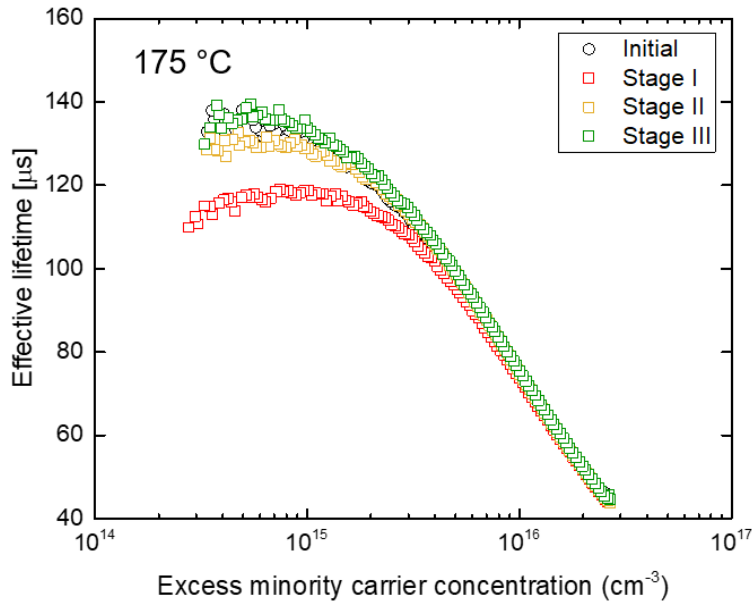


Fig. 6-8. Injection-dependent effective lifetime curves of a fired n^+/SiN_x sample at the end of each stage.

Injection-dependent lifetime curves of the fired n^+/SiN_x sample at the end of each stage are presented in Fig. 6-8. Substantial variation is seen in low to medium injection, but there is nearly no change at high injection. The lifetime curve at the end of Stage III is almost identical to the initial value.

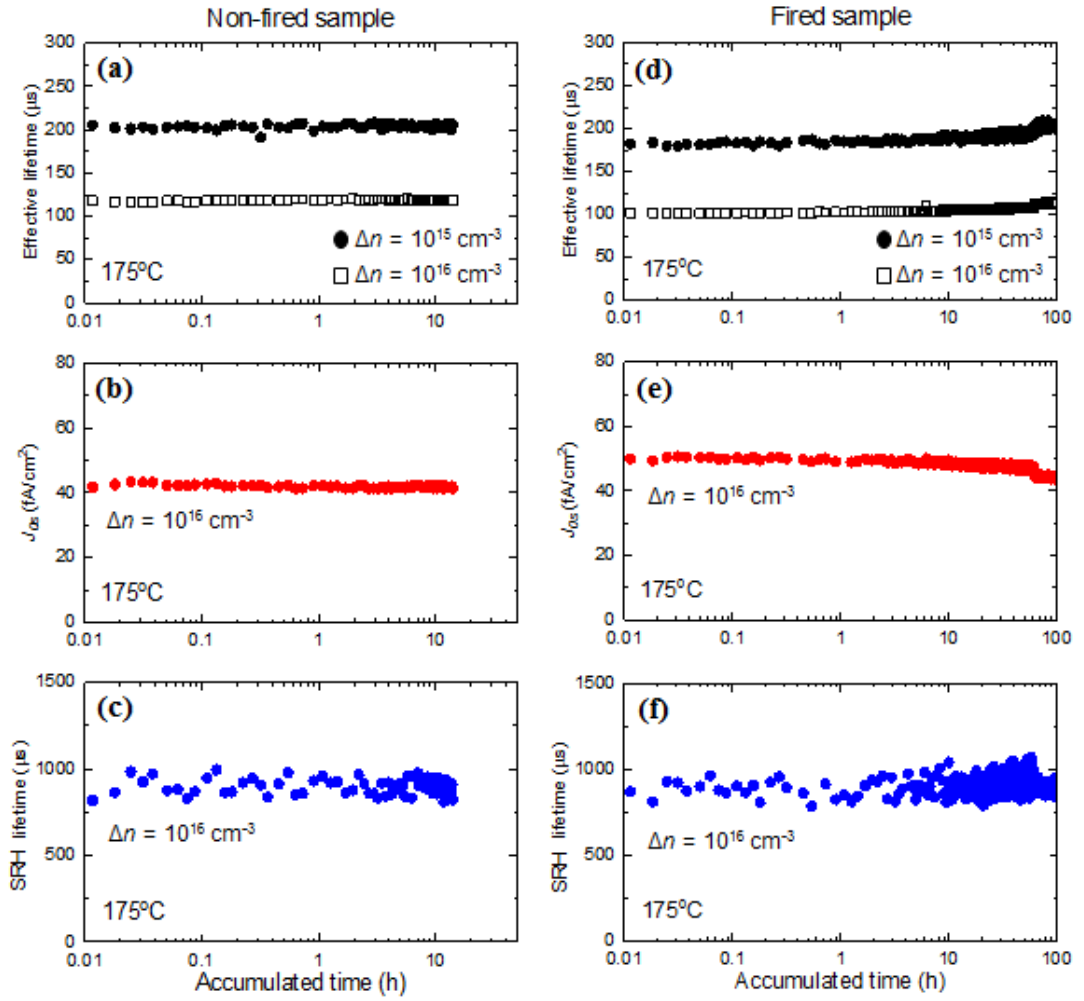


Fig. 6-9. Evolution of (a) τ_{eff} , (b) J_{0s} , (c) τ_{SRH} for non-fired n^+ /SiO₂ sample and (d) τ_{eff} , (e) J_{0s} , (f) τ_{SRH} for fired n^+ /SiO₂ sample during DA.

6.3.4 n^+ /SiO₂ structure

Fig. 6-9 presents the results for the thermally grown SiO₂ sample (Structure D in Fig. 6-1). No significant changes are noted in any of the parameters during the DA process for both fired and non-fired wafers (less than 6%). This is very different from all the other layers studied in this work. The noticed low τ_{eff} is not due to B-O defects as they are not been activated under this dark annealing. Therefore, a direct comparison can be made between these results and the results presented in the previous section (6.3.3). The wafers were processed together and have the same diffused n^+ layer; the only difference is the surface passivation layer. Therefore the different behaviours of the fired wafers [Fig. 6-7 (d)-(f) and Fig. 6-9 (d)-(f)] may indicate involvement of hydrogen in the degradation and recovery processes. I assume that the hydrogen concentration in the SiO₂ is very low, if not zero. This may also support numerous studies [118], [243], [247]–[249] that suggested hydrogen involvement in CID. In a recent study, we

observed a correlation between released hydrogen fraction and the degradation extent in mc-Si wafers [233].

6.3.5 Lifetime fitting using Quokka 2

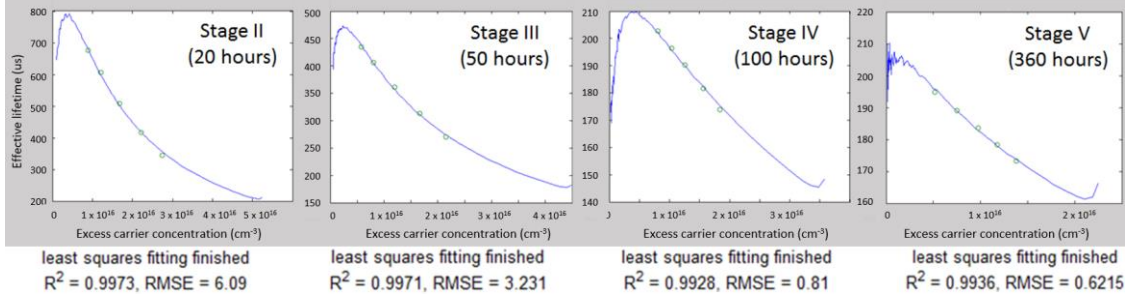


Fig. 6-10. Quokka 2 modelling results for each stage of the fired $\text{AlO}_x/\text{SiN}_x$ sample.

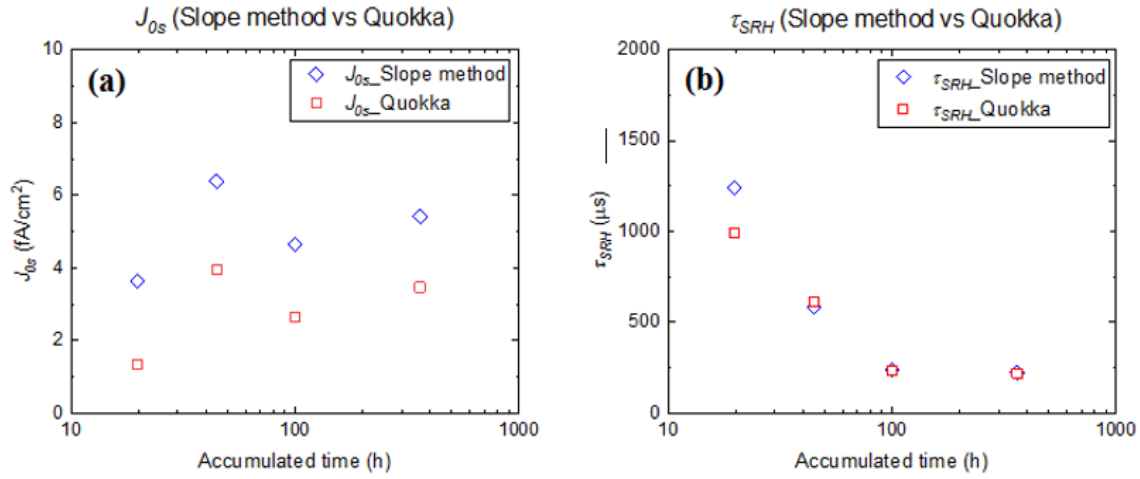


Fig. 6-11. Comparison between the values extracted by the slope method and Quokka fitting for (a) J_{0s} and (b) τ_{SRH} .

As discussed in *Section 4.1.4*, the advanced physical models in Quokka 2 [63] were used to fit the lifetime measurements. Two approaches were tested: (1) fitting using an injection-dependent τ_{SRH} and a constant J_{0s} , and (2) fitting using a constant τ_{SRH} (at high injection) and a constant J_{0s} . Since the measurements were performed at high injection, I have not observed any advantage of using injection-dependent τ_{SRH} . The fit quality and the extracted values were similar to the second approach. Therefore, constant τ_{SRH} (at high injection) and a constant J_{0s} are used for the fit. To investigate the uniqueness of the fit and the associated uncertainty, J_{0s} was fixed at 10% and 20% lower and higher values than the optimum value and τ_{SRH} was re-fitted. I have noticed that a 10% variation in J_{0s} is sufficient to reduce the quality of the fit, indicating that the extracted values form unique parameter pairs. J_{0s} and τ_{SRH} were extracted from the excellent fits ($R^2 > 0.99$) at the end of each stage for all the cases. I have also noted that at $\Delta n = 10^{16}$

cm^{-3} , J_{0s} is sensitive to the injection level and 10 % difference is sufficient to assess the fit. Fig. 6-10 presents representative Quokka-based fits, while Fig. 6-11 shows a comparison between values obtained by the two methods. Although the slope-based method results in higher J_{0s} values, the trends obtained by the two methods agree very well, which is the key information of this study. Similar results are obtained for τ_{SRH} .

6.4 Proposed hydrogen-based models

In this section, possible root causes of degradation/regeneration and how they may be explained with regard to the behaviour of hydrogen in the samples are discussed. Main observations are:

- (a) There is a significant difference between fired and non-fired samples [Fig. 6-2, Fig. 6-4 and Fig. 6-7].
- (b) The bulk degrades earlier than the surface for the fired samples [Fig. 6-2 (d)-(f) and Fig. 6-4 (d)-(f)].
- (c) The starting point for surface degradation appears to be very close to the point at which the initial bulk degradation reaches saturation [Fig. 6-2 (d)-(f)] and starts to “regenerate” [Fig. 6-4 (d)-(f)].
- (d) None of the observations above [(a)-(c)] occur in the sample passivated with SiO_2 which is believed not to contain hydrogen.

Observations (a) and (d) can be explained by assuming that the bulk defects formed in Stage I are related to the hydrogen concentration in the Si bulk. This is supported by a range of studies in the literature [230], [233], [265]. Therefore, the initial decay of the bulk lifetime [Observation (b)] can be explained as the formation of hydrogen-related bulk defects. According to Voronkov *et al.*, the timescale of the degradation is determined by the release rate of hydrogen from recombination *inactive* states (so called hydrogen dimers or similar [266]) throughout the bulk. In the case of non-fired SiN_x , much less hydrogen is released from the dielectric layer, and hence this initial bulk degradation is not observed.

It may still be asked what the cause of the subsequent “regeneration” is and whether it can be related to an increase in surface recombination [Observation (c)]. There are at least three plausible hydrogen-related explanations according to Hamer *et al.* [264]:

- a) Firstly, when additional hydrogen becomes available, it passivates the hydrogen-related defects and reduces their recombination activity. Studies

investigating the interaction of hydrogen with several interstitial metals can support this [267]–[272].

- b) Secondly, hydrogen de-bonds from the hydrogen-related defect over time and forms more stable, recombination-inactive forms.
- c) Thirdly, in a special case of the second explanation, hydrogen de-bonds from the defects and migrates from the Si bulk towards the surface. This has been simulated at elevated temperatures in the presence of an emitter [264]; however, the results of Bredemeier *et al.* [273] support the view that it is also possible where no emitter is present.

Among the three explanations only the third one can be linked to recombination at the surface based on the results discussed in this chapter. In order to account for the results presented in this study, the migration of hydrogen to the surface must have different effects for different passivation layers and doping profiles.

In the case of non-fired SiN_x, the surface degradation is significantly less; again, much less hydrogen is released from the dielectric layer in that case. In the case of a SiN_x-passivated *p*-type Si surface, it is expected that an inversion layer is present at the surface because SiN_x is positively charged [201], [274], [275]. Examining the changes in Fig. 6-2 (e) and (f) during Stages III and IV indicates that the changes in J_{0s} and τ_{SRH} are almost exactly correlated. This could be a result of the formation and subsequent dissolution of hydrogen-related defects within the inversion layer, as previously observed and modelled by Steingrube *et al.* [276]. The hydrogen that forms these defects comes from the Si bulk rather than the surface and can explain why the surface degradation continues until the bulk degrades completely (Stages II and III).

In contrast, the surface of a *p*-type wafer passivated by a fired AlO_x/SiN_x stack is expected to be in accumulation [17], [89]. Not only is the formation of hydrogen-related defects likely to be different under these conditions, but the effect of these defects (if present) on the total effective lifetime will be reduced. This is in reasonable agreement with the modest changes in J_{0s} observed in Fig. 6-4 (e). It should also be noted that the electric field in the accumulation condition due to negative fixed charge in the AlO_x layer will drive H⁺—the dominant form of interstitial hydrogen in *p*-type Si [277], [278]—further towards the surface and may result in more significant effusion of hydrogen from the Si surface. More H⁺ effusion towards surface in accumulation condition means that there is less degradation of chemical passivation. This means that

loss of negative fixed charge is more dominant factor which contribute surface degradation, which is a good agreement with the observation reported by the Sperber *et al.* [279].

In the case where the surface is heavily doped [Fig. 6-7 (d)-(f)], migrating hydrogen is likely to be trapped in the heavily phosphorus-doped region as modelled by Hamer *et al.* [264]. Given the high availability of ionised dopant ions that act as effective traps for hydrogen [280], the formation of hydrogen-related defects is likely suppressed; hence, no significant change in J_{0s} is observed.

Although this model [264] explains most of the results, it still leaves two observations unexplained. The first is the two-stage degradation in bulk lifetime observed in fired samples passivated with $\text{AlO}_x/\text{SiN}_x$ [Fig. 6-4 (f)]. The second is the correlated increase in surface and bulk degradation observed in unfired samples passivated with $\text{AlO}_x/\text{SiN}_x$ [Fig. 6-4 (b) and (c)].

At this stage, my best explanation for the second degradation in bulk lifetime is a dissociation of hydrogen from previously passivated bulk defects. If effusion of hydrogen from the *p*-type bulk is indeed enhanced by the presence of an accumulation region, as compared to an inversion region, it is possible that the bulk of the wafer becomes so denuded that previously passivated defects cannot be re-passivated once hydrogen has dissociated from them. While this explanation requires much more rigorous investigation, it can be supported by the observation that the lifetime decays to a similar level as a non-fired SiN_x sample that is presumed to contain minimal hydrogen. It is also possible that a second source of hydrogen with a different activation energy for slower release exists in the bulk that causes the second degradation, as reported in previous studies [117], [281].

The behaviour of the non-fired $\text{AlO}_x/\text{SiN}_x$ sample, which contains hydrogen released from the AlO_x layer during the SiN_x deposition, is also difficult to explain. Since the hydrogen diffuses into the bulk at temperatures of about 350 °C (which is about the same as the wafer's temperature during the SiN_x deposition process), there is likely to be a significant concentration gradient from the surface to the bulk. With subsequent annealing at 175 °C this hydrogen may diffuse further into the sample forming recombination-active defects as seen in other samples.

6.5 Chapter summary

Stability of surface passivation and Si bulk passivation at elevated temperature in the dark was studied. It was confirmed that different surface passivation layers demonstrate different behaviours in terms of the surface passivation and the Si bulk quality. By investigating the separated components of the surface and the bulk, it was possible to identify that their degradations have different kinetics and severity. For the same surface passivation layer, it is the firing process that activates the degradation. It was also found that even the deposition temperature can activate the degradation.

Changes in J_{0s} and τ_{SRH} were detected only in cases where hydrogen is assumed to be released into the wafer from the dielectric ($\text{AlO}_x/\text{SiN}_x$ stack and fired SiN_x layer). No degradation has been observed in wafers passivated by thermally grown SiO_2 , which is assumed to contain no hydrogen. It was also shown that the presence of a heavily doped n^+ region has significant impact on the modulation of both surface and bulk passivation.

The results were explained based on possible involvement of hydrogen in both the degradation and the recovery processes. Further investigation is required to enable greater certainty around this explanation and its implications for other types of degradation in crystalline Si solar cells.

7 Conclusions

The first part of this thesis (Chapters 4 and 5) were focused on improving the surface passivation quality of the c-Si surface by AlO_x using an industrial PECVD system. The impact of the deposition parameters on the surface passivation quality was studied in depth. In addition, the electrical and chemical properties of the AlO_x layer were investigated in conjunction with the deposition parameters. The findings can be directly used by PV manufacturers. The second part of the thesis (Chapter 6) studies the degradation mechanism of the c-Si surface and bulk by applying different types of surface passivation layers.

7.1 Main conclusions and original contributions

In **Chapter 4**, both electrical and chemical properties of the AlO_x layer as a surface passivation layer were studied. The investigations were carried out for both non-diffused *p*-type c-Si and non-diffused *n*-type c-Si surfaces to evaluate the surface passivation efficacy. The main conclusions from this chapter are:

Deposition conditions:

- 1) The impact of the five deposition parameters (MWP, TGFR, Temperature, Pressure, $\text{N}_2\text{O}/\text{TMA}$ flow rate ratio) of a widely-used industrial type inline PECVD system on the c-Si surface passivation quality was intensively studied. The MWP-to-TGFR ratio was found to be a critical factor for the thermal stability of the deposited AlO_x layer. The significant of this parameter has not been identified before this research.
- 2) GFRR was found to have the most significant impact on both the electrical and chemical properties of as-deposited and fired layers. The higher GFRR is preferred for fired samples, whereas lower GFRR is ideal for non-fired samples for promising surface passivation. This finding is the same for both *p*-type and *n*-type surfaces.
- 3) The higher GFRR was found to achieve better surface passivation. This finding can reduce production cost by less use of expensive TMA yet without sacrificing the surface passivation quality.

- 4) It was shown that GFRR has a critical impact on the hydrogen depth profile within the AlO_x layer and on the hydrogen release behaviour through the firing process.

Electrical properties:

- 1) The impact of D_{it} and Q_{tot} on the surface passivation is different for as-deposited and fired wafers. For better surface passivation, a reduction of D_{it} is critical for as-deposited samples, whereas both lower D_{it} and higher Q_{tot} play an important role for fired samples. These findings are the same for both p -type and n -type surfaces.
- 2) Similar quality of surface passivation was found for p -type and n -type wafers for both as-deposited and fired wafers. However, the n -type wafers deposited at low temperature (350 °C) did not improve much through firing.

Chemical composition:

- 1) Correlation between the Al to O ratio and Q_{tot} was identified. Slightly more Al and less O than the stoichiometric ratio results in higher Q_{tot} , which reduces J_{0s} to 4 fA/cm².
- 2) The studied PECVD AlO_x layers are almost stoichiometric regardless of the wide range of deposition conditions. However, STEM image of the c-Si/ AlO_x interface reveals a difference in the interfacial layer for different conditions.

In **Chapter 5**, a sub-nanoscale investigation on the c-Si/ AlO_x interface was presented. The open questions issued in Chapter 4 such as the origin of the difference in Q_{tot} and the D_{it} were investigated in this chapter. The main conclusions from this chapter are:

- 1) It is found that different interfacial layer is formed at the c-Si/ AlO_x interface for the samples with different GFRR. This indicates that the different surface passivation quality is originated dominantly from the property of the interface.
- 2) Aluminium vacancies and oxygen interstitials in PECVD AlO_x layers can be negatively charged by the effusion of oxygen.
- 3) The ratio of T-Al/O-Al at the c-Si/ AlO_x interface, and not within the AlO_x layer, has strong correlation with the amount of Q_{tot} in the PECVD AlO_x layer. A linear correlation between Q_{tot} and the T-Al/O-Al was found.

- 4) The $\text{SiO}_2/\text{T-Al}$ ratio of the interfacial layer shows an inversely linear relationship to D_{it} . This is much clearer for thicker interfacial layers (greater than 2 nm thick).

In **Chapter 6**, the stability of surface passivation and bulk passivation was studied. The AlO_x passivation was compared with other dielectric layers such as SiN_x and SiO_x to identify the root cause of the degradation. The main conclusions from this chapter are:

- 1) Different surface passivation layers demonstrate different behaviours in terms of the surface passivation and the Si bulk quality. By investigating the separate components of the surface and the bulk, the degradations that occur in the two different components are found to have different kinetics and severity.
- 2) The firing process activates both the passivation and the degradation. It was also found that even the deposition temperature of the SiN_x can activate the degradation.
- 3) Changes in J_{0s} and τ_{SRH} are detected only in cases where hydrogen is assumed to be released into the wafer from the dielectric ($\text{AlO}_x/\text{SiN}_x$ stack and fired SiN_x layer). No degradation has been observed in wafers passivated by thermally grown SiO_2 , which is assumed to contain no hydrogen. Possible involvement of hydrogen, in both the degradation and the recovery processes, was therefore suggested.

7.2 Future works

During the works for this thesis a number of topics have been identified for the future work:

- 1) Deep-level transient spectroscopy (DLTS) of the c-Si/ AlO_x interface to identify capture cross-section of electrons and holes is required to reveal more detail regarding the interface.
- 2) Combining AlO_x and the capping SiN_x layer as one layer such as aluminium nitride (AlN_x) can create an interesting material, as far as the AlN_x layer can provide a similarly good level of surface passivation to AlO_x . If the AlN_x layer can achieve high RI in the range of 2.00 to 2.10 (at 633 nm wavelength) it can be also applied for diffused boron emitters on the front side for n -type solar cells.

- 3) A residual gas analyser in conjunction with optical emission spectroscopy (OES; see *Appendix 5*) may be able to lead to an optimum process gas usage. This may be useful for PV manufacturers to optimise the AlO_x process while minimising process gas consumption and yet maintaining the surface passivation quality.

Appendix 1: Publications list

Journal papers

1. **K. Kim**, N. Borojevic, S. Winderbaum, Z. Hameiri, “Investigation of industrial PECVD AlO_x films with very low surface recombination,” *Solar Energy.*, vol. 186, pp. 94–105, 2019.
2. **K. Kim**, S. Lim, N. Nandakumar, X. Zheng, Z. Hameiri, “Sub-nanoscale investigation of the interface between c-Si and PECVD AlO_x analyzed by EELS,” **under review** for *ACS Applied Nano Materials*.
3. **K. Kim**, R. Chen, D. Chen, P. Hamer, S. R. Wenham, Z. Hameiri, “Degradation of surface passivation and bulk in monocrystalline silicon wafers at elevated temperature,” *IEEE J. Photovoltaics.*, vol. 9, no. 1, pp. 97–105, 2019.
4. **K. Kim**, S. Winderbaum, and Z. Hameiri, “In-situ diagnostics of PECVD AlO_x deposition by optical emission spectroscopy,” *Surf. Coatings Technol.*, vol. 328, 2017.

Co-authored journal papers

5. P. Jongsung, H. Jialiang, Y. Jaesung, L. Fangyang, O. Zi, S. Heng, Y. Chang, S. Kaiwen, **K. Kim**, S. Jan, C. Shiyu, G. M. A., and H. Xiaojing, “The Role of Hydrogen from ALD- Al_2O_3 in Kesterite $\text{Cu}_2\text{ZnSnS}_4$ Solar Cells: Grain Surface Passivation,” *Adv. Energy Mater.*, vol. 0, no. 0, p. 1701940, 2018
6. C. Y. Lee, S. Deng, T. Zhang, X. Cui, K. T. Khoo, **K. Kim**, and B. Hoex, “Evaluating the Impact of Thermal Annealing on c-Si/ Al_2O_3 Interface: Correlating Electronic Properties to Infrared Absorption,” *Appl. Phys.*, pp. 1–12, 2018.
7. C. Vargas, **K. Kim**, G. Coletti, D. Payne, C. Chan, S. Wenham, and Z. Hameiri, “Carrier-induced degradation in multicrystalline silicon: Dependence on the silicon nitride passivation layer and hydrogen released during firing,” *IEEE J. Photovoltaics*, vol. 8, no. 2, pp. 413–420, 2018.
8. D. Chen, M. Kim, B. V. Stefani, B. J. Hallam, M. D. Abbott, C. E. Chan, R. Chen, D. N. R. Payne, N. Nampalli, A. Ciesla, T. H. Fung, **K. Kim**, and S. R. Wenham, “Evidence of an identical firing-activated carrier-induced defect in monocrystalline and multicrystalline silicon,” *Sol. Energy Mater. Sol. Cells*, vol. 172, pp. 293–300, 2017.
9. Z. Hameiri, N. Borojevic, L. Mai, N. Nandakumar, **K. Kim**, and S. Winderbaum, “Low-absorbing and thermally stable industrial silicon nitride films with very low surface recombination,” *IEEE J. Photovoltaics*, vol. 7, no. 4, pp. 996–1003, 2017.
10. H. Li, **K. Kim**, B. Hallam, B. Hoex, S. Wenham, and M. Abbott, “ POCl_3 diffusion for industrial Si solar cell emitter formation,” *Front. Energy*, vol. 11, no. 1, 2017.

11. J. Yun, J. Huang, A. Teal, **K. Kim**, S. Varlamov, and M. A. Green, "Correlation of the crystal orientation and electrical properties of silicon thin films on glass crystallized by line focus diode laser," *Thin Solid Films*, vol. 609, 2016.
12. R. Evans, **K. H. Kim**, X. Wang, A. Sugianto, X. Chen, R. Chen, and M. A. Green, "Simplified technique for calculating mismatch loss in mass production," *Sol. Energy Mater. Sol. Cells*, vol. 134, 2015.

Conference presentations

1. C.-Y. Lee, X. Cui, T. Zhang, R. Deng, **K. Kim**, B. Hoex, "Evaluating the impact of thermal annealing on Al₂O₃/c-Si interface properties by non-destructive measurements," in *7th IEEE World Conference on Photovoltaic Energy Conversion*, 2018.
2. C. Vargas, **K. Kim**, G. Coletti, D. Payne, C. Chan, S. Wenham, and Z. Hameiri, "Influence of silicon nitride and its hydrogen content of carrier-induced degradation in multicrystalline silicon," *Proceeding 33rd Eur. Photovolt. Sol. Energy Conf. Exhib. Amsterdam*, p. 561, 2017.
3. **K. Kim**, Z. Hameiri, and S. Winderbaum, "In-situ diagnostics of PECVD AlO_x deposition by optical emission spectroscopy," *26th Photovoltaic Science and Engineering Conference*, 2016
4. **K. Kim**, N. Borojevic, S. Duttagupta, and Z. Hameiri, "Impact of deposition condition and thermal process on industrial PECVD AlO_x layer for surface passivation," *26th Photovoltaic Science and Engineering Conference*, 2016.
5. **K. Kim**, Z. Hameiri, N. Borojevic, S. Duttagupta, and S. Winderbaum, "Outstanding as-deposited surface passivation by industrial PECVD aluminum oxide," in *Proceedings of the 43rd IEEE Photovoltaic Specialists Conference*, 2016, pp. 2917–2921.
6. Z. Hameiri, N. Borojevic, L. Mai, N. Nandakumar, **K. Kim**, and S. Winderbaum, "Should the refractive index at 633 nm be used to characterize silicon nitride films?," *2016 IEEE 43rd Photovolt. Spec. Conf.*, no. August, pp. 2900–2904, 2016.
7. Z. Hameiri, N. Borojevic, L. Mai, N. Nandakumar, **K. Kim**, S. Winderbaum, "On the limitation of the refractive index at 633 nm to characterize silicon nitride films", *3rd International Conference on Emerging Electronics*, 2016.
8. Z. Hameiri, N. Borojevic, L. Mai, N. Nandakumar, **K. Kim**, S. Winderbaum, "Development of low-absorption and thermally-stable silicon nitride films for surface passivation of silicon solar cells", *26th International Photovoltaic Science and Engineering Conference*, 2016

Appendix 2: List of acronyms

Acronym	Description
AlO _x	Aluminium Oxide
CDA	Clean Dry Air
C-V	Capacitance-Voltage
Cz	Czochralski
FZ	Float-Zone
GFRR	Gas Flow Rate Ratio
MWP	Micro Wave Power
PC	Photoconductance
PECVD	Plasma Enhanced Chemical Vapor Deposition
PERC	Passivated Emitter and Rear Cell
PV	Photovoltaic
Si	Silicon
SiN _x	Silicon Nitride
SiO _x	Silicon Oxide
TGFR	Total Gas Flow Rate
TMA	Trimethyl Aluminium

Appendix 3: Plasma diagnostics for remote PECVD process⁵

Introduction

The AlO_x layer has become increasingly important in photovoltaics (PV) manufacturing due to its outstanding capability to passivate the surfaces of silicon (Si) solar cells, in particular for p -type and p^+ surfaces [9], [17], [89], [101], [179], [282]. The material provides both excellent field effect passivation - due to a high density of negative charge within the film - and chemical passivation, due to its high concentration of hydrogen atoms [9], [17], [89], [101], [179], [282].

Plasma-enhanced chemical vapor deposition (PECVD), which is widely used for the formation of dielectric films in both the nano-electronics [283]–[301] and PV manufacturing industries [89], [97], [101], [102], [104], [108], [109], is typically used to deposit AlO_x layers. Optimisation of the deposition process is a key requirement to ensure optimised device performance. Common characterisation methods used in the PV community include excess carrier lifetime measurements to assess the surface passivation quality of the obtained film [50], [58], [110], [128], [302]–[306] and Fourier transform infrared spectroscopy (FTIR) to determine the chemical bonding configuration of the deposited film [17], [70], [104], [106], [307]–[311].

However, these characterisation methods can be used only after the deposition process, in separate systems. Development of *in-situ* monitoring methods can be valuable since process information and possible errors can be detected in real time during manufacturing. Optical emission spectroscopy (OES) is one of the most widely used methods for *in-situ* process monitoring in the nano-electronics industry [283]–[301]. However, it is not commonly used in the PV industry [312]. In this study, an OES-based method to monitor PECVD AlO_x is investigated; then an attempt is made to correlate the detected radicals with the chemical properties of the film and interface passivation quality.

⁵ This chapter is summarised and *published* in *Surface & Coatings Technology* (DOI: <https://doi.org/10.1016/j.surfcoat.2017.08.034>).

As critical process parameters, the gas flow rate ratio (GFRR) between nitrous oxide (N_2O) and tri-methyl aluminium (TMA), the deposition pressure, and the deposition temperature were varied. These parameters are known to have a major impact on the film properties [313], [314]. Total gas flow rate and microwave power are also important parameters; however, they were fixed at 900 sccm and 1500 W (32% duty cycle) in this study, to allow for a detailed study of the other three parameters. The density of aluminium (Al^*), oxygen (O^*), and hydrogen (H_α^* and H_β^*) radicals in the plasma were monitored by spectrophotometry as the intensity of the emitted light from the electronic transitions. H_α^* and H_β^* are spectral lines in the Balmer series which are detected when a hydrogen electron falls from the third (H_α^*) and fourth (H_β^*) lowest energy levels to the second lowest energy level. The impact of these parameters on the density of different radicals are analysed using a statistical software package (STATISTICA) [150], [151]. Although no strong correlation between the density of the forming radicals (Al^* and O^*) in the plasma and the surface passivation quality has been noted, the PECVD condition to achieve an optimum surface passivation layer is determined. However, this study highlights the limited knowledge that currently exists within the PV community regarding plasma characterisation and the relationship between the plasma species and surface recombination behaviour.

Experimental methods

The OES was installed in an industrial PECVD system (MAiA, Meyer Burger). The schematic diagram of the modified system is shown in Fig. A- 1. Light emission from an electronic transition of the radicals in the microwave plasma is transferred by an optical fibre which is mounted at view-port of the process chamber. The transferred light is analysed by a miniature spectrometer (Ocean Optics USB 2000+) with a detectable wavelength range of 340–1020 nm. The density of the plasma radical is represented as the magnitude of the associated emission peak. Fig. A- 2 shows the peak information of the OES signal during a typical deposition process. The Al^* , H_α^* , H_β^* , N^* and O^* related peaks are detected at the wavelengths 391.9 nm, 656.6 nm, 486.9 nm, 762.9 nm and 777.8 nm, respectively [292], [315]. It is noted that the N^* peak is observed since N_2O gas was used as an oxygen source and it can be also a source of nitrogen at the same time. The detection of N can be unique for PECVD process but not for ALD process. It is because the nitrogen peak will not be observed for thermal ALD due to both absence of nitrogen in oxygen precursor and inherent difference in deposition mechanism.

Two groups of wafers were used in this study. The first group consists of 60 *p*-type, Czochralski (Cz), random-upright-pyramid textured wafers (resistivity of $\sim 1.8 \text{ } \Omega\cdot\text{cm}$, thickness of $190 \pm 10 \text{ } \mu\text{m}$ and size of $45 \times 45 \text{ mm}^2$). The second group consists of 15 2'' double-side-polished (DSP) *p*-type Cz wafers (resistivity $10 \text{ } \Omega\cdot\text{cm}$ and thickness $175 \pm 10 \text{ } \mu\text{m}$). The first group (Cz wafers) were used for electrical property measurements (excess carrier lifetime), while the second group (DSP wafers) was used for chemical property measurements (FTIR). The wafers went through an RCA (Radio Corporation of America) clean [156] and hydrofluoric acid (HF) dip before depositing AlO_x and the silicon nitride (SiN_x) capping layer.

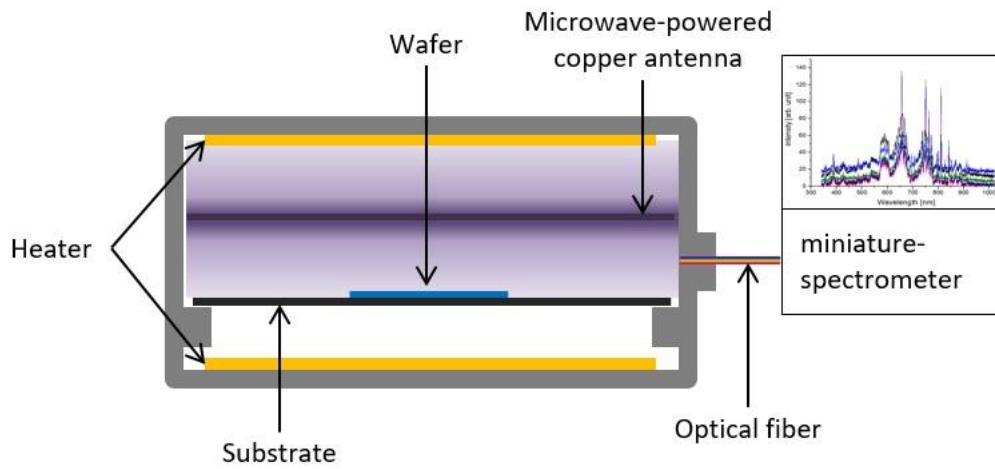


Fig. A- 1. Schematic diagram of OES set-up and the deposition system

For AlO_x deposition, N_2O and TMA were used as process gases with argon (Ar) as a carrier gas for TMA. Silane (SiH_4) and ammonia (NH_3) were used for the SiN_x deposition. The same SiN_x capping layer was used for all the Cz samples. Although the SiN_x was not deposited onto the DSP wafers, they received the same thermal treatment by passing through the PECVD system with the plasma sources switched off, while keeping the same setting for the heaters and for the transport. The AlO_x layer thickness was targeted at 25 nm to avoid thickness dependence of the surface passivation performance. In this work, FTIR and lifetime results are limited to as-deposited samples to avoid any possible modification of the film property by the subsequent thermal process.

With regard to characterisation of the resulting film, effective surface recombination velocity (S_{eff}) was extracted from photoconductance-based effective lifetime measurements (using a WCT-120 from Sinton Instruments). For extracting S_{eff} , I used the following equation:

$$S_{eff} = \frac{W}{2} \left(\frac{1}{\tau_{eff}} - \frac{1}{\tau_{int}} \right) \quad \text{Equation A-1}$$

where τ_{int} is the intrinsic (Auger and radiative) lifetime. Here I assume that τ_{SRH}^{-1} (infinite bulk lifetime) equals zero since the quality of the bulk is low due to inherent B-O and iron in Cz wafers. In this case, the calculated S_{eff} is at its upper limit.

Each wafer was measured in quasi-steady-state mode [50]. An FTIR spectrometer (Nicolet 5700 from Thermo) was used to measure the infra-red absorption by various chemical bonds in the AlO_x films.

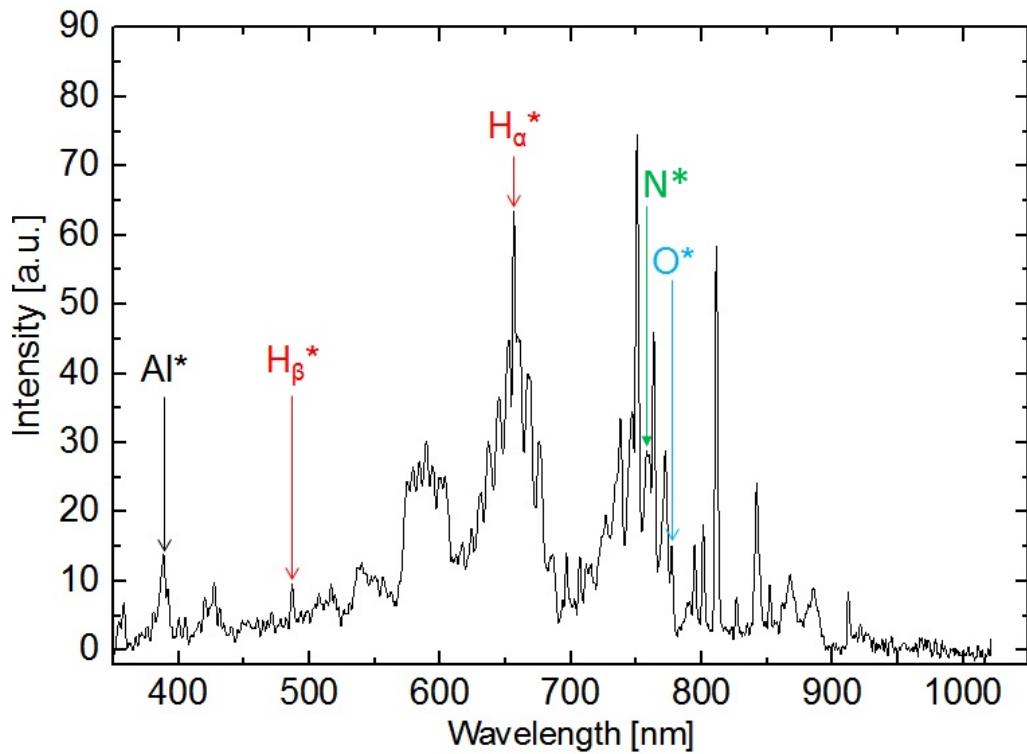


Fig. A- 2. A representative example of an OES signal as a function of wavelength; the peaks of Al^* , $\text{H}\beta^*$, $\text{H}\alpha^*$, N^* and O^* are marked.

Analysis of the data was done using STATISTICA. The experiment was designed as a Box-Behnken (3 factors/1 block/15 runs with 3 levels) with the three independent factors chosen to be GFRR of N_2O to TMA, the deposition pressure, and the deposition temperature. Using STATISTICA, a model to predict the intensity of the OES signal as a function of the three process parameters was developed. Peak heights were calculated after subtracting the baseline to quantify the OES signal intensity; in this study the baseline is defined where there is no emission (from 950 nm to 1020 nm). Regarding the FTIR analysis, peak heights were calculated after subtracting the baseline that was defined where there is zero absorption (from 1900 cm^{-1} to 2400 cm^{-1}). For both OES and

FTIR raw data, the Savitzky-Golay method was used for smoothing to optimise the signal-to-noise ratio [178].

The accuracy of the model was determined by comparison of the measured and the predicted values and by examination of the R -squared value of the fit. The statistical significance of the independent factors on the tested parameters was assessed by the ‘ p -Test’ value. A p -value below 0.05 indicates a significant effect of the independent factor on the tested parameter.

Results and discussion

Fig. A- 3 shows a contour plot, based on the STATISTICA model, of the OES intensities of observed radicals in the plasma as a function of the deposition parameters. The R -squared values of all the models are higher than 0.99. The dots in the contour map indicate the actual deposition conditions, as designed by STATISTICA. Fig. A- 3 (a) shows that Al^* in the OES spectrum is significantly impacted by both GFRR ($p < 0.004$) and the pressure ($p < 0.037$). With regard to O^* , both the GFRR ($p < 0.0002$) and the pressure ($p < 0.023$) have a significant effect on its generation, as shown in Fig. A- 3 (b).

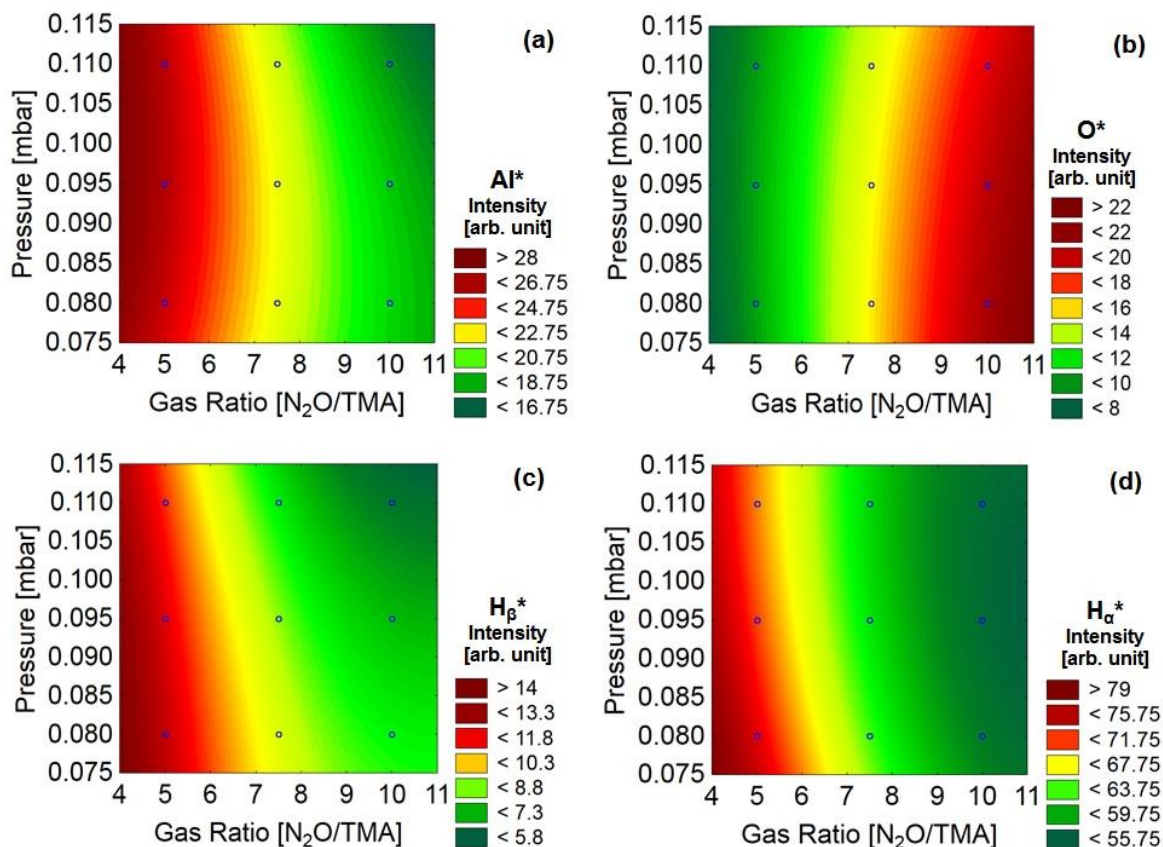


Fig. A- 3. Intensity of emitted light during electronic transition in the plasma by (a) Al^* , (b) O^* , (c) H_β^* , and (d) H_α^*

It was found that GFRR has the strongest impact on H_{β}^* with ($p < 0.001$), as shown in Fig. A- 3 (c) and on H_{α}^* with ($p < 0.0007$) [Fig. A- 3 (d)]. Temperature and pressure have only a minimal effect on both hydrogen radicals. For all the four observed radicals (Al^* , O^* , H_{α}^* and H_{β}^*), it was found that GFRR has a significant linear impact. It is clear that GFRR is a meaningful index, since its numerator (N_2O) is the only source of oxygen while its denominator (TMA) is the only source of aluminium; these two elements form the AlO_x layer. In addition, hydrogen can be dissociated from TMA and the GFRR clearly shows that it has an inversely linear relationship with the H-related radicals.

Contour plots based on the STATISTICA model for the FTIR measurements are studied to determine the chemical properties of the resulting AlO_x films. I focus on the Al-O, O-H and C-H bonds, denoted [Al-O], [O-H] and [C-H], respectively. Fig. A- 4 (a), (b), and (c) presents absorption of chemical bonds as measured by FTIR as a function of the deposition parameters. GFRR has the most significant impact, not only on the density of [Al-O] with p -value < 0.0106 , but also on the density of [O-H] with $p < 0.0282$ and [C-H] with $p < 0.0119$. Temperature shows only a small impact on [C-H], while pressure does not have any significant impact. For all the three detected chemical bonds densities ([Al-O], [O-H], and [C-H]), GFRR has a significant quadratic impact.

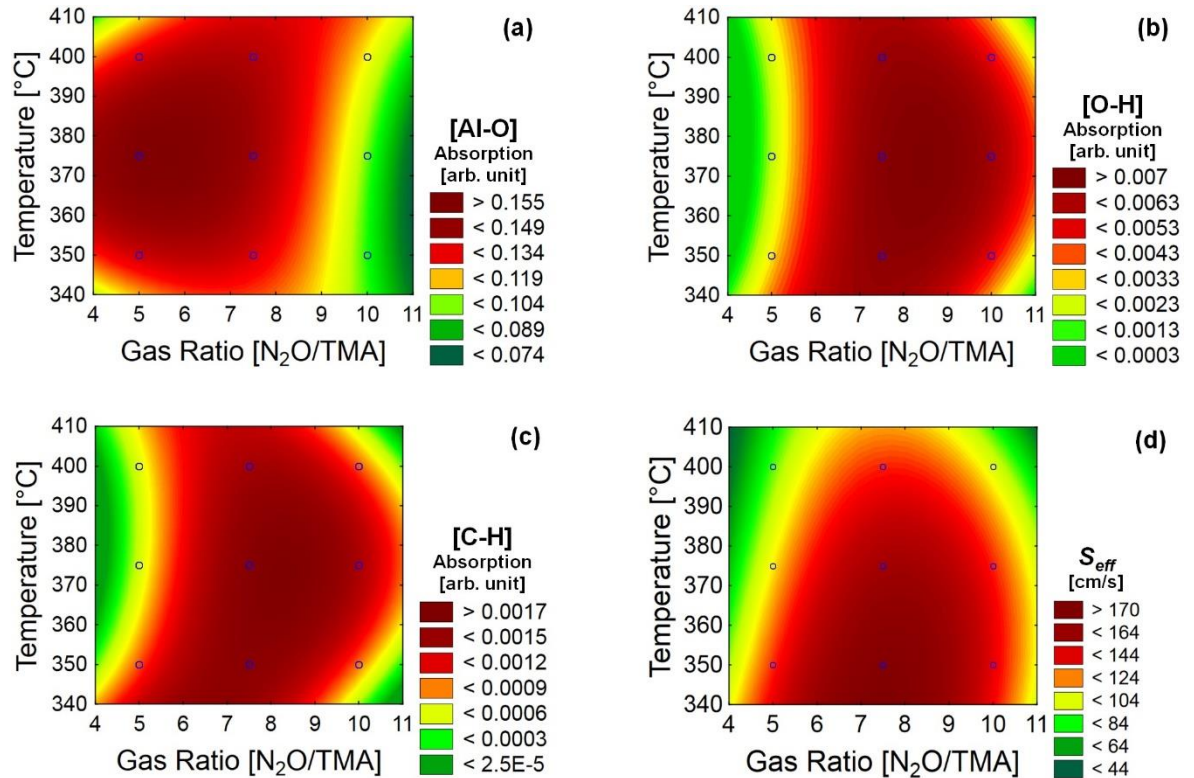


Fig. A- 4. FTIR absorption of chemical bond configurations in the AlO_x layer: (a) Al-O bond, (b) O-H bond, (c) C-H bond, and (d) S_{eff} .

Surface saturation current density was also investigated as an electrical property of the resulting film. Fig. A- 4 (d) shows a contour plot of S_{eff} at an excess carrier concentration of 10^{15} cm^{-3} . The R -squared value of the model is higher than 0.99. Temperature ($p < 0.009$) is the most significant factor on S_{eff} followed by GFRR ($p < 0.013$).

I also investigated the correlation between the OES measurements and the resulting film properties (chemical bonds as measured by FTIR and S_{eff}) using the statistical software package JMP which has powerful functions to identify correlations between sets of data and a strong graph-building capability.

Firstly, I studied a correlation related to layer-forming atoms (aluminium and oxygen). Fig. A- 5 (a) shows the correlation between S_{eff} acquired from the measured lifetime and the ratio of Al^* to O^* (Al^*/O^*) determined by OES. The ratio Al^*/O^* in OES is assumed to be more meaningful than either Al^* or O^* radicals, as $[\text{Al-O}]$ is supposed to exist as a certain ratio of Al^* and O^* [107]. Individual data points are coloured according to the three different GFRR values as it is an independent factor which has the strongest impact on all the characterisation results, as discussed above. It is interesting to note the weak impact of Al^*/O^* on S_{eff} . A wide range of S_{eff} was obtained for similar Al^*/O^* . In Fig. A- 5 (b), the correlation between Al^*/O^* and the $[\text{Al-O}]$ absorption peak is presented. It seems that the concentration of $[\text{Al-O}]$ bonds saturates for $\text{Al}^*/\text{O}^* \geq 2$. No correlation was found between S_{eff} and $[\text{Al-O}]$ absorption, although lower S_{eff} was extracted for high $[\text{Al-O}]$ as shown in Fig. A- 5.

Further investigation on the correlations OES to FTIR and S_{eff} is shown in Fig. A- 7. I investigated the impact of the independent Al^* and O^* , and the sum of Al^* and O^* ; however, none of them demonstrates a strong correlation by itself.

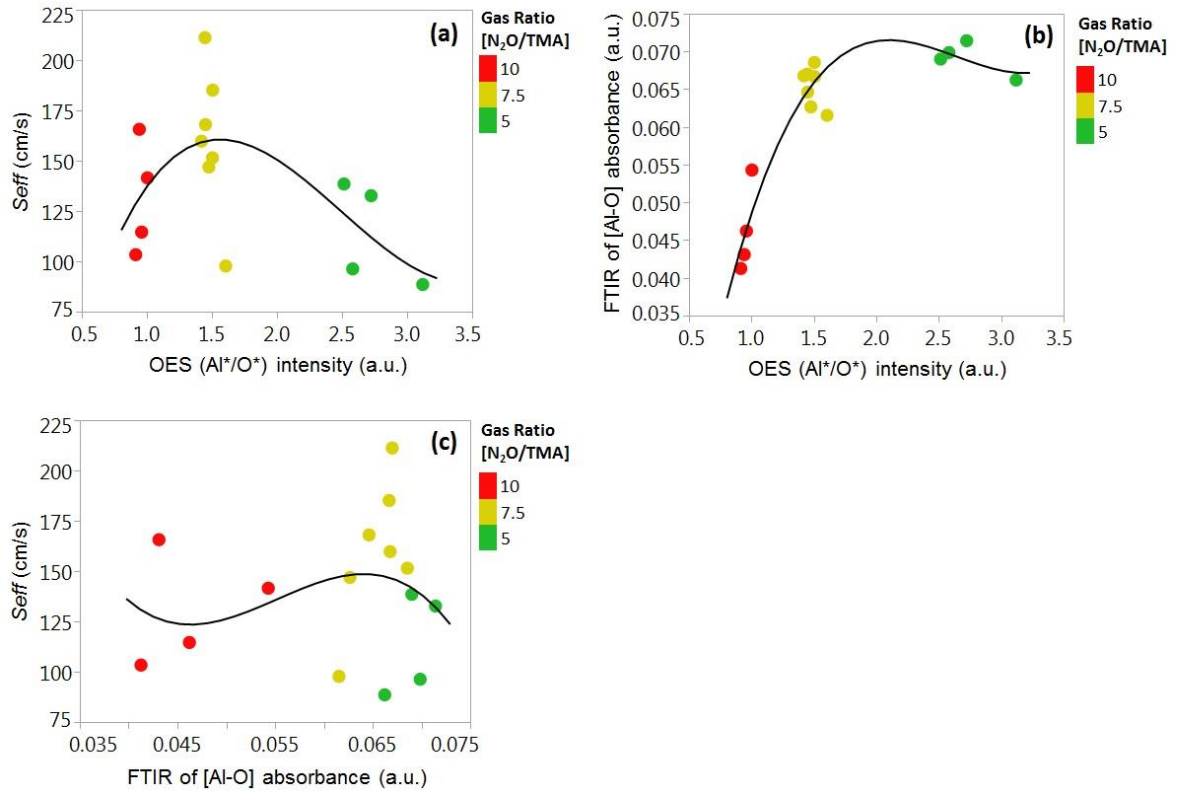


Fig. A- 5. Correlation between (a) S_{eff} and Al^*/O^* (OES), (b) [Al-O] (FTIR) and Al^*/O^* (OES), and (c) S_{eff} and [Al-O]. The lines only serve as guides to the eyes.

I then studied the correlations related to hydrogen atoms. Fig. A- 6 (a) shows the correlation between OES intensity (sum of H_{α}^* and H_{β}^*) and density of hydrogen-related bonds obtained from the absorption peaks of the FTIR measurements (sum of [O-H] and [C-H]). It is observed that the density of hydrogen-related bonds increases with a higher density of hydrogen radicals (sum of H_{α}^* and H_{β}^*) until a certain value (sum of H_{α}^* and H_{β}^* = ~70). However, less [O-H] and [C-H] are detected in the resulting layer as the sum of H_{α}^* and H_{β}^* increases above that value. It seems that excessive hydrogen radicals in the plasma decreases the mean free path of radicals and leads to fewer [O-H] and [C-H] bonds in the resulting AlO_x layer. Fig. A- 6 (b) indicates that the best surface passivation is achieved when more H_{α}^* and H_{β}^* are generated in the plasma, although this condition also resulted in minimum [O-H] and [C-H] bonds. Fig. A- 6 (c) indicates that there is no strong correlation between S_{eff} and the density of hydrogen-related bonds. However, high quality surface passivation is achieved with the lowest density of [O-H] and [C-H] bonds. A possible explanation is that the majority of generated species within the plasma are exhausted out of the chamber and only a small amount is engaged to form the film and react with the surface of the substrate. Therefore, additional plasma diagnostic methods such as quadrupole mass spectrometry (QMS)

should be employed to reveal the uncertainty of the plasma [316]. Further investigations regarding the correlations between OES and FTIR and between OES and S_{eff} are shown in Fig. A- 8.

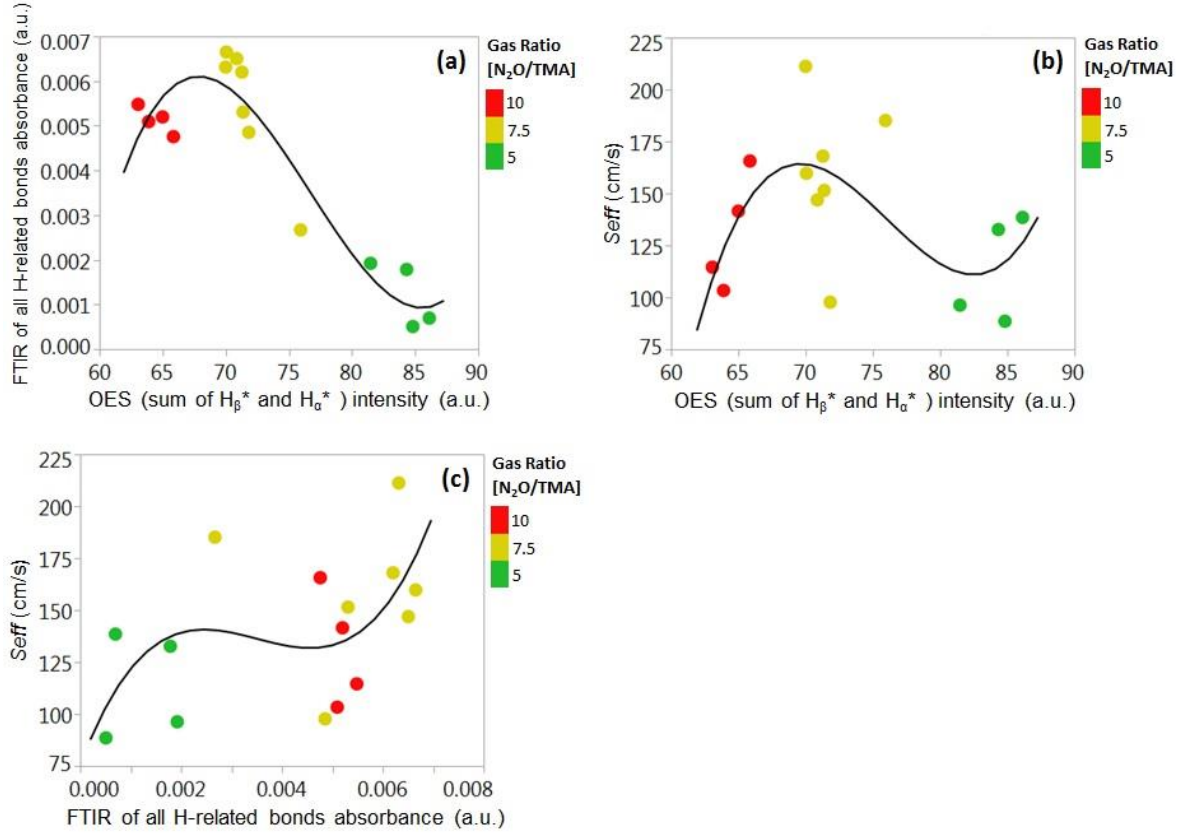


Fig. A- 6. Correlation between (a) $([O-H] + [C-H])$ from FTIR and $(H_{\beta}^* + H_{\alpha}^*)$ and (b) S_{eff} and $(H_{\beta}^* + H_{\alpha}^*)$ from OES, and (c) S_{eff} and $([O-H] + [C-H])$. The lines only serve as guides to the eyes.

Additional information

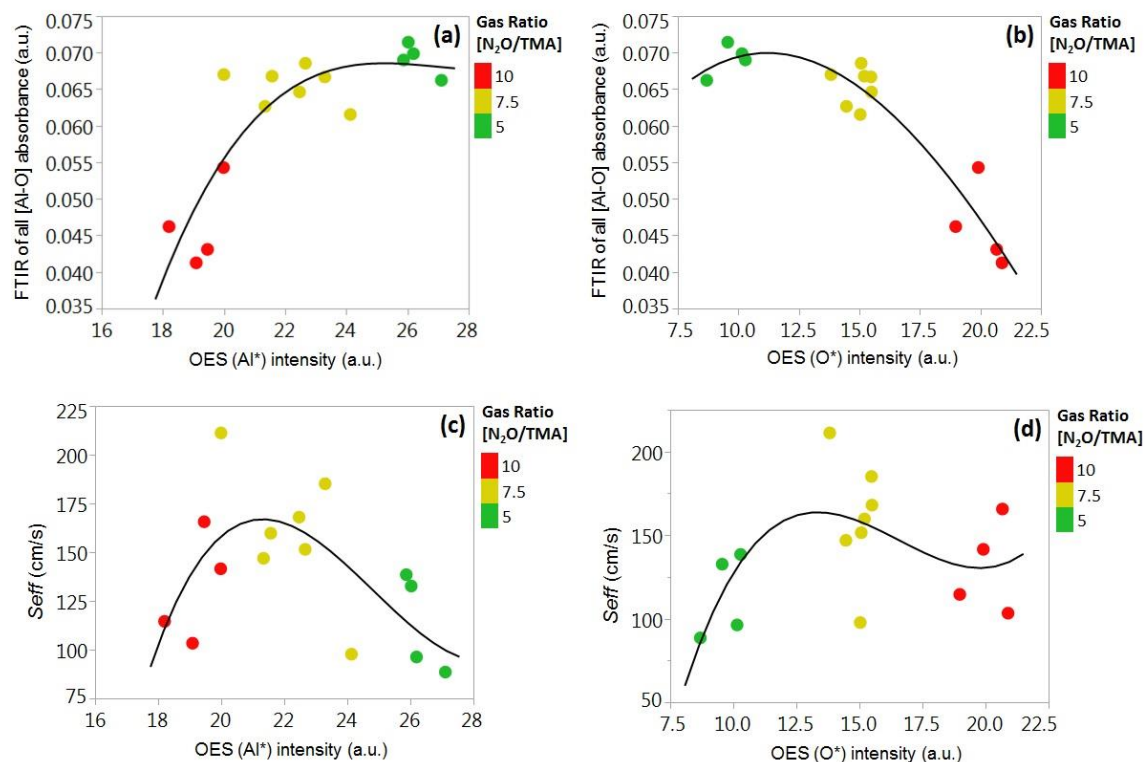


Fig. A- 7. Correlation between [Al-O] (FTIR) and (a) Al* (OES), (b) O* (OES) and correlation between S_{eff} and (c) Al* (OES), (d) O* (OES). The lines only serve as guides to the eyes.

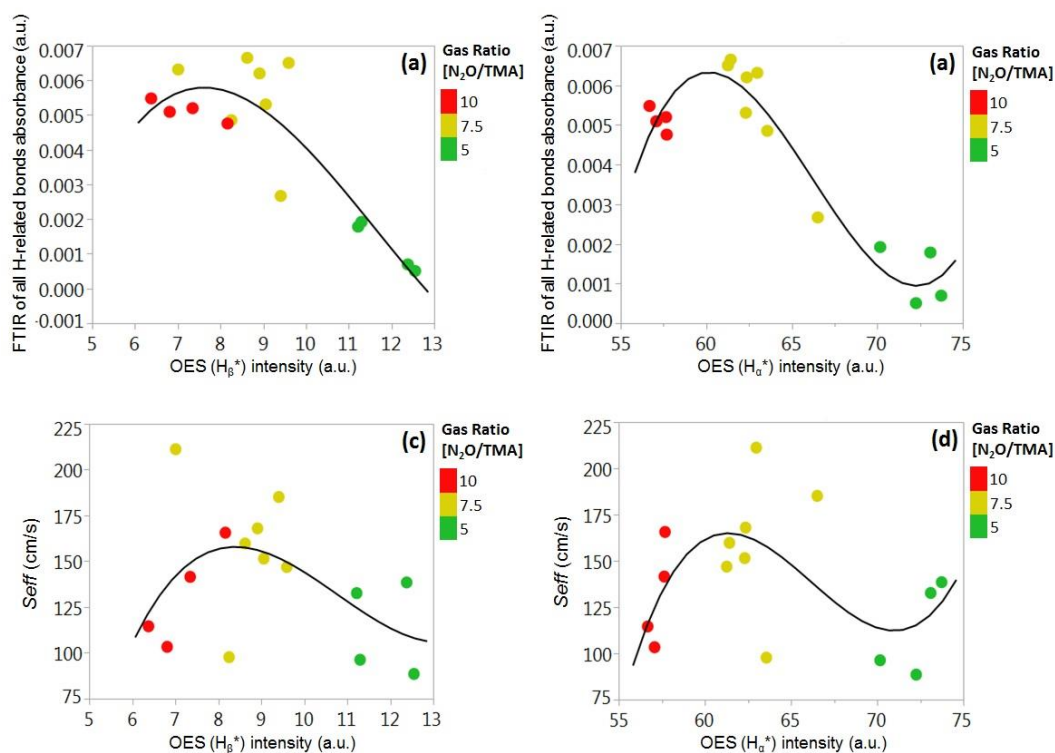


Fig. A- 8. Correlation between sum of ([O-H] + [C-H]) from FTIR and (a) H_β* (OES), (b) H_α* (OES). Correlation between S_{eff} and (c) H_β* (OES), and (d) H_α* (OES). The lines only serve as guides to the eyes.

Conclusion

I investigated the impact of the PECVD process conditions on the density of radicals generated by the plasma using OES. I tried to correlate the radical densities with the chemical and electrical properties of the obtained film. I found that GFRR has the most significant impact on the density of all the detected radicals (Al^* , O^* , H_α^* and H_β^*). GFRR also has a significant impact on both the chemical and electrical properties of the film. However, no strong correlations between the radicals and the film properties have been identified. It is found that the optimum surface passivation is achieved with a certain ratio between Al^* and O^* ; interestingly, it is not directly reflected in the density of $[\text{Al-O}]$ in the layer. It was also observed that the surface passivation quality is higher with higher density of hydrogen radicals in the plasma. This study highlights the need for further investigations of the plasma characteristics during PECVD processes for PV applications.

Bibliography

- [1] R. L. Peters and J. D. S. Darling, "The Greenhouse Effect and Nature Reserves," *Bioscience*, vol. 35, no. 11, pp. 707–717, 1985.
- [2] E. A. G. Schuur *et al.*, "Climate change and the permafrost carbon feedback," *Nature*, vol. 520, p. 171, Apr. 2015.
- [3] K. Mersmann, E. T. Gray, P. Lynch, and G. A. Schmidt, "2018 Was the Fourth Hottest Year on Record," NASA, 2019. [Online]. Available: <https://svs.gsfc.nasa.gov/13142>.
- [4] R. A. Houghton and G. M. Woodwell, "Global Climatic Change," *Sci. Am.*, vol. 260, no. 4, pp. 36–47, 1989.
- [5] M. Urban, "Accelerating extinction risk from climate change," 2015.
- [6] D. Dudley, "Renewable energy will be consistently cheaper than fossil fuels by 2020, report claims," *Forbes*, Jan-2018.
- [7] R. F. Service, "Is it time to shoot for the sun?," *Science* (80-.), vol. 309, no. 5734, pp. 548–551, 2005.
- [8] T. Lüder, G. Hahn, and B. Terheiden, "Passivation of Si wafers by ALD- Al_2O_3 films with different surface conditioning," *Energy Procedia*, vol. 8, pp. 660–665, 2011.
- [9] M. A. Green, "The passivated emitter and rear cell (PERC): From conception to mass production," *Sol. Energy Mater. Sol. Cells*, vol. 143, pp. 190–197, 2015.
- [10] ITRPV, "International Technology Roadmap for Photovoltaic," no. September, p. 4, 2015.
- [11] ITRPV, "International technology roadmap for photovoltaic (ITRPV)," *ITRPV*, 2016. [Online]. Available: <http://www.itrpv.net/>.
- [12] ITRPV, "C-Si PV : Manufacturing Trends & Challenges - ITRPV 8 th edition update," *ITRPV*, 2017. .
- [13] ITRPV, "International technology roadmap for photovoltaic (ITRPV)," *ITRPV*, 2018. [Online]. Available: <http://www.itrpv.net/>.
- [14] B. Hoex, S. B. S. Heil, E. Langereis, M. C. M. Van De Banden, and W. M. M. Kessels, "Ultralow surface recombination of c-Si substrates passivated by plasma-assisted atomic layer deposited Al_2O_3 ," *Appl. Phys. Lett.*, vol. 89, no. 4, pp. 1–4, 2006.
- [15] G. Agostinelli *et al.*, "Very low surface recombination velocities on p-type silicon wafers passivated with a dielectric with fixed negative charge," *Sol. Energy Mater. Sol. Cells*, vol. 90, no. 18–19, pp. 3438–3443, 2006.
- [16] J. Schmidt, A. Merkle, R. Brendel, B. Hoex, M. C. M. van de Sanden, and W. M. M. Kessels, "Surface passivation of high-efficiency silicon solar cells by atomic-layer-deposited Al_2O_3 ," *Prog. Photovoltaics Res. Appl.*, no. 16, pp. 461–466, 2008.
- [17] G. Dingemans and E. Kessels, "Status and prospects of Al_2O_3 -based surface passivation schemes for silicon solar cells," *J. Vac. Sci. Technol. A Vacuum, Surfaces Film.*, vol. 30, no. 4, pp. 1–27, 2012.
- [18] J.-A. Becca, "Sunshot 2030," in *44th IEEE Photovoltaic Specialist Conference*, 2017, pp. 15–20.
- [19] W. Shockley and H. J. Queisser, "Detailed balance limit of efficiency of p-n junction solar cells," *J. Appl. Phys.*, vol. 32, no. 3, pp. 510–519, 1961.
- [20] B. Veith-wolf, R. Witteck, A. Morlier, H. Schulte-huxel, and J. Schmidt, "Effect of UV illumination on the passivation quality of $\text{AlO}_x/\text{c-Si}$ interfaces," in *Proceedings of the 43th IEEE Photovoltaic Specialists Conference*, 2016, no. 1, pp. 12–15.
- [21] T. Niewelt, W. Kwapil, M. Selinger, A. Richter, and M. C. Schubert, "Long-term stability of aluminum oxide based surface passivation schemes under illumination at elevated temperatures," *IEEE J. Photovoltaics*, vol. 7, no. 5, pp. 1197–1202, 2017.
- [22] A. G. Aberle, *Crystalline silicon solar cells: advanced surface passivation and analysis*. University of New South Wales, 1999.
- [23] A. G. Aberle, "Surface passivation of crystalline silicon solar cells: a review," *Prog. Photovoltaics Res. Appl.*, vol. 8, no. 5, pp. 473–487, Sep. 2000.

- [24] V. S. Vavilov, "RADIATIVE RECOMBINATION IN SEMICONDUCTORS," *Sov. Phys. Uspekhi*, vol. 2, no. 3, pp. 455–464, 1959.
- [25] G. P. Agrawal and N. K. Dutta, "Recombination Mechanisms in Semiconductors BT - Semiconductor Lasers," G. P. Agrawal and N. K. Dutta, Eds. Boston, MA: Springer US, 1993, pp. 74–146.
- [26] P. Auger, "Sur les rayons β secondaires produits dans un gaz par des rayons X.," *CR Acad. Sci.(F)*, vol. 177, p. 169, 1923.
- [27] M. S. Tyagi and R. Van Overstraeten, "Minority carrier recombination in heavily-doped silicon," *Solid. State. Electron.*, vol. 26, no. 6, pp. 577–597, 1983.
- [28] R. Häcker and A. Hangleiter, "Intrinsic upper limits of the carrier lifetime in silicon," *J. Appl. Phys.*, vol. 75, no. 11, pp. 7570–7572, Jun. 1994.
- [29] S. J. Pearton, "Chapter 5 Neutralization of Deep Levels in Silicon," in *Hydrogen in Semiconductors*, vol. 34, J. I. Pankove and N. M. B. T.-S. and S. Johnson, Eds. Elsevier, 1991, pp. 65–89.
- [30] S. M. Myers *et al.*, "Hydrogen interactions with defects in crystalline solids," *Rev. Mod. Phys.*, vol. 64, no. 2, pp. 559–617, 1992.
- [31] M. A. Green, *Operating principles, technology and system application*. University of New South Wales, 1998.
- [32] A. B. Sproul, "Dimensionless solution of the equation describing the effect of surface recombination on carrier decay in semiconductors," *J. Appl. Phys.*, vol. 76, no. 5, pp. 2851–2854, 1994.
- [33] W. P. Dumke, "Spontaneous radiative recombination in semiconductors," *Phys. Rev.*, vol. 105, no. 1, p. 139, 1957.
- [34] Y. P. Varshni, "Band-to-band radiative recombination in groups IV, VI, and III-V semiconductors (I)," *Phys. status solidi*, vol. 19, no. 2, pp. 459–514, 1967.
- [35] P. P. Altermatt, F. Geelhaar, T. Trupke, X. Dai, A. Neisser, and E. Daub, "Injection dependence of spontaneous radiative recombination in c-Si: experiment, theoretical analysis, and simulation," in *NUSOD '05. Proceedings of the 5th International Conference on Numerical Simulation of Optoelectronic Devices, 2005.*, 2005, pp. 47–48.
- [36] D. Kiliani, G. Micard, B. Steuer, B. Raabe, A. Herguth, and G. Hahn, "Minority charge carrier lifetime mapping of crystalline silicon wafers by time-resolved photoluminescence imaging," *J. Appl. Phys.*, vol. 110, no. 5, 2011.
- [37] J. Schmidt and A. Cuevas, "Electronic properties of light-induced recombination centers in boron-doped Czochralski silicon," *J. Appl. Phys.*, vol. 86, no. 6, pp. 3175–3180, 1999.
- [38] W. Shockley and W. T. Read, "Statistics of recombination of holes and electrons," *Phys. Rev.*, vol. 87, no. 5, pp. 835–842, 1952.
- [39] R. N. Hall, "Electron-hole recombination in germanium," *Phys. Rev.*, vol. 87, no. 6, p. 387, 1952.
- [40] W. H. Brattain, "Surface Properties of Semiconductors," *Science (80-)*, vol. 126, no. 3265, pp. 151 LP – 153, Jul. 1957.
- [41] H. Ibach and J. E. Rowe, "Hydrogen adsorption and surface structures of silicon," *Surf. Sci.*, vol. 43, no. 2, pp. 481–492, 1974.
- [42] H. Neergaard Waltenburg and J. Yates, "Surface chemistry of silicon," *Chem. Rev.*, vol. 95, no. 5, pp. 1589–1673, 1995.
- [43] W. D. Eades and R. M. Swanson, "Calculation of surface generation and recombination velocities at the Si-SiO₂ interface," *J. Appl. Phys.*, vol. 58, no. 11, pp. 4267–4276, Dec. 1985.
- [44] A. S. Grove and D. J. Fitzgerald, "Surface effects on p-n junctions: Characteristics of surface space-charge regions under non-equilibrium conditions," *Solid. State. Electron.*, vol. 9, no. 8, pp. 783–806, 1966.
- [45] D. J. Fitzgerald and A. S. Grove, "Surface recombination in semiconductors," in *International Electron Devices Meeting*, 1968.
- [46] K. R. McIntosh and L. E. Black, "On effective surface recombination parameters," *J. Appl. Phys.*, vol. 116, no. 1, 2014.

- [47] Y. S. Kim, C. I. Drowley, and C. Hu, "A new method of measuring diffusion length and surface recombination velocity," in *14th Photovoltaic Specialists Conference*, 1980, pp. 596–600.
- [48] P. De Visschere, "Comment on G.J. Rees 'surface recombination velocity—a useful concept?,'" *Solid. State. Electron.*, vol. 29, no. 11, pp. 1161–1165, 1986.
- [49] R. A. Sinton and A. Cuevas, "Contactless determination of current–voltage characteristics and minority-carrier lifetimes in semiconductors from quasi-steady-state photoconductance data," *Appl. Phys. Lett.*, vol. 69, no. 17, pp. 2510–2512, 1996.
- [50] H. Nagel, C. Berge, and A. G. Aberle, "Generalized analysis of quasi-steady-state and quasi-transient measurements of carrier lifetimes in semiconductors," *J. Appl. Phys.*, vol. 86, no. 11, pp. 6218–6221, 1999.
- [51] R. A. Sinton, A. Cuevas, and M. Stuckings, "Quasi-steady-state photoconductance, a new method for solar cell material and device characterization," in *25th IEEE Photovoltaic Specialists Conference*, 1996, pp. 457–460.
- [52] A. L. Blum, J. S. Swirhun, R. A. Sinton, and A. Kimmerle, "An updated analysis to the WCT-120 QSSPC measurement system using advanced device physics," in *28th European Photovoltaic Solar Energy Conference and Exhibition*, 2013, pp. 1521–1523.
- [53] D. K. Schroder, *Material and device semiconductor material and device*, Third edit., vol. 44, no. 4. 2006.
- [54] A. B. Sproul, M. A. Green, and A. W. Stephens, "Accurate determination of minority carrier- and lattice scattering-mobility in silicon from photoconductance decay," *J. Appl. Phys.*, vol. 72, no. 9, pp. 4161–4171, Nov. 1992.
- [55] N. E. Grant, F. E. Rougieux, D. MacDonald, J. Bullock, and Y. Wan, "Grown-in defects limiting the bulk lifetime of p -type float-zone silicon wafers," *J. Appl. Phys.*, vol. 117, no. 5, 2015.
- [56] N. E. Grant, V. P. Markevich, J. Mullins, A. R. Peaker, F. Rougieux, and D. Macdonald, "Thermal activation and deactivation of grown-in defects limiting the lifetime of float-zone silicon," *Phys. Status Solidi - Rapid Res. Lett.*, vol. 10, no. 6, pp. 443–447, 2016.
- [57] D. Sperber, A. Graf, D. Skorka, A. Herguth, and G. Hahn, "Degradation of Surface Passivation on Crystalline Silicon and its Impact on Light Induced Degradation Experiments," pp. 1–9, 2017.
- [58] D. E. Kane and R. M. Swanson, "Measurement of the emitter saturation current by a contactless photoconductivity decay method," in *18th IEEE Photovoltaic Specialists Conference*, 1985, pp. 578–583.
- [59] M. J. Kerr, "Surface, emitter and bulk recombination in silicon and development of silicon nitride passivated solar cells," Australian National University, 2002.
- [60] A. Cuevas, "The effect of emitter recombination on the effective lifetime of silicon wafers," *Sol. Energy Mater. Sol. Cells*, vol. 57, no. 3, pp. 277–290, 1999.
- [61] K. R. McIntosh *et al.*, "An examination of three common assumptions used to simulate recombination in heavily doped silicon," in *28th European Photovoltaic Solar Energy Conference and Exhibition*, 2013, pp. 1672–1679.
- [62] A. Fell, K. R. McIntosh, M. Abbott, and D. Walter, "Quokka version 2 : selective surface doping , luminescence modeling and data fitting," in *23rd Photovoltaic Science and Engineering Conference (PVSEC), Taipei, 2013*, 2013.
- [63] A. Fell, "A free and fast three-dimensional/two-dimensional solar cell simulator featuring conductive boundary and quasi-neutrality approximations," *IEEE Trans. Electron Devices*, vol. 60, no. 2, pp. 733–738, 2013.
- [64] A. G. Aberle, "Overview on SiN surface passivation of crystalline silicon solar cells," *Sol. Energy Mater. Sol. Cells*, vol. 65, no. 1–4, pp. 239–248, 2001.
- [65] R. S. Bonilla, B. Hoex, P. Hamer, and P. R. Wilshaw, "Dielectric surface passivation for silicon solar cells: A review," *Phys. Status Solidi*, vol. 214, no. 7, p. 1700293, 2017.
- [66] J. Schmidt, R. Peibst, and R. Brendel, "Surface passivation of crystalline silicon solar cells: Present and future," *Sol. Energy Mater. Sol. Cells*, vol. 187, no. July, pp. 39–54, 2018.

- [67] G. Agostinelli *et al.*, "Surface passivation of silicon by means of negative charge dielectrics," in *Proceedings of the 19th European Photovoltaic Solar Energy Conference, Paris, France, 2004*, vol. 1, pp. 132–134.
- [68] T. M. Klein *et al.*, "Evidence of aluminum silicate formation during chemical vapor deposition of amorphous Al_2O_3 thin films on Si(100)," *Appl. Phys. Lett.*, vol. 75, no. 25, pp. 4001–4003, Dec. 1999.
- [69] E. P. Gusev, M. Copel, E. Cartier, I. J. R. Baumvol, C. Krug, and M. A. Gribelyuk, "High-resolution depth profiling in ultrathin Al_2O_3 films on Si," *Appl. Phys. Lett.*, vol. 76, no. 2, pp. 176–178, Jan. 2000.
- [70] R. S. Johnson, G. Lucovsky, and I. Baumvol, "Physical and electrical properties of noncrystalline Al_2O_3 prepared by remote plasma enhanced chemical vapor deposition," *J. Vac. Sci. Technol. A Vacuum, Surfaces, Film.*, vol. 19, no. 4, p. 1353, 2001.
- [71] K. Jaeger and R. Hezel, "A novel thin silicon solar cell with Al_2O_3 as surface passivation," in *IEEE photovoltaic specialists conference. 18*, 1985, pp. 1752–1753.
- [72] R. Hezel, K. Jaeger, H. L. Tsai, W. F. Richardson, and R. H. Womack, "Low-temperature surface passivation of silicon for solar cells," *J. Electrochem. Soc.*, vol. 136, no. 2, pp. 518–523, 1989.
- [73] F. Fertig *et al.*, "Mass production of p-type Cz silicon solar cells approaching average stable conversion efficiencies of 22 %," *Energy Procedia*, vol. 124, pp. 338–345, 2017.
- [74] B. Hoex, J. J. H. Gielis, M. C. M. Van De Sanden, and W. M. M. Kessels, "On the c-Si surface passivation mechanism by the negative-charge-dielectric Al_2O_3 ," *J. Appl. Phys.*, vol. 104, no. 11, 2008.
- [75] L. E. Black, "New Perspectives on Surface Passivation: Understanding the Si- Al_2O_3 Interface," no. April, 2016.
- [76] W. Zhang, F. Wang, K. O. Davis, K. Jiang, W. V. Schoenfeld, and J. P. Looney, "Interfacial structure and passivation properties of Al_2O_3 on silicon," in *44th IEEE Photovoltaic Specialist Conference (PVSC)*, 2016.
- [77] B. Hoex, M. Bosman, N. Nandakumar, and W. M. M. Kessels, "Silicon surface passivation by aluminium oxide studied with electron energy loss spectroscopy," *Phys. status solidi - Rapid Res. Lett.*, vol. 7, no. 11, pp. 937–941, 2013.
- [78] F. Kersten, A. Schmid, S. Bordihn, J. W. Müller, and J. Heitmann, "Role of annealing conditions on surface passivation properties of ALD Al_2O_3 films," *Energy Procedia*, vol. 38, no. 3494, pp. 843–848, 2013.
- [79] D.-G. Park *et al.*, "Characteristics of n^+ polycrystalline-Si/ Al_2O_3 /Si metal–oxide–semiconductor structures prepared by atomic layer chemical vapor deposition using $\text{Al}(\text{CH}_3)_3$ and H_2O vapor," *J. Appl. Phys.*, vol. 89, no. 11, pp. 6275–6280, Jun. 2001.
- [80] J. J. H. Gielis, B. Hoex, M. C. M. van de Sanden, and W. M. M. Kessels, "Negative charge and charging dynamics in Al_2O_3 films on Si characterized by second-harmonic generation," *J. Appl. Phys.*, vol. 104, no. 7, p. 73701, Oct. 2008.
- [81] D. N. Goldstein, J. a. McCormick, and S. M. George, " Al_2O_3 atomic layer deposition with trimethylaluminum and ozone studied by in situ transmission FTIR spectroscopy and quadrupole mass spectrometry," *J. Phys. Chem. C*, vol. 112, no. 49, pp. 19530–19539, 2008.
- [82] V. Verlaan *et al.*, "The effect of composition on the bond structure and refractive index of silicon nitride deposited by HWCVD and PECVD," *Thin Solid Films*, vol. 517, no. 12, pp. 3499–3502, 2009.
- [83] G. Dingemans *et al.*, "Stability of Al_2O_3 and $\text{Al}_2\text{O}_3/\text{a-SiN}_x\text{:H}$ stacks for surface passivation of crystalline silicon," *J. Appl. Phys.*, vol. 106, no. 11, p. 114907, 2009.
- [84] A. Richter, S. Henneck, J. Benick, M. Hörteis, M. Hermle, and S. W. Glunz, "Firing stable $\text{Al}_2\text{O}_3/\text{SiN}_x$ layer stack passivation for the front side boron emitter of n-type silicon solar cells," in *EUPVSEC*, 2010, no. September, pp. 6–10.
- [85] G. Dingemans, N. M. Terlinden, D. Pierreux, H. B. Profijt, M. C. M. van de Sanden, and W. M. M. Kessels, "Influence of the oxidant on the chemical and field-effect passivation of Si by ALD Al_2O_3 ," *Electrochem. Solid-State Lett.*, vol. 14, no. 1, p. H1, 2011.

- [86] S. Bordihn *et al.*, "Surface passivation by Al_2O_3 and a-SiN_x:H films deposited on wet-chemically conditioned Si surfaces," *ECS J. Solid State Sci. Technol.*, vol. 1, no. 6, pp. P320–P325, 2012.
- [87] J. A. Aboaf and D. R. Kerr, "Charge in SiO₂-Al₂O₃ Double Layers on Silicon," *New York*, pp. 1103–1106.
- [88] S. Miyajima, J. Irikawa, A. Yamada, and M. Konagai, "Hydrogenated aluminum oxide films deposited by plasma enhanced chemical vapor deposition for passivation of p-type crystalline silicon," in *EUPVSEC*, 2008, no. September, pp. 1029–1032.
- [89] P. Saint-Cast, D. Kania, M. Hofmann, J. Benick, J. Rentsch, and R. Preu, "Very low surface recombination velocity on p-type c-Si by high-rate plasma-deposited aluminum oxide," *Appl. Phys. Lett.*, vol. 95, no. 15, p. 151502, 2009.
- [90] B. Veith, F. Werner, D. Zielke, R. Brendel, and J. Schmidt, "Comparison of the thermal stability of single Al_2O_3 layers and $\text{Al}_2\text{O}_3/\text{SiN}_x$ stacks for the surface passivation of silicon," *Energy Procedia*, vol. 8, no. April, pp. 307–312, 2011.
- [91] H. P. Sperlich, D. Decker, P. Saint-Cast, E. Erben, and L. Peters, "High productive solar cell passivation on Roth and Rau MAiA MW-PECVD inline machine," in *EUPVSEC*, 2010, no. September, pp. 1352–1357.
- [92] Finlay Colville, "Meyer Burger confirmed as leading pv equipment supplier for 2015 but what next?," *PV-Tech*, 2015.
- [93] M. H. Norouzi *et al.*, "Development and characterization of $\text{AlO}_x/\text{SiN}_x$:B layer systems for surface passivation and local laser doping," *IEEE J. Photovoltaics*, vol. 7, no. 5, pp. 1244–1253, 2017.
- [94] K. Kim *et al.*, "Degradation of surface passivation and bulk in p-type monocrystalline silicon wafers at elevated temperature," *IEEE J. Photovoltaics*, vol. 9, no. 1, pp. 97–105, 2019.
- [95] P. Saint-Cast *et al.*, "P-type Cz-si PERC solar cells applying PECVD aluminum oxide rear surface passivation," in *This Conference, 25th EUPVSEC*, 2010.
- [96] P. Saint-Cast *et al.*, "Variation of the layer thickness to study the electrical property of PECVD $\text{Al}_2\text{O}_3/\text{c-Si}$ interface," *Energy Procedia*, vol. 8, pp. 642–647, 2011.
- [97] P. Saint-cast *et al.*, "A review of PECVD aluminum oxide for surface passivation," in *EUPVSEC*, 2012.
- [98] P. Saint-Cast *et al.*, "High-temperature stability of c-Si surface passivation by thick PECVD Al_2O_3 with and without hydrogenated capping layers," *Appl. Surf. Sci.*, vol. 258, no. 21, pp. 8371–8376, Aug. 2012.
- [99] A. Laades *et al.*, "On the impact of interfacial SiO_x -layer on the passivation properties of PECVD synthesized aluminum oxide," *Phys. Status Solidi Curr. Top. Solid State Phys.*, vol. 9, no. 10–11, pp. 2120–2123, 2012.
- [100] S. Kühnhold *et al.*, "Impact of thermal treatment on PECVD Al_2O_3 passivation layers," *Energy Procedia*, vol. 27, pp. 273–279, 2012.
- [101] S. Duttagupta, F. Lin, Shetty Kishan Devappa, Aberle Armin G., and B. Hoex, "Excellent boron emitter passivation for high-efficiency Si wafer solar cells using $\text{AlO}_x/\text{SiN}_x$ dielectric stacks deposited in an industrial inline plasma reactor," *Prog. Photovoltaics Res. Appl.*, vol. 21, pp. 760–764, 2013.
- [102] J. A. Töfflinger *et al.*, "PECVD- $\text{AlO}_x/\text{SiN}_x$ passivation stacks on wet chemically oxidized silicon: Constant voltage stress investigations of charge dynamics and interface defect states," *Sol. Energy Mater. Sol. Cells*, vol. 135, no. September 2015, pp. 49–56, 2015.
- [103] S. Gatz, F. Einsele, T. Dullerver, and R. Brendel, "Firing stability of $\text{SiN}_y/\text{SiN}_x$ surface passivation stacks for crystalline silicon solar cells," in *26th European Photovoltaic Solar Energy Conference and Exhibition*, 2011, pp. 1132–1136.
- [104] A. Laades *et al.*, "Interface issues of all-PECVD synthesized $\text{AlO}_x/\text{SiN}_x$ passivation stacks for silicon solar cells," in *27th European Photovoltaic Solar Energy Conference and Exhibition*, 2012.
- [105] S. Miyajima, J. Irikawa, A. Yamada, and M. Konagai, "High quality aluminum oxide

- passivation layer for crystalline silicon solar cells deposited by parallel-plate plasma-enhanced chemical vapor deposition,” *Appl. Phys. Express*, vol. 3, no. 1, pp. 3–6, 2010.
- [106] S. Kühnhold, P. Saint-Cast, B. Kafle, M. Hofmann, F. Colonna, and M. Zacharias, “High-temperature degradation in plasma-enhanced chemical vapor deposition Al_2O_3 surface passivation layers on crystalline silicon,” *J. Appl. Phys.*, vol. 116, no. 5, 2014.
 - [107] C. Cibert *et al.*, “Properties of aluminum oxide thin films deposited by pulsed laser deposition and plasma enhanced chemical vapor deposition,” *Thin Solid Films*, vol. 516, no. 6, pp. 1290–1296, 2008.
 - [108] J. A. Töfflinger *et al.*, “PECVD- $\text{AlO}_x/\text{SiN}_x$ passivation stacks on silicon: Effective charge dynamics and interface defect state spectroscopy,” *Energy Procedia*, vol. 55, pp. 845–854, 2014.
 - [109] S. Duttagupta, F. J. Ma, S. F. Lin, T. Mueller, A. G. Aberle, and B. Hoex, “Progress in surface passivation of heavily doped n-type and p-type silicon by plasma-deposited $\text{AlO}_x/\text{SiN}_x$ dielectric stacks,” *IEEE J. Photovoltaics*, vol. 3, no. 4, pp. 1163–1169, 2013.
 - [110] A. Richter, S. W. Glunz, F. Werner, J. Schmidt, and A. Cuevas, “Improved quantitative description of Auger recombination in crystalline silicon,” *Phys. Rev. B - Condens. Matter Mater. Phys.*, vol. 86, no. 16, pp. 1–14, 2012.
 - [111] T. Nicolet, “Introduction to fourier transform infrared spectrometry,” 2001.
 - [112] G. S. and A. Z. Evgeniy N. Gribov, Olena Zavorotynska, Giovanni Agostini, Jenny G. Vitillo, Gabriele Ricchiardi, “FTIR spectroscopy and thermodynamics of CO and H_2 adsorbed on c-, d- and a- Al_2O_3 ,” *Phys. Chem. Chem. Phys.*, vol. 12, pp. 6309–6329, 2010.
 - [113] C. Y. Lee *et al.*, “Evaluating the Impact of Thermal Annealing on c-Si/ Al_2O_3 Interface: Correlating Electronic Properties to Infrared Absorption,” *Appl. Phys.*, vol. 075204, pp. 1–12, 2018.
 - [114] I. P. Jain, A. Jain, and P. Jain, “ERDA : Technique for Hydrogen Content and Depth Profile in Thin Film Metal Hydride This document appeared in ERDA : Technique for Hydrogen Content and Depth Profile in Thin Film Metal Hydride,” vol. 78, 2010.
 - [115] F. Fertig, K. Krauß, and S. Rein, “Light-induced degradation of PECVD aluminium oxide passivated silicon solar cells,” *Phys. status solidi - Rapid Res. Lett.*, vol. 9, no. 1, pp. 41–46, 2015.
 - [116] D. Sperber, A. Herguth, and G. Hahn, “Instability of dielectric surface passivation quality at elevated temperature and illumination,” *Energy Procedia*, vol. 92, pp. 211–217, 2016.
 - [117] D. Bredemeier, D. Walter, and J. Schmidt, “Light-induced lifetime degradation in high-performance multicrystalline silicon: Detailed kinetics of the defect activation,” *Sol. Energy Mater. Sol. Cells*, vol. 173, no. July, pp. 2–5, 2017.
 - [118] D. Sperber, A. Herguth, and G. Hahn, “A 3-state defect model for light-induced degradation in boron-doped float-zone silicon,” *Phys. status solidi - Rapid Res. Lett.*, vol. 11, no. 3, p. 201600408, 2017.
 - [119] D. Sperber, A. Graf, D. Skorka, A. Herguth, and G. Hahn, “Degradation of surface passivation on crystalline silicon and its impact on light-induced degradation experiments,” *IEEE J. Photovoltaics*, vol. 7, no. 6, pp. 1627–1634, 2017.
 - [120] D. Sperber, A. Heilemann, A. Herguth, and G. Hahn, “Temperature and light induced changes in bulk and passivation quality of boron-doped float-zone silicon coated with $\text{SiN}_x\text{:H}$,” *IEEE J. Photovoltaics*, vol. 7, no. accepted, pp. 463–470, 2017.
 - [121] D. Sperber, A. Herguth, and G. Hahn, “On improved passivation stability on highly-doped crystalline silicon and the long-term stability of regenerated Cz-Si,” *Sol. Energy Mater. Sol. Cells*, vol. 185, no. March, pp. 277–282, 2018.
 - [122] R. Hezel and R. Schörner, “Plasma Si nitride - A promising dielectric to achieve high-quality silicon MIS/IL solar cells,” *J. Appl. Phys.*, vol. 52, no. 4, pp. 3076–3079, 1981.
 - [123] W. a. Lanford and M. J. Rand, “The hydrogen content of plasma-deposited silicon nitride,” *J. Appl. Phys.*, vol. 49, no. 4, pp. 2473–2477, 1978.
 - [124] M. Sheoran *et al.*, “Hydrogen diffusion in silicon from PECVD silicon nitride,” *Proc. 33rd IEEE Photovoltaic Spec. Conf.*, no. 0, pp. 1–4, 2008.
 - [125] Z. Hameiri, N. Borojevic, L. Mai, N. Nandakumar, K. Kim, and S. Winderbaum, “Low-

- absorbing and thermally stable industrial silicon nitride films with very low surface recombination,” *IEEE J. Photovoltaics*, vol. 7, no. 4, pp. 996–1003, 2017.
- [126] M. Cardona, “Vibrational-Spectra of Hydrogen in Silicon and Germanium,” *Phys. Status Solidi B*, vol. 118, no. 2, pp. 463–481, 1983.
 - [127] Z. Yin and F. W. Smith, “Optical dielectric function and infrared absorption of hydrogenated amorphous silicon nitride films: Experimental results and effective-medium-approximation analysis,” *Phys. Rev. B*, vol. 42, no. 6, pp. 3666–3675, 1990.
 - [128] F. Giorgis *et al.*, “Optical, structural and electrical properties of device-quality hydrogenated amorphous silicon-nitrogen films deposited by plasma-enhanced chemical vapour deposition,” *Philos. Mag. Part B*, vol. 77, no. 4, pp. 925–944, 1998.
 - [129] H. MäcKel and R. Lüdemann, “Detailed study of the composition of hydrogenated SiN_x layers for high-quality silicon surface passivation,” *J. Appl. Phys.*, vol. 92, no. 5, pp. 2602–2609, 2002.
 - [130] J. Hong, W. M. M. Kessels, W. J. Soppe, a. W. Weeber, W. M. Arnoldbik, and M. C. M. van de Sanden, “Influence of the high-temperature ‘firing’ step on high-rate plasma deposited silicon nitride films used as bulk passivating antireflection coatings on silicon solar cells,” *J. Vac. Sci. Technol. B Microelectron. Nanom. Struct.*, vol. 21, no. 5, p. 2123, 2003.
 - [131] J. D. Moschner, J. Henze, J. Schmidt, and R. Hezel, “High-quality surface passivation of silicon solar cells in an industrial-type inline plasma silicon nitride deposition system,” *Prog. Photovoltaics Res. Appl.*, vol. 12, no. 1, pp. 21–31, 2004.
 - [132] H. F. W. Dekkers, S. De Wolf, G. Agostinelli, F. Duerinckx, and G. Beaucarne, “Requirements of PECVD SiN_x:H layers for bulk passivation of mc-Si,” *Sol. Energy Mater. Sol. Cells*, vol. 90, no. 18–19, pp. 3244–3250, 2006.
 - [133] A. Cuevas, F. Chen, J. Tan, H. MäcKel, S. Winderbaum, and K. Roth, “FTIR analysis of microwave-excited pecvd silicon nitride layers,” *Conf. Rec. 2006 IEEE 4th World Conf. Photovolt. Energy Conversion, WCPEC-4*, vol. 1, pp. 1148–1151, 2007.
 - [134] H. MäcKel, D. M. Hulji, and R. Lüdemann, “Passivation Quality and Thermal Stability of Silicon Nitride Layers on Silicon and Phosphorus-Diffused Siliconsolar Cell Emitters,” pp. 1665–1674, 2001.
 - [135] M. Stavola *et al.*, “Hydrogenation of Si from SiN/sub x/:H films: how much hydrogen is really in the Si?,” in *Photovoltaic Energy Conversion, 2003. Proceedings of 3rd World Conference on*, 2003, vol. 1, pp. 909–912 Vol.1.
 - [136] J. K. Holt, D. G. Goodwin, A. M. Gabor, F. Jiang, M. Stavola, and H. A. Atwater, “Hot-wire chemical vapor deposition of high hydrogen content silicon nitride for solar cell passivation and anti-reflection coating applications,” *Thin Solid Films*, vol. 430, no. 1–2, pp. 37–40, 2003.
 - [137] S. Winderbaum, A. J. Leo, S. P. Shea, T. D. Koval, and B. Kumar, “Characterisation of industrial-scale remote PECVD SiN depositions,” *IEEE 3rd World Conf. Photovolt. Energy Convers.*, pp. 1128–1130, 2003.
 - [138] W. Soppe, H. Rieffe, and A. Weeber, “Bulk and surface passivation of silicon solar cells accomplished by silicon nitride deposited on industrial scale by microwave PECVD,” *Prog. Photovoltaics Res. Appl.*, vol. 13, no. 7, pp. 551–569, 2005.
 - [139] Z. Hameiri, N. Borojevic, L. Mai, N. Nandakumar, K. Kim, and S. Winderbaum, “Thermally Stable and Low-Absorbing Industrial Silicon Nitride Films with very Low Surface Recombination,” pp. 1–8, 2017.
 - [140] P. S. Peercy, H. J. Stein, B. L. Doyle, S. T. Picraux, and S. Laboratoriest, “Hydrogen concentration profiles and chemical bonding in silicon nitride,” *J. Electron. Mater.*, vol. 8, no. 1, pp. 11–24, 1979.
 - [141] M. Takahashi, M. Maeda, and Y. Sakakibara, “Determination of hydrogen concentration in PCVD silicon nitride films by elastic recoil detection analysis,” *Jpn. J. Appl. Phys.*, vol. 26, no. 9, pp. 1606–1607, 1987.
 - [142] S. Joos, Y. Schiele, B. Terheiden, H.-W. Becker, D. Rogalla, and G. Hahn, “Fundamental studies of hydrogen at the silicon / silicon nitride interface,” *Energy Procedia*, vol. 00,

- pp. 1–5, 2014.
- [143] F. Jiang *et al.*, “Hydrogenation of Si from SiN_x(H) films: Characterization of H introduced into the Si,” *Appl. Phys. Lett.*, vol. 83, no. 5, pp. 931–933, 2003.
 - [144] T. Niewelt, W. Kwapil, M. Selinger, A. Richter, and M. C. Schubert, “Stability of effective lifetime of float-zone silicon wafers with AlO_x surface passivation schemes under illumination at elevated temperature,” *Energy Procedia*, vol. 124, no. September, pp. 146–151, 2017.
 - [145] J. J. Mei, H. Chen, W. Z. Shen, and H. F. W. Dekkers, “Optical properties and local bonding configurations of hydrogenated amorphous silicon nitride thin films,” *J. Appl. Phys.*, vol. 100, no. 7, 2006.
 - [146] M. L. Reed and J. D. Plummer, “Chemistry of Si-SiO₂ interface trap annealing,” *J. Appl. Phys.*, vol. 63, no. 12, pp. 5776–5793, Jun. 1988.
 - [147] M. L. Green, E. P. Gusev, R. Degraeve, and E. L. Garfunkel, “Ultrathin (<4 nm) SiO₂ and Si–O–N gate dielectric layers for silicon microelectronics: Understanding the processing, structure, and physical and electrical limits,” *J. Appl. Phys.*, vol. 90, no. 5, pp. 2057–2121, Aug. 2001.
 - [148] A. G. Aberle, S. Glunz, and W. Warta, “Impact of illumination level and oxide parameters on Shockley-Read-Hall recombination at the Si-SiO₂ interface,” *J. Appl. Phys.*, vol. 71, no. 9, pp. 4422–4431, 1992.
 - [149] H. Jin, K. J. Weber, N. C. Dang, and W. E. Jellett, “Defect generation at the Si–SiO₂ interface following corona charging,” *Appl. Phys. Lett.*, vol. 90, no. 26, p. 262109, Jun. 2007.
 - [150] TIBCO, “StatisticaTM.” [Online]. Available: <https://www.tibco.com/products/tibco-statistica#resources>.
 - [151] J. M. Hilbe and J. M. Hilbe, “STATISTICA 7: An overview,” *Am. Stat.*, vol. 61, no. 1, pp. 91–94, 2007.
 - [152] G. E. P. Box and K. B. Wilson, “On the experimental attainment of optimum conditions Author (s): G. E. P. Box and K. B. Wilson,” *R. Stat. Society. Ser. B*, vol. 13, no. 1, pp. 1–45, 1951.
 - [153] M. P. Iwundu, “The Effects of Addition of n c Center Points on the Optimality of Box-Benhken and Box-Wilson Second-Order Designs,” *Int. J. Probab. Stat.*, vol. 6, no. 2, pp. 20–32, 2017.
 - [154] G. E. P. Box and D. W. Behnken, “Some new three level designs for the study of variables quantitative,” *Technometrics*, vol. 2, no. 4, pp. 455–475, 1960.
 - [155] W. R. Rice, “Analyzing tables of statistical tests,” *Evolution (N. Y.)*, vol. 43, no. 1, pp. 223–225, 1989.
 - [156] W. Kern and J. E. Soc, “The evolution of silicon wafer cleaning technology,” *J. Electrochem. Soc.*, vol. 137, no. 6, pp. 1887–1892, 1990.
 - [157] M. Burger, “MAiA manual,” 2001.
 - [158] D. T. Stevenson and R. J. Keyes, “Measurement of Carrier Lifetimes in Germanium and Silicon,” *J. Appl. Phys.*, vol. 26, no. 2, pp. 190–195, Feb. 1955.
 - [159] R. A. Sinton, “WCT-120 Photoconductance Lifetime Tester: User Manual,” 2006.
 - [160] A. Cuevas and D. Macdonald, “Measuring and interpreting the lifetime of silicon wafers,” *Sol. Energy*, vol. 76, no. 1–3, pp. 255–262, 2004.
 - [161] C. Berge, J. Schmidt, B. Lenkeit, H. Nagel, and A. G. Aberle, “Comparison of effective carrier lifetimes in silicon determined by transient and quasi-steady-state photoconductance measurements,” *2nd World Conf. Exhib. Photovolt. Sol. Energy Convers.*, no. JULY, pp. 1426–1429, 1998.
 - [162] T. Tiedje, J. I. Haberman, R. W. Francis, and A. K. Ghosh, “An rf bridge technique for contactless measurement of the carrier lifetime in silicon wafers,” *J. Appl. Phys.*, vol. 54, no. 5, pp. 2499–2503, May 1983.
 - [163] A. Schenk, “Finite-temperature full random-phase approximation model of band gap narrowing for silicon device simulation,” *J. Appl. Phys.*, vol. 84, no. 7, pp. 3684–3695, 1998.

- [164] R. Dumbrell, M. K. Juhl, T. Trupke, and Z. Hameiri, "Extracting metal contact recombination parameters from effective lifetime data," *IEEE J. Photovoltaics*, vol. Accepted, 2018.
- [165] F. J. Ma, S. Duttagupta, M. Peters, G. S. Samudra, A. G. Aberle, and B. Hoex, "Numerical modelling of silicon p+ emitters passivated by a PECVD $\text{AlO}_x/\text{SiN}_x$ stack," *Energy Procedia*, vol. 33, pp. 104–109, 2013.
- [166] Lachlan E. Black, *New perspectives on surface passivation: Understanding the Si- Al_2O_3 interface*, no. April. Canberra: Springer, 2016.
- [167] M. Pawlik *et al.*, "Electrical and chemical studies on Al_2O_3 passivation activation process," *Energy Procedia*, vol. 60, no. C, pp. 85–89, 2014.
- [168] A. G. Aberle, S. W. Glunz, and W. Warta, "Impact of illumination level and oxide parameters recombination at the Si- SiO_2 interface," vol. 4422, no. 1992, pp. 4422–4431, 1992.
- [169] Z. Xin *et al.*, "An Improved Methodology for Extracting the Interface Defect Density of Passivated Silicon Solar Cells," *IEEE J. Photovoltaics*, vol. 6, no. 5, pp. 1–10, 2016.
- [170] M. Wilson, "COCOS (corona oxide characterization of semiconductor) non-contact metrology for gate dielectrics," *AIP Conf. Proc.*, vol. 550, pp. 220–225, 2001.
- [171] M. Wilson *et al.*, "The present status and recent advancements in Corona-Kelvin non-contact electrical metrology of dielectrics for IC-manufacturing," *ECS Trans.*, vol. 3, no. 3, pp. 3–24, 2006.
- [172] P. Edelman, A. M. Hoff, L. Jastrzebski, and J. Lagowski, "New approach to measuring oxide charge and mobile ion concentration," *Proc. SPIE - Int. Soc. Opt. Eng.*, vol. 2337, no. September 1994, 1994.
- [173] J. Lagowski and P. Edelman, "Defect recognition and image processing in semiconductors," in *Proceedings of the Seventh International Conference, Berlin, Germany*, 1997, vol. 160, p. 133.
- [174] S. S. Li, *Semiconductor physics electronics*, 2nd ed., no. 1. 2006.
- [175] M. Wilson, "Semilab SDI PV2000A: Non contact dielectric metrology," 2016.
- [176] S. Kühnhold-Pospischil, P. Saint-Cast, A. Richter, and M. Hofmann, "Activation energy of negative fixed charges in thermal ALD Al_2O_3 ," *Appl. Phys. Lett.*, vol. 109, no. 6, 2016.
- [177] P. R. Griffiths and J. A. De Haseth, *Fourier transform infrared spectrometry*, vol. 171. John Wiley & Sons, 2007.
- [178] K. Kitamura and K. Hozumi, "Effect of the degree of polynomials in the Savitzky-Golay method for calculation of second-derivative spectra," *Anal. Chim. Acta*, vol. 172, no. C, pp. 111–118, 1985.
- [179] B. Min, H. Wager, M. Müller, H. Neuhaus, R. Brendel, and P. P. Altermatt, "Incremental Efficiency Improvements of Mass-produced PERC Cells up to 24%, Predicted solely with continuous Development of Existing Technologies and Wafer Materials," *31st Eur. Photovolt. Sol. Energy Conf. Exhib.*, no. January 2016, pp. 473–476, 2015.
- [180] G. Dingemans, F. Einsele, W. Beyer, M. C. M. Van de Sanden, and W. M. M. Kessels, "Influence of annealing and Al_2O_3 properties on the hydrogen-induced passivation of the Si/ SiO_2 interface," *J. Appl. Phys.*, vol. 111, no. 9, p. 93713, 2012.
- [181] J. Schmidt, F. Werner, B. Veith, and D. Zielke, "Industrially relevant Al_2O_3 deposition techniques for the surface passivation of Si solar cells," in *EUPVSEC*, 2010, no. September, pp. 4–7.
- [182] V. Naumann, M. Otto, R. B. Wehrspohn, and C. Hagendorf, "Chemical and structural study of electrically passivating $\text{Al}_2\text{O}_3/\text{Si}$ interfaces prepared by atomic layer deposition," *J. Vac. Sci. Technol. A Vacuum, Surfaces, Film.*, vol. 30, no. 4, p. 04D106, 2012.
- [183] J. Yang, B. S. Eller, M. Kaur, and R. J. Nemanich, "Characterization of plasma-enhanced atomic layer deposition of Al_2O_3 using dimethylaluminum isopropoxide," *J. Vac. Sci. Technol. A Vacuum, Surfaces, Film.*, vol. 32, no. 2, p. 021514, 2014.
- [184] X. Fang, Y. Li, X. Wang, J. Ding, and N. Yuan, "Ultrathin interdigitated back-contacted silicon solar cell with light-trapping structures of Si nanowire arrays," *Sol. Energy*, vol. 116, pp. 100–107, 2015.

- [185] X. Y. Chen, W. J. Xue, Y. Qin, X. L. Jiang, H. P. Yin, and W. Shan, "Effect of Al_2O_3 film on silver paste contact formation at silicon surface," *Sol. Energy*, vol. 158, pp. 917–921, 2017.
- [186] P. J. Cousins *et al.*, "Generation 3: Improved performance at lower cost," in *Conference Record of the IEEE Photovoltaic Specialists Conference*, 2010, pp. 275–278.
- [187] F. Werner, Y. Larionova, D. Zielke, T. Ohrdes, and J. Schmidt, "Aluminum-oxide-based inversion layer solar cells on n -type crystalline silicon: Fundamental properties and efficiency potential," *J. Appl. Phys.*, vol. 115, no. 7, 2014.
- [188] B. Hoex, M. C. M. van de Sanden, J. Schmidt, R. Brendel, and W. M. M. Kessels, "Surface passivation of phosphorus-diffused n+-type emitters by plasma-assisted atomic-layer deposited Al_2O_3 ," *Phys. Status Solidi - Rapid Res. Lett.*, vol. 6, no. 1, pp. 4–6, 2012.
- [189] A. Richter, J. Benick, A. Kimmerle, M. Hermle, and S. W. Glunz, "Passivation of phosphorus diffused silicon surfaces with Al_2O_3 : Influence of surface doping concentration and thermal activation treatments," *J. Appl. Phys.*, vol. 116, no. 24, 2014.
- [190] Tom Kenning, "LONGi hits record 23.6% conversion efficiency for mono PERC solar cells," *PV-Tech*, 2018.
- [191] Thermofisher, "Advantage Data System," *Thermofisher*, 2008. [Online]. Available: <https://www.thermofisher.com/order/catalog/product/IQLAADGACKFAKRMAVI>.
- [192] M. Belyansky, *Thin film deposition for front end of line: The effect of the semiconductor scaling, strain engineering and pattern effects*. Elsevier Inc., 2018.
- [193] K. Kimoto *et al.*, "Coordination and interface analysis of atomic-layer-deposition Al_2O_3 on Si(001) using energy-loss near-edge structures," *Appl. Phys. Lett.*, vol. 83, no. 21, pp. 4306–4308, 2003.
- [194] K. Kim, Z. Hameiri, N. Borojevic, S. Duttgupta, and S. Winderbaum, "Outstanding as-deposited surface passivation by industrial PECVD aluminum oxide," in *Proceedings of the 43rd IEEE Photovoltaic Specialists Conference*, 2016, pp. 2917–2921.
- [195] M. Wilson *et al.*, "Experimental study on the role of parameters affecting surface recombination and emitter passivation," *2014 IEEE 40th Photovolt. Spec. Conf. PVSC 2014*, pp. 713–718, 2014.
- [196] A. G. Aberle, S. W. Glunz, A. W. Stephens, and M. A. Green, "High-efficiency silicon solar cells: Si/ SiO_2 , interface parameters and their impact on device performance," *Prog. Photovoltaics Res. Appl.*, vol. 2, no. 4, pp. 265–273, Oct. 1994.
- [197] A. Shih, S. H. Yeh, S. C. Lee, and T. R. Yang, "Structural differences between deuterated and hydrogenated silicon nitride/oxyntiride," *J. Appl. Phys.*, vol. 89, no. 10, pp. 5355–5361, 2001.
- [198] K. Bordo and H. G. Rubahn, "Effect of deposition rate on structure and surface morphology of thin evaporated al films on dielectrics and semiconductors," *Medziagotyra*, vol. 18, no. 4, pp. 313–317, 2012.
- [199] I. Levin and D. Brandon, "Metastable alumina polymorphs: Crystal structures and transition sequences," *J. Am. Ceram. Soc.*, vol. 81, no. 8, pp. 1995–2012, 1998.
- [200] K. Kimura, "Recent developments in polycrystalline silicon solar cells," in *Technical Digest, International PVSEC-1*, 1984, vol. 3741.
- [201] A. Cuevas, M. J. Kerr, and J. Schmidt, "Passivation of crystalline silicon using silicon nitride," in *Proceedings of 3rd World Conference on Photovoltaic Energy Conversion*, 2003, pp. 913–918.
- [202] H. Yoshioka, M. Yamazaki, and S. Harada, "Reduction of interface states by hydrogen treatment at the aluminum oxide/4H-SiC Si-face interface," *AIP Adv.*, vol. 6, no. 10, pp. 1–7, 2016.
- [203] K. Matsunaga, T. Tanaka, T. Yamamoto, and Y. Ikuhara, "First-principles calculations of intrinsic defects in Al_2O_3 ," *Phys. Rev. B*, vol. 68, no. 8, p. 085110, 2003.
- [204] L. E. Black, T. C. Kho, K. R. McIntosh, and A. Cuevas, "The influence of orientation and morphology on the passivation of crystalline silicon surfaces by Al_2O_3 ," *Energy Procedia*, vol. 55, pp. 750–756, 2014.
- [205] T. T. Li and A. Cuevas, "Effective surface passivation of crystalline silicon by rf

- sputtered aluminum oxide,” *Phys. Status Solidi - Rapid Res. Lett.*, vol. 3, no. 5, pp. 160–162, 2009.
- [206] P. G. Vermont, V. Kuznetsov, and E. H. A. Granneman, “High-throughput solar cell passivation on in-line levitrack al₂O₃ system-demonstration of process performance,” in *Proceedings of the 26th European Photovoltaic Solar Energy Conference, Hamburg, Germany*, 2011, pp. 1644–1647.
 - [207] P. Saint-cast, “Passivation of Si Surfaces by PECVD Aluminum Oxide,” 2012.
 - [208] B. Hoex, M. Bosman, N. Nandakumar, and W. M. M. Kessels, “C-Si surface passivation by aluminium oxide studied with electron energy loss spectroscopy,” in *39th IEEE photovoltaic specialists conference*, 2013, no. 1, pp. 3333–3336.
 - [209] F. Werner *et al.*, “Electronic and chemical properties of the c-Si/Al₂O₃ interface,” *J. Appl. Phys.*, vol. 109, no. 11, p. 113701, 2011.
 - [210] K. Kim, N. Borojevic, S. Winderbaum, S. Duttagupta, X. Zhang, and J. Park, “Investigation of industrial PECVD AlO_x films with very low surface recombination,” *Sol. Energy*, vol. 186, pp. 94–105, 2019.
 - [211] T. Trupke, B. Mitchell, J. W. Weber, W. McMillan, R. A. Bardos, and R. Kroeze, “Photoluminescence imaging for photovoltaic applications,” *Energy Procedia*, vol. 15, no. 2011, pp. 135–146, 2012.
 - [212] D. Mitchell, “SITools - DigitalMicrograph™ Scripting.” [Online]. Available: www.dmscripting.com/sitools.html.
 - [213] K. Kimoto, K. Ishizuka, T. Mizoguchi, I. Tanaka, and Y. Matsui, “The study of Al-L₂₃ ELNES with resolution-enhancement software and first-principles calculation,” *J. Electron Microsc. (Tokyo)*, vol. 52, no. 3, pp. 299–303, 2003.
 - [214] G. Kissinger, D. Kot, M. Klingsporn, M. A. Schubert, A. Sattler, and T. Müller, “Investigation of the copper gettering mechanism of oxide precipitates in silicon,” *ECS J. Solid State Sci. Technol.*, vol. 4, no. 9, pp. N124–N129, 2015.
 - [215] J. R. Weber, A. Janotti, and C. G. Van de Walle, “Native defects in Al₂O₃ and their impact on III-V/Al₂O₃ metal-oxide-semiconductor-based devices,” *J. Appl. Phys.*, vol. 109, no. 3, p. 033715, 2011.
 - [216] D. Bouchet and C. Colliex, “Experimental study of ELNES at grain boundaries in alumina: Intergranular radiation damage effects on Al-L₂₃ and O-K edges,” *Ultramicroscopy*, vol. 96, no. 2, pp. 139–152, 2003.
 - [217] T. Lauinger, J. Schmidt, A. G. Aberle, and R. Hezel, “Surface passivation properties of silicon/silicon oxide/silicon nitride structures for solar cells,” *Proceeding 13th Eur. Photovolt. Sol. Energy Conf. Nice, Fr.*, no. May 2014, pp. 1291–1294, 1995.
 - [218] K. Wefers and C. Misra, “Oxides and hydroxides of aluminum,” *Alcoa Tech. Pap.*, vol. 19, pp. 1–100, 1987.
 - [219] R. -S Zhou and R. L. Snyder, “Structures and transformation mechanisms of the η , γ and θ transition aluminas,” *Acta Crystallogr. Sect. B*, vol. 47, no. 5, pp. 617–630, 1991.
 - [220] P. S. Santos, H. S. Santos, and S. P. Toledo, “Standard transition aluminas. Electron microscopy studies,” *Mater. Res.*, vol. 3, no. 4, pp. 104–114, 2000.
 - [221] G. Busca, “The surface of transitional aluminas: A critical review,” *Catal. Today*, vol. 226, pp. 2–13, 2014.
 - [222] L. Shi, “Contact resistance study on polycrystalline silicon thin-film solar cells on glass,” Thesis (Masters) - University of New South Wales, 2008.
 - [223] S. Mack *et al.*, “Silicon surface passivation by thin thermal oxide/PECVD layer stack systems,” *IEEE J. Photovoltaics*, vol. 1, no. 2, pp. 135–145, 2011.
 - [224] T. W. Swaddle, “Chapter 7 - Silicates, Aluminates, and Phosphates,” in *Inorganic Chemistry*, T. W. B. T.-I. C. Swaddle, Ed. San Diego: Academic Press, 1997, pp. 129–152.
 - [225] J. Koga, S. Takagi, and A. Toriumi, “Observation of Oxide Dependent Interface Roughness,” *Jpn. J. Appl. Phys.*, vol. 35, no. 1, pp. 1440–1444, 1996.
 - [226] D. Sperber, F. Furtwängler, A. Herguth, and G. Hahn, “On the stability of dielectric passivation layers under illumination and temperature treatment,” in *32nd European*

- Photovoltaic Solar Energy Conference and Exhibition*, 2016, pp. 523–526.
- [227] S. W. Glunz, S. Rein, W. Warta, J. Knobloch, and W. Wettling, “Degradation of carrier lifetime in Cz silicon solar cells,” *Sol. Energy Mater. Sol. Cells*, vol. 65, no. 1, pp. 219–229, 2001.
 - [228] K. Bothe and J. Schmidt, “Electronically activated boron-oxygen-related recombination centers in crystalline silicon,” *J. Appl. Phys.*, vol. 99, no. 1, pp. 013701-1-013701-11, 2006.
 - [229] K. Nakayashiki *et al.*, “Engineering solutions and root-cause analysis for light-induced degradation in p-type multicrystalline silicon PERC modules,” *IEEE J. Photovoltaics*, vol. 6, no. 4, pp. 860–868, 2016.
 - [230] M. A. Jensen, A. E. Morishige, J. Hofstetter, D. B. Needleman, and T. Buonassisi, “Evolution of p-type LeTID defects in multicrystalline silicon during degradation and regeneration,” *IEEE J. Photovoltaics*, vol. 7, no. 4, pp. 980–987, 2017.
 - [231] T. Niewelt, J. Sch, W. Warta, S. W. Glunz, and M. C. Schubert, “Degradation of crystalline silicon due to boron–oxygen defects,” *IEEE J. Photovoltaics*, vol. preprint, no. 1, pp. 383–398, 2016.
 - [232] B. Hallam *et al.*, “Eliminating light-induced degradation in commercial p-type Czochralski silicon solar cells,” *Appl. Sci.*, vol. 8, no. 10, pp. 1–19, 2017.
 - [233] C. Vargas *et al.*, “Carrier-induced degradation in multicrystalline silicon : Dependence on the silicon nitride passivation layer and hydrogen released during firing,” *IEEE J. Photovoltaics*, vol. 8, no. 2, pp. 413–420, 2018.
 - [234] K. Ramspeck *et al.*, “Light induced degradation of rear passivated mc-Si solar cells,” in *27th European Photovoltaic Solar Energy Conference and Exhibition*, 2012, pp. 861–865.
 - [235] K. Krauss, F. Fertig, D. Menzel, and S. Rein, “Light-induced degradation of silicon solar cells with aluminium oxide passivated rear side,” *Energy Procedia*, vol. 77, pp. 599–606, 2015.
 - [236] F. Kersten *et al.*, “Degradation of multicrystalline silicon solar cells and modules after illumination at elevated temperature,” *Sol. Energy Mater. Sol. Cells*, vol. 142, pp. 83–86, 2015.
 - [237] J. Lindroos and H. Savin, “Review of light-induced degradation in crystalline silicon solar cells,” *Sol. Energy Mater. Sol. Cells*, vol. 147, pp. 115–126, 2016.
 - [238] A. E. Morishige *et al.*, “Lifetime spectroscopy investigation of light-induced degradation in p-type multicrystalline silicon PERC,” *IEEE J. Photovoltaics*, vol. 6, no. 6, pp. 1466–1472, 2016.
 - [239] C. E. Chan *et al.*, “Rapid stabilization of high-performance multi-crystalline p-type silicon PERC cells,” *IEEE J. Photovoltaics*, vol. 6, no. 6, pp. 1473–1479, 2016.
 - [240] D. N. R. Payne *et al.*, “Rapid passivation of carrier-induced defects in p-type multicrystalline silicon,” *Sol. Energy Mater. Sol. Cells*, vol. 158, pp. 102–106, 2016.
 - [241] K. Petter *et al.*, “Dependence of LeTID on brick height for different wafer suppliers with several resistivities and dopants,” *9th Int. Work. Cryst. Silicon Sol. Cells*, vol. 6, no. 4, pp. 1–17, 2016.
 - [242] D. N. R. Payne *et al.*, “Rapid passivation of carrier-induced defects in p-type multicrystalline silicon,” *Sol. Energy Mater. Sol. Cells*, vol. 158, no. Part 1, pp. 102–106, 2016.
 - [243] D. Chen *et al.*, “Evidence of an identical firing-activated carrier-induced defect in monocrystalline and multicrystalline silicon,” *Sol. Energy Mater. Sol. Cells*, vol. 172, pp. 293–300, 2017.
 - [244] D. Bredemeier, D. Walter, S. Herlufsen, and J. Schmidt, “Lifetime degradation and regeneration in multicrystalline silicon under illumination at elevated temperature,” *AIP Adv.*, vol. 6, no. 3, pp. 6–14, 2016.
 - [245] R. Eberle, W. Kwapil, F. Schindler, M. C. Schubert, and S. W. Glunz, “Impact of the firing temperature profile on light induced degradation of multicrystalline silicon,” *Phys. Status Solidi - Rapid Res. Lett.*, vol. 10, no. 12, pp. 861–865, 2016.
 - [246] D. Sperber, A. Herguth, and G. Hahn, “Investigating possible causes of light induced

- degradation in boron-doped float-zone silicon,” in *EUPVSEC*, 2017, pp. 565–568.
- [247] F. Kersten, J. Heitmann, and J. W. Muller, “Influence of Al₂O₃ and SiN_x passivation layers on LeTID,” *Energy Procedia*, vol. 92, pp. 828–832, 2016.
 - [248] S. Wilking, A. Herguth, and G. Hahn, “Influence of hydrogen on the regeneration of boron-oxygen related defects in crystalline silicon,” *J. Appl. Phys.*, vol. 113, no. 19, 2013.
 - [249] N. Nampalli, B. Hallam, C. Chan, M. Abbott, and S. Wenham, “Evidence for the role of hydrogen in the stabilization of minority carrier lifetime in boron-doped Czochralski silicon,” *Appl. Phys. Lett.*, vol. 106, no. 173501, 2015.
 - [250] A. Kimmerle, J. Greulich, and A. Wolf, “Carrier-diffusion corrected J₀-analysis of charge carrier lifetime measurements for increased consistency,” *Sol. Energy Mater. Sol. Cells*, vol. 142, pp. 116–122, 2015.
 - [251] A. Cuevas and D. Yan, “Misconceptions and misnomers in solar cells,” *IEEE J. Photovoltaics*, vol. 3, no. 2, pp. 916–923, 2013.
 - [252] H. Li, B. Hallam, S. Wenham, and M. Abbott, “Oxidation drive-in to improve industrial emitter performance by POCl₃ diffusion,” *IEEE J. Photovoltaics*, vol. 7, no. 1, pp. 144–152, 2017.
 - [253] H. Li, K. Kim, B. Hallam, B. Hoex, S. Wenham, and M. Abbott, “POCl₃ diffusion for industrial Si solar cell emitter formation,” *Front. Energy*, vol. 11, no. 1, pp. 42–51, 2017.
 - [254] J. M. Dorkel and P. Leturcq, “Carrier mobilities in silicon semi-empirically related to temperature, doping and injection level,” *Solid State Electron.*, vol. 24, no. 9, pp. 821–825, 1981.
 - [255] A. B. Sproul and M. A. Green, “Improved value for the silicon from 275 to 375 K intrinsic carrier concentration,” *J. Appl. Phys.*, vol. 70, no. 2, pp. 846–854, 1991.
 - [256] S. Wang and D. MacDonald, “Temperature dependence of Auger recombination in highly injected crystalline silicon,” *J. Appl. Phys.*, vol. 112, no. 11, pp. 3–7, 2012.
 - [257] R. A. Sinton, “private communication,” Mar-2016.
 - [258] A. Richter, F. Werner, A. Cuevas, J. Schmidt, and S. W. Glunz, “Improved parameterization of Auger recombination in silicon,” *Energy Procedia*, vol. 27, pp. 88–94, 2012.
 - [259] B. Min, A. Dastgheib-Shirazi, P. P. Altermatt, and H. Kurz, “Accurate determination of the emitter saturation current density for industrial p-diffused emitters,” in *29th European Photovoltaic Solar Energy Conference and Exhibition*, 2014, pp. 463–466.
 - [260] M. Kessler, T. Ohrdes, P. P. Altermatt, and R. Brendel, “The effect of sample edge recombination on the averaged injection-dependent carrier lifetime in silicon,” *J. Appl. Phys.*, vol. 111, no. 5, 2012.
 - [261] B. Veith *et al.*, “Injection dependence of the effective lifetime of n-type Si passivated by Al₂O₃: An edge effect?,” *Sol. Energy Mater. Sol. Cells*, vol. 120, no. PART A, pp. 436–440, 2014.
 - [262] C. E. Chan, M. D. Abbott, M. K. Juhl, B. J. Hallam, B. Xiao, and S. R. Wenham, “Assessing the performance of surface passivation using low-intensity photoluminescence characterization techniques,” *IEEE J. Photovoltaics*, vol. 4, no. 1, pp. 100–106, 2014.
 - [263] H. MacKel and K. Varner, “On the determination of the emitter saturation current density from lifetime measurements of silicon devices,” *Prog. Photovolt Res. Appl.*, vol. 21, pp. 850–866, 2013.
 - [264] P. Hamer, B. Hallam, R. S. Bonilla, P. P. Altermatt, P. Wilshaw, and S. Wenham, “Modelling of hydrogen transport in silicon solar cell structures under equilibrium conditions,” *J. Appl. Phys.*, vol. 043108, 2018.
 - [265] C. Chan *et al.*, “Modulation of carrier-induced defect kinetics in multi-crystalline silicon PERC cells through dark annealing,” *Phys. status solidi - Rapid Res. Lett.*, vol. 1, no. 2, p. 1600028, 2017.
 - [266] V. V. Voronkov and R. Falster, “Formation, dissociation, and diffusion of various hydrogen dimers in silicon,” *Phys. Status Solidi B*, vol. 254, no. 6, p. 1600779, 2017.
 - [267] P. M. Williams, G. D. Watkins, S. Uftring, and M. Stavola, “Structure-sensitive

- spectroscopy of transition-metal-hydrogen complexes in silicon,” *Phys. Rev. Lett.*, vol. 70, no. 24, pp. 3816–3819, 1993.
- [268] J.-U. Sachse, E. Ö. Sveinbjörnsson, W. Jost, and J. Weber, “Electrical properties of platinum-hydrogen complexes in silicon,” *Phys. Rev. B*, vol. 55, no. 24, pp. 16176–16185, 1997.
- [269] J.-U. Sachse, E. Ö. Sveinbjörnsson, N. Yarykin, and J. Weber, “Similarities in the electrical properties of transition metal-hydrogen complexes in silicon,” *Mater. Sci. Eng. B Solid-State Mater. Adv. Technol.*, vol. 58, no. 1, pp. 134–140, 1999.
- [270] S. Knack and J. Weber, “Copper-hydrogen complexes in silicon,” vol. 65, pp. 1–8, 2002.
- [271] N. Yarykin and A. Samples, “Deep levels of copper-hydrogen complexes in silicon,” vol. 085205, pp. 1–7, 2013.
- [272] L. Scheffler, V. Kolkovsky, J. Weber, L. Scheffler, V. Kolkovsky, and J. Weber, “Electrical levels in nickel doped silicon,” vol. 173704, no. 2014, 2017.
- [273] D. Bredemeier, D. C. Walter, and J. Schmidt, “Possible candidates for impurities in mc-Si wafers responsible for light-induced lifetime degradation and regeneration,” *Sol. RRL*, vol. 2, no. 1700159, 2018.
- [274] J. R. Elmiger and M. Kunst, “Investigation of charge carrier injection in silicon nitride/silicon junctions,” *Appl. Phys. Lett.*, vol. 69, no. 4, pp. 517–519, 1996.
- [275] G. Beylier, S. Bruyère, D. Benoit, and G. Ghibaudo, “Refined electrical analysis of two charge states transition characteristic of ‘borderless’ silicon nitride,” *Microelectron. Reliab.*, vol. 47, no. 4-5 SPEC. ISS., pp. 743–747, 2007.
- [276] S. Steingrube, P. P. Altermatt, D. S. Steingrube, J. Schmidt, and R. Brendel, “Interpretation of recombination at c-Si/SiNx interfaces by surface damage,” *J. Appl. Phys.*, vol. 108, no. 014506, 2010.
- [277] S. J. Pearton, J. W. Corbett, and J. T. Borenstein, “Hydrogen in crystalline semiconductors,” *Appl. Phys. A*, vol. 43, no. 3, pp. 153–195, 1987.
- [278] C. Herring, N. M. Johnson, and C. G. Van de Walle, “Energy levels of isolated interstitial hydrogen in silicon,” *Phys. Rev. B*, vol. 64, no. 12, p. 125209, 2001.
- [279] D. Sperber, A. Schwarz, A. Herguth, and G. Hahn, “Enhanced stability of passivation quality on diffused silicon surfaces under light-induced degradation conditions,” *Sol. Energy Mater. Sol. Cells*, vol. 188, no. December 2018, pp. 112–118, 2018.
- [280] C. D. J. Johnson, N. M. Herring c, “Interstitial hydrogen and neutralization of shallow-donor impurities in single-crystal silicon,” *Phys. Rev. Lett.*, vol. 56, no. 7, pp. 769–772, 1986.
- [281] A. Ciesla *et al.*, “Hydrogen-induced degradation,” in *7th World Conference on Photovoltaic Energy Conversion*, 2018.
- [282] J. Schmidt *et al.*, “Advances in the surface passivation of silicon solar cells,” *Energy Procedia*, vol. 15, no. 2011, pp. 30–39, 2012.
- [283] C.-M. Chou, C.-C. Chuang, C.-H. Lin, C.-J. Chung, and J.-L. He, “Plasma diagnostics for pulsed-dc plasma-polymerizing para-xylene using QMS and OES,” *Surf. Coatings Technol.*, vol. 205, no. 21–22, pp. 4880–4885, 2011.
- [284] J. S. Chun, “Characterization of trimethylaluminum-N₂/O₂-He glow discharge in chemical vapor deposition of aluminum oxide films,” *Thin Solid Films*, vol. 258, pp. 67–74, 1995.
- [285] K. Mackenzie, D. Johnson, C. Johnson, and L. Martinez, “Recent Developments in Real-Time Thickness Control Of Plasma Deposited Thin Film Dielectrics Using Optical Emission Interferometry,” *CS MANTECH Conf.*, no. 727, pp. 419–422, 2013.
- [286] A. Meiners, M. Leck, and B. Abel, “Multiple parameter optimization and spectroscopic characterization of a dielectric barrier discharge in N₂,” *Plasma Sources Sci. Technol.*, vol. 18, p. 045015, 2009.
- [287] S. Y. Moon, W. Y. Kim, H. C. Lee, S. W. Ahn, H. M. Lee, and W. Choe, “Measurement of rotational temperature using SiH (A₂ - X₂) emission spectrum in SiH₄ - H₂ plasmas,” *Phys. Plasmas*, vol. 17, no. 8, p. 083501, 2010.
- [288] M. Novotný *et al.*, “Optical emission and mass spectroscopy of plasma processes in

- reactive DC pulsed magnetron sputtering of aluminium oxide,” *J. Optoelectron. Adv. Mater.*, vol. 12, no. 3, pp. 697–700, 2010.
- [289] J. Perrin and E. Delafosse, “Emission spectroscopy of SiH in a silane glow-discharge,” *J. Phys. D. Appl. Phys.*, vol. 13, no. 5, pp. 759–765, 1980.
- [290] B. B. Sahu, J. G. Han, K. S. Shin, K. Ishikawa, M. Hori, and Y. Miyawaki, “Plasma diagnostic approach for high rate nanocrystalline Si synthesis in RF/UHF hybrid plasmas using a PECVD process,” *Plasma Sources Sci. Technol.*, vol. 24, no. 2, p. 25019, 2015.
- [291] B. Strahm, A. Feltrin, R. Bartlome, and C. Ballif, “Optical emission spectroscopy to diagnose powder formation in SiH₄-H₂ discharges,” in *SPIE conference on Thin Film Solar Technology*, 2009.
- [292] P. Tristant *et al.*, “Microwave plasma enhanced CVD of aluminum oxide films: OES diagnostics and influence of the RF bias,” *Thin Solid Films*, vol. 390, no. 1–2, pp. 51–58, 2001.
- [293] H. Yokoyama, “Optical Emission Spectroscopy of the SiH₄-NH₃-H₂ Plasma during the Growth of Silicon Nitride.pdf,” *Jpn. J. Appl. Phys.*, vol. 117, 1981.
- [294] Fantz, “Spectroscopic diagnostics and modelling of silane microwave plasmas,” *Plasma phys. Control Fusion*, vol. 1035, 1998.
- [295] O. Gabriel, S. Kirner, M. Klingsporn, F. Friedrich, B. Stannowski, and R. Schlattmann, “On the Plasma Chemistry During Plasma Enhanced Chemical Vapor Deposition of Microcrystalline Silicon Oxides,” *Plasma Process. Polym.*, vol. 12, no. 1, pp. 82–91, 2015.
- [296] Y.-H. Ham, K.-H. Kwon, and H.-W. Lee, “Deposition by the Plasma Diagnostics,” *J. Korean Inst. Electr. Electron. Mater. Eng.*, vol. 24, no. 2, pp. 89–94, 2011.
- [297] S. E. Hicks and R. a G. Gibson, “A spectroscopic investigation of growth regimes in silane-ammonia discharges used for plasma nitride deposition,” *Plasma Chem. Plasma Process.*, vol. 11, no. 4, pp. 455–472, 1991.
- [298] a a Howling, B. Strahm, P. Colsters, L. Sansonnens, and C. Hollenstein, “Fast equilibration of silane/hydrogen plasmas in large area RF capacitive reactors monitored by optical emission spectroscopy,” *Plasma Sources Sci. Technol.*, vol. 16, no. 4, pp. 679–696, 2007.
- [299] F. J. Kampas, “An optical emission study of the glow-discharge deposition of hydrogenated amorphous silicon from argon-silane mixtures,” *J. Appl. Phys.*, vol. 54, no. 5, pp. 2276–2280, 1983.
- [300] S. J. Kang and V. M. Donnelly, “Optical absorption and emission spectroscopy studies of ammonia-containing plasmas,” *Plasma Sources Sci. Technol.*, vol. 16, no. 2, pp. 265–272, 2007.
- [301] H. J. Lee, D. S. Seo, G. S. May, and S. J. Hong, “Use of in-situ optical emission spectroscopy for leak fault detection and classification in plasma etching,” *J. Semicond. Technol. Sci.*, vol. 13, no. 4, pp. 395–401, 2013.
- [302] M. Blech *et al.*, “Detailed study of PECVD silicon nitride and correlation of various characterization techniques,” in *24th European Photovoltaic Solar Energy Conference and Exhibition*, 2009, pp. 507–511.
- [303] M. J. Kerr and A. Cuevas, “General parameterization of Auger recombination in crystalline silicon,” *J. Appl. Phys.*, vol. 91, no. 3, pp. 2473–2480, 2002.
- [304] A. Richter, M. Hermle, and S. W. Glunz, “Reassessment of the limiting efficiency for crystalline silicon solar cells,” *IEEE J. Photovoltaics*, vol. 3, no. 4, pp. 1184–1191, 2013.
- [305] R. Sinton and T. Mankad, “Contactless Carrier-Lifetime Measurement in Silicon Wafers, Ingots, and Blocks,” pp. 1–14, 2010.
- [306] M. Ziaurrahman and M. J. Alam, “Bulk Recombination Lifetime of Minority Carrier in Compensated p-Si Solar Cell,” vol. 3, no. 4, pp. 3–6, 2013.
- [307] J. Irikawa, S. Miyajima, S. Kida, T. KidaWatahiki, and M. Konagai, “Effects of annealing and atomic hydrogen treatment on aluminum oxide passivation layers for crystalline silicon solar cells,” *Jpn. J. Appl. Phys.*, vol. 50, no. 1, pp. 1–5, 2011.
- [308] Y.-C. Kim, H.-H. Park, J. S. Chun, and W.-J. Lee, “Compositional and structural analysis

- of aluminum oxide films prepared by plasma-enhanced chemical vapor deposition,” *Thin Solid Films*, vol. 237, no. 1–2, pp. 57–65, 1994.
- [309] W. Liang, D. Suh, J. Yu, J. Bullock, and K. J. Weber, “Degradation of the surface passivation of plasma-assisted ALD Al_2O_3 under damp-heat exposure,” *Phys. Status Solidi Appl. Mater. Sci.*, vol. 212, no. 2, pp. 274–281, 2015.
 - [310] J. A. Töfflinger, “Interface investigations of passivating oxides and functional materials on crystalline silicon,” 2014.
 - [311] V. Verlaan, L. R. J. G. Van Den Elzen, G. Dingemans, M. C. M. Van De Sanden, and W. M. M. Kessels, “Composition and bonding structure of plasma-assisted ALD Al_2O_3 films,” *Phys. Status Solidi Curr. Top. Solid State Phys.*, vol. 7, no. 3–4, pp. 976–979, 2010.
 - [312] O. Gabriel, S. Kirner, M. Klick, B. Stannowski, and R. Schlatmann, “Plasma monitoring and PECVD process control in thin film silicon-based solar cell manufacturing,” *EPJ Photovoltaics*, vol. 5, p. 55202, Feb. 2014.
 - [313] K. O. Davis *et al.*, “Influence of precursor gas ratio and firing on silicon surface passivation by APCVD aluminium oxide,” *Phys. status solidi - Rapid Res. Lett.*, vol. 7, no. 11, pp. 942–945, 2013.
 - [314] T. Lüdera, T. Lauermann, a. Zuschlag, G. Hahn, and B. Terheiden, “ $\text{Al}_2\text{O}_3/\text{SiN}_x$ -stacks at increased temperatures: Avoiding blistering during contact firing,” *Energy Procedia*, vol. 27, no. April, pp. 426–431, 2012.
 - [315] M. . S.-C. P. Hofmann, M.; Jacklein, “Plasma Process Analysis of ICP-PECVD of AlO_x layers for c-Si surface passivation,” no. June, pp. 20–24, 2016.
 - [316] G. Dingemans, M. C. M. Van De Sanden, and W. M. M. Kessels, “Plasma-enhanced chemical vapor deposition of aluminum oxide using ultrashort precursor injection pulses,” *Plasma Process. Polym.*, vol. 9, no. 8, pp. 761–771, 2012.